LEABHARLANN CHOLÁISTE NA TRÍONÓIDE, BAILE ÁTHA CLIATH
Ollscoil Átha Cliath

TRINITY COLLEGE LIBRARY DUBLIN
The University of Dublin

Terms and Conditions of Use of Digitised Theses from Trinity College Library Dublin

Copyright statement

All material supplied by Trinity College Library is protected by copyright (under the Copyright and Related Rights Act, 2000 as amended) and other relevant Intellectual Property Rights. By accessing and using a Digitised Thesis from Trinity College Library you acknowledge that all Intellectual Property Rights in any Works supplied are the sole and exclusive property of the copyright and/or other IPR holder. Specific copyright holders may not be explicitly identified. Use of materials from other sources within a thesis should not be construed as a claim over them.

A non-exclusive, non-transferable licence is hereby granted to those using or reproducing, in whole or in part, the material for valid purposes, providing the copyright owners are acknowledged using the normal conventions. Where specific permission to use material is required, this is identified and such permission must be sought from the copyright holder or agency cited.

Liability statement

By using a Digitised Thesis, I accept that Trinity College Dublin bears no legal responsibility for the accuracy, legality or comprehensiveness of materials contained within the thesis, and that Trinity College Dublin accepts no liability for indirect, consequential, or incidental, damages or losses arising from use of the thesis for whatever reason. Information located in a thesis may be subject to specific use constraints, details of which may not be explicitly described. It is the responsibility of potential and actual users to be aware of such constraints and to abide by them. By making use of material from a digitised thesis, you accept these copyright and disclaimer provisions. Where it is brought to the attention of Trinity College Library that there may be a breach of copyright or other restraint, it is the policy to withdraw or take down access to a thesis while the issue is being resolved.

Access Agreement

By using a Digitised Thesis from Trinity College Library you are bound by the following Terms & Conditions. Please read them carefully.

I have read and I understand the following statement: All material supplied via a Digitised Thesis from Trinity College Library is protected by copyright and other intellectual property rights, and duplication or sale of all or part of any of a thesis is not permitted, except that material may be duplicated by you for your research use or for educational purposes in electronic or print form providing the copyright owners are acknowledged using the normal conventions. You must obtain permission for any other use. Electronic or print copies may not be offered, whether for sale or otherwise to anyone. This copy has been supplied on the understanding that it is copyright material and that no quotation from the thesis may be published without proper acknowledgement.

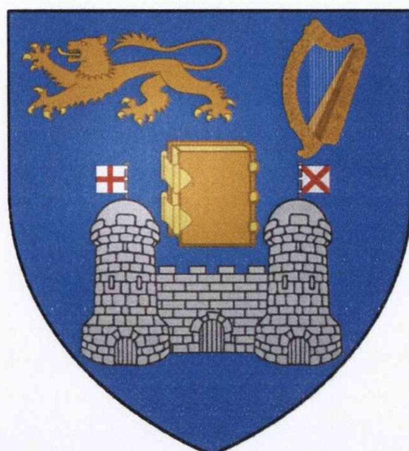

TRINITY COLLEGE DUBLIN

Novel System Development for Combined Scanning Tunneling Microscopy & Surface Stress Measurements to Investigate the Origins of Surface Forces

- Oxidation of the Si(111)-7x7 Surface

A thesis presented to the University of Dublin, Trinity College for the degree of Doctor of Philosophy

Niall T. Kinahan

School of Chemistry

Supervisor: Prof. John J. Boland

January 30th, 2009.

Declaration:

I hereby declare that:

This thesis has not been submitted as an exercise for a degree at this or any other University.

This work contained herein is entirely my own, except where otherwise cited, referenced, acknowledged or accredited.

I agree that the library of the University of Dublin, may at their discretion, lend or copy the thesis upon request.

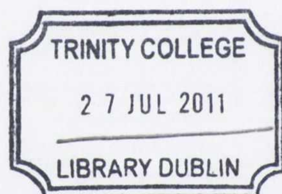
TRINITY COLLEGE
2 7 JUL 2011
LIBRARY DUBLIN
THESIS
9249

Acknowledgements

- I would like to thank my supervisor Prof. John Boland for all his support, advice and guidance throughout the years. I could not have completed this project without your encouragement, patience and constant optimism.

- I would also like to thank all current and former members of the Boland research group. I could not have hoped to have worked with a more supportive, talented and friendly group of individuals and I know that I have made many life-long friends. It has been a real pleasure to work with you all.

- I would especially like to thank Dr. Tetsuya Narushima for his enormous effort with the project and for his constant support and teachings. Your knowledge, humility and generosity cannot be overstated. Thank you for your friendship and I look forward to continuing to work closely with you in the future.

- I want to say a special thanks to my colleagues David Meehan and Steffen Sachart whom I have worked closely with over the course of my PhD. You both made every day in the lab interesting, different and thoroughly enjoyable. Thanks to each of you for your friendship, efforts and perseverance.

- In addition, I would like to extend thanks to our group administrator Mary McCarthy for all her hard work, dedication and kindness.

- I could never have achieved anything without the wonderful support of my family. My parents Brendan and Bernadette, I owe you more than I can say and I thank you for your love, help, complete support and advice now and always. I also want to thank my brother Thomas and my sisters Emer, Ashling and Therese. Your companionship and support is amazing. To my grandmother Teresa I extend

particular thanks. You have played a huge role in my life and I thank you for your love and support every day.

- I would like to thank my friends Dave, John, Bob, Sean and Yenny. Thank you for humour, encouragement and fantastic memories. I can't wait to see what you all do next and I look forward to many more happy adventures together in the near future.

- I would like to say a huge thanks to my girlfriend Evelyn. You have been my rock and my best friend. Thank you for your love, support, companionship and patience. You're simply the best.

- I would also like to thank our chief collaborator Prof. Kazushi Miki and his group members. Your efforts and contributions are very much appreciated.

- Finally, thanks to Science Foundation Ireland (SFI) and Intel Ireland for financial support which made this experience possible, and to my Intel mentor Chris Murray for his help and guidance.

Abstract

The oxidation of the silicon surface has been widely studied due to its vast scientific and technological importance. However, despite extensive work on the topic the exact details of the oxidation reaction still remain a contentious issue. It has been proposed that surface stress measurements may prove useful in elucidating this and related issues. In the case of adsorption on solid-state surfaces, induced surface stresses arise primarily from differences in atomic size and electronegativity, in addition to changes in surface morphology and defect formation. It is expected that the role of these induced stresses will become increasingly important as the scale of surface features is reduced and surface effects dominate. In order to address the effects of stress on surface chemical reactions we have developed an entirely novel system combining both surface stress measurement and scanning tunnelling microscopy (STM) capabilities. The former measurement is based on minute displacement monitoring of a large cantilever sample using capacitive sensing, which is capable of detecting strain energy changes with ~1-10 meV/atom resolution. The latter measurement permits direct observation of the atomic structure on the same cantilever. Nonetheless, such high precision combined measurements are extremely difficult to realise due to the architecture of the cantilever.

To achieve the desired goal, it was necessary to address two major difficulties: a) self-oscillation of the cantilever sample; b) sample heating. Following the implementation of novel ideas to tackle these and numerous other challenges, the atomic scale structural origins of reaction induced forces on surfaces can be elucidated. The combined application of these two measurement capabilities is extremely useful in providing a deeper understanding of atomic scale reaction processes on surfaces. In addition, our system is also equipped with a device for pushing the cantilever sample, which can be utilised to study the effects of artificially applied stress on reaction processes at the atomic level. In this thesis, the details of our novel measurement system will be presented, a discussion into the technical challenges encountered during the development process will be provided, along with a demonstration of the system performance through an investigation into the room temperature oxidation of the Si(111)-7x7 surface.

In relation to the oxidation process, we show that the initial oxidation period involves two compressive stress stages with different growth signatures. The atomic scale origins of the measured surface stress evolution will be discussed and supported via complementary STM data. In particular, we demonstrate that the initial rapid rise in compressive stress is associated with selective oxidation of the faulted-half units of the 7x7 reconstruction. The effects of an artificially applied stress as a means to alter the unit selectivity during the oxidation process will also be presented.

Table of Contents

DECLARATION ii

ACKNOWLEDGEMENTS iii

ABSTRACT v

TABLE OF CONTENTS vii

CHAPTER 1: INTRODUCTION 1

1.1. FORCES AT SURFACES 2

1.2. REVEALING THE ATOMIC SCALE ORIGINS OF SURFACE STRESS 6

1.2.1 Electron Stimulated Athermal Recrystallisation of Si(100) 6

1.2.2 Etching Enhanced Surface Stress Relaxation during Initial Ozone Oxidation ... 7

1.3. EFFECT OF ARTIFICIAL STRESS ON SURFACE PHENOMENA 11

1.4. RESEARCH OBJECTIVES 11

REFERENCES 13

CHAPTER 2: SCANNING TUNNELING MICROSCOPY 15

2.1. TUNNELING THEORY 15

2.2. METAL-INSULATOR-METAL TUNNELING: THEORY & EXPERIMENT... 19

2.3. BIRTH OF THE STM 24

2.4. CONSTANT CURRENT MODE: INTERMIXING OF GEOMETRIC & ELECTRONIC EFFECTS 26

2.5. SCANNING TUNNELING SPECTROSCOPY 29

2.6. INSTRUMENTATION 33

2.6.1 High Precision Mechanism 33

2.6.2 Coarse Approach Mechanism 35
2.6.3 Electronic Design 37
2.6.4 Vibration Isolation 39
2.7. TIP PREPARATION & TREATMENT 41
2.8. SURFACE PREPARATION TECHNIQUES 44
2.8.1 High Temperature Preparation 44
2.8.2 Intermediate Temperature Preparation 45
REFERENCES 46

CHAPTER 3: INTRODUCTION TO ULTRA-HIGH VACUUM 49
3.1. THE NECESSITY FOR ULTRA-HIGH VACUUM 50
3.2. ULTRA-HIGH VACUUM PUMPS 51
3.2.1 Rotary Pumps 53
3.2.2 Turbomolecular Pumps 55
3.2.3 Ion Pumps 58
3.3. VACUUM GAUGES 60
3.4. RESIDUAL GAS ANALYSERS 62
REFERENCES 66

CHAPTER 4: SURFACE STRESS - GENERAL DISCUSSION 68
4.1. DEFINITION OF SURFACE STRESS 69
4.2. THE CHARGE DISTRIBUTION AND SURFACE STRESS ON CLEAN SURFACES 70
4.3. ADSORBATE INDUCED STRESSES 74
4.4. EXPERIMENTAL TECHNIQUES TO MEASURE SURFACE STRESS 78
4.5. STONEY EQUATION 80
REFERENCES 85

CHAPTER 5: Si(111)-7x7 SURFACE RECONSTRUCTION 87

5.1. DIMER-ADATOM-STACKING FAULT MODEL 90

5.2. ELECTRONIC STRUCTURE 93

5.3. INHERENTLY STRAINED STRUCTURE 94

5.4. CHEMICAL REACTIVITY 98

REFERENCES 100

CHAPTER 6: SYSTEM DEVELOPMENT FOR COMBINED SCANNING TUNNELING MICROSCOPY & SURFACE STRESS MEASUREMENTS TO ELUCIDATE THE ORIGINS OF SURFACE FORCES 102

6.1. EXPERIMENTAL DESIGN AND CHALLENGES 103

6.1.1 Sample Bending Detection 104

6.1.2 Visualisation via STM 105

6.1.3 Design Concepts 110

6.1.4 Determination of Sample Bending 119

6.1.5 Heating a Cantilever Sample 121

6.1.5.1 Simple Controlled Heating Method for a Free-Standing Cantilever Sample using Bimetallic Strips 123

6.1.5.2 Localised Heating of a Cantilever Sample via Electron Bombardment . 130

6.1.5.3 Heating a Cantilever Sample Using an Infrared (IR) Radiation Source & Quartz Light Guide 138

6.2. STM IMAGING ON THE CANTILEVER SAMPLE 143

6.3. CAPACITANCE MEASUREMENTS: DETECTION LIMIT & STABILITY .. 146

6.4. ACCURATE DETERMINATION OF THE AXIAL LENGTHS: L_0, L & L´.... 148

6.5. INVESTIGATIONS TO DATE 150

REFERENCES 151

CHAPTER 7: UNIT SELECTIVE OXIDATION OF THE Si(111)-7x7 SURFACE & THE INFLUENCE OF ARTIFICIALLY APPLIED STRESS ... 154

7.1. INTRODUCTION TO THE INITIAL OXIDATION OF THE SI(111)-7X7 SURFACE ... 155
7.2. UNIT SELECTIVE OXIDATION: EXPERIMENTAL RESULTS & DISCUSSION ... 157
7.3. PROBING THE ORIGIN OF UNIT SELECTIVITY ... 182
7.4. EFFECTS OF ARTIFICIAL APPLIED STRESS ON THE OXIDATION PROCESS ... 184
REFERENCES ... 190

CONCLUSIONS ... 193

APPENDIX A: STANDARD DESIGN FOR SCANNING TUNNELING MICROSCOPY (STM) UNDER ULTRA-HIGH VACUUM (UHV) ... 194

A.1. STM UNIT ... 194
A.2. VACUUM SYSTEM ... 197
A.3. MANIPULATOR FOR SAMPLE PREPARATION ... 200
A.4. SI(111)-7x7 SURFACE ... 202
REFERENCES ... 203

APPENDIX B: ELECTICAL BY-PASS UNIT FOR ACCURATE CAPACITANCE BASED DEFLECTION MEASUREMENTS OF HIGH RESISTENCE SAMPLES ... 204

B.1. SERIES VERSUS PARALLEL CIRCUIT MODELS ... 205
B.2. HIGH RESISTENCE SAMPLES- EVIDENCE OF PARASITIC EFFECTS ... 206
B.3. ACCURATE DEFLECTION MEASUREMENTS ... 213
REFERENCES ... 219

APPENDIX C: TIP ACCESSING OF THE CANTILEVER SAMPLE TO PERFORM STM MEASUREMENTS ... 220

C.1. TALL TIP STRUCTURES ... 220
C.2. RAISED TRIPOD SCANNER ASSEMBLY ... 221

APPENDIX D: SHIELD UNIT FOR SAMPLE HEATING METHODS ... 223

D.1. KALREZ ... 223
D.2. SHIELD UNIT ... 225
REFERENCES ... 226

APPENDIX E: BIMETALLIC HEATING OF A CANTILEVER SAMPLE ... 227

E.1. BIMETALLIC HEATING PROCEDURE ... 227
E.2. RESULTANT SURFACE CONDITION ... 229
REFERENCES ... 230

APPENDIX F: POTENTIAL COMMERCIAL APPLICATIONS OF OUR BIMETALLIC HEATING SET-UP ... 231

F.1. VALVES ... 231
F.2. PUMPS ... 232
F.3. GRIPPERS ... 233
F.4. MOTORS ... 234
F.5. TEMPERATURE DISTRIBUTION CONTROLLERS ... 236
F.6. VOLTAGE SOURCES ... 237
F.7. REGIONALISED POLARISATION CONTROLLER ... 238
F.8. ELECTROHYDRODYNAMICS ... 238
F.9. HEAT VALVE ... 239
F.10. SMART SOURCE ... 240
REFERENCES ... 241

APPENDIX G: REDUCING THE SAMPLE WIDTH- IMPLICATIONS FOR STM AND SURFACE STRESS MEASUREMENT CAPABILITIES **242**

G.1. IMPROVING HEATING UNIFORMITY DURING ELECTRON BOMBARDMENT 242

G.2. STM CAPABILITY- EFFECT OF A REDUCED SAMPLE WIDTH 244

G.3. STRESS MEASUREMENT CAPABILITY- EFFECT OF A REDUCED SAMPLE WIDTH 245

REFERENCES 246

APPENDIX H: ELECTRON BOMBARDMENT HEATING OF A CANTILEVER SAMPLE **247**

H.1. ELECTRON BOMBARDMENT HEATING 248

H.2. CLEAN SI(111)-7X7 SURFACES 250

REFERENCES 251

APPENDIX I: CAPACITANCE BRIDGE OPERATION **252**

I.1. CAPACITANCE BRIDGE OPERATION PRINCIPLE 252

I.2. MEASURES TO ENSURE ACCURATE SENSING 253

REFERENCES 254

Chapter 1

Introduction

Since the invention of the transistor in 1947, there has been a widespread and continuing interest in understanding the physical and chemical properties of semiconductor surfaces [1]. Despite the fact that the first transistor was made from germanium, silicon has received by far the lion's share of this attention, due largely in part to the presence of robust native oxide on silicon surfaces. Many of the rapid advances in microelectronics over the years, particularly since the advent of the personal computer, have been attained in two ways. First, the transistor has become smaller, with the latest devices measuring a thousandth of their original size [2]. Second, the number of transistors that can be interconnected on a single chip has risen from a few tens to hundreds of millions [2]. In order to extend *Moore's Law* [2, 3], it is imperative that reaction processes on silicon surfaces are understood and controlled at the atomic level. Such processes include oxidation and hydrogenation, for surface passivation and electrical isolation, in addition to halogenation which is used to define surface features by means of an etching process [4]. Despite extensive studies on these topics due to their vast scientific and technological importance, many questions remain unanswered regarding the precise details of the atomic scale processes involved [4]. However, it has been proposed, that forces acting in the surface region as a result of atomic scale strain, i.e. surface stress, may prove useful in elucidating such issues [5, 6].

Recent advances in the understanding of the role of surface stress in surface reconstruction, self-assembled pattern formation, alloying, shape and structural transitions, and surface adsorption have highlighted its importance throughout the nanoscience community [5, 7]. It is expected that the inclusion of surface stress in the discussion of various atomic phenomena will be of growing interest and relevance with the ongoing shrinkage of lateral and vertical dimensions of nanoscale systems, due to the dominant influence of surface effects in this size regime [5-8]. In addition, surface stress is known to have an important influence on electronic and magnetic properties; e.g.

strained silicon used in the microelectronics industry is currently being used to improve device performance by increasing charge carrier mobility without necessitating a reduction in transistor dimensions [9].

While surface stress measurements and theoretical calculations are extremely useful in explaining various surface phenomena and properties, they ideally need to be correlated with actual atomic structure measurements [5, 10, 11]. Previously, surface stress measurements combined with *independent* Scanning Tunneling Microscopy (STM) studies were found to be extremely useful in revealing the underlying origins of the measured surface stress evolutions [12-14]. To realise this simultaneously, we have developed a novel system to observe atomic structure via STM on a cantilever sample that is capable of detecting changes in surface stress [15, 16]. This combined system provides us with structural, dynamical and interactional information and is proving to be extremely useful in heightening understanding of reaction processes on surfaces. In addition, our system is also equipped with a *sample pusher* which can be used to study the effects of artificially applied stress on processes and properties at the atomic level. While our research interests lie predominantly with silicon processing it is imperative to note that our novel system is extremely versatile and can be applied to a wide range of research problems. This chapter presents a brief introduction to surface stress, an overview regarding previous research activities on the topic which motivated our novel system design, along with a short account of the main experimental aims.

1.1. Forces at Surfaces [16]

Feynman said that "many of the problems of molecular structure are concerned essentially with forces" [17]. This assertion is also valid for atomic scale structures and phenomena on surfaces. Consequently, the role of surface stress in the physics and chemistry of surfaces and their interfaces has become a matter of considerable interest and debate in recent years [5-7]. In particular, it has been widely discussed in relation to surface reconstruction, surface adsorption and thin film growth [7]. For example, in the case of nonmetallic samples, when a new surface is created, the excess surface energy due to unsaturated dangling bonds can be lowered by forming additional bonds. The

creation of these additional bonds involves atomic displacements which results in surface strain [18-20]. Competition between the energy lowering effect of additional bond creation and the energy raising effect of surface strain, ultimately results in the formation of a reconstructed surface which possesses its own intrinsic surface stress. In the case of surface adsorption, the reaction of an adsorbate species with a surface often results in the propagation of stress throughout the surface, heavily influenced by: a) the redistribution of charge along the surface; b) atomic size mismatch between the adsorbate and surface atoms; and c) the bonding topology of the surface [21]; see Figure 1.1. Furthermore, in relation to ultrathin film growth, surface and interface stress plays an important role in determining the subsequent growth mode [22, 23]. Despite the significant influence of surface stress upon these and other technologically important processes, its effects remain largely neglected due to the success with which many processes are explained using existing theories and techniques. However, as the size of surface features approaches the atomic scale, the application of these methods will no longer prove adequate; the effects of surface stress must be considered if these processes are to be more fully understood [6, 7, 12, 13, 22, 24, 25]. Several methods have already been developed to determine the effects of these forces at surfaces [7].

While it is not yet possible to determine the absolute surface stress experimentally with acceptable accuracy, techniques have been developed for the measurement of the changes in the surface stress when the surface is exposed to adsorbates or undergoes a modification [7]. Some stress change measurements are based on lattice distortion such as the use of X-ray diffraction (XRD), electron beam diffraction (LEED, RHEED), infrared spectroscopy (FTIR) and Raman spectroscopy (SERS). The others are based on measurements of sample bending of cantilever samples. The former enables us to detect the periodicity of ordered structures and/or local information regarding sample distortion. Sample bending, on the other hand, captures and integrates the effects of all forces present. In fact, the measurements of sample bending have led to the discovery of new methods and phenomena, for example, defect counting and athermal stress relaxation [12, 13], which could never have been identified via measurements of the lattice distortion. This clearly indicates that the measurement of surface forces has the potential to provide fundamental insights into surface structure and adsorption phenomena. In

reality, however, it is difficult to discuss the atomic scale origins of new stress phenomena using measurements of sample bending only. For this reason, some other complementary method should be available. To investigate the origins of surface stress from the viewpoint of atomic surface morphology, direct observation of the surface structure is necessary.

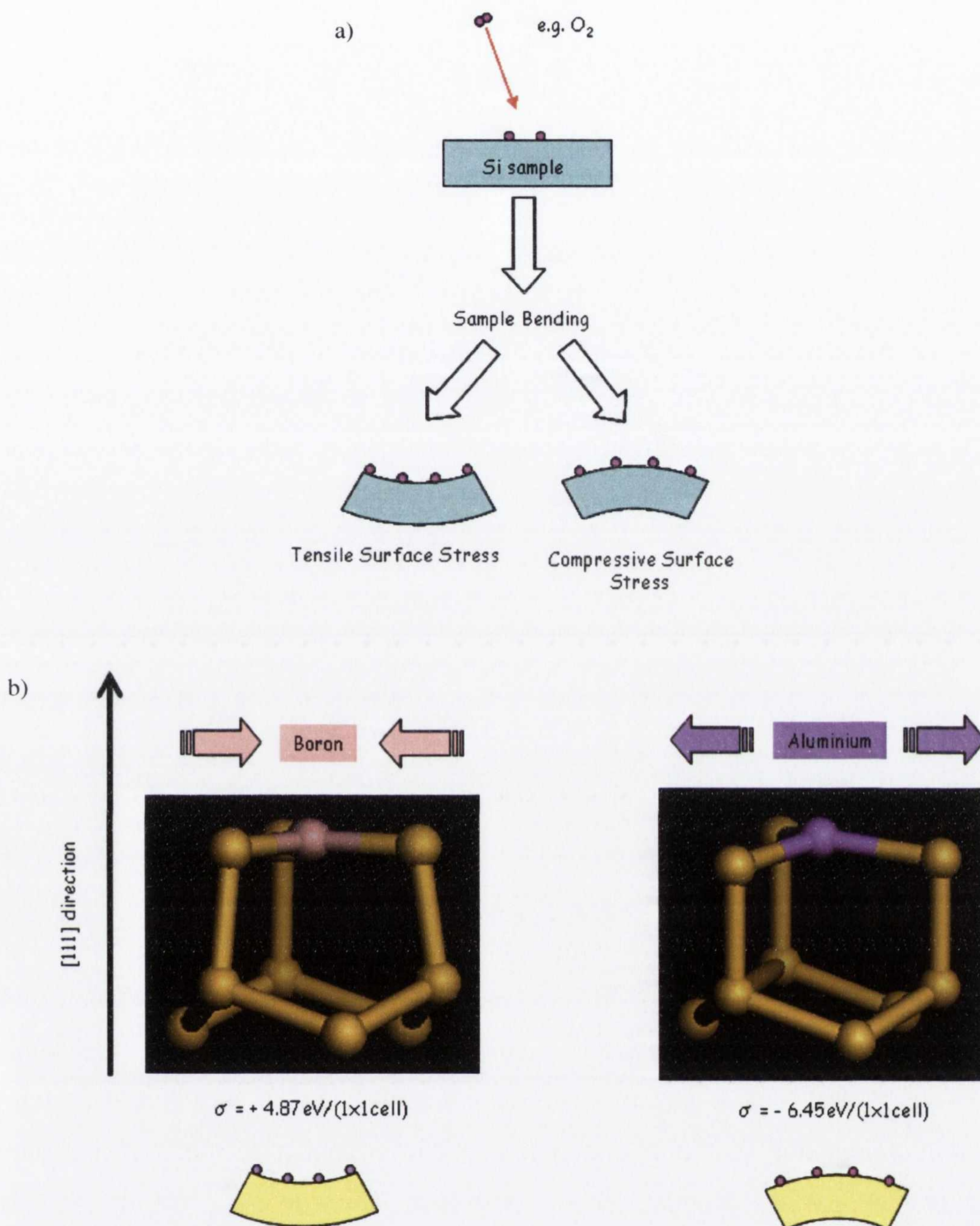

Fig. 1.1: a) In general, once a reaction occurs on any sample surface, stress-induced sample bending can be observed as a result of atomic scale strain. This sample bending can be simply divided into two types of surface stress condition. One is a tensile stress condition, whereby surface shrinkage occurs, while the other is a compressive condition, characterised by surface expansion; b) Illustration of the atomic size effect on surface stress. The atomic radius of boron is less than that of aluminium. Theoretical calculations have shown that B adsorbed on Si(111) generates a tensile surface stress while Al results in a compressive condition [21].

1.2. Revealing the Atomic Scale Origins of Surface Stress

Previously, surface stress measurements based on sample bending were combined with independent STM studies and were found to be extremely beneficial in displaying the underlying atomic scale origins of the measured surface stress [12-14]. By way of introduction we consider now two specific studies conducted by *Narushima et al.* which highlight this important point, namely, *Electron Stimulated Athermal Recrystallisation of Si(100)* [13, 14] and *Etching-enhanced Surface Stress Relaxation during Initial Ozone Oxidation* [26]. These studies were key motivating factors for us in the development of our novel system.

1.2.1 Electron Stimulated Athermal Recrystallisation of Si(100) [13, 14]

Electronic excitation is a remarkably effective tool for controlled modification of materials. Even low energy electron beams, typically under 5000 eV, are routinely used to investigate the structural and chemical properties of surfaces, where it is assumed that they do not cause any structural change to the surface region. However, such an assumption is incorrect as electrons with energies between 90- 2000 eV have been found to create defects on clean silicon surfaces [27]. *Narushima et al.* have found a more surprising result: complete restoration of the disorder induced surface stress of Si(100) occurs for electrons of low energies, namely 3.75- 40eV [13]. Upon irradiating the disordered silicon surface, disorder induced compressive stress was completely relaxed. The stress relaxation was found to depend only on the number of irradiated electrons and was independent of the total energy deposition. This indicates that the underlying mechanism is athermal in nature. But what is occurring at the atomic level?

To investigate this, the authors demonstrated, using an independent STM study, that the origin of the athermal surface stress relaxation is recrystallisation of the surface atoms [14]. *Narushima's* extremely low-energy electron irradiation achieves restoration of a surface which had been destroyed by argon ion bombardment. In demonstrating that surfaces have the capacity of self-healing, these results suggest the opportunity for atomic scale engineering. In addition it demonstrates the strength of STM in displaying the

atomic scale origins of measured stress signatures and the capability of macroscopic surface stress measurements in capturing atomic scale phenomena. The correlated data from each independent experimental set-up is shown in Fig. 1.2.

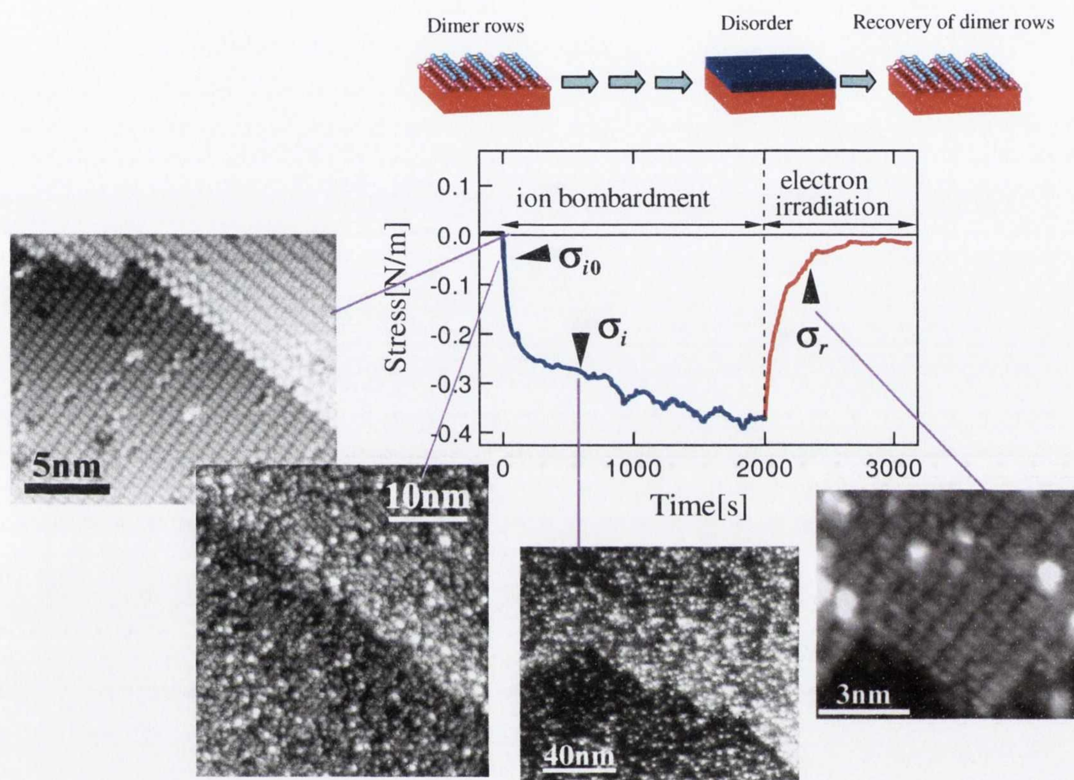

Fig. 1.2: Graph- time dependence of the surface stress change during ion bombardment followed by electron irradiation. Ion bombardment was performed at an energy of 65 eV for 2000 s and the subsequent electron irradiation was at 10 eV for a duration of approx. 1000 s [13]; Correlated STM images- acquired using an independent experimental set-up to examine the surface structure at various times throughout the experimental process [14].

1.2.2 Etching Enhanced Surface Stress Relaxation during Initial Ozone Oxidation [26]

Heterostructures are of critical importance in the micro and nano electronics industry. Here, as the dimensions of heterostructures are reduced, interface effects between constituent materials start to play an important role and cannot be ignored. For example, in state of the art transistor fabrication, it is a key technology to control the electronic structure of the transition layer at interfaces. Currently a mixture of silicon and

germanium is being used for this purpose, as it has the effect of increasing charge carrier mobility [9]. However this process requires a high temperature treatment. Presently, lower temperature processes are preferable for further integration of nanoscale electronic devices, to suppress changes in properties due to thermal diffusion [14]. For this purpose, ozone which is used for oxidation appears to be a promising candidate. By use of such species instead of molecular oxygen, different transition layer structures and interfacial stress can be expected.

Narushima et al. studied the surface stress evolution and atomic scale structure during the initial ozone oxidation of the Si(100) surface and compared results with oxidation via molecular oxygen [26]. Again two independent experimental set-ups were employed. As a result they found that the surface stress evolutions during ozone exposure showed a monotonic increase in compressive stress, while no remarkable surface stress change was observed for molecular oxygen exposure; see Fig. 1.3. In addition heavier surface etching was observed even at room temperature for ozone. Fig. 1.4 displays surfaces exposed at room temperature to different amounts of ozone. The exposure quantity was estimated from the pressure increase, and deemed to represent the surface condition on initial exposure as highlighted in Fig. 1.3. The authors attributed the origin of the compressive stress, not to local Si-O bond formation but to the reduction of the intrinsic tensile surface stress of the reconstructed Si(100)-2x1 surface via the etching process. Ozone can produce very thin SiO_x/Si transition layers [8, 27] with good electrical characteristics [27, 28], due to the release of the intrinsic stress for small exposures. Its characteristics are much more beneficial than those of molecular oxygen. Using stress controlled techniques ozone appears to have potential to be utilized for future nanoscale devices. Again the merit of a correlated approach using stress measurements and STM is emphasised.

As a result of such studies, it is clear that STM can reveal atomic scale structures on the surface where reactions occurred and provide us with valuable information to extrapolate the origins of the measured surface stress evolutions. Ideally surface stress and STM measurements should be performed in-situ on the same sample. To realize a simultaneous capability to measure both stress and STM, we have developed a measurement system in which STM is performed on the same cantilever sample used for

measuring sample bending. After overcoming several challenges in the implementation of this system we are now in a position to directly and visually explore the origins of forces during reaction processes on silicon surfaces (see Fig. 1.5). Now let us briefly examine another important effect to consider when examining various surface phenomena, namely, the influence of artificially applied stress.

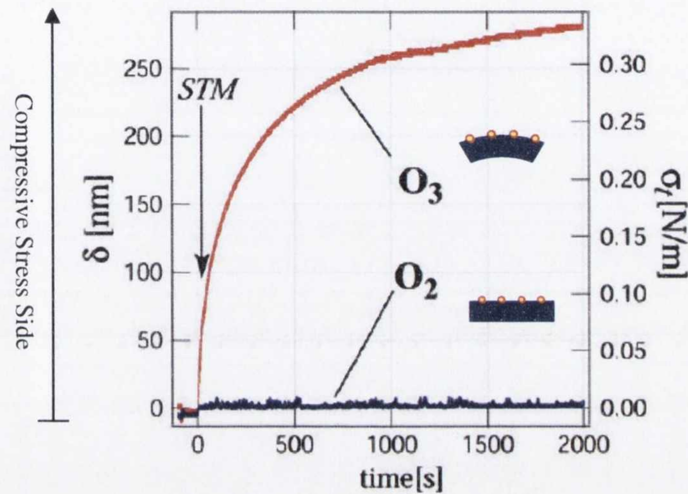

Fig. 1.3: Sample deflection (δ) and the surface stress evolution (σ) during ozone (O_3) and molecular oxygen (O_2) gas exposure. In both cases during measurements, pressures in pipeline and substrate temperatures are set to be 0.2 Torr and room temperature, respectively. A large difference between both stress evolutions is clearly evident. The arrow indicates the approximate point where the STM images of Fig. 1.4 were taken using an independent set-up [26].

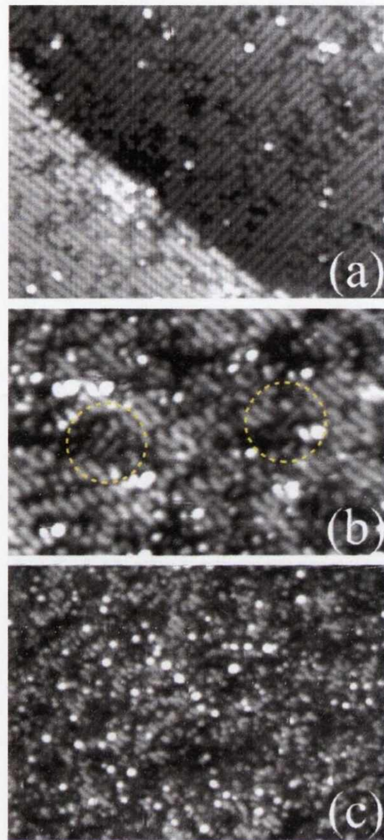

Fig. 1.4: STM images of the Si(100) surface for the initial stage of ozone oxidation at room temperature. The amount of ozone exposures increases from (a) to (c) [26].

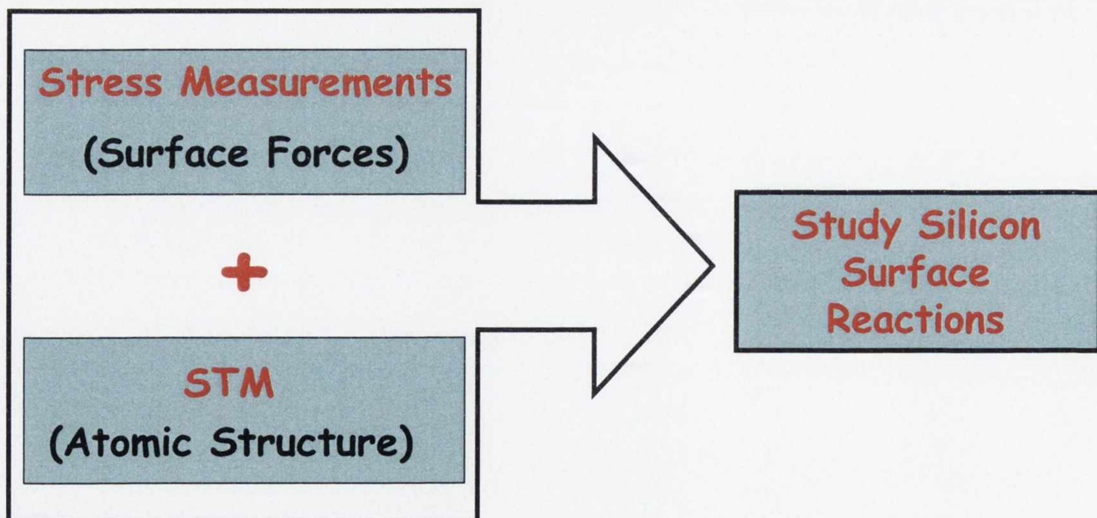

Fig. 1.5: Representation of our experimental set-up to for combined in-situ STM and surface stress measurements to study reaction processes on silicon surfaces [15, 16].

1.3. Effect of Artificial Stress on Surface Phenomena

It is apparent from both theory and experiments that surface stress is an important ingredient in the physics and chemistry of surfaces. However, it is also useful to be able to apply an artificial stress to the surface in order to study its effect on atomic scale processes. With this capability one is free to perform the following range of experiments: determination of the strain-temperature phase diagram for reconstructed surfaces, lift the surface energy degeneracy of orientation domains and perhaps prepare single domain surfaces, observe the effect of strain on surface segregation in which differences in atomic sizes are important, alter the misfit for incommensurate overlayers, and study the effect of stress on electronic and magnetic properties [11, 29]. *Men, Packard* and *Webb* conducted experiments regarding the Si(100) surface to an externally applied stress [29]. They showed that stressing a nominally flat Si(100) surface produces unequal populations of the 2x1 and 1x2 domains [11]. One might then expect that stress within the surface region of a crystal introduced by external influences should change its adsorptive properties. This was investigated by *Gsell, Jakob* and *Menzel* [30]. Here, the authors provide direct evidence for the effect of local strain at a surface on the bonding strength for adsorbates. In addition, *Uesugi-Saitow* and *Yata* examined the influence of external stress on surface reaction dynamics [31].

Applying an external force to bend the sample seems to be the best way to study the intrinsic effect of stress on the adsorption properties of various gases [30]. Consequently, we have implemented a *sample pusher* into our novel system design to investigate the influence of artificially applied stress on reaction processes at the atomic level [16]. This tool is proving to be a very important component of our system and offers exciting research opportunities for the future.

1.4. Research Objectives

The main aim of my research was to design and implement a special monitoring system to investigate the role of surface stress in the processing of silicon surfaces and to

explore the consequences of artificially applied stress on these processes. The main stages involved were:

- Design of a special sample holder for a cantilever sample to permit combined in-situ surface stress and STM measurements
- Development of a suitable UHV system to conduct experiments
- Development of a conventional STM system to accommodate our special sample holder for dual measurements
- Realisation of heating methods to prepare clean sample surfaces and study high temperature reaction processes on cantilever samples
- Successful implementation of a stress measurement system using a cantilever sample which can provide sufficient resolution to detect atomic scale processes on surfaces
- Successful atomic scale imaging of a cantilever surface using STM
- Implementation of the dual system to study silicon surface reaction processes, with an emphasis on the oxidation of Si(111)-7x7 at room temperature
- Preliminary investigation into the influence of artificially applied stress on the room temperature oxidation process of Si(111)-7x7

While the design and implementation of this novel system was by no means trivial, we successfully overcame all of the major challenges involved. Consequently, we are now in a strong position to make real headway in addressing the challenges detailed above. The individual experimental components, their integration into the system and the design challenges associated therewith are detailed in this thesis. A study of the initial oxidation of Si(111)-7x7 at room temperature is also presented to emphasis the capabilities of this novel measurement system.

References:

[1] J. Bardeen, and W. H. Brattain, Physical Review **74**, 230 (1948).

[2] http://physicsworld.com/cws/article/print/23012.

[3] http://www.intel.com/museum/archives/history_docs/mooreslaw.htm.

[4] V. G. Lifshits, *Surface Phases on Silicon: Preparation, Structures & Properties* (John Wiley & Sons Ltd., Chichester [England], 1994).

[5] D. Sander, Current Opinion in Solid State and Materials Science **7**, 51 (2003).

[6] C. F. Herrmann, D. Chen, and J. J. Boland, Physical Review Letters **89**, 096102 (2002).

[7] H. Ibach, Surface Science Reports **29**, 195 (1997).

[8] K. Nakamura, A. Kurokawa, and S. Ichimura, Thin Solid Films **343-344**, 361 (1999).

[9] T. Tezuka, Symp. on VLSI Technology, 96 (2002).

[10] C. E. Bach *et al.*, Physical Review Letters **78**, 4225 (1997).

[11] M. B. Webb, Surface Science **299-300**, 454 (1994).

[12] T. Narushima *et al.*, Applied Surface Science **159-160**, 25 (2000).

[13] T. Narushima *et al.*, Applied Physics Letters **79**, 605 (2001).

[14] T. Narushima, M. Kitajima, and K. Miki, Journal of Physics: Condensed Matter **16**, L193 (2004).

[15] T. Narushima, N. T. Kinahan, and J. J. Boland, Review of Scientific Instruments **76**, 095113 (2005).

[16] T. Narushima, N. T. Kinahan, and J. J. Boland, Review of Scientific Instruments **78**, 053903 (2007).

[17] R. P. Feynman, Physical Review **56**, 340 (1939).

[18] J. J. Boland, Journal of Vacuum Science and Technology B **9**, 764 (1991).

[19] J. J. Boland, Surface Science **261**, 17 (1992).

[20] J. J. Boland, and G. N. Parsons, Science **256**, 1304 (1992).

[21] R. D. Meade, and D. Vanderbilt, Physical Review Letters **63**, 1404 (1989).

[22] R. Koch, D. Winau, and K. H. Rieder, Physica Scripta **T49**, 539 (1993).

[23] A. J. Schell-Sorokin, and R. M. Tromp, Physical Review Letters **64**, 1039 (1990).

[24] M. Fouchier, and J. J. Boland, Physical Review B **57**, 8997 (1998).

[25] A. Kurokawa *et al.*, Japanese Journal of Applied Physics **43**, 281 (2004).

[26] T. Narushima *et al.*, Surface Science **601**, 1384 (2007).

[27] K. Nakayama, and J. H. Weaver, Physical Review Letters **82**, 980 (1999).

[28] T. Nishiguchi *et al.*, Applied Physics Letters **81**, 2190 (2002).

[29] F. K. Men, W. E. Packard, and M. B. Webb, Physical Review Letters **61**, 2469 (1988).

[30] M. Gsell, P. Jakob, and D. Menzel, Science **280**, 717 (1998).

[31] Y. Uesugi-Saitow, and M. Yata, Physical Review Letters **88**, 256104 (2002).

Chapter 2
Scanning Tunneling Microscopy

Since its invention in 1982 by *Binnig* and *Rohrer* [1], the Scanning Tunneling Microscope (STM) has steadily become established and is now an indispensable tool for surface analysis and surface manipulation. In the STM, a metallic tip is advanced towards the sample to a distance at which the wave functions of the tip and the sample overlap. The application of a bias voltage between the tip and sample results in an electron tunneling current which flows through the gap separating both electrodes. This tunneling current is detected and controlled by sophisticated apparatus. Scanning the tip along the sample surface provides the possibility for real space imaging of surfaces on a scale which extends down to atomic dimensions [2, 3]. Scanning tunneling microscopy has proved to be an extremely powerful technique for the determination of the local atomic and electronic structures of surfaces. The structural information obtained by this method is unique as most other surface probes, e.g. High Resolution Electron Energy Loss Spectroscopy (HREELS), average information over a large number of atoms. The ability to observe reactions at an atomic level using scanning tunneling microscopy has made it a pivotal tool for studying the types of surface-adsorbate reactions discussed in Chapter 1. This technique is an ideal candidate to extract the atomic scale structural origins of the measured surface stress signatures that evolve during reaction processes on surfaces. This chapter presents an overview of the basic principles that provide the foundation for the STM method, an introduction to Scanning Tunneling Spectroscopy (STS), a description of the basic mechanical and electronic requirements for successful STM operation, as well as an account of tip and surface preparation techniques.

2.1. Tunneling Theory

The operating principle of the STM is based on the quantum mechanical phenomenon of tunneling; the transmission of electrons through a vacuum barrier between two conductors when they are brought into very close proximity [4]. In classical

mechanics such an occurrence is deemed impossible if the energy of the electron is less than that of the vacuum barrier. In the classical case the energy of an electron in a potential, $U(x)$, is described by

$$\frac{p^2}{2m} + U(x) = E \qquad \text{... (2.1)}$$

where, m is the mass of the electron, p is the momentum, and E is the energy. In regions where $E>U(x)$, the electron has a non zero momentum. On the other hand, the electron cannot penetrate into any region with $E<U(x)$, or a *potential barrier*. In quantum mechanics, however, such penetration is possible due to the wave nature of the electron owing to its small mass. In the quantum picture, the electron can be described by a wave function, $\psi(x)$, which satisfies the time independent Schrödinger equation

$$-\frac{\hbar^2}{2m}\frac{d^2}{dx^2}\psi(x) + U(x)\psi(x) = E\psi(x). \qquad \text{... (2.2)}$$

Consider a 1-dimensional finite rectangular potential barrier of height, V_0, as shown in Fig. 2.1.

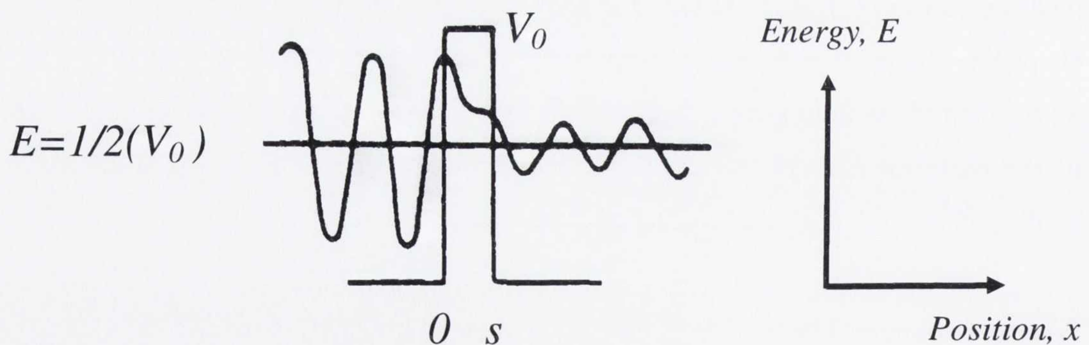

Fig. 2.1: Illustration of quantum mechanical tunneling displaying the wave function ψ, for an electron with kinetic energy, $E = ½(V_0)$, penetrating a thin potential barrier of width, s, and height, V_0. In this case the electron is incident on the barrier from the electrode on the left and the wave function is shown to decay exponentially within the barrier. In both left and right electrodes the wave function is oscillatory [4].

For an electron of energy, $E=1/2(V_0)$, incident on this barrier from the left, equation 2.2 can be solved for each of the regions displayed and has solutions

$$\psi(x) = \begin{cases} Ae^{+ikx} + Be^{-ikx} & (x < 0) \\ Ce^{-\kappa x} + De^{+\kappa x} & (0 < x < s) \\ Fe^{+ikx} & (x > s) \end{cases} \quad \ldots (2.3)$$

where

$$k = \sqrt{2mE/\hbar^2} \text{ and } \kappa = \sqrt{2m(V_0 - E)/\hbar^2}. \quad \ldots (2.4)$$

k, represents the wave vector and κ, the decay constant. The wave function decays exponentially into the classically forbidden region, $0<x<s$, with a decay length of $1/\kappa$. Therefore quantum mechanics allows a finite, albeit small, number of electrons to transverse the barrier, if the barrier width is small. The transmission coefficient, T; which is the ratio of the transmitted current density and the incident current density, can be obtained by matching the boundary conditions on ψ and $d\psi/dx$ at $x=0$ and $x=s$. This gives

$$T = \left|\frac{F}{A}\right|^2 = \frac{1}{1 + \frac{(k^2+\kappa^2)^2 \sinh^2(\kappa s)}{4k^2\kappa^2}}. \quad \ldots (2.5)$$

For a barrier of width, s, that is much thicker than the wave function decay length, $1/\kappa$, allows the transmission coefficient to be approximated as

$$T \approx \frac{16k^2\kappa^2}{(k^2+\kappa^2)} e^{-2\kappa s}. \quad \ldots (2.6)$$

Therefore the probability for tunneling between two electrodes is an exponential function of the barrier width, s, and the square root of the effective barrier height, $(V_0-E)^{1/2}$. It is

these exponential dependences that lie at the heart of STM. Assuming a barrier width of *5 Å* and an effective barrier height of *4 eV*, gives a value of about 10^{-5} for the exponential factor. Changing the barrier width by *1 Å* leads to a change in the transmission coefficient of approximately one order of magnitude. The extreme sensitivity of the tunneling barrier transmission to the barrier width led *Binnig, Rohrer* and coworkers to the idea that a microscope based on tunneling should provide extremely high spatial resolution.

It is important to note that tunneling through a 1-dimensional rectangular potential barrier, such as the situation depicted in Fig. 2.1, is bi-directional. An electron of energy, $E=1/2(V_0)$, incident on this barrier from the right, has an equal probability of being transmitted across the barrier as an electron with the same energy travelling from the left. It is also important to realize that the analysis above represents an elastic tunneling event, i.e. the energy of the electron is conserved in the tunneling process.

An extension to potential barriers of arbitrary shape can be made using the *Wentzel-Brillouin-Kramer* (WKB) approximation [5]. The WKB approximation is based on treating Planck's constant as a small number. The following expression for the probability, $D(E_x)$, that an electron of energy, E_x, can penetrate a 1-dimensional barrier of arbitrary shape, $V(x)$, is given by [6]

$$\begin{aligned} D(E_x) &= \exp\left\{-\frac{4\pi}{h}\int_{s_1}^{s_2}[2m(V(x)-E_x)]^{1/2}\,dx\right\} \\ &= \exp\left\{-2\int_{s_1}^{s_2}\kappa(x,E_x)\,dx\right\} \end{aligned} \qquad \text{... (2.7)}$$

where, s_1 and s_2 are the classical turning points and (s_2-s_1) is the width of the barrier. The WKB approximation is adequate only if the energy, E_x, is not near or above the top of the barrier $(E<<V)$ and if the sides of the barrier at s_1 and s_2 are gently sloping.

2.2. Metal-Insulator-Metal Tunneling: Theory & Experiment

Planar metal-insulator-metal tunneling junctions can be described by a simple 1-dimensional potential energy diagram as described earlier. Consider similar metal electrodes with free electron behaviour, separated by a thin insulating layer. The insulator can be treated as if it were a vacuum barrier. Also assume that both electrodes are in thermal equilibrium. In order to generate a net tunneling current a bias voltage, *V*, needs to exist between both electrodes. *Simmons* calculated the tunneling current density through a 1-dimensional potential barrier of arbitrary shape using the WKB approximation [7]. This hypothetical tunneling junction is displayed in Fig. 2.2 and results in a net tunneling current flowing from *electrode 1* to *electrode 2*.

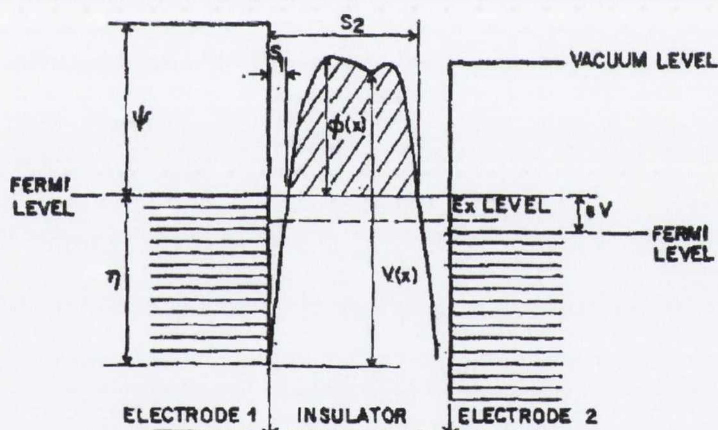

Fig. 2.2: A 1-dimensional tunnel barrier of arbitrary shape between two similar metal electrodes [7].

Using the WKB approximation the probability, $D(E_x)$, that an electron of energy, E_x, can penetrate this barrier is given by

$$D(E_x) = \exp\left\{ -\frac{4\pi}{h} \int_{s_1}^{s_2} [2m(\eta + \phi(x) - E_x)]^{1/2} dx \right\} \quad \dots (2.8)$$

where, s_1 and s_2 are the limits of the barrier at the Fermi level of *electrode 1*. It is obvious from this expression for the tunneling probability that electrons with a large energy

component, E_x, close to the Fermi energy, η, of *electrode 1* can tunnel most effectively. The reason is, of course, that these electrons experience the lowest effective potential barrier height. According to *Simmons* the most general expression for the current density, J, at zero Kelvin, is given by [7]

$$J = J_0 \left\langle \bar{\phi} \exp(-A\bar{\phi}^{1/2}) - (\bar{\phi} + eV)\exp\left[-A(\bar{\phi} + eV)^{1/2}\right] \right\rangle \qquad \text{... (2.9)}$$

where,

$$A = \frac{4\pi\beta\Delta s(2m)^{1/2}}{h}, \quad J_0 = \frac{e}{2\pi h(\beta\Delta s)^2}, \quad \beta \approx 1, \quad \bar{\phi} = \frac{1}{\Delta s}\int_{s_1}^{s_2} \phi(x)dx. \qquad \text{... (2.10)}$$

Here, $\phi(x)$ is the potential energy of an electron between the two metal surfaces and $\bar{\phi}$ is the mean barrier height between s_1 and s_2. Equation 2.9 can be interpreted as a current density, $J_0\bar{\phi}\exp(-A\bar{\phi}^{1/2})$, flowing from *electrode 1* to *electrode 2* while a current density , $J_0(\bar{\phi} + eV)\exp[-A(\bar{\phi} + eV)^{1/2}]$, flows in the opposite direction, with the difference resulting in a net current density, J. If no bias is applied *(V=0)*, the current density flowing in either direction is the same and the net current density vanishes.

It is useful to consider the expressions for J for rectangular barriers in the low, intermediate and high bias regimes, as displayed in Fig. 2.3. These voltage ranges were investigated by *Simmons* [7]. For low applied bias, with $V \approx 0, \Delta s = s, \bar{\phi} = \phi_0$, the expression can be simplified to

$$J = 3.16x10^{10} \phi_0^{1/2} (V/s) \exp[-1.025 s \phi_0^{1/2}] \qquad \text{... (2.11)}$$

where, J is expressed in A/cm^2, ϕ_0 in V, and s in Å. In this equation the current density is a linear function of V, so that the junction is ohmic for very low voltages. In this limit tunneling occurs due to the finite overlap of the decaying wave functions from electrodes 1 and 2, with the tunnel barrier only slightly changed due to the applied bias [4]. Current

flow is proportional to the applied bias as this bias opens up an energy window of allowed states for tunneling that is eV wide. The current density varies exponentially with the gap spacing s, and the square root of the barrier height, ϕ_0, in agreement with the variation of the transmission coefficient for the rectangular 1-dimensional barrier shown in equation (2.6).

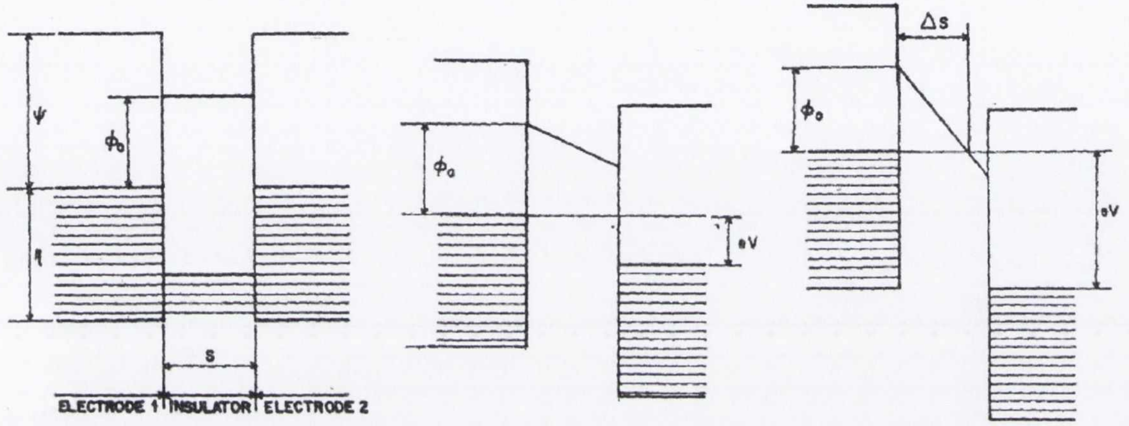

Fig. 2.3: Rectangular potential barrier in insulating film between metal electrodes for: (a) $V \approx 0$ (low bias voltage range); (b) $V < \phi_0/e$ (intermediate bias voltage range); (c) $V > \phi_0/e$ (high bias voltage range) [7].

For the intermediate voltage range, $V < \phi_0 / e, \Delta s = s, \bar{\phi} = (\phi_0 - eV/2)$. Substituting these values into equation (2.9) gives

$$J = (6.2x10^{10} / s^2)\{(\phi_0 - V/2)\exp[-1.025s(\phi_0 - V/2)^{1/2}] \\ - (\phi_0 + V/2)\exp[-1.025s(\phi_0 + V/2)^{1/2}]\}. \quad \ldots (2.12)$$

For the high-voltage range, with $V > \phi_0 / e, \Delta s = s\phi_0 / eV, \bar{\phi} = 1/2\phi_0$, the current density is

$$J = \left(\frac{2e^2 (F/\beta)^2}{8\pi h \phi_0}\right)\left(\begin{matrix} \exp\left[\dfrac{-4\pi\beta m^{1/2}\phi_0^{3/2}}{eF}\right] - \\ \left(\dfrac{1+2eV}{\phi_0}\right)\exp\left[\dfrac{-4\pi\beta m^{1/2}\phi_0^{3/2}}{eF}\left(\dfrac{1+2eV}{\phi_0}\right)\right]\end{matrix}\right) \quad \ldots (2.13)$$

where, $F = V / s$ is the field strength in the barrier. For very high voltages (where $V > (\phi_0 + \eta) / e$) electrons cannot tunnel from *electrode 2* to *electrode 1*, since there are no unoccupied states available to tunnel into. In this limit the second term in equation (2.8) becomes negligible, and the current density is determined by the Fowler-Nordheim equation [8] for field emission from *electrode 1*

$$J = \left(\frac{2e^2 (F / \beta)^2}{8\pi h \phi_0} \right) \exp\left[\frac{-4\pi \beta m^{1/2} \phi_0^{\ 3/2}}{eF} \right]. \qquad \ldots (2.14)$$

In this limit the applied bias strongly perturbs the tunnel barrier such that electrons near the Fermi level of electrode 1 can leak through it, largely independent of the proximity of electrode 2.

Equation (2.9) can also be applied to barriers which include the image potentials at both surfaces. The effect of the image force on a 1-dimensional rectangular barrier is to reduce the area of the potential barrier by rounding off the corners and reducing the thickness of the barrier and, hence, increasing the flow of current between both electrodes [7]. *Simmons* also considered expressions for the net current density between metal-insulator-metal tunnel junctions with dissimilar metal electrodes having different work functions [9]. Here an intrinsic electric field develops within the insulator as a result of the contact potential that exists between two dissimilar electrodes. As a result of this the potential barrier becomes asymmetric and the dependence of the tunneling current on the applied voltage becomes polarity dependent. At relatively low bias voltage, the greater current flows when the electrode with the lower work function is positively biased [9]. At higher bias voltages, the direction of rectification is reversed, i.e. greater current flows when the electrode with the lower work function is negatively biased [9].

Some very important early experimental studies of tunneling phenomena in planar oxide junctions were carried out in the 1960's by *Giaever* [10, 11] for which he received the 1973 Nobel Prize in Physics. However several limitations of the planar oxide tunnel junctions can be recognized from the works of *Giaever* and others. An important drawback is the existence of inhomogeneities in the junction. Owing to the roughness of the metal-oxide interfaces on the nanometer scale, leads to inhomogeneities in the

tunneling current flow because of the strong exponential distance dependence of the tunneling current [6]. Additional inhomogeneities in the chemical composition of the oxide layer can lead to greater difficulties. An alternative is complete removal of the oxide layer and replacement with a vacuum. However, though vacuum tunneling had long been considered superior to tunneling through oxide layers, the serious obstacle of vibration posed a serious challenge [12].

In 1971 *Young et al.* overcame this issue and succeeded in measuring current-voltage characteristics in the tunneling, intermediate and field emission regimes [13, 14]. The instrument used was the *topographiner* and it served as the precursor to the STM [4, 15]. In this instrument, a field emitter is mounted on a servo-system designed to keep the emitter at a constant distance above the surface [4]. Two other piezocrystals are used to scan the emitter parallel to the surface. A schematic diagram of this system [4, 16], in a configuration that was later developed into the STM is shown in Fig. 2.4.

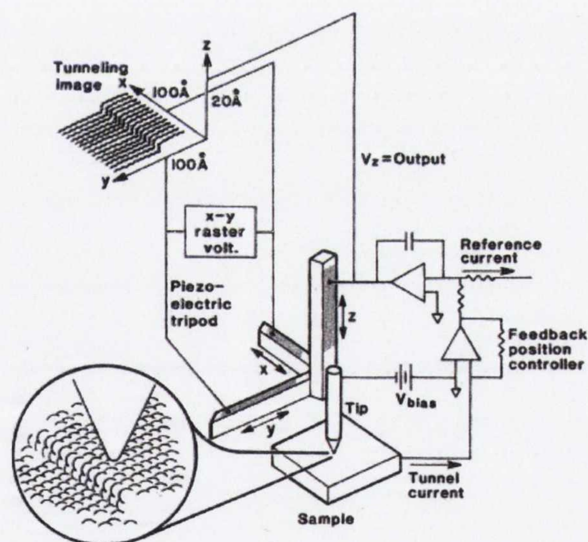

Fig. 2.4: Schematic illustration of a tunneling microscope. Due to its mounting on a piezoelectric tripod actuator, a tungsten tip can be moved in the (x-y) plane and also in the z direction normal to the surface which is to be examined. The tunneling image of the surface is obtained through plotting the feedback voltage, V_z, as a function of the tip's x-y position on the surface [4, 16].

By recording the vertical height of the tip, *z*, i.e. by recording the servo-signal as a function of lateral position, *(x,y)*, a topographic map, *z(x,y)*, is obtained. With the

topographiner, instrumental limitations required operation with a gap spacing of at least 20 Å while scanning, so that atomic resolution imaging was not possible at vacuum tunneling biases [4]. However, using the servo-system and disconnecting the scanning piezos, it was possible to advance the tip to within 12Å of the surface and make the first observation of metal-vacuum-metal (MVM) tunneling. The linear dependence of the current density on tip bias predicted by equation (2.11) is shown in Fig. 2.5. By varying the gap distance, the intermediate and Fowler-Nordheim regions were also observed.

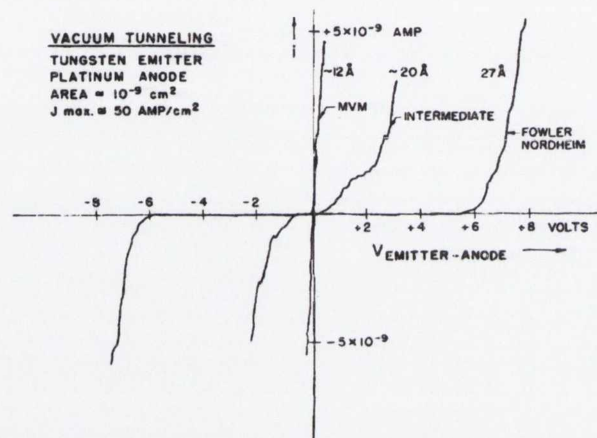

Fig. 2.5: Illustration of the tunneling current versus voltage characteristics for three different tip-sample spacing's. As predicted by *Simmons*, the *I-V* relationship is linear in the MVM region, which is the regime typically utilised for tunneling microscope experiments. At this point, the wavefunctions of the sample and tip have a significant overlap due to their respective closeness. Linearity of the *I-V* characteristic is lost if the tip and sample are separated by 20Å (intermediate regime). In the final case, i.e. the Fowler-Nordheim regime, where the tip and sample are separated by 27Å, no significant tunneling is observed until the bias between the tip and sample exceeds the work function, and the barrier is substantially deformed by the applied bias [4, 13, 14].

2.3. Birth of the STM

The successful combination of vacuum tunneling with a scanning capability was achieved in the early 1980's by *Binnig, Rohrer, Gerber* and *Weibel* when they invented the STM. This was achieved by reducing the vibration and electronic noise levels to such an extent that it was possible to scan the surface in the MVM regime. In 1981, they succeeded in making the first log *I-s* measurements [17], showing the exponential

dependence of the current, I, on the separation distance, s, as shown in Fig. 2.6 (a). For this they used a tungsten tip and a platinum sample in conjunction with a piezoelectric tripod scanner. This date has been identified as the birth of the STM. However, the real breakthrough for the STM was achieved in 1982, when *Binnig, Rohrer, Gerber* and *Weibel*, succeeded in obtaining an atomic resolution image of the Si(111)-7x7 surface [15, 18]. This atomic resolution image is shown in Fig. 2.6 (b).

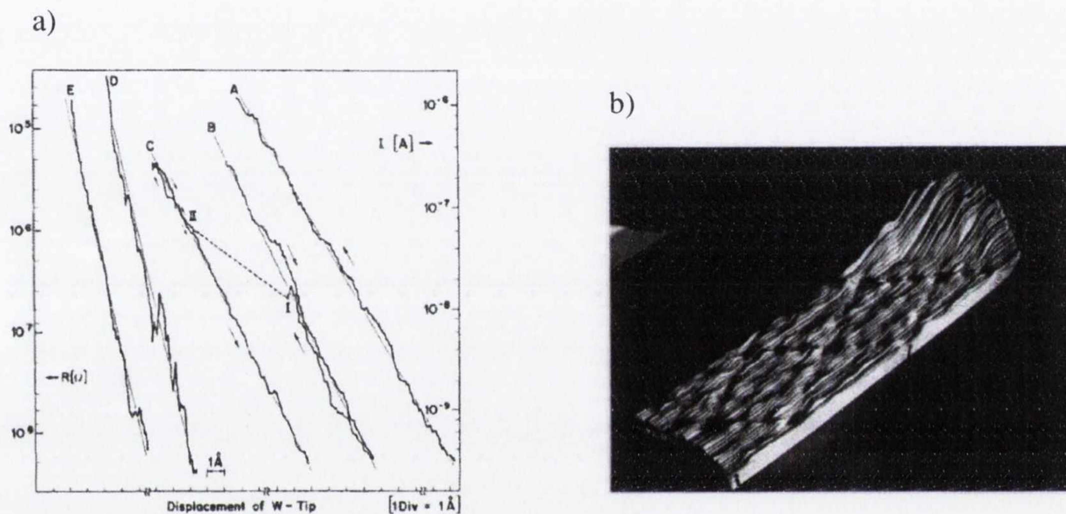

Fig. 2.6: a) Tunneling current versus displacement for a tungsten tip and platinum sample [17]; b) topography of the 7x7 reconstruction obtained using the STM showing two complete unit cells [15, 18].

The extremely high vertical and lateral resolutions make the STM an outstanding microscope and its birth revolutionised the field of surface science. The atomic resolution capability in real space has several important consequences [6]:

a) Surface structures, can be monitored and controlled at the atomic level.
b) The tip can be positioned with atomic accuracy above a pre-selected site and local experiments conducted.
c) Capabilities a) and b) above provide the ability to perform manipulation at the atomic level, allowing atomic scale devices to be created.

2.4. Constant Current Mode: Intermixing of Geometric & Electronic Effects

The most commonly used mode of imaging via the STM is the constant current mode, shown in Fig. 2.7. In this mode, a feedback loop and piezoelectric drive ensure that the tip is kept at such a distance from the sample surface that the tunneling current remains constant. By recording the voltage which has to be applied to the piezoelectric drive in order to keep the current constant, a topographical image at the atomic level can be achieved. To understand what this tip height variation corresponds to, it is necessary to go beyond a 1-dimensional analysis to a 3-dimensional model.

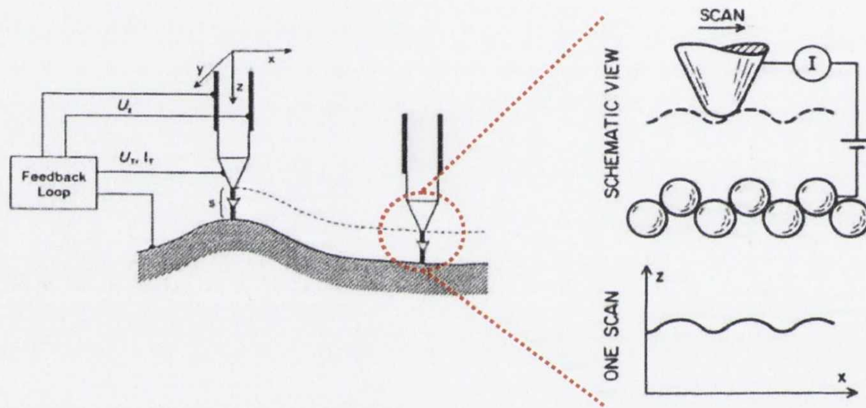

Fig. 2.7: Schematic illustration of the constant current mode of the STM [6].

In section 2.1 the tunneling probability for a 1-dimensional potential barrier was derived based on the time-independent Schrödinger equation (wave-matching method). For the 3-dimensional case, the method of matching wave functions across the interface poses an extremely difficult problem. Nevertheless, *Bardeen's* transfer Hamiltonian approach, based on the pertubative treatment of tunneling [19], can be applied more easily. Within *Bardeen's* formalism, the tunneling current, I, can be evaluated in first-order time-dependent perturbation theory according to

$$I = (2\pi e/\hbar)\sum_{\mu\nu}\{f(E_\mu)[1-f(E_\nu+eV)] - f(E_\nu+eV)[1-f(E_\mu)]\} \\ .|M_{\mu\nu}|^2\,\delta(E_\nu - E_\mu) \quad \dots (2.15)$$

where, $f(E)$ is the Fermi function, V is the applied voltage, $M_{\mu\nu}$ is the tunneling matrix element between the unperturbed electronic states ψ_μ of the tip and ψ_ν of the sample surface, and E_μ (E_ν) is the energy of the state ψ_μ (ψ_ν) in the absence of tunneling [20, 21]. The delta function insures the conservation of energy for the case of elastic tunneling. An energy diagram illustrating these quantities is shown in Fig. 2.8.

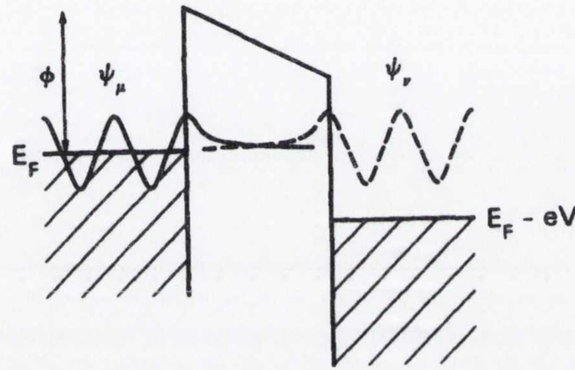

Fig. 2.8: Energy diagram illustration of the wave function overlap which leads to tunneling between two electrodes. ψ_μ is the wave function of the electron in the left electrode which has a work function ϕ, whilst ψ_ν is the wave function of the electron in the right electrode. E_F is the Fermi energy of each of the electrodes [4, 22].

For small applied voltage and temperature, equation (2.15) can be simplified to [20]

$$I = (2\pi e^2 / \hbar) V \sum_{\mu\nu} | M_{\mu\nu} |^2 \ \delta(E_\nu - E_F)\delta(E_\mu - E_F). \qquad \text{... (2.16)}$$

The essential problem is to calculate the tunneling matrix element which, according to *Bardeen* is given by

$$M_{\mu\nu} = \frac{-\hbar^2}{2m} \int d\vec{S}.(\psi_\mu * \nabla \psi_\nu - \psi_\nu \nabla \psi_\mu *) \qquad \text{... (2.17)}$$

where the integral is over any surface lying entirely within the vacuum region separating both electrodes [19, 20]. The quantity in brackets in equation (2.17) can be identified as a

current density, $\vec{j}_{\mu\nu}$. To obtain an expression for $M_{\mu\nu}$, explicit expressions for the wave functions ψ_μ and ψ_ν of the tip and sample are required. Unfortunately the exact atomic structure of the tip is generally not known and therefore a model wave function for the tip is necessary to calculate the tunneling current [6]. *Tersoff* and *Hamann* used the simplest possible model for the tip with a local spherical symmetry as shown in Fig. 2.9.

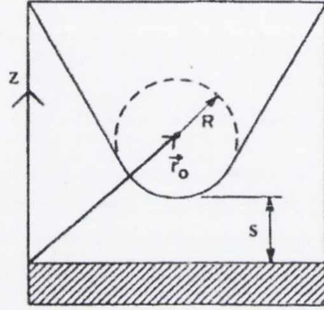

Fig. 2.9: Schematic picture of the tunneling geometry in the *Tersoff-Hamann* model. The probe has arbitrary shape but is assumed locally spherical with radius of curvature, *R*, where it approaches nearest the surface (shaded). Distance of nearest approach is *s*. The centre of curvature of the tip is labeled $\vec{r}_0$ [6, 20].

In this model, the tunneling matrix element is evaluated for an s-type tip wave function (orbital quantum number $l = 0$). As a result the following expression can be obtained

$$I \propto V.n_t(E_F).\exp(2\kappa R).\sum_{\nu} |\psi_\nu(\vec{r}_0)|^2 \delta(E_\nu - E_F) \qquad \ldots (2.18)$$

where, $n_t(E_F)$ is the density of states at the Fermi level of the tip [6]. The quantity

$$n_s(E_F, \vec{r}_0) = \sum_{\nu} |\psi_\nu(\vec{r}_0)|^2 \delta(E_\nu - E_F) \qquad \ldots (2.19)$$

is the surface local density of states (LDOS) at E_F at the position of the point probe. Thus the images obtained at low bias in the constant current mode represent a contour map of constant surface LDOS, i.e. charge density from sample states at the Fermi level. Since

the sample wave functions decay exponentially in the z-direction normal to the surface towards the vacuum region, we find that

$$|\psi_{\nu}(\vec{r}_0)|^2 \propto \exp[-2\kappa(s+R)]. \qquad \ldots (2.20)$$

In this equation s denotes the distance between the sample surface and the front end of the tip (Fig. 2.9). Therefore, the tunneling current, given in equation (2.18) becomes exponentially dependent on the distance s as expected:

$$I \propto \exp(-2\kappa s). \qquad \ldots (2.21)$$

As is evident from equations (2.18) and (2.21), association of an STM image obtained in constant current mode cannot be directly associated with a topographic image of the surface. In general a topographic image obtained by maintaining a constant tunneling current by feedback techniques is actually a combination of geometric and electronic features [23]. The constant current image only reflects true height changes if the LDOS of the sample is constant across the surface. Unfortunately, the simple interpretation of *Tersoff* and *Hamann* is no longer valid for high bias or for tip wave functions with an angular dependence but it is very successful model in many cases [4].

2.5. Scanning Tunneling Spectroscopy

An important feature of the STM is its ability to perform Scanning Tunneling Spectroscopy (STS) measurements. STS provides a means of probing the LDOS on surfaces at the atomic scale. Since the tunneling current in the STM only flows in a region with diameter 5 Å, STS is unique in comparison with other spectroscopic techniques that average information over a large surface region. An energy diagram [24] of the features that are relevant in STS is shown in Fig. 2.10. In the upper portion of the diagram, at zero applied bias, the Fermi levels of the tip and the semiconductor sample are equal. The middle portion represents how the Fermi levels of the tip and sample are off-set by the applied positive sample bias, V_T, and only those states within the generated

energy window are able to contribute to the tunneling current. The bottom portion of the figure displays the I-V spectrum.

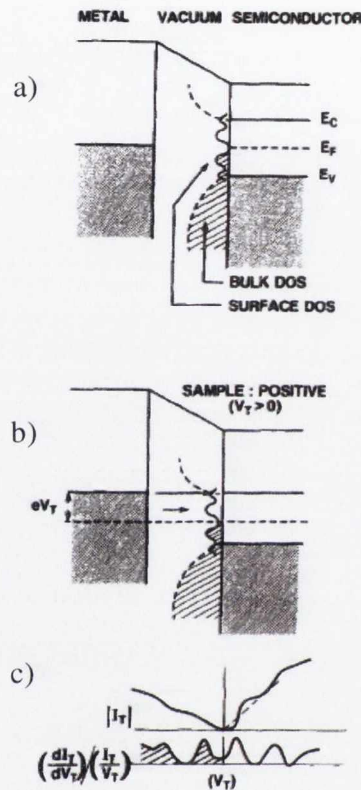

Fig 2.10: a) Schematic of the energy diagram for a metal-vacuum-semiconductor junction at zero applied bias in which it can be seen that both Fermi levels are equal. The solid line inside the gap represents the surface density of states (DOS), while the dashed line outside of the gap signifies the density of states of the bulk. (Occupied states are indicated by the hatched area); b) junction biased with the sample positive (or tip negative). This results in tunneling from tip to sample, where most of the tunneling current is derived from the Fermi level of the tip, as these electrons have the lowest barrier for tunneling (this is indicated by the arrows in this figure). Tunneling from the filled sample states to the empty tip states occurs under the opposite biasing condition. In this case the majority of the tunneling current comes from the highest filled sample states as these have the lowest barrier for tunneling. This makes it difficult to use to the STM to obtain spectroscopic information regarding the lowering lying filled sample states that are not near the Fermi level; c) illustration of the current and normalized differential conductance versus tunnel bias V_T [4, 24].

Such *I-V* spectra are typically obtained by a modulation technique [25]. Using this method a constant current topograph and spatially resolved *dI/dV* can be acquired simultaneously. A small, high frequency sinusoidal modulation voltage is superimposed on the direct current (d.c.) tip-sample bias. The modulation frequency is chosen higher than the cut-off frequency of the feedback loop which keeps the average tunneling current constant. The alternating current (a.c.) component of the tunneling current is recorded using a lock-in amplifier and the component in phase with the tip-sample bias modulation gives *dI/dV* directly. In order to obtain a simultaneous topographic image, a sample-and-hold circuit is employed in the feedback loop. This circuit freezes the supplied voltage to the z-piezo on the scanner assembly which holds the defined tip-sample distance constant at the desired location [26]. The tip-sample bias is then swept through the specified range (typically -2 to +2 V) and the *I-V* spectrum is recorded. After this acquisition process, the tip-sample bias is returned to the scanning value and the scan resumes. *I-V* spectra features result from new tunneling states being introduced into the tunneling window with the changing of the bias voltage.

In order to explain features in STS measurements, a resurgence of interest in tunneling theories begun [27-29]. For spectroscopic measurements performed on semiconductor samples the applied bias is typically between -2 to +2 V, and is therefore not within the low voltage limit which defines the tunneling current of equation (2.16). Under these conditions, the tunneling current arises from a range of states lying within eV of the Fermi level. As a consequence of this the tunneling current at a fixed location, $\vec{r}_0$, on the surface can be approximated by means of the WKB theory as

$$I \propto \int_0^{eV} n_t(\vec{r}_0, E-eV)\, n_s(\vec{r}_0, E)\, T(\vec{r}_0, E, eV)\, dE \qquad \ldots (2.22)$$

where, $n_t(\vec{r}_0, E)$ and $n_s(\vec{r}_0, E)$ are the density of states associated with the tip and sample at location $\vec{r}_0$ and the energy E, measured with respect to their individual Fermi levels [30]. In the case of negative sample bias, $eV<0$ and for positive sample bias, $eV>0$.

$T(\vec{r}_0, E, eV)$ represents the transmission probability for electrons with energy, E and applied voltage, V and is given by

$$T(E,eV) = \exp\left(-\frac{2s\sqrt{2m}}{\hbar}\sqrt{\frac{\phi_t + \phi_s}{2} + \frac{eV}{2} - E}\right) \quad \ldots (2.23)$$

where, s is the distance from the tip to the sample, ϕ_t is the work function of the tip and ϕ_s is the work function of the sample. One important feature of the transmission probability should be noted. Examination of $T(E, eV)$ shows that for negative sample bias ($eV<0$) the transmission probability is greatest for $E=0$ (corresponding to electrons at the Fermi level of the sample). Similarly, for positive sample bias ($eV>0$) the probability is largest for $E=eV$ (corresponding to electrons at the Fermi level of the tip) [30]. Thus the tunneling probability is always largest for electrons at the Fermi level of whichever electrode is negatively biased.

From equation (2.22) it is evident that the tunneling current is a convolution of the tip and sample density of states. Therefore both quantities would be expected to play an important role in tunneling spectra. However, in general it is the density of states of the sample that are of interest. Two important factors allow sample states to dominate tunneling spectra, at least for the determination of unoccupied sample states. Firstly metallic tips can be prepared by various methods such that the density of states is largely featureless [4]. Secondly, the tunnel barrier selects electrons close to the Fermi level of the source electrode, since these electrons have the lowest barrier to tunneling and hence dominate the current [4]. Therefore when the tip injects electrons into unoccupied states of the sample the density of states of the tip can be taken as constant with respect to the voltage. This results in *I-V* spectra that predominantly reflect the density of unoccupied sample states. It should be emphasized, however, that under opposite biasing conditions, the density of states of the sample are largely independent of the applied voltage and such spectra are dominated by the tip density of states.

Stroscio et. al showed that a plot of $(dI/dV)/(I/V)$ against eV roughly corresponds to the density of states of the sample in the vicinity of E_F [31]. However, this association is by no means trivial. Firstly each spectrum contains a background that is assumed to

vary smoothly at least on the scale of the width of the features in these spectra [4]. Secondly, it is assumed that the density of states of the tip do not contribute to the observed spectra. Although this condition may be achieved by a pure metallic tip, contamination of the tip will yield a tip that has pronounced electronic structure [31]. While such tips may provide extremely high resolution images, interpretation of the corresponding STS spectra is extremely challenging.

2.6. Instrumentation

There are many important design criteria that need to be considered in the construction of the STM. A brief overview of the main principles involved will be provided in this section. The STM has four basic elements:

a) High precision scanning mechanism that enables the tip to raster the sample surface
b) Coarse approach mechanism to bring the tip and sample into tunneling range
c) Control electronics to adjust the tip-sample separation via a feedback mechanism
d) Structural design measures to minimise influences from ambient noise and vibrations

2.6.1 High Precision Mechanism

For high resolution STM images, the scanning probe needs to be positioned with an accuracy of about 0.01 nm normal to the surface (z-direction) and about 0.1 nm laterally (x and y directions). As a result of this very fine tolerance level for positioning the tip, conventional mechanical positioning devices are deemed unsuitable. Piezoelectric ceramics are therefore widely employed as electromechanical transducers to obtain accurate x, y, z motion. A piezoelectric actuator is an electromechanical device that undergoes a dimensional change when an electric voltage is applied [32]. Single crystals of many anisotropic compounds, quartz for instance, possess piezoelectric properties. More recently, polycrystalline ceramic materials such as lead zirconate titanate (PZT) have been extensively developed for their piezoelectric properties. The as-made isotropic PZT ceramics do not exhibit piezoelectric behaviour due to the random arrangement of the electric dipoles. These ceramics differ from single crystals in that they must undergo a

poling process in order for the piezoelectric phenomenon to occur. After this process the dipoles are aligned which produces a permanent electric polarisation and the piece of material becomes anisotropic, resulting a strong piezoelectric effect. PZT materials can convert electric potential signals of 1 mV to 1000 V into mechanical motion in the range less than 1 Å to a few μm and are available in a variety of compositions, shapes and configurations [32].

Tripod piezoelectric scanners are a common choice as the high precision scanning mechanism in the STM. An illustration of a tripod scanner is shown in Fig. 2.11 (a). The displacements along the x, y, and z directions are actuated by three mutually perpendicular PZT transducers. Each PZT transducer is typically rectangular in shape and metalized on two opposite sides. By applying a voltage, V, between the two metal surfaces of a piezo, for example the *x piezo*, the displacement is

$$\delta x = d_{31} V \frac{L}{h} \qquad \text{... (2.24)}$$

where, L is the length of the piezo, h is its thickness and d_{31} is the transverse piezoelectric coefficient [33]. A typical value for d_{31} is 0.262 nm/V (PZT-5H). Therefore in order to elongate a bar of length 1 cm by 1 μm, a voltage of 380 V needs to be applied across a thickness of 1 mm [34]. These numbers imply that high voltage amplification is required to drive the piezoelectric actuators. Tripod scanners typically have low resonant frequencies (1-5 kHz) and are susceptible to cross-talk particularly for large displacements [4, 6, 35]. High resonant frequencies are required for fast scan rates, while reducing cross talk is essential for distortion-free imaging. Replacing the three rectangular piezo elements of the tripod scanner with similar sized hollow piezoelectric tubes reduces cross talk, increases the resonance frequency, and improves the scanner sensitivity [6, 36]. As an alternative, a compact single tube can be used for full 3-dimensional movement as illustrated in Fig. 2.11 (b). The elongation of a tube of piezoelectric material is used for the vertical movement, while the bending accomplishes the horizontal scanning movement [34]. For this purpose the outside of the tube is contacted by four symmetric electrodes separated along the tube. By applying equal but

opposite voltages to opposing electrodes the tube will bend due to expansion and contraction. The inner wall is contacted by a single electrode for application of the actuating voltage for vertical movement [6]. Tube scanners are compact and rigid and can have resonant frequencies up to 100 kHz for vibrational modes along the length of the tube [4]. They also typically have larger scan ranges than tripod scanners [6]. The drawback is that the movement in the (x, y)-plane and along the z-axis is no longer independent, which results in inherent issues [34]. Moreover, a complex controller module is required to translate (x, y, z)-values into voltages.

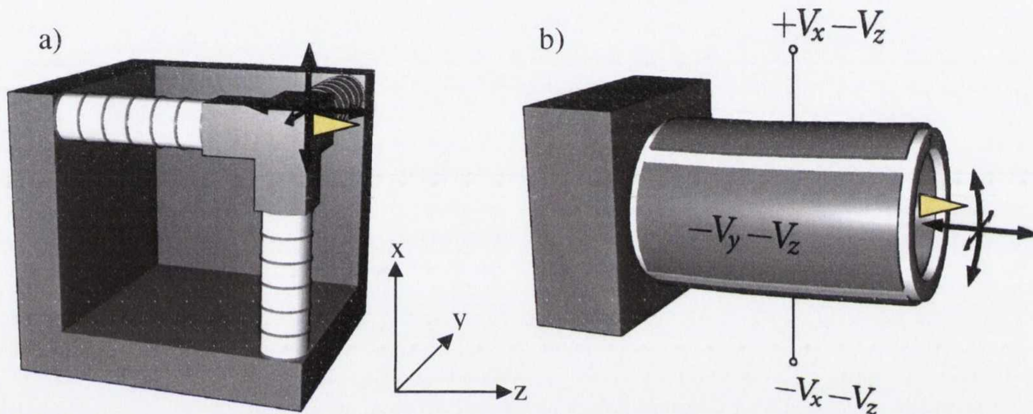

Fig. 2.11: a) PZT tripod scanner consisting of three separate piezoelectric arms that allow the tip to move in the x, y and z directions; b) PZT tube scanner consisting of all three arms on the same crystal.

The permanent polarisation of PZT ceramics used in piezoelectric scanners can be lost either gradually after long use or suddenly by heating above the *Curie temperature* [33]. Therefore the calibration of actuators has to be repeated regularly. The material may even have to be repolarised by heating it above its Curie temperature and applying a high voltage, followed by cooling with the voltage still applied. Other concerns in relation to piezoelectric scanner assemblies are hysteresis, creep and thermal drift [6].

2.6.2 Coarse Approach Mechanism

The coarse approach mechanism is required to bring the tip and sample into close proximity such that tunneling can be achieved as previously mentioned. The minimum

requirement for such a mechanism is to move the sample in 1-dimension from millimeter to submicron distances. The smallest step size for this movement has to be smaller than the total range of the *z-piezo* for the tip in order to avoid accidental tip crash during the electronically controlled approach process. The means of reducing the gap distance to within *z-piezo* range may involve a piezowalker [15], an inchworm [37], a stepper motor [38], or an inertial slider [39]. Inertial sliders are commonly used in modern STM systems for the following reasons: no high precision mechanical parts; highly reliable and reproducible operation; large translational range with step sizes available down to the nanometer scale; operation can be a single step or recurrent with speeds up to 1 mm per second; ultra-high vacuum compatibility; extremely simple driver electronics; one wire connection (plus ground) per translator; work over a wide temperature range; can be designed to have high resonant frequencies; produce no motional noise when inactive.

The basic principle of translational stages based on slip-stick inertial motion is the controllable use of the inertia of a sliding block and was initially designed by *Pohl* in 1987 [39]. The original prototype design is displayed in Fig. 2.12. To create a translational movement using *Pohl's* set-up, an asymmetric sawtooth voltage is applied to the piezotube. During the slow ramp of the sawtooth, the stage is kept in position with respect to the support owing to static friction forces. The steep decay period, however, causes such a large acceleration of the support that the inertial force of the stage exceeds the static friction limit. The support begins to slide under the stage. The result is a net displacement of the stage with respect to the support. Various modifications based on *Pohl's* original mechanism have meant that inertial sliders have become the most widely used mechanism for coarse positioning in modern STM systems. Depending on the form of the applied asymmetric saw tooth voltage, as illustrated in Fig. 2.13, the sliding block can move in both positive and negative directions. Such inertial sliders move with various step sizes and frequencies, depending on the applied waveform. This allows for convenient sample and tip loading as well as reducing tip-sample seperations from macroscopic to tunneling distances. In addition, 2-dimensional positioning of the sample in the surface (x, y)-plane is required in order to select a specific area of interest on the sample surface [6]. However, most STM designs omit the complicated coarse positioning

in the vertical direction for reasons of design complexity and positioning is possible only along the length of the sample.

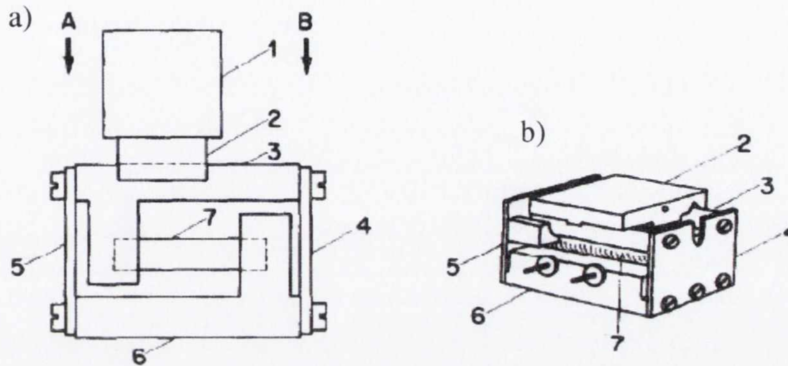

Fig 2.12: Prototype inertial slider designed by *Pohl* - a) schematic, b) actual design (1 load, 2 stage on steel rails, 3 support, 4,5 elastic metal plates, 6 base, 7 piezo tube, AB translation range) [39].

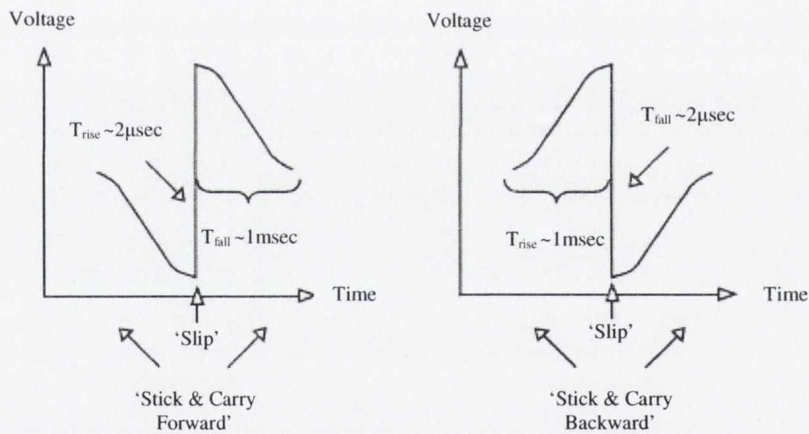

Fig 2.13: Example of typical voltage signatures applied to piezos during slip/stick motion.

2.6.3 Electronic Design

The STM electronic components have to be designed very carefully in order to avoid electrical noise and pick-up or feedback loop instabilities [6]. A typical block diagram is shown in Fig. 2.14. The tip (or sample) voltage is applied using a computer controlled digital-to-analog converter (DAC). Once the approach mechanism has attained tunneling range the control electronics takes over and adjusts the tip-sample separation

via the *z-piezo* to achieve the demanded current (typically between 10 pA and 10 nA). The demand current is the 'set-point' current of the tip positioning servo-system [4]. If the tunneling current exceeds the set-point value the tip is retracted back from the surface by applying the appropriate signal to the *z-piezo* control until the demanded current is re-established. If on the other hand the tunneling current is below the set-point value the tip is advanced towards the sample surface to the desired position. This operation is based on the principle of negative feedback [36, 38]. The voltage applied to the *z-piezo* to maintain a constant tunneling current is recorded as the surface topography as the tip raster scans the surface. The rastering ability is achieved by applying appropriate linear voltage ramps via computer controlled DAC's to the inputs of the *x*- and *y-piezo* amplifiers. The function of the feedback circuit is to make the tip accurately follow the constant tunneling current contour at the highest possible speed. Spectroscopic studies may be performed by inserting a sample-and-hold amplifier circuit before the main feedback amplifiers [4]. This fixes the distance between the tip and the sample and allows *I-V* curves to be obtained.

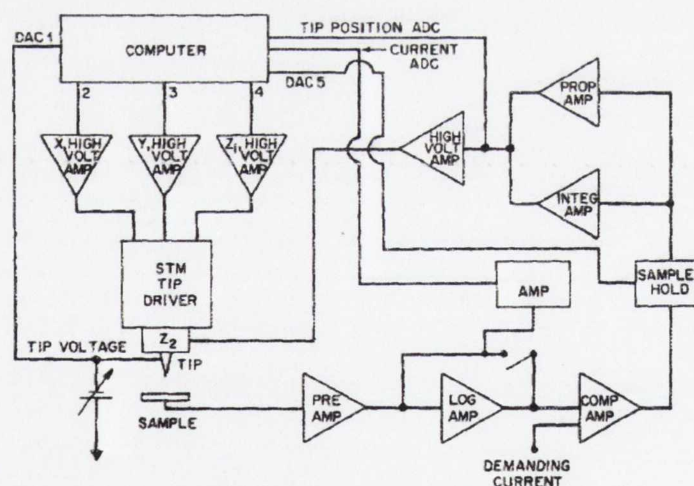

Fig. 2.14: STM feedback circuit- Following measurement of the tunneling current via an internal preamplifier (gain 10^6-10^9 V/A), its exponential dependence on the gap width can be linearised using a logarithmic amplifier. It can then be compared to the set-point value. This results in an error signal which is fed into the main feedback amplifier and the ensuing feedback output signal is finally fed into the *z-piezo* driver which adjusts the tip position as required [4, 36].

2.6.4 Vibration Isolation

Good vibration isolation is essential for successful operation of the STM. Since the corrugation on many surfaces is 0.1 Å or less, the distance between the tip and the sample must be maintained with an accuracy of approximately 0.01 Å or better. The sensitivity of the STM to external and internal vibrational sources is dependent on the structural rigidity of the STM unit, the intrinsic properties of the vibrational isolation system employed, and the nature of the sources of vibration [4]. An effective vibration isolation system is one in which the response of the system to internal and external vibrational sources is less than the desired tip-sample gap accuracy of the instrument [4]. Typical vibrations have frequencies in the range 1-20 kHz with amplitudes up to several microns. Additional vibrations are encountered at 50 Hz and correspond to electrically powered motors, transformers and ventilation ducts. For a 1 μm excitation amplitude a stability of 0.01 Å requires a vibration isolation system with an overall transfer function, $T(v)$, of 10^{-6}.

The effectiveness of any vibration isolation system depends on its response to an excitation source. Vibration isolation involves separating the external noise source from the microscope by means of a damped spring system [4]. For a simple extension spring the resonance frequency is given by

$$v_\eta = 0.5/(\Delta L)^{1/2} \qquad \ldots (2.25)$$

where, ΔL is the spring extension in centimetres following its extension under the mass of the microscope [33]. The typical transfer function for such a spring system is

$$T_s(v) = \left[\frac{1 + (2\xi v / v_\eta)^2}{(1 - v^2 / v_\eta^2)^2 + (2\xi v / v_\eta)^2} \right]^{1/2} \qquad \ldots (2.26)$$

which is shown in Fig. 2.15. In this equation, v is the external excitation frequency, and ξ is the dampening ratio. Below the resonance frequency of the spring complete amplitude

transfer occurs. At the resonance frequency amplification occurs, the extent of which decreases with increasing viscous dampening. In the STM dampening is usually achieved using elastomers, e.g. viton or magnetic eddy-current dampening [33]. At frequencies above the resonance frequency of the spring the amplitude of the transfer function decreases rapidly. However it should be noticed that the rate of decrease is reduced for heavily damped systems, and as a result a compromise between dampening and vibration isolation at higher frequencies is required. Clearly, the best vibration isolation systems have the lowest resonance frequencies. In the case of an extension spring system this may require prohibitively long springs (e.g. 1 Hz resonance frequency requirement for a single spring system demands a 25 cm long spring) or a two-stage spring system [38, 40]. Two-spring systems typically consist of an outer set of springs which supports an inner spring arrangement to which the microscope stage is attached, or a vibration isolation table upon which the vacuum chamber containing the microscope with a spring system is mounted [4].

However, the most important consideration for vibration isolation is the resonant frequency of the microscope itself. The transfer function of the microscope is given by

$$T_m(\nu) = \frac{(\nu/\nu_m)^2}{[(1-\nu^2/\nu_m^2)^2 + (\nu/\nu_m Q)^2]^{1/2}} \qquad \ldots (2.27)$$

where, ν_m is the lowest mechanical resonant frequency of the microscope and Q is the quality factor of the tip-sample junction [4]. The total transfer function, $T(\nu)$ is given by

$$T(\nu) = T_s(\nu)T_m(\nu). \qquad \ldots (2.28)$$

The rapid fall off in the transfer function of isolation systems at higher frequencies guarantees that STM assemblies with high resonance frequencies (ν_m) are insensitive to external excitation. The total transfer function over the frequency range $\nu_m \geq \nu \geq \nu_\eta$ can be approximated as [33]

$$T(\nu) = (\nu_\eta / \nu_m)^2 . \qquad \ldots (2.29)$$

Therefore if ν_η is 2 Hz and ν_m is 20 kHz the amplitude of the transfer function is approximately 10^{-8} or 160 dB, which is sufficient to provide the required stability at the tip-sample tunneling junction.

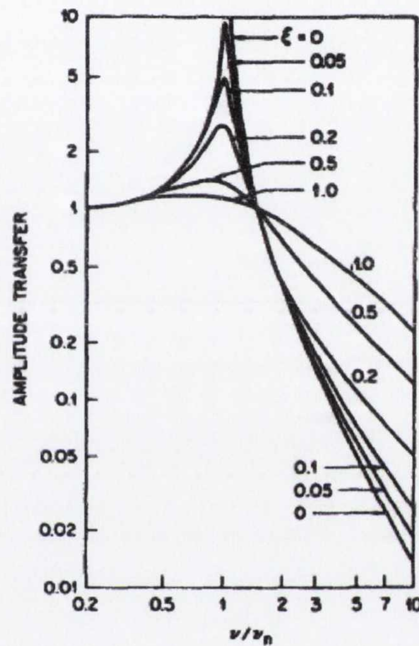

Fig. 2.15: Amplitude transfer function, $T_s(\nu)$, for a one-stage spring isolation system, with resonant frequency, ν_η, as a function of frequency and dampening ratio [4, 36].

2.7. Tip Preparation & Treatment

An important aspect of the STM is the reliable formation of tunneling tips. The size, shape and chemical identity of the tip not only influences the resolution and shape of the STM scan, but also the measured electronic spectra. STM tips are typically fabricated from tungsten (*W*) or platinum-iridium (*Pt-Ir*) wire by several methods [41]. The goal is to produce a sharp tip with a low aspect ratio (tip length/tip shank) to minimise flexure vibration [41]. Ideally the tip should be atomically sharp, but in reality most techniques produce a jagged tip end with many asperities, where the end closest to the surface is

responsible for tunneling. *Pt-Ir* tips are typically used in ambient conditions due to the sensitivity of tungsten to corrosion. Here the preparation and treatment of *W* tips will be discussed as it is the typical material of choice for high resolution UHV STM studies.

The preferred method for making *W* tips is the *d.c. drop-off method* [41]. The basic set-up is shown in Fig. 2.16. It comprises of a beaker of aqueous NaOH solution, typically 1-2 molar. A tungsten wire, approximately 0.5 mm diameter, is mounted on a micrometer and is located in the centre of the beaker. The height of the wire relative to the surface can then be adjusted. This electrode forms the anode. The cathode is formed using a piece of stainless steel (or platinum) which is typically formed into a cylinder and placed around the anode. It has been reported however, that the shape and location of the cathode has very little effect on the etching process, so it can be chosen for convenience [33]. A positive d.c. voltage (typically 4 to 12 V) is applied to the anode. This induces the following electrochemical reaction:

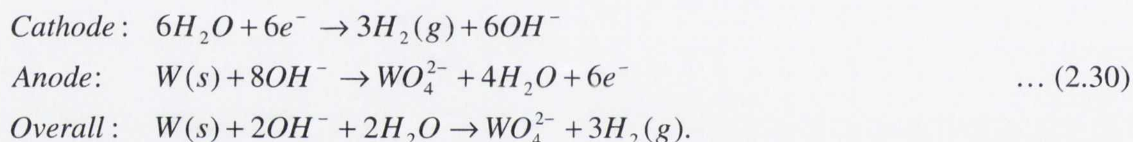

$$\begin{aligned} &Cathode: \quad 6H_2O + 6e^- \rightarrow 3H_2(g) + 6OH^- \\ &Anode: \quad W(s) + 8OH^- \rightarrow WO_4^{2-} + 4H_2O + 6e^- \\ &Overall: \quad W(s) + 2OH^- + 2H_2O \rightarrow WO_4^{2-} + 3H_2(g). \end{aligned} \qquad \ldots (2.30)$$

This reaction involves the oxidative dissolution of *W* wire to soluble tungstate (WO_4^{2-}) anions at the anode and the reduction of water to form bubbles of hydrogen gas and OH^- ions at the cathode. The etching process takes a few minutes and occurs at the air/electrolyte interface, causing the portion of wire in solution to 'drop-off' when its weight exceeds the tensile strength of the etched or necked-down region. In fact this procedure produces two tips simultaneously; the part below the air/electrolyte interface that drops off and the part remaining above. To remove residual NaOH, a thorough rinsing with deionised water and alcohol is necessary.

Several parameters affect the shape and sharpness of the resulting STM tip. These include: the shape of the meniscus, the length of wire in solution, the etch potential, and the solution concentration [33, 41]. However, the most important parameter that affects the final shape of the tip end is the time for the etching current to switch off after the lower part drops off. The shorter the cut-off time the sharper the tip end. This cut-off time

can be minimised using a simple electronic circuit [41]. Optimisation of all parameters produces very sharp tips with radii of curvature down to 10 nm or even less. An example of a tip prepared by the d.c. drop-off method is shown in Fig. 2.17.

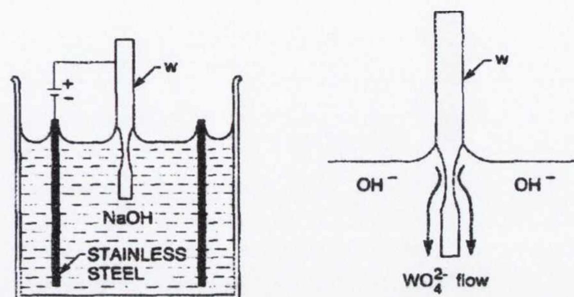

Fig. 2.16: Electrochemical etching of W wire using an aqueous solution of NaOH [33].

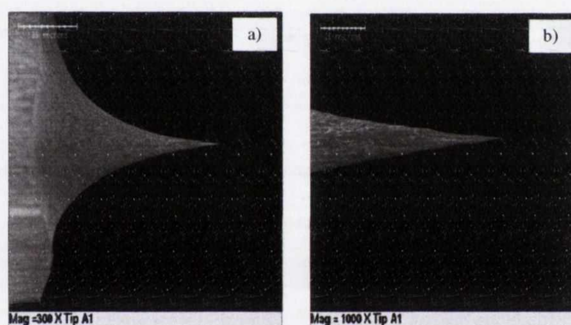

Fig. 2.17: Secondary Electron Microscope (SEM) images of a W tip following an electrochemical etching process via the d.c. drop-off method. Magnification- a) 300 times b) 1000 times.

After etching, the tip is covered with a dense oxide layer (usually WO_3), and is often contaminated with sodium compounds from the etchant solution, as well as organic molecules [33]. In order to remove the contaminants and oxide layer from the tip, it undergoes an annealing process. This is readily achieved by heating the tip *in vacuo* to approx. 900 K at which point the volatile tungsten oxides and contaminants sublime leaving a clean tungsten surface. Typical heating methods include resistive heating and electron bombardment [33]. Tips should be heated in the vertical position to minimise possible sagging that may occur during the heating process. Following completion of the annealing process, the tip can be transferred to the STM for imaging. It is also worth noting that special tip treatments can be conducted during actual tunneling to improve

image resolution. Methods include the application of a high electric-field to the tip [42] and controlled collision of the tip with the sample surface [43].

2.8. Surface Preparation Techniques

Several approaches to the preparation of silicon surfaces for STM investigations have been reported [4]. Here a brief description of the issues involved will be discussed. Cleaning the sample in order to obtain a well reconstructed surface is an important aspect of the STM because the sample surface strongly influences the stability of its operation.

2.8.1 High Temperature Preparation

The stable reconstructions of low-index silicon surfaces are most readily prepared by high temperature annealing in UHV. Here, heating to approx. 1200 °C for a short time period produces high quality, defect-free surfaces via removal of the native oxide layer [44]. The heat treatment is typically provided by direct current heating or electron bombardment of the sample surface [33]. Nonetheless, one must keep in mind the potential for thermally activated changes in the near-surface region during high-temperature anneals [4]. Indeed, carbon contaminants originally on the surface are thought to diffuse into the bulk of the sample and dopants have been known to surface segregate from the bulk of heavily doped samples [4, 44]. To limit outgassing from the sample and its holder during the high-temperature treatment, the sample assembly should be degassed for several hours at approx. 700 °C [4]. A calibrated pyrometer is typically used to monitor the sample temperature. This temperature should be maintained until the pressure remains in the 10^{-10} Torr range. At this low temperature the native SiO_2 layer remains intact and therefore acts as a protective shield for the underlying surface. For all of the thermal surface preparation techniques it is critically important to construct the sample holder carefully with appropriate high-temperature materials. Stainless steel components should never be used because they act as a source of nickel contamination [45]. Appropriate high temperature metallic materials are the refractory metals such as molybdenum, tantalum and tungsten.

2.8.2 Intermediate Temperature Preparation

As an alternative to high-temperature annealing, sputter-anneal cycles can be used to prepare Si surfaces [4, 32]. This has the advantage of a lower preparation temperature and hence minimises outgassing and possible contamination of the surface. Some possible drawbacks include: a) extended preparation times, b) the possibility of sputtering metallic components of the sample holder onto the sample surface and c) possible residual damage to the crystal substrate [4, 46, 47]. Another intermediate-temperature method for preparing clean silicon surfaces is the *Shiraki etch* [48]. In this technique a wet chemical etch is used to eliminate carbon contaminants. The clean surface is then capped *ex-situ* by a thin oxide film that can be removed *in-situ* by heating the sample to only 800 °C [4]. Since the Shiraki etch is an intermediate temperature method, carbon contaminants that are not removed from the surface by the etch, or that are transferred to the surface from the sample holder, tend to coalesce into SiC islands. These SiC particles can act as pinning sites for steps. Another wet chemical treatment involves hydrogen passivation of the silicon surface which can subsequently be mildly annealed in UHV to produce a clean surface [49].

(This chapter provided a general discussion concerning scanning tunneling microscopy theory, instrumentation and techniques. For a description of the specifics regarding our conventional STM system design, the reader is directed to Appendix A.)

References:

[1] G. Binnig, and H. Rohrer, Surface Science **126**, 236 (1983).

[2] F. Salvan *et al.*, Annales De Physique **13**, 133 (1988).

[3] R. M. Tromp, Journal of Physics: Condensed Matter, 10211 (1989).

[4] J. A. Kubby, and J. J. Boland, Surface Science Reports **26**, 61 (1996).

[5] F. S. Levin, *An Introduction to Quantum Theory* (Cambridge University Press, New York, 2002).

[6] R. Wiesendanger, *Scanning Probe Microscopy and Spectroscopy- Methods & Applications* (Cambridge University Press, Cambridge, United Kingdom, 1994).

[7] J. G. Simmons, Journal of Applied Physics **34**, 1793 (1963).

[8] R. H. Fowler, and L. Nordheim, Proceedings of the Royal Society **119**, 173 (1928).

[9] J. G. Simmons, Journal of Applied Physics **34**, 2581 (1963).

[10] I. Giaever, Physical Review Letters **5**, 147 (1960).

[11] I. Giaever, Physical Review Letters **5**, 464 (1960).

[12] I. Giaever, Reviews of Modern Physics **46**, 245 (1974).

[13] R. Young, J. Ward, and F. Scire, Physical Review Letters **27**, 922 (1971).

[14] R. Young, J. Ward, and F. Scire, Review of Scientific Instruments **43**, 999 (1972).

[15] G. Binnig, and H. Rohrer, Helvetica Physica Acta **55**, 726 (1982).

[16] J. A. Golovchenko, Science **232**, 48 (1986).

[17] G. Binnig *et al.*, Applied Physics Letters **40**, 178 (1982).

[18] G. Binnig *et al.*, Physical Review Letters **50**, 120 (1983).

[19] J. Bardeen, Physical Review Letters **6**, 57 (1961).

[20] J. Tersoff, and D. R. Hamann, Physical Review Letters **50**, 1998 (1983).

[21] J. Tersoff, and D. R. Hamann, Physical Review B **31**, 805 (1985).

[22] R. J. Behm, N. Garcia, and H. Rohrer, *Scanning Tunneling Microscopy & Related Methods* (Kluwer Academic Publishers, Dordrecht, 1990).

[23] J. J. Boland, Advances in Physics **42**, 129 (1993).

[24] D. K. Biegelsen, Proceedings of SPIE **946**, 211 (1988).

[25] R. M. Feenstra, W. A. Thompson, and A. P. Fein, Physical Review Letters **56**, 608 (1986).

[26] http://en.wikipedia.org/wiki/Scanning_tunneling_spectroscopy.

[27] R. M. Feenstra, J. A. Stroscio, and A. P. Fein, Surface Science **181**, 295 (1987).

[28] N. D. Lang, Physical Review B **34**, 5947 (1986).

[29] A. Selloni *et al.*, Physical Review B **31**, 2602 (1985).

[30] D. A. Bonnell, *Scanning Probe Microscopy and Spectroscopy : Theory, Techniques, & Applications* (Wiley, New York, 2001).

[31] J. A. Stroscio, R. M. Feenstra, and A. P. Fein, Physical Review Letters **57**, 2579 (1986).

[32] C. Bai, *Scanning Tunneling Microscopy & Its Application* (Springer, London, 1995).

[33] J. C. Chen, *Introduction to Scanning Tunneling Microscopy* (Oxford University Press, United Kingdom, 1993).

[34] E. Meyer, H. J. Hug, and R. Bennewitz, *Scanning Probe Microscopy- The Lab on a Tip* (Springer-Verlag, Berlin, 2004).

[35] H. C. Zhang *et al.*, The Journal of Vacuum Science and Technology B **12**, 1669 (1994).

[36] Y. Kuk, and P. J. Silverman, Review of Scientific Instruments **60**, 165 (1989).

[37] I. Burleigh Instrumaents, Burleigh Park, Fischers, New York, 14453.

[38] S. Park, and C. F. Quate, Review of Scientific Instruments **58**, 2010 (1987).

[39] D. W. Pohl, Review of Scientific Instruments **58**, 54 (1987).

[40] M. Okano, K. Kajimura, and S. Wakiyama, The Journal of Vacuum Science and Technology A **5**, 3313 (1987).

[41] J. P. Ibe, P. P. Bey, and S. Brandow, Journal of Vacuum Science and Technology A **8**, 3575 (1990).

[42] J. Wintterlin *et al.*, Physical Review Letters **62**, 59 (1989).

[43] J. E. Demuth, U. Koehler, and R. J. Hamers, Journal of Microscopy **151**, 289 (1988).

[44] B. S. Swartzentruber *et al.*, The Journal of Vacuum Science and Technology A **7**, 2901 (1989).

[45] J. A. Martin *et al.*, Physical Review Letters **56**, 1936 (1986).

[46] J. C. Bean *et al.*, Journal of Applied Physics **48**, 907 (1977).

[47] J. H. Comfort, L. M. Garverick, and R. Reif, Journal of Applied Physics **62**, 3388 (1987).

[48] A. Ishizaka, and Y. Shiraki, The Journal of The Electrochemical Society **133**, 666 (1986).

[49] G. S. Higashi *et al.*, Applied Physics Letters **58**, 1656 (1991).

Chapter 3

Introduction to Ultra-high Vacuum

From the experimental point of view, the development of modern surface science is intimately related to the advent and advance of ultra-high vacuum (UHV) techniques. In order to prepare well-defined surfaces with negligible contamination, UHV is required, which is defined by a pressure range lower than 10^{-8} Pa. Under UHV conditions a freshly prepared surface can stay clean for several hours. This pressure condition also permits the use of low energy electron and ion based experimental techniques to be conducted without undue interference from gas phase scattering [1]. The surface of a solid under atmospheric pressure is far removed from a surface in UHV. A fresh, clean surface is very reactive to impinging gas phase species. Therefore a clean surface exposed to atmospheric conditions is very complex and undefined. It consists of many different physisorbed and chemisorbed species which form a complex adlayer on the topmost atomic layers of the surface [2]. This contamination adlayer hinders the controlled adsorption of a single and pure selected species. UHV on the other hand permits such an occurrence on freshly cleaned surfaces and permits surface analysis techniques to carry out detailed investigations into the adsorption processes. Hence, UHV is a necessity to study reaction processes on solid state surfaces via STM and is also critical to establish true surface stress evolutions for the investigated species. Typical modern UHV systems consist of a stainless steel chamber, in which the surface studies or processes are conducted, a series of pumps to help generate the desired pressure, in addition to gauges covering different pressure ranges. A mass spectrometer is also typically added to monitor the residual gas. In order to achieve the UHV regime the vacuum system must not only be pumped adequately but it must be free of true and virtual leaks. The later arises from gases, especially water, desorbing from the interior chamber walls and instruments [1]. At room temperature these gases will desorb constituting a large virtual leak that can last for years. These are eliminated in a matter hours by heating the chamber uniformly to approx. 150 ^{o}C [1]. Great care must also be taken to ensure no oils or high vapour pressure materials are used within the UHV system [1, 3]. The necessity for UHV

to study the fundamental processes involved in surface reactions will be discussed in this chapter. In addition, the instrumentation and techniques used to generate this condition and monitor its status will also be presented.

3.1. The Necessity for Ultra-high Vacuum

The simplest interface one can think of is that between a crystalline surface and a vacuum. The surface, of course, has to be prepared as a fresh, clean surface within this vacuum. In order to conduct experiments with this clean surface, the background pressure must be such that the time required for contaminant build-up from these unwanted residual gases is substantially greater than that required to conduct the experiment. The contaminant layer prohibits any controlled systematic investigation of surface properties and results from the flux of residual gas species striking the surface, i.e. the number of molecules striking the surface per unit area per unit time. From the kinetic theory of gases, the molecular flux, Z, is given by the Hertz-Knudsen equation

$$Z = \frac{Nc}{4V} \qquad \text{... (3.1)}$$

where, N/V is the number of molecules per unit volume and c is the average speed of the molecules [4]. For a gas with molecular weight, M, at temperature, T,

$$c = \sqrt{\frac{8RT}{\pi M}} \qquad \text{... (3.2)}$$

with, R representing the gas constant [4]. Combining equations (3.1) and (3.2) with the ideal gas equation, $PV=nRT$, and writing $N=nN_A$, where N_A is Avogadro's number, gives [3]:

$$Z = \frac{N_A P}{\sqrt{2\pi MRT}}. \qquad \text{... (3.3)}$$

For pressure, P, given in Pa (1 Pa≡1 $N/m^2 \approx 7.5x10^{-3}$ Torr≈$9.9x10^{-3}$ mbar) and molecular weight, M, in g/mol, substitution of the relevant constant values in equation (3.3) leads to

$$Z = \frac{2.635x10^{24} P}{\sqrt{MT}} \text{ collisions m}^{-2}\text{ s}^{-1}. \qquad \ldots (3.4)$$

The rate of molecular impingement is therefore dependent upon the molecular weight, the temperature and the pressure of the gas involved. At atmospheric pressure ($1.01325x10^5$ Pa) the flux is extremely high, e.g. for nitrogen gas at room temperature, Z=$2.91x10^{27}$ collisions m^{-2} s^{-1}. Since a typical surface has an exposed atomic density of approx. $2x10^{19}$ atoms m^{-2}, each surface atom will be struck by approx. $1.5x10^8$ molecules every second [3]. At a pressure of 10^{-8} Pa (UHV) the average time interval for a surface atom to be struck by a gas molecule is about $7x10^4$ seconds or 19 hours [3]. Contamination time is the time taken for one monolayer of contaminant to form on a surface. This is not only dependent on the molecular flux and surface atomic density but also on the reactivity of the system in question. The later can be simply expressed as a sticking probability, S. For many systems, S is close to unity, i.e. nearly every impinging species sticks to the surface. Therefore, in order to keep a surface clean over a period of the order of hours to conduct experiments, it is necessary to work under UHV conditions where contamination effects from residual gases can be neglected.

For surface science experiments conducted under UHV conditions, physicists have introduced a convenient exposure or dosage unit for clean surfaces: 1 Langmuir (1 L) is the dosage corresponding to exposure of the surface for 1 second to a gas pressure 10^{-6} Torr. For a surface with a sticking coefficient of unity this exposure results in an adsorbate coverage of approx. one monolayer. Exposure values expressed in Langmuir, therefore, convey a direct gauging for the maximum amount of adsorbate coverage.

3.2. Ultra-high Vacuum Pumps

A combination of different pumps is required to obtain background pressures in the main UHV chamber on the order of 10^{-10} Torr, since each pump can only operate over

a limited pressure range. A bake cycle is critical in achieving this level of UHV. Figure 3.1 represents a schematic view of a standard UHV chamber design. The UHV range is typically achieved using ion and turbomolecular pumps. Starting pressures for ion pumps are in the range 10^{-2} to 10^{-4} Torr. Therefore, the chamber has to be pumped down from atmospheric pressure to this range prior to operation; this process is known as *roughing* [2]. A turbomolecular pump can operate at atmospheric pressure and can operate down into the UHV regime but a *backing pump* is necessary [2]. Roughing of the chamber and backing of the turbomolecular pump is typically achieved using a rotary pump. Valves are necessary to separate the pumps from one another and from the UHV chamber, since a pump that has reached its operating limit can potentially act as a leak for other pumps operating down to lower pressures. In general, only the ion pumps are utilised to maintain UHV conditions when conducting STM and other precision measurements. This is due to the fact that turbomolecular pumps can introduce unwanted vibrations during their operation. However, turbomolecular pumps do play an important role in initially generating UHV and in pumping large gas volumes under certain experimental circumstances. The operation mechanisms for the above mentioned pumps will now be discussed.

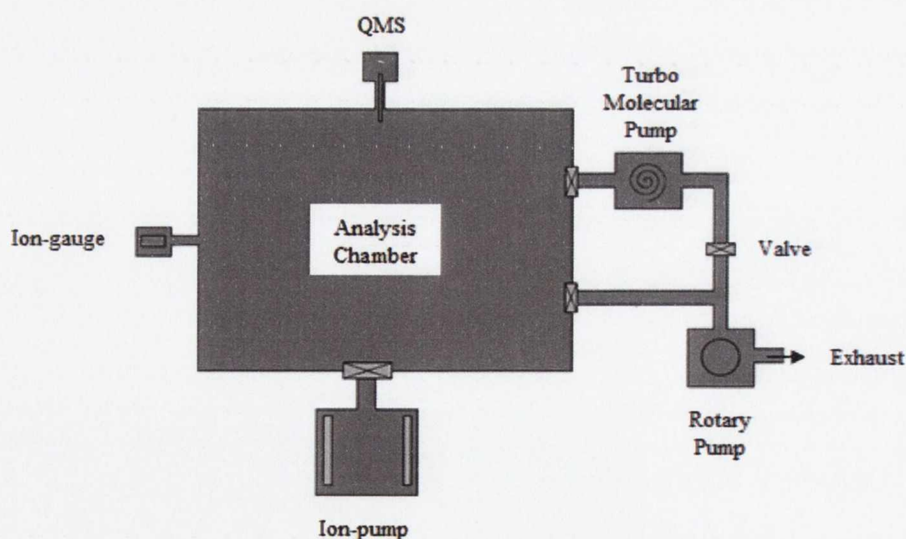

Fig. 3.1: Illustration of a UHV system- stainless steel UHV vessel pumped by different pumps. The quadrupole mass spectrometer (QMS) and ion-gauge are used for monitoring the residual gas. Essentially the entire system must be baked in order to achieve a good UHV condition.

3.2.1 Rotary Pumps

The rotary piston pump and the rotary vane pump are two oil-sealed pumps commercially available for pumping gas in the pressure ranges 1-10^5 Pa [1]. Of the two, the rotary vane pump is the most commonly used in medium sized vacuum systems. Rotary vane pumps of 10-200 m^3/hour displacement are used for rough pumping and backing turbomolecular pumps [1]. Rotary pumps are essentially gas compressors. An oil-sealed mechanical pump isolates, with each revolution, a sample of gas which is then compressed and either passed onto a second stage for further compression or expelled via an exhaust valve [2].

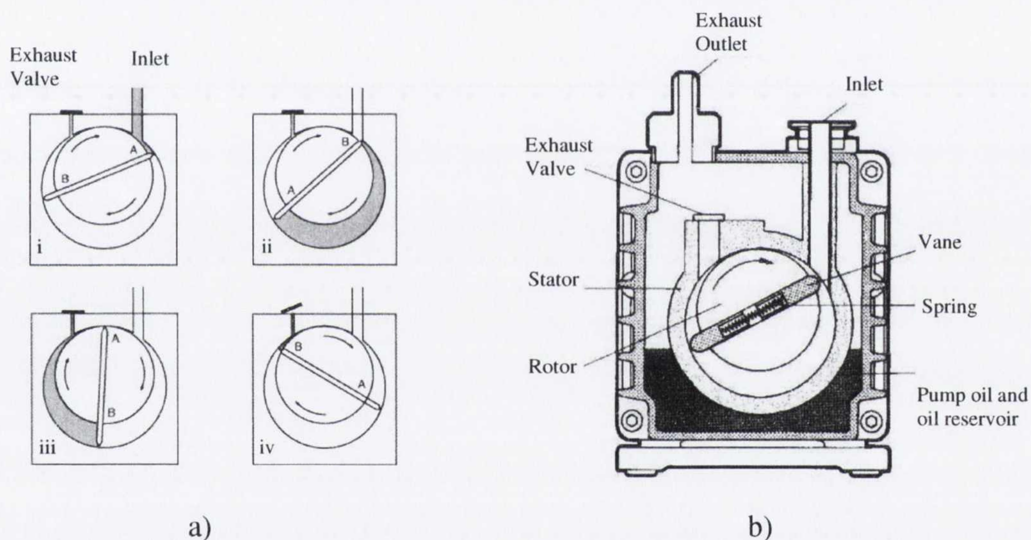

Fig. 3.2: a) Schematic representation of the pumping process in a rotary vane pump. The inlet volume expands during the gas inlet stage and further rotation of the eccentric rotor causes compression of this volume until the outlet stage is reached [5]; b) Detailed sectional view of a rotary vane pump [6].

The pumping process is shown in Fig. 3.2 (a). The four main stages involved are as follows: i) during the inlet phase, gas/vapour enters the pump chamber; ii) gas/vapour within the pump is isolated from the source and compression begins; iii) gas/vapour is compressed to a pressure just below that required to open the exhaust valve (at this point there is a danger that the vapour may condense and contaminate the fluid); iv) compression has reached a stage (approx. 1-2 bar) where the exhaust valve opens and the

gas/vapour is expelled. If condensation is an issue the pump will become contaminated, the ultimate pressure (typically 10^{-3}-10^{-7} Torr) will increase and gum deposits will form on the moving parts [1]. The pump may even seize under certain circumstances. In order to prevent this occurrence, rotary vane pumps can be fitted with a ballast valve. The ballast valve allows gas, usually atmospheric air, to enter the chamber during the compression stage. This causes the exhaust valve to open prematurely (before the partial pressure of the vapour being pumped exceeds its saturated vapour pressure) so that the vapour is discharged without liquefaction [7]. It should be noted that rotary vane pumps adopting a ballast valve configuration have higher ultimate pressures than rotary vane pumps without this arrangement. In Fig. 3.2 (a) gas from the system is compressed and expelled in one cycle. This is a single-stage rotary vane pump. An alternative exists, i.e. a two-stage rotary vane pump, whereby the compressed gas is sent to a second stage for further compression before being expelled. This produces lower ultimate pressures as a result [2]. Fig. 3.2 (b) shows the construction of a typical single stage rotary vane pump in greater detail. Within the pump body, there is an eccentrically-mounted rotor which is driven by a motor. The rotor is fitted with radially sliding vanes which are in contact with the inner wall of the pump chamber.

The fluid used in oil sealed rotary vane pumps has three functions [8]: 1) lubrication of the bearings and sliding surfaces; 2) sealing between the vanes and the walls of the pump chamber; and 3) heat dissipation. The choice of fluid must fit all of the above requirements. If it fails, or if its function is impaired through chemical, thermal or mechanical interference, then the pump performance will decline [8]. These constraints imply that the pump fluid should exhibit the following characteristics: suitably low vapour pressure, good thermal stability, good wetting ability, good resistance to a range of pump gases and exhibit a range of desired solvent properties [8]. Oils typically used in rotary vane pumps are either mineral oils or synthetic fluids. Oil sealed pumps are sources of potential problems in UHV systems. Misused or inadequately trapped, they can cause significant contamination of the UHV chamber and can also pose potential health hazards [1]. As a result dry vacuum pumps, in which the gas handling chamber is free of sealants, have been developed for roughing and backing purposes. The scroll pump is an example of typical dry vacuum pump used for this purpose [1].

3.2.2 Turbomolecular Pumps

The turbomolecular pump (TMP) is a bladed turbine that compresses gas by momentum transfer from high speed rotating blades to the gas molecules [9]. The pump operates with rotation speeds in the range 24,000-80,000 revolutions per minute (rpm). This puts considerable strain on the bearings which have to be efficiently lubricated by a flowing oil system and water cooled. A typical TMP design is shown in Fig. 3.3. The relative velocity and orientation between the alternate rotor and stator blades makes it probable that a gas molecule will be transported from the pump inlet to the pump outlet [1]. When the mean free path of the gas species is larger than the spacing between rotor and stator blades (molecular flow range in a TMP, typically $<10^{-3}$ Torr), particles collide predominantly with the rotor blades, resulting in an efficient pumping process, and there is no interacting influence of the different gases [7]. In the laminar flow range ($> 10^{-3}$ Torr), the action of the rotor is reduced by the frequent collisions between the particles [7]. As a consequence of this, the TMP is not capable of pumping gas against atmospheric pressure. Therefore, a backing pump, such as a rotary vane pump, is required to generate a suitable environment for efficient TMP operation. The TMP is the only mechanical vacuum pump, which together with a backing pump can achieve pressures in the UHV range.

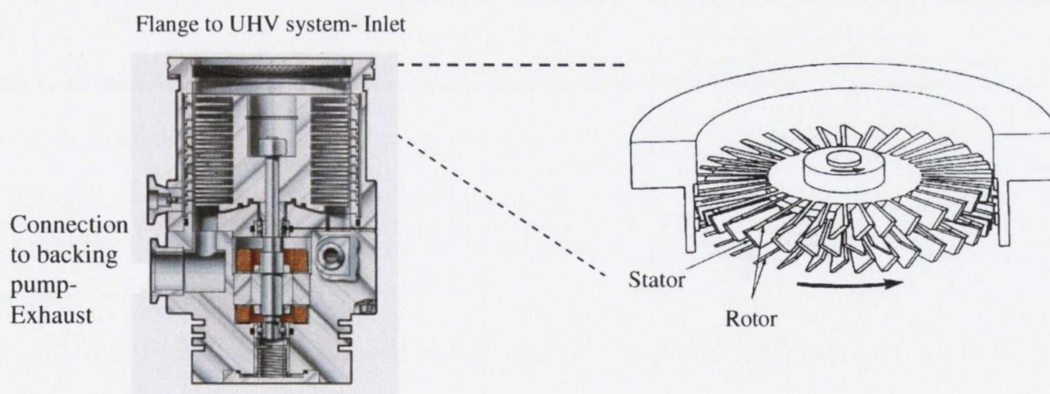

Fig. 3.3: Sectional view of a typically turbomolecular pump design. The pump is comprised of a series of disks with a row of blades, alternately between fixed and moving. In each disk the blades are inclined with respect to the disk plane, in one direction for the blades of the moving disks (rotors) and in the other for the blades of the fixed disks (stators). This arrangement produces an efficient pumping process [6, 7, 10].

The mechanism for the operation of this pump is illustrated in Fig. 3.4. Here, assume that the blade speed is large compared with the molecular speeds of the gases present. If gas molecules are drifting towards rotating blades their relative velocities will make a rather sharp angle to the direction of rotation and they will impinge on the edges of the blades as illustrated [11]. If diffuse reflection is assumed, incident molecules on *side 1* re-emitted within the angle θ_1 will return to *side 1* whilst those re-emitted within angle θ_3 will escape to *side 2*. Those molecules re-emitted within angle θ_2 may ultimately escape to either to *side 1* or *side 2*. A similar analysis can be applied to molecules incident from *side 2*, with relevant angles in this case being $\theta_1^{'}$, $\theta_2^{'}$, $\theta_3^{'}$. The probability that a molecule will be transferred from one side of the blade to the other is dependent on the ratio of the angles present, and it is evident from the diagram that the probability of molecules travelling from *side 1* to *side 2* is much greater than that for the reverse direction. The mechanism has been treated theoretically by *Kruger* and *Shapiro* via Monte-Carlo calculations [12]. They showed that depending on the blade speed and angle the probability of molecules travelling form *side 1* to *side 2* was some 10-40 times higher than molecules going in the opposite direction. The net flow of gas across the blade will not only depend on the transfer probabilities but is also dependent on the compression ratio [7, 12]. Generally it was shown that the design for maximum pumping speed gave the lowest compression ratio and vice versa so that a compromise between pumping speed and compression ratio has to be chosen [12]. The velocity the impinging molecules receive in the direction of the blade rotation ensures that they will also collide with the stator blade at glancing angles. Since the stator blades are angled in the opposite direction a similar favorable flow through the blades is achieved. In practical design there are a number of sets of rotor/stator pairs, with each set representing a pumping stage. It is common in modern TMP to have some pumping stages designed for maximum pumping speed whilst those nearest the outlet are designed to have a greater compression ratio [11].

The ultimate pressure for a gas species, P_u, achieved using the TMP can be calculated as:

$$P_u = P_0 / K_{\max} \quad \ldots (3.5)$$

where, P_0 is the pressure at the outlet side of the pump and K_{max} is the maximum compression ratio [9]. The increase of the maximum compression ratio with molecular weight of the particles pumped means that heavy molecules are highly compressed and have a low back-flow probability [11, 12]. Because of the high compression ratio for heavy molecules, oil vapour from the bearings does not back-stream and the pump is claimed to give a hydrocarbon free vacuum [12]. However, when the pump is not rotating, there is a danger of oil from the bearings and the backing pump migrating to the vacuum system. Therefore, precautions should be taken against such an occurrence. The smaller compression for light gases is the reason why that the residual gas atmosphere consists mainly of H_2. The ultimate pressure of a commercial TMP is generally between 10^{-9}-10^{-10} Torr for a two-stage rotary vane pump. The partial pressure of H_2 above a two-stage rotary vane pump is approx 5×10^{-7} Torr [9]. Assuming a K_{max} value of 10^3, and using equation (3.5), gives an ultimate pressure for H_2 above the TMP of 5×10^{-10} Torr [9]. This corresponds to the typical value of the ultimate pressure of this pump combination. Ion pumps are typically used to reduce the partial pressure of hydrogen in UHV systems and achieve a lower pressure range as a result [1].

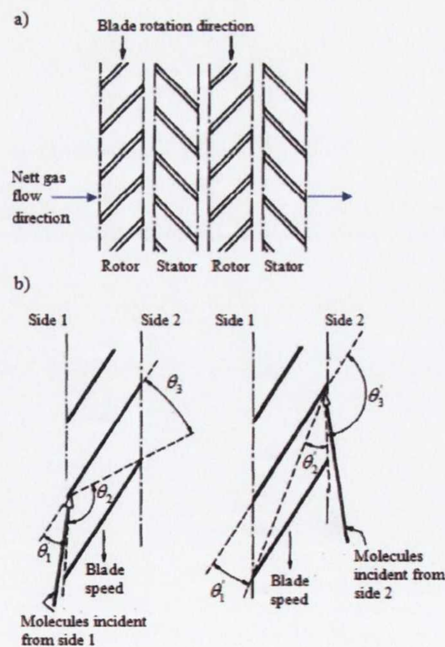

Fig. 3.4: a) Rotor and stator arrangement for the TMP; b) Illustration of the pumping mechanism for a single rotor. In comparison to molecular speeds of gases present, the blade speed is assumed large [11].

3.2.3 Ion Pumps

Sputter ion pumps have no rotating parts and are very convenient pumps for generating and maintaining UHV. These pumps exploit a phenomenon formerly considered detrimental to ion gauge operation- pumping gases by ions in Bayard-Alpert and Penning gauges [1, 11]. Ions are pumped easily because they are more reactive with surfaces than neutral species. In addition if the ions have sufficient energy they can physically embed themselves in walls on which they impinge. If the ions were generated in a simple parallel plate glow discharge, for example, the pumping mechanism would be restricted to a rather narrow pressure range. At 1 Pa and above electrons cannot gain enough energy to ionise the gas species due to frequent collisions, while below 10^{-1}-10^{-2} Pa the electron mean free path becomes so long that electrons collide with a wall before they encounter a gas molecule [1]. Nonetheless, ions can be generated at low pressures by increasing the path length of the energetic electrons using certain combinations of electric and magnetic fields.

The pumping action of a magnetically confined d.c. discharge was firstly observed by *Penning* [13]. However, it was not until two decades later that *Hall* conveniently combined several Penning cells in parallel in one envelope to transform the phenomenon into a functional pump [14]. The pump design for a *diode* sputter ion pump produced by *Hall* is shown in Fig. 3.5 (a). Typically, magnetic field strengths of 0.1-0.2 T and cathode voltages of approx. 5 kV are used. The electric fields present in each Penning cell trap the electrons in a potential well between the two cathodes and the axial magnetic field forces the electrons into circular orbits thus preventing them from reaching the anode [1]. The ions produced by collisions are accelerated towards the titanium cathode. On impact, sputtering of the cathode occurs, along with the generation of secondary electrons, which in turn are accelerated by the field. The pumping action of the sputter ion pump is a result of several mechanisms which can be explained with reference to Fig. 3.5 (b). These include [1]:

a) Precipitation or adsorption following molecular dissociation.

b) *Gettering* (chemical combination) by freshly sputtered cathode material.

c) Surface burial under sputtered cathode material.

d) Ion burial following ionisation in the discharge.

e) Fast neutral atom burial.

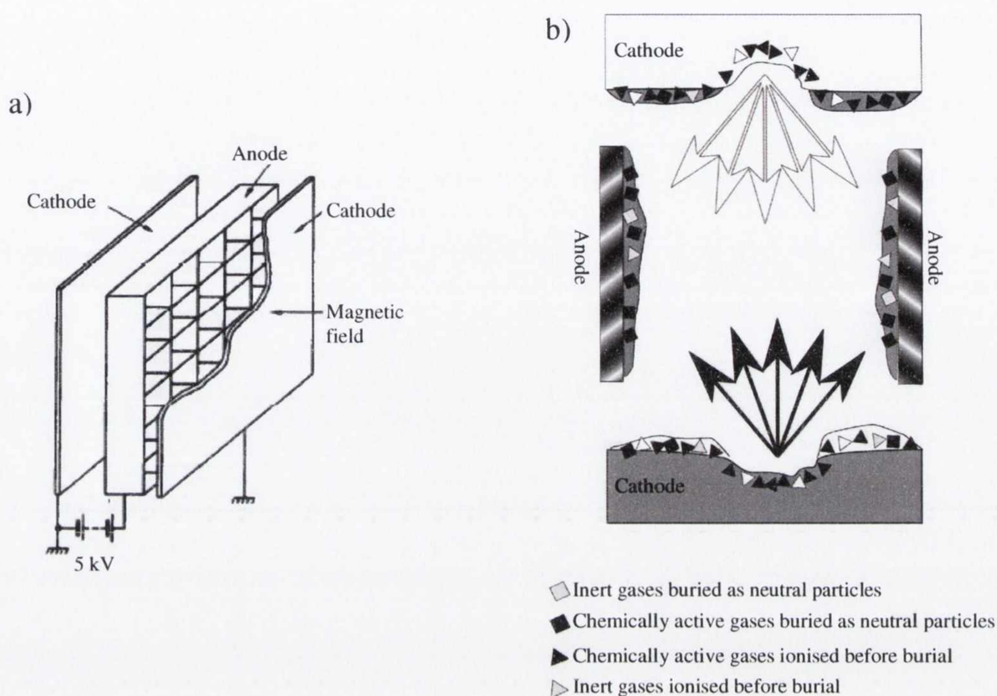

Fig. 3.5: a) Schematic of the basic construction of the diode sputter ion pump as designed by *Hall* [14]; b) Illustration showing sputter deposition and pumping mechanisms in a Penning cell. Due to the fact that ions are not produced uniformly across the cell (and the field is also non-uniform), erosion of the cathodes by sputtering is more pronounced in certain areas than others [11].

Active gases such as oxygen, carbon monoxide and nitrogen are pumped by reaction with titanium which is sputtered on the anode surfaces, and by ion burial in the cathode. These species are easily pumped as they form stable titanium compounds [15]. Hydrogen behaves differently. For hydrogen, the sputtering rate is negligible due to its light mass. It is initially pumped by ion burial and neutral adsorption, before diffusing into the bulk of the material and forming hydrides [16]. The hydrogen pumping speed does not rate limit unless the cathode surfaces are covered with compounds which prevent indiffusion [1]. Trace amounts of nitrogen can reduce hydrogen's pumping speed by contaminating the cathode surfaces [17]. Such contaminants can be removed, however, by pumping small amounts of inert gases, e.g. argon [18]. Noble gases are not pumped

very effectively using a diode sputter ion pump. They are pumped by ion burial in the cathodes and by reflected neutral burial in the anodes and cathodes [1]. Argon, in particular, also suffers from pumping instabilities. Periodically the argon pressure will rise as pumped gas is released from the cathodes. Nevertheless, different sputter ion pump designs exist for increasing noble gas pumping speeds and reducing or eliminating pumping instabilities, of which the *triode* and the *differential diode* are the most widely used [11].

Sputter ion pumps are available with a wide range of pumping speeds. The pressure range covered is 10^{-4} to less than 10^{-12} Torr; thus a roughing of the chamber is required to start the ion pump as previously mentioned. The base pressure of a sputter ion pump is limited by the equilibrium between pumped and desorbed molecules and not by the absence of discharge. The ultimate pressure range of 10^{-12} Torr can only be reached after baking the pump [19]. Additional pumping by gettering can be achieved using a titanium sublimation pump. In this pump an alternating current heats a titanium filament, which sublimes the titanium and deposits it on adjacent walls [1].

3.3. Vacuum Gauges

The pressure inside a UHV chamber can vary from atmospheric pressure to approx. 10^{-12} Torr. No single gauge can measure across this wide pressure range. Two commonly used indirect pressure reading gauges are the *Pirani gauge* [20] and the *Bayard-Alpert* gauge [21]. Indirect gauges record the pressure by measuring a gas property that changes in a predictable way with gas density. Pirani gauges are found on every vacuum system for measuring pressure in the medium vacuum range, while Bayard Alpert gauges are typically used for measurements in the UHV region. The Pirani gauge is an example of a thermal conductivity gauge. Thermal conductivity gauges operate by measuring the heat transfer between a hot filament and its surroundings [1]. Energy transfer by the gas is pressure dependent. It is this effect that is used to make a thermal conductivity based pressure sensor. In a Pirani gauge a metal filament, usually tungsten is held within a metal tube connected to the vacuum system and is heated using an electric current. The variation of the filament temperature (and thus the filaments resistance) is

monitored using a Wheatstone bridge configuration which if properly calibrated provides accurate pressure readings [1]. The Pirani gauge may be used for pressure measurements in the region from atmospheric pressure to approx. 10^{-4} Torr [1]. The most important gauge used in UHV systems is typically the Bayard-Alpert (B.A.) ion gauge which monitors the UHV region.

The operation principle of the B.A. ion gauge is based on electron impact ionisation. The basic hot cathode design is shown in Fig. 3.6. It consists of a heated cathode (usually a thoriated tungsten or thoriated iridium filament) which emits electrons that are accelerated towards a positively charged (100-200 V) cylindrical grid. Energetic electrons, collide with, and may ionise gas particles. Positive ions are attracted to the collector. The ionised current to the collector is proportional to the pressure, provided all the parameters, including the temperature, are held constant [1]. The proportionality between the collector current and pressure is given by:

$$I_c = SI_eP \qquad \ldots (3.6)$$

or

$$P = \frac{1}{S}\frac{I_c}{I_e} \qquad \ldots (3.7)$$

where, I_c and I_e are the collector and emission currents, respectively, and S is the sensitivity of the gauge tube [1]. The sensitivity is dependent on a number of factors. These include the tube geometry, grid and collector voltages, the type of control circuitry, and the nature of the gas being measured [1]. Ion gauges are typically calibrated for nitrogen. The pressure of other gases, $P(x)$, other than nitrogen can be measured, however, using the flowing expression:

$$P(x) = \frac{P(metering)}{S(x)_{relative}} \qquad \ldots (3.8)$$

where, $S(x)_{relative}$ is the ratio of the absolute sensitivity of the gas to that of nitrogen [1].

Despite its relatively simple design and operating principle, measurement of pressure in the UHV region using a hot cathode gauge demands considerable care. Numerous effects can alter the indicated ion current. These include, x-ray generated photocurrent, electron stimulated grid and collector desorption, wall gassing as a result of thermal heating by the hot cathode, chemical effects on heated cathodes, controller errors, wall diameter, and cathode evaporation [1, 18, 22, 23]. Historically most attention has been paid to reducing the x-ray generated photocurrent. Soft x-rays generated by electrons striking the grid, collide with the collector wire and cause photoelectrons to flow from the collector to the grid. Different variations of the B.A. gauge exist which can reduce this parasitic x-ray effect, as well as improving overall operation and performance. The range of a modern B.A. gauge is approx. 10^{-3}-10^{-12} Torr. The upper pressure limit is due to the non-linear response of the ion current with pressure, in addition to filament burn-out, while the lower limit determined by x-ray emission from the grid [1].

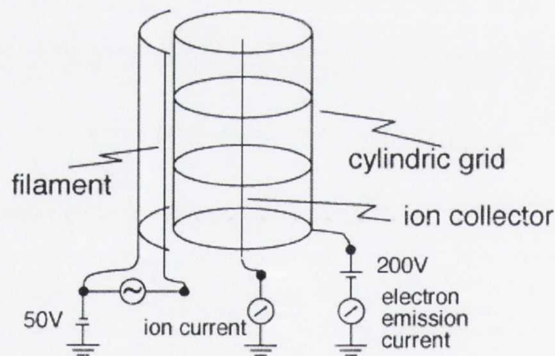

Fig. 3.6: Schematic diagram of a Bayard-Alpert gauge [5].

3.4. Residual Gas Analysers

Residual gas analysers are used in most cases to monitor the quality of the vacuum and easily detect minute traces of impurities in the low-pressure gas environment [24]. They are also used as a means to identify leak spots, when operated as sensitive helium leak detectors. A residual gas analyser is essentially a mass spectrometer, consisting basically of an ion source, a mass analyser, an ion detector and a display

system [8]. The ion source generates ions from the gas to be analysed, while the mass analyser sorts these ions according to their mass-to-charge (*m/z*) ratio [8]. Ions from the mass analyser are then detected, measured and displayed as ion currents. The basic set-up of a quadrupole mass spectrometer (QMS) is displayed in Fig. 3.7. These instruments are capable of resolving approximately single mass units ($\Delta m/z \approx 1$), and they scan a mass-to-charge range of 1-400 [1].

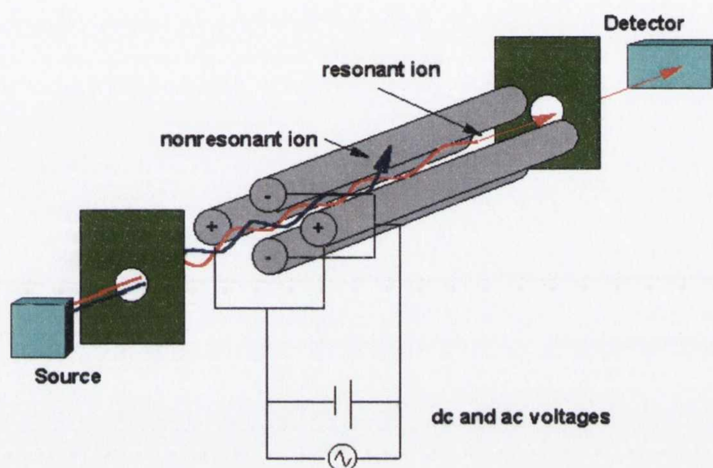

Fig. 3.7: Quadrupole mass spectrometers consist of an ion source, ion optics in order to accelerate and focus the ions through an aperture into the quadrupole filter. Also present is the quadrupole filter itself with control voltage supplies, an exit aperture, an ion detector, and detection electronics. The QMS operates from approx. 10^{-5} Torr to UHV conditions [1, 25].

The common technique used to generate positive ions in commercial residual gas analysers is electron impact ionisation. The choice of ion source for a partial pressure analyser depends on the pressure regime for the gases to be analysed and the accuracy and precision required for the measurement application [7]. The ion source is either immersed in the vacuum ambient (open source) or locally isolated by the nearby walls (closed source) [1]. For residual gases in the UHV regime, an open source with a high conductance to the vacuum system is required, similar to the design of a total pressure ion gauge. Process gas in the vacuum system is often monitored for minor impurities, and this low level detection can be achieved via a closed source. The residual gas composition

measured by the residual gas analyser can include a significant contribution from the outgassing and electron stimulated desorption of the hot cathode ionisation source [7]. Ion sources for UHV are designed to minimise these effects. Focus plates are placed in front of the ion source at potentials that focus the ion beam for maximum transmission through the mass analyser [7].

The quadrupole mass analyser is the most popular mass analyser used for vacuum partial pressure measurements because of its rapid scanning capability, compact size, linear mass scale and relatively low cost [7]. It consists of four parallel conductive rods arranged in square structure as shown in Fig. 3.7. Each opposing rod pair is connected electrically in parallel and a radio frequency voltage is applied between each rod pair. A direct current voltage is then superimposed on the radio frequency voltage. Ions entering from the ion source are accelerated down the quadrupole in between the rods. Only ions of a certain mass-to-charge ratio will reach the detector for a given ratio of voltages [24]. Other ions have unstable trajectories and will collide with the rods, are neutralised and are therefore lost from the beam [26]. This allows selection of a particular ion, or scanning by varying the voltages.

Ion currents can be measured directly from a mass analyser with an electrometer as ions strike a plate or Faraday cup [7]. Ion detection occurs when electrons flow to the plate in order to neutralise the charge of the ions that arrive. An appropriate electrometer circuit is used to measure this current. The detection limit of a Faraday detector is typically the noise limit of $3x10^{-16}$ A in modern field effect transistor electrometers [7].

The method of interpreting mass-to-charge scans is based on detailed knowledge of the cracking patterns of gases and vapours found in the UHV system [1]. Qualitative analysis of many major constituents is rather straightforward, whereas precise quantitative analysis requires careful calibration and complex analysis techniques [1]. On ionisation of molecules of gas and vapour, fragments of several mass-to-charge ratios are generated. The mass-to-charge values are unique for each cracked species, whereas the peak amplitudes are dependent on the gas and instrumental conditions. Each cracking pattern forms a fingerprint that may be used to identify the gases or vapours present in the UHV chamber. A very simple spectrum is displayed in Fig. 3.8.

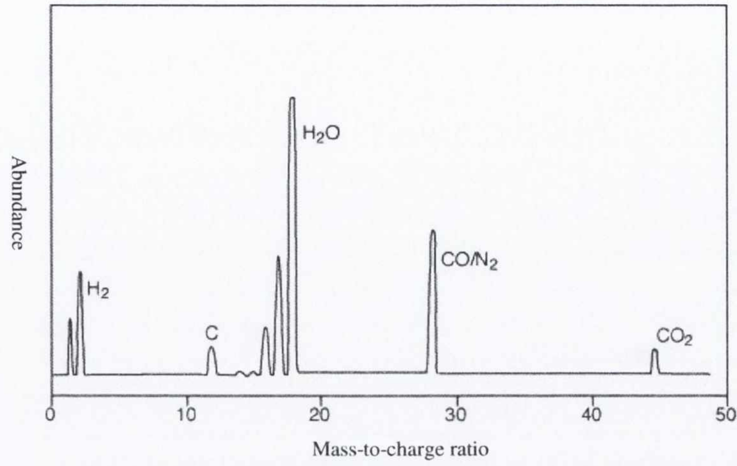

Fig. 3.8: An example of a typical mass spectrum before chamber baking [5].

(For details concerning the particulars of our UHV system design, please see Appendix A.)

References:

[1] J. F. O'Hanlon, *A Users Guide to Vacuum Technology* (Wiley & Sons, Hoboken, New Jersey, 2003).

[2] H. Luth, *Surfaces and Interfaces of Solid Materials* (Springer, Berlin, 1995).

[3] D. J. O'Connor, and B. A. Sexton, *Surface Analysis Methods in Material Science* (Springer, Berlin, 2003).

[4] W. J. Moore, *Physical Chemistry* (Longman, London, 1972).

[5] http://www.phys.au.dk/~philip/q1_05//surflec/node7.html.

[6] http://www.cbem.imperial.ac.uk/EM_Faculty/Equipment/Rotary_Pump.htm.

[7] J. M. Lafferty, *Foundations of Vacuum Science and Technology* (Wiley, Chichester, New York, 1998).

[8] D. J. Hucknall, *Vacuum Technology and Applications* (Butterworth-Heinemann, Oxford, United Kingdom, 1991).

[9] D. M. Hoffman, B. Singh, and J. H. Thomas, *Handbook of Vacuum Science & Technology* (London Academic Press, San Diego, California, 1998).

[10] http://uweb.txstate.edu/~wg06/manuals/ModulabPVD/PVDHome.htm.

[11] G. F. Weston, Vacuum **28**, 209 (1978).

[12] H. Kruger, and A. H. Shapiro, *Transcripts from the 7th National Vacuum Symposium 1960* (Pergamon, New York, 1961).

[13] F. M. Penning, Physica **4**, 71 (1937).

[14] L. D. Hall, Review of Scientific Instruments **29**, 367 (1958).

[15] S. L. Rutherford, S. L. Mercer, and R. L. Jepsen, *Transcripts from the 7th National Vacuum Symposium 1960* (Pergamon, New York, 1961).

[16] R. L. Jepsen, *Proceedings of the 4th International Vacuum Congression 1968* (Institute of Physics and Physical Society, London, 1969).

[17] J. H. Singleton, The Journal of Vacuum Science and Technology **8**, 275 (1971).

[18] J. H. Singleton, The Journal of Vacuum Science and Technology **6**, 316 (1969).

[19] http://www.chem.elte.hu/departments/altkem/vakuumtechnika/CERN05.pdf.

[20] M. Pirani, Verhandl. Dent. Physik. Ges. **8**, 686 (1906).

[21] R. T. Bayard, and D. Alpert, Review of Scientific Instruments **21**, 571 (1950).

[22] B. R. F. Kendall, The Journal of Vacuum Science and Technology A **17**, 2041 (1999).

[23] F. Watanabe, Vacuum **53**, 151 (1999).

[24] http://en.wikipedia.org/wiki/Residual_gas_analyzer.

[25] http://www.chem.vt.edu/chem-ed/ms/quadrupo.html.

[26] http://en.wikipedia.org/wiki/Quadrupole_mass_analyser.

Chapter 4

Surface Stress- General Discussion

As the size of surface features approaches the atomic scale, the application of current methodologies will no longer prove adequate in explaining a variety of surface phenomena. The effects of surface stress should be considered if these issues are to be resolved. Surface stress has been discussed since the time of *Gibbs* as part of his treatment on the thermodynamics of surfaces and interfaces [1], and is a quantity which affords a macroscopic description of surfaces. Qualitatively speaking surface stress is a reversible work per area to stretch a surface elastically. In the past decades, the science of solid state surfaces has developed largely with the emphasis to gain insights into atomic scale structures on surfaces [2]. It is only recently that the value of a thermodynamic description is again appreciated [2]. The particular value of this description results from the fact that one is able to draw conclusions about qualitative and even some quantitative aspects of surface phenomena without explicit knowledge of all atomistic processes involved [2-10]. As a consequence of this, the role of surface stress in the physics and chemistry of surfaces and their interfaces has become a matter of substantial interest in recent years as discussed in chapter 1. In particular, it has been widely discussed in relation to the explanation of mechanisms underlying single-crystal reconstruction, surface adsorption and thin film growth, each of which are profoundly influenced by its effects [2]. Deciphering the close correlation between macroscopic surface stress and microscopic atomic structure is a key step in developing a heightened understanding of atomic scale surface phenomena; hence our novel system design for combined surfaces stress and scanning tunneling microscopy (STM) measurements [11, 12]. While it is not yet possible to determine accurate measures of the absolute surface stress experimentally, techniques have been developed for the measurement of changes in surface stress when a surface is exposed to adsorbate species. Even such a macroscopic surface stress measurement has the possibility to reveal detailed atomic scale phenomena [13, 14].

Starting from the definition of surface stress, this chapter deals with a general discussion into current understanding of the physical origins of the surface stress on clean

and adsorbate covered metal and semiconducting surfaces. It will also present the cantilever bending method as a means of measuring changes in surface stress, in addition to a derivation of the *Stoney equation* [15]. This chapter is predominantly based on an excellent and tangible review on the topic of surface stress by *Ibach* [2].

4.1. Definition of Surface Stress [2]

Surface stress can be defined in a variety of ways. Let's commence with a definition which involves the change in the bulk stress tensor near a surface or an interface (an alternative definition in terms of the difference between the electronic charge distribution near the surface and the bulk which will be given in section 4.2). Let z represent the coordinate perpendicular to the surface/interface and x and y the coordinates in the surface. The tensor components which refer to the x and y axes are denoted as i and j, respectively (Fig. 4.1). The surface stress is then defined as the integral

$$\tau_{ij}^{(s)} = \int_{-\infty}^{+\infty} (\tau_{ij}(z) - \tau_{ij}^{(b)})dz \qquad \dots (4.1)$$

where, $\tau_{ij}^{(s)}$ denotes the component of the surface stress tensor and $\tau_{ij}(z)$ are the components of the bulk stress tensor as a function of z, which can be different from the bulk stress $\tau_{ij}^{(b)}$ in the vicinity of the surface) [2]. Surface stress has units of force per unit length, as apposed to units of force per unit area for bulk stress. The sign of the surface stress is positive if the surface would like to contract under its own stress [2]. The surface stress is identified as *'tensile'* when the surface stress is positive and *'compressive'* when the stress is negative.

The definition provided by equation 4.1 is particularly useful for a consideration of experimental means to determine the surface stress. Experimental techniques are based on the bending of a thin sheet of material under the influence of a change in the surface stress at one of the two surfaces [16]. The bending can be calculated from the elastic bulk properties of the plate using the definition in equation 4.1. Therefore, a measurement of

the bending sheet allows the determination of the change of a surfaces stress due to adsorption or deposition of atoms.

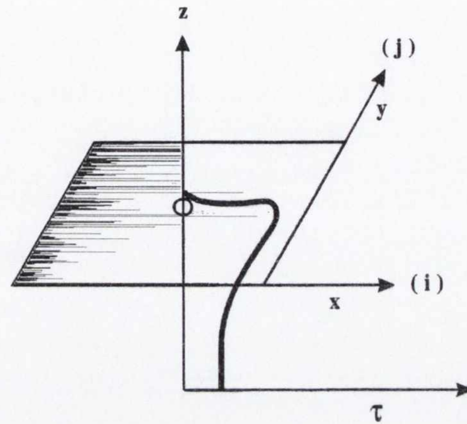

Fig. 4.1: Illustration of the variation of the bulk stress tensor, $\tau_{ij}(z)$, near the surface (solid thick line). This defines the surface stress according to equation 4.1. The components of the stress tensor in the x and y direction are denoted by the indices *i* and *j*, respectively [2].

4.2. The Charge Distribution and Surface Stress on Clean Surfaces [2]

When a surface is created, the electrons respond to the absence of atoms above the surface. As a result the charge distribution near the surface differs from that of the bulk [2]. The surface stress which is the integral over the difference between the stress near the surface and the bulk stress, as defined by equation 4.1, is a consequence of this redistribution of charge [2]. Since we are interested in the microscopic origin of the surface stress, it is useful to define the surface stress in such a way that the definition relates to microscopic forces while retaining the correct continuum limit [17]. In this definition we make use of the fact that by virtue of the *Hellmann-Feynman Theorem* [18, 19], all forces on the atomic nuclei originate from the Coulomb forces of the electronic charge density and the nuclear charges [17]. Consider a plane intersecting a solid surface at a right angle as illustrated in Fig. 4.2. In a 'thought experiment' remove all atoms and the electronic charge density on one side of the plane. In order to keep the mean forces on the nuclei on the other side of the plane balanced, one has to place forces on each atom such that the mean position of the atoms remains unchanged [17]. The

surface stress is then defined as the sum of all these forces per unit length, l, of intersection of the cutting plane and the surface, minus the sum of the forces one would have to place on the atoms, if there was no surface [2, 17]. While this definition may sound artificial at first glance, it has the advantage that it immediately relates the surface stress to the difference between the electronic charge distribution near the surface and the bulk. The consideration of the Hellmann-Feynman forces is, therefore, useful for a qualitative discussion of the effect of adsorbates and the role of the charge transfer on the surface stress.

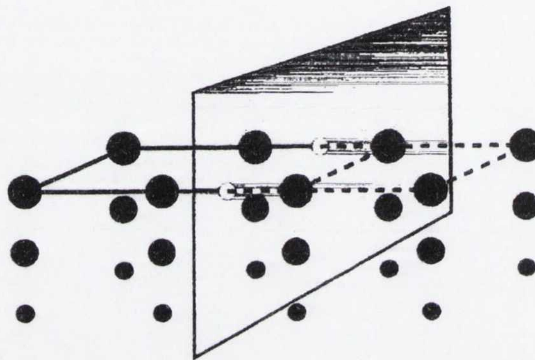

Fig. 4.2.: This schematic assists in illustrating the discussion of the surface stress in terms of the electronic charge density between the atoms near the surface. The distribution of electronic charge is determined by quantum mechanics, whilst the Coulomb forces on the atoms arise from the charge distribution [2].

At this point, we will discuss qualitatively the consequences of the charge redistribution for the surface stress of clean surfaces. The first case we will consider is the situation where the electronic charge gathers between the atoms in the form of a bond charge. However, this bonding scenario does not have the directionality of covalent bonding. This situation is typical for transition metals and noble metals [2]. The result of these considerations is that the surface stress should be positive (tensile) for clean surfaces of these materials. A tensile stress is also characteristic for free electron metals [2, 18, 19]. For the above cases, because of the missing bonds, charge migrates from above the surface into the peripheral of the solid, as depicted in Fig. 4.3 (a). Due to this charge relocation to the area between the first and second layer atoms, backbonds are strengthened. This results in the bonds becoming shorter, and contraction of the distance

between the first and second layer would occur. To a lesser or larger degree, such a contraction is found in many metal surfaces [2, 20]. There are exceptions, however, which include the nearly free electron metals Al(100), Al(111), and Mg(0001) [2, 21-23]. For metals where one finds a contraction, the contraction is the largest the more open the structure of the surface [2]. Electronic charge may also accumulate between the surface atoms. As a consequence of this a contraction of the equilibrium bond length between the surface atoms occurs. As the positions of the surface atoms are required to be held in registry with the crystal structure they cannot respond to this contraction of the equilibrium length of the lateral bonds, and a tensile surface stress arises [2]. This qualitative approach suggests that the surface stress on a clean metal surface should be tensile. It must be stated that it is not known whether these arguments hold for all metal surfaces since no general theorem to that effect has been proven [2]. The first principles calculations carried out to date, however, reveal that the surface stress on clean metal surfaces is in general tensile [2].

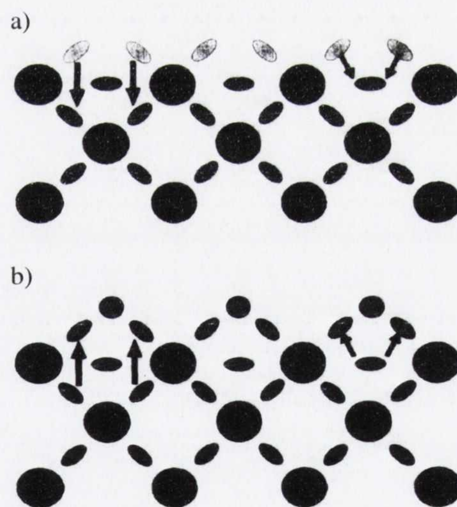

Fig. 4.3: Illustration of a simple picture of the origin of the surface stress. Bond charges near the surface for (a) a clean surface and (b) a surface which is covered by an electronegative adsorbate. On a clean surface, the bond charge in the absent bonds is redistributed. This redistribution strengthens backbonds between the first and second layers and reduces the equilibrium bond length between the surface atoms. As a result a tensile surface stress is expected on metal surfaces. The adsorption of electronegative atoms on the surface , however, removes charge between the surface atoms and causes a compressive surface stress [2].

The argument that the surface stress should be tensile as outlined above is true only if the surface does not reconstruct as a result of yielding to the surface stress. It must also be noted that the general discussion regarding the charge redistribution does not refer explicitly to the relative population of *s*, *p* and *d* states. The modified balance between *s*, *p* and *d* electrons as well as relativistic effects must be taken into account for the understanding of the particular large stress on the unreconstructed Ir(100) and Pt(100) surfaces [17, 24].

While such considerations call for a tensile stress on clean metal surfaces regardless of the surface structure, this does not hold for semiconductor surfaces. Here, the sign of the surface stress depends on the structure of the surface in question because of the effects of bond directionality and rehybridisation of orbitals near the surface [2]. The clean, unreconstructed Si(111) surface is an informative example in that regard [2, 25, 26]. Because of the dangling bonds, the surface atoms rehybridise from the bulk sp^3 configuration towards a planar sp^2 configuration. Since the Si-Si equilibrium bond distance, in the tetrahedral arrangement, remains virtually the same for the sp^2 hybridisation, the Si surface atoms are drawn inwards and push the Si atoms in the second layer sideways [2]. This situation is exemplified in Fig. 4.4. Therefore, this change in hybridisation introduces a compressive stress. In the case of a clean surface this value is relatively small (-0.63 N/m [2, 25]). However, on substitution of the Si surface atom by Ga, a larger compressive stress results (-5.6 N/m [2, 26]). The origin of this lies in the fact that Ga has only three valence electrons and as a result there is a stronger compulsion towards sp^2 hybridisation. Substitution by As reverses the sign of the surface stress to a tensile condition (+3.95 N/m [26]). The reason is that As has two electrons in a lone pair orbital and prefers to hybridise with bond angles less than those of a perfect tetrahedron. The resulting surface stress in the cases described above, depend not only on the degree of surface hybridisation but also on the size of the atom by which the Si is substituted. If the Si surface atom is substituted by the small atom B, then the stress still becomes tensile, despite the sp^2 hybridisation [2, 26]. Contrary to the Si(111) surface, the Si(100) and Ge(100) surfaces have a tensile surface stress [2, 27]. Here, the tensile stress results from the overlap of the half filled dangling bonds as illustrated in Fig. 4.5.

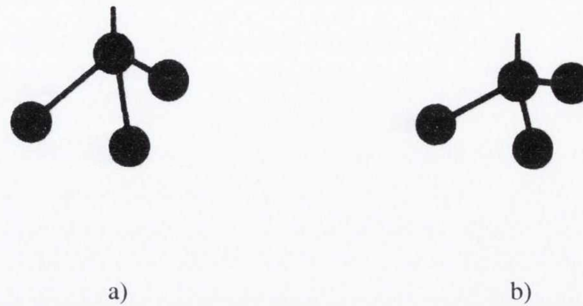

Fig. 4.4: Surface atom configuration at the Si(111) surface. The electronic configuration changes from sp^3 in the bulk towards sp^2 due to the dangling bond of the Si(111) surface atom. In comparison to a perfect tetrahedron (Fig. 4.4 (a)) the surface atom is pulled inward and the Si atoms in the second layer are pushed sideways (Fig. 4.4 (b)). This causes a compressive stress on the clean Si(111) surface [2].

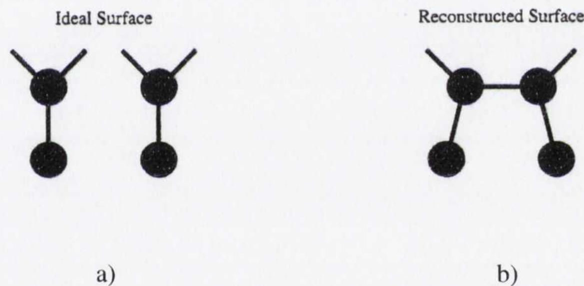

Fig. 4.5: Surface atoms with dangling bonds on a Si(100) or Ge(100) surface (Fig. 4.5 (a)). In this case the surface reconstructs to form Si or Ge dimers at the surface (Fig. 4.5 (b)). Dimer formation requires bending to occur and this bending causes a tensile stress in the dimer direction [2].

4.3. Adsorbate Induced Stresses [2]

It is obvious from what has been said thus far that the deposition of adsorbate onto the surface modifies the surface stress. With regard to the substrate atoms the charge redistributes as a result of the adsorption process and forms a more bulk like configuration. Let's consider the case of metal surfaces as a starting point for this discussion. The chemisorption of atoms on a metal surface restores the bonds between the surface atoms and the atomic entities above them [2]. Applying the aforementioned

qualitative reasoning, this should cause a reduction of the expected tensile surface stress provided that bonding to the surface saturates the bonding possibilities of the adsorbed atoms [2]. In the case of the deposition of atoms which form heteropolar bonds with the surface, large changes in the surface stress can be expected due to the strong influence of these species on the surface charge distribution. If the adsorbate is electronegative with respect to the underlying surface, i.e. capable of attracting electron density, one can envisage charge migrating from the bonds between the substrate surface atoms to reside on the adsorbate atoms. According to the proposed model, the removal of charge between the surface atoms should reduce the tensile stress nature of metal surfaces and in some cases may even turn the surface stress into a compressive condition [2]. The effect is amplified by an additional repulsion between charged adsorbate atoms. At close distances the effect of repulsive interaction results from the Coulomb repulsion of the dipole moments associated with the adsorbed atoms. However, this interaction is believed to be small when compared with the charge distribution effect [2, 17]. For the electronegative adsorbate atoms carbon, nitrogen and oxygen on various clean metal surfaces, the induced surface stress was experimentally determined to be compressive and by such an amount that the tensile stress turned compressive [2, 17, 28-30]. (A negative/compressive surface stress does not violate a stability criterion [2]. If the compressive stress becomes very large, certain surface vibrational modes can become soft, creating structural transitions of the surface [2]. *Ibach* discusses examples of negative surface stresses, i.e. compressive, on adsorbate covered surfaces in his review and the particular structural instabilities which can arise as a result of large compressive or large tensile surface stresses [2].)

If the adsorbate atoms are electron donors, the charge density between the surface bonds should be enhanced. As a result the tensile nature of the surface stress should be increased. Again, repulsive force interactions between the charged adsorbate atoms must be taken into account. Because of this charge, the induced tensile stress is partly compensated by the repulsion between the adsorbate atoms. The net effect should nevertheless be a tensile stress, since the distance between the charged adsorbate atoms is larger than the distance between the enhanced bond charges in the surface and the positively charged surface ion cores [2]. An example of the trends with electron donating and

electron withdrawing adsorbates is shown in Fig. 4.6. For carbon adsorption on the Ni(111) surface, the change in the surface stress is towards the compressive side [2]. In fact, the change is so large that the intrinsic surface stress of approximately 1.44 N/m on the clean surface turns into a compressive state [2, 31]. However, in the case of Cs adsorption, the tensile stress increases substantially. Interestingly, the increase persists above one monolayer (ML) coverage which is at $\Theta = 0.26$ [2]. It is important to note that these two examples illustrate the effects of strong heteropolar bonding. A calculation of the induced adsorbate surface stress for H on Pt(111) was conducted by *Feibelman* [2, 32]. This result indicates that at least for an adsorption process which involves only small charge transfers the sign of the induced stress may not follow the qualitative interpretation presented [2]. From the work function change hydrogen appears to be an electron donor, nevertheless, the induced surface stress is compressive [2, 32]. *Feibelman* has also pointed out a discrepancy in the above argument. On the Pt as well as on the Ni surface, the empty orbitals are antibonding [2, 32]. Charge transfer into the surface should cause a filling of antibonding orbitals, and according to *Feibelman* that filling of antibonding orbitals should increase the equilibrium bond distance, therefore, causing a compressive stress [2, 32]. This is in contrast with the majority of experimental observations [2]. In summary, the simple rule established by the reasoning presented by *Ibach* seems to be followed by most adsorbate-induced surface stress experiments on metals. In addition, theory is also in a position to calculate adsorbate-induced surface stresses which are in good agreement with experimental data [2]. The qualitative understanding of the adsorbate-induced stress on metal surfaces is still in its infancy. However, present experimental and theoretical investigations are paving the way for a better understanding in the future.

The situation appears to be better for semiconductors. Again, the role of the effects discussed for adsorption on metal surfaces can also be applied [2]. However, for these surfaces, the adsorbate-induced surface stress can also be qualitatively understood in terms of the local covalent bonding [2]. For example, for oxygen adsorption on unreconstructed Si(111) and Si(100), the sign and even the magnitude of the induced stress can be estimated (through a valence force model) from the bond angles and bond distances of the Si-O bond, and the stiffness of these bond lengths and angles with regard

to distortions [2, 33, 34]; see Table 4.1. Experimental results presented in [33] are in reasonable agreement with the proposed model. However, further insight into the role of dangling bonds and the surface reconstruction in the oxygen induced surface stress requires first-principals total energy calculations [2, 33].

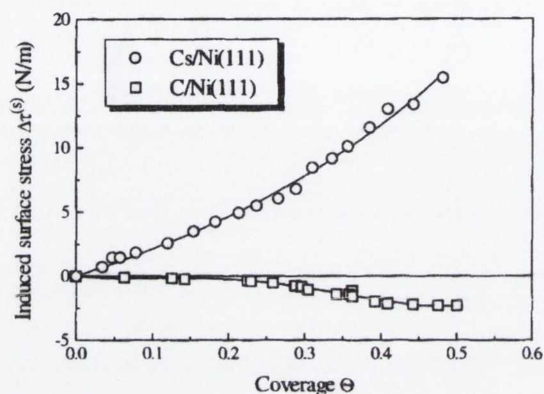

Fig. 4.6: Diagram showing the change in surface stress of a single crystal Ni(111) surface due to deposition of carbon (squares) and cesium (circles). The coverage's involved are scaled relative to the number of Ni atoms. In the case of cesium the first monolayer is completed at Θ= 0.26 and beyond this coverage the Cs atoms are deposited in the second layer (at this juncture the observed continuing increase in the stress is not well understood) [2].

Geometrical data	Values
Bond length Si—Si	2.35 Å
Bond length Si—O	1.60 Å
Bond angle Si—Si—Si	109.47°
Bond angle Si—O—Si	144.00°
Force constants	**dyn/cm**
Bond stretching Si—Si	4.85×10^{4}
Bond stretching Si—O	3.72×10^{5}
Bond bending Si—Si—Si	9.7×10^{3}
Bond bending Si—Si—O	3.71×10^{4}
Bond bending Si—O—Si	6.1×10^{4}

Table 4.1: Equilibrium bond length, bond angles, and force constants used for the model calculation [33, 34].

4.4. Experimental Techniques to Measure Surface Stress [2, 35]

Currently no experimental technique is available which accurately measures the surface stress of clean surfaces *directly*, as the simple existence of a force within a surface layer of a material has proven difficult to measure. Due to the lack of techniques capable of determining the absolute surface stress on well defined surfaces, other *indirect* methodologies have recently attracted interest. The effect of surface stress on other measureable quantities, such as surface phonons is clearly anticipated to bridge this gap [35]. A quantitative value of surface stress can be derived from phonon dispersion data with the aid of model calculations, which allow surface phonons to serve as an indirect source for surface stress data [35].

The concept of surface stress suggests that work has to be done against a surface stress when straining a solid body [35]. In the case of thin samples, the surface stress contributes significantly to the elastic response of the sample [35]. As a result deviations in the elastic response between measurements on thicker versus thinner samples can be utilised to derive the surface stress [35]. *Muller* and *Kern* suggested an experimental approach in which the bending of a thin circular disc in the gravitational field was measured, where the resultant deflection depends on the sign and magnitude of the surface stress [35, 36]. Unfortunately, such experiments have not been performed to date. However, it is proposed that advancements in both micro-machining and finite-element-modeling of bending make these experiments viable.

For nanoscale particles, surface and interface stress may lead to a measurable change of the atomic structure as compared to macroscopic specimens. Electron diffraction experiments have been performed on nanometer size particles [35]. The inadequacy of this approach is that the elastic properties of the particles have to be described by a model. As a consequence of this the calculated surface stress is expected to depend critically on the assumed three-dimensional shape [35]. The examples above have shown that although the absolute value of surface stress is related to measurable quantities, its model-free determination remains a challenge.

While the experimental determination of the absolute surface stress remains a challenge, the experimental technique to measure changes in the surface stress is well

established as previously mentioned. This technique was pioneered by *Koch* and *Abermann* [37]. They demonstrated that the bending of a cantilever due to an adsorbate surface stress can be measured with sufficient sensitivity that the deposition of a single monolayer on one side of the cantilever can be detected. The principle of the measurement is shown in Fig. 4.7.

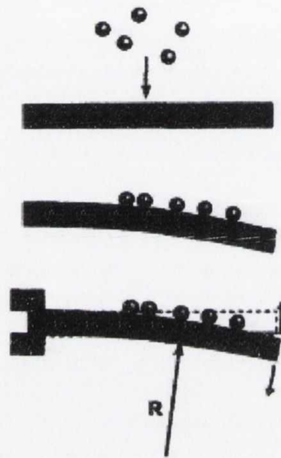

Fig. 4.7: Illustration of the principle of the cantilever bending method. When a layer of material is deposited on one side of the cantilever it bends due to an induced stress. In this case a compressive stress is shown; i.e. surface expansion. *R* represents the radius of curvature of the cantilever sample [2].

In the work of *Koch* and *Abermann* the bending of a cantilever, i.e. radius of curvature *R*, is measured as the change of the gap of a capacitor using a three terminal capacitance method [2, 38]. The bending can also be measured with sufficient sensitivity by deflection of the beam of a laser using a position sensitive detector, provided that the sample is thin enough [2, 39-41], or by a rather elegant method using STM that measures the change in the tunnel gap [2].

4.5. Stoney Equation

The Stoney equation [15], describes the relationship between the radius of curvature, R, and the total surface stress change due to adsorption on a single side of a thin cantilever sample, $\Delta\sigma$. To derive this equation, let's start by introducing the some important variables, along with their interrelationships. If an isotropic elastic body is acted on by an external force, the action propagates into the body through the interface. Producing internal drag against the external action prevents the form of the body from being destructed. As shown in Fig. 4.8, dP is an internal force acting on an infinitesimal area, dS, and ϕ is the angle between dP and the normal axis. The normal (dN) and parallel (dT) components of dP are

$$dN = dP\cos\phi, \quad dT = dP\sin\phi. \qquad \text{... (4.2)}$$

In this case, the stress along the normal axis, σ_n, and parallel to the plane, σ_t, can be written as

$$\sigma_n = dN / dS, \quad \sigma_t = dT / dS. \qquad \text{... (4.3)}$$

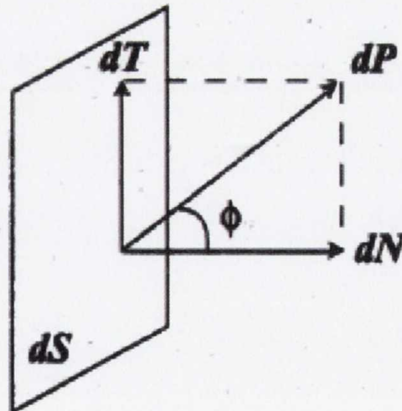

Fig. 4.8: Internal force, dP, acting on an infinitesimal area, dS. dT : parallel component of dP; dN: normal component of dP.

Now consider a bar of length, L, and diameter, d, which is extended such that length and diameter become $L^{'}$ and $d^{'}$ respectively. Here, the longitudinal strain, ε, and transverse strain, $\varepsilon^{'}$, are defined as

$$\varepsilon = (L^{'} - L)/L, \quad \varepsilon^{'} = (d^{'} - d)/d \qquad \ldots (4.4)$$

where, ε and $\varepsilon^{'}$ are dimensionless quantities. Since the diameter decreases if the bar is extended, the sign of the transverse strain is opposite to that of the longitudinal strain. Poisson's ratio, ν, is given by the ratio of these two strain quantities, i.e. $\nu = -\varepsilon^{'}/\varepsilon$. In the case of two parallel planes which are set a distance, L^{*}, apart and slip by a length, l, with shear angle, α, the shear strain, γ, is defined as follows

$$\gamma = l/L^{*} = \tan\alpha \qquad \ldots (4.5)$$

Restricting the discussion to small strains, the stress is directly proportional to the strain. This is Hook's law:

$$\varepsilon = \sigma_n / E, \quad \gamma = \sigma_t / G \qquad \ldots (4.6)$$

where, E and G are Young's modulus and Rigidity modulus respectively [42]. In general for a plane in isotropic materials, one can always select an orthogonal set of three planes where no shear stress acts. These three planes are called principle planes and normal stress which acts on each plane are the principle stresses of the crystal. The principal strains in an isotropic material are given by the principle stresses:

$$\begin{aligned} \varepsilon_{xx} &= [\sigma_{xx} - \nu(\sigma_{yy} + \sigma_{zz})]/E \\ \varepsilon_{yy} &= [\sigma_{yy} - \nu(\sigma_{xx} + \sigma_{zz})]/E. \\ \varepsilon_{zz} &= [\sigma_{zz} - \nu(\sigma_{xx} + \sigma_{yy})]/E \end{aligned} \qquad \ldots (4.7)$$

On growing a film on a substrate, the stress in the film is parallel to the interface while being bound within the plane parallel to the interface between the substrate and the film [43]. Being free from the substrate along the normal direction results in no stress acting in this direction. Therefore, if the x and y axes are set in the interface and the z-axis is set to be normal to the plane, the stresses in the film are given by

$$\sigma = \sigma_{xx} = \sigma_{yy}, \sigma_{zz} = \sigma_{xz} = \sigma_{zy} = \sigma_{xy} = 0 . \quad \ldots (4.8)$$

The strains can be written as

$$\varepsilon = \varepsilon_{xx} = \varepsilon_{yy} = \sigma(1-\nu)/E, \varepsilon_{zz} = -2\nu\sigma/E . \quad \ldots (4.9)$$

We assumed the stress uniformly acts on the sectional plane of the sample thus far. However it is not uniform in general [43]. Consider Fig. 4.9 below.

Fig. 4.9: A shell of radius of curvature, R.

This represents a rectangular shaped shell of radius of curvature, R, which is stressed by the film and substrate system. As triangles non_1 and s_1n_1s' are similar the strain, ε, at a distance, z, from neutral plane, nn_1, is given by

$$\varepsilon = s's_1 / nn_1 = z / R \qquad \dots (4.10)$$

where, nm is parallel to n_1s_1. Hence the stress as a function of z, is

$$\sigma(z) = \varepsilon E / (1-\nu) = zE / R(1-\nu)\,. \qquad \dots (4.11)$$

In order to derivate Stoney's equation, one can assume that the stress in the film is constant if $t >> h$, where t and h are the thicknesses of the substrate and film respectively, while the stress in the substrate remains a function of z [43]; see Fig. 4.10.

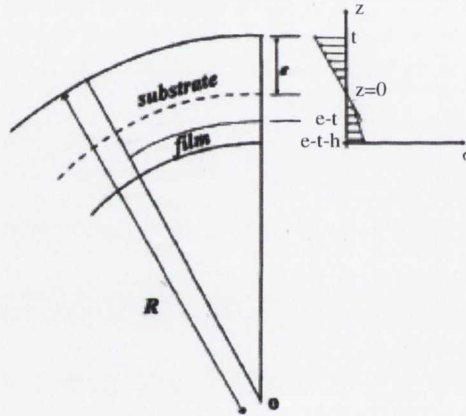

Fig. 4.10: Stress distribution as a function of z of a film and substrate system.

Using Young's modulus, E, Poisson's ratio, ν, substrate width, a, and from the balanced equation for the force, one obtains:

$$a\int_{e-t-h}^{e-t} \sigma dz + a\int_{e-t}^{e} \sigma(z) dz = a\sigma h + \frac{aEt}{2R(1-\nu)}(2e-t) = 0\,. \qquad \dots (4.12)$$

In addition the balanced equation for the moment leads to:

$$a\int_{e-t-h}^{e-t} \sigma z\, dz + a\int_{e-t}^{e} \sigma(z) z\, dz = \frac{a\sigma h}{2}[(2(e-t)-h)] + \frac{aEt}{3R(1-\nu)}(3e^2 - 3et + t^2) = 0\,. \quad \dots (4.13)$$

Using equations 4.12 and 4.13 the constant stress in the film is given by

$$\sigma = \frac{Et^2}{6R(1-\upsilon)h} \qquad [\text{N/m}^2]\,. \qquad \ldots (4.14)$$

This is Stoney's equation [15]. Measuring the deflection of a cantilever sample, one is observing the total surface stress change, $\Delta\sigma$, which is given by

$$\Delta\sigma = \sigma h = \frac{Et^2}{6R(1-\upsilon)} \qquad [\text{N/m}] \qquad \ldots (4.15)$$

(Note: further adaptations of this equation relating to our deflection measurement system and sample geometry are given in Chapter 6)

References:

[1] J. W. Gibbs, *The Scientific Papers of J. Willard Gibbs Volume 1* (Longmans-Green, London, 1906).

[2] H. Ibach, Surface Science Reports **29**, 195 (1997).

[3] N. C. Bartelt *et al.*, Physical Review B **48**, 15453 (1993).

[4] N. C. Bartelt, R. M. Tromp, and E. D. Williams, Physical Review Letters **73**, 1656 (1994).

[5] M. Giesen-Seibert *et al.*, Physical Review Letters **71**, 3521 (1993).

[6] S. V. Khare, and T. L. Einstein, Physical Review B **54**, 11752 (1996).

[7] L. Kuipers, M. S. Hoogeman, and J. W. M. Frenken, Physical Review Letters **71**, 3517 (1993).

[8] K. Morgenstern, G. Rosenfeld, and G. Comsa, Physical Review Letters **76**, 2113 (1996).

[9] K. Morgenstern *et al.*, Physical Review Letters **74**, 2058 (1995).

[10] A. Pimpinelli *et al.*, Surface Science **295**, 143 (1993).

[11] T. Narushima, N. T. Kinahan, and J. J. Boland, Review of Scientific Instruments **76**, 095113 (2005).

[12] T. Narushima, N. T. Kinahan, and J. J. Boland, Review of Scientific Instruments **78**, 053903 (2007).

[13] T. Narushima, M. Kitajima, and K. Miki, Journal of Physics: Condensed Matter, L193 (2004).

[14] T. Narushima *et al.*, Surface Science **601**, 1384 (2007).

[15] G. G. Stoney, Proceedings of the Royal Society of London, Series A **82**, 172 (1909).

[16] K. Dahmen, S. Lehwald, and H. Ibach, Surface Science **446**, 161 (2000).

[17] H. Ibach, The Journal of Vacuum Science and Technology A **12**, 2240 (1994).

[18] R. J. Needs, Physical Review Letters **58**, 53 (1987).

[19] R. J. Needs, M. J. Godfrey, and M. Mansfield, Surface Science **242**, 215 (1991).

[20] P. R. Watson, M. A. V. Hove, and K. Hermann, *In: NIST Surface Structure Database-Ver. 2.0* (NIST, Gaithersburg, Maryland, 1996).

[21] W. Berndt *et al.*, Surface Science **330**, 182 (1995).

[22] P. T. Sprunger *et al.*, Surface Science **297**, L48 (1993).

[23] C. Stampfl *et al.*, Physical Review B **49**, 4959 (1994).

[24] V. Fiorentini, M. Methfessel, and M. Scheffler, Physical Review Letters **71**, 1051 (1993).

[25] D. Vanderbilt, Physical Review Letters **59**, 1456 (1987).

[26] R. D. Meade, and D. Vanderbilt, Physical Review Letters **63**, 1404 (1989).

[27] M. C. Payne *et al.*, Surface Science **211-212**, 1 (1989).

[28] D. Sander, U. Linke, and H. Ibach, Surface Science **272**, 318 (1992).

[29] H. Ibach, Physics Letters Bl **48**, 705 (1992).

[30] A. Grossman, W. Erley, and H. Ibach, Surface Review and Letters **2**, 543 (1995).

[31] P. Gumbsch, and M. S. Daw, Physical Review B **44**, 3934 (1991).

[32] P. J. Feibelman, Physical Review B **56**, 2175 (1997).

[33] D. Sander, and H. Ibach, Physical Review B **43**, 4263 (1991).

[34] I. Ohdomari *et al.*, Journal of Non-Crystalline Solids **89**, 239 (1987).

[35] D. Sander, Solid State and Material Science **7**, 51 (2003).

[36] P. Müller, and R. Kern, Surface Science **301**, 386 (1994).

[37] R. Koch, and R. Abermann, Thin Solid Films **129**, 63 (1985).

[38] H. Ibach, Physica Status Solidi (b) **31**, 625 (1969).

[39] D. Sander, A. Enders, and J. Kirschner, Review of Scientific Instruments **66**, 4734 (1995).

[40] R. E. Martinez, W. M. Augustyniak, and J. A. Golovchenko, Physical Review Letters **64**, 1035 (1990).

[41] A. J. Schell-Sorokin, and R. M. Tromp, Physical Review Letters **64**, 1039 (1990).

[42] K. Symon, *Mechanics* (Addison-Wesley, Reading, Maryland, 1971).

[43] R. W. Hoffman, *"Mechanical Properties of Nonmetallic Thin Films" in Physics of Nonmetallic Thin Films by S. Dupuy & A.A. Cachard* (Plenum Press, New York, 1976).

Chapter 5

Si(111)-7x7 Surface Reconstruction

Crystalline silicon arranges itself in a tetrahedral diamond structure, i.e. the atoms are sp^3 hybridised and bond to four nearest neighbours. The covalent bonds are 2.35 Å long and each has a bond strength of 226 kJ/mol [1]. On cleaving the crystal, i.e. cutting it, bonds are broken leaving dangling bonds at the surface. The number and direction of these dangling bonds will depend on the macroscopic direction of the surface normal, as illustrated in Fig. 5.1 below [1, 2].

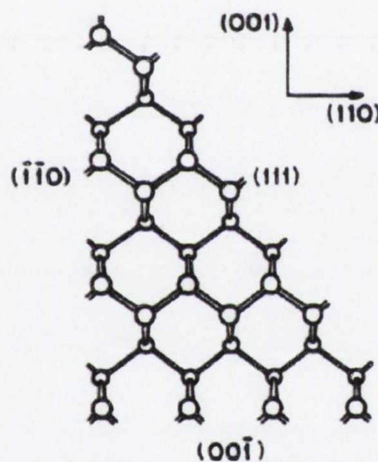

Fig. 5.1: The dangling bond formation on the unreconstructed surfaces of the three low index planes of Si. Each Si atom is tetrahedrally bonded to four nearest neighbours. The sizes of the Si atoms are shown to decrease away from the page [1, 2].

The surface energy is lowered by reducing the number of dangling bonds. As a result, the surface atoms rearrange and form new bonds resulting in a wide variety of surface reconstructions on silicon surfaces. The formation of new bonds at the surface can occur between neighbouring atoms or by *adatoms* that must be supplied by surface diffusion from nearby sources such as steps [3]. These two distinctly different processes illustrate the distinction between activated and activationless surface reconstructions. Activated surface reconstructions have energetic barriers ($\Delta E > kT$) that must be overcome in order

to obtain them, whereas activationless surface reconstructions have little or no barrier ($\Delta E < kT$) to obtain the reconstruction [3]. In many cases which reconstruction is obtained (activated/activationless) depends on how the surface is prepared, i.e. cleavage versus heating (thermal anneal) and beating (ion bombardment) [1, 3]. The surface structure observed will be the lowest energy structure kinetically accessible under the preparation condition [3].

On cleaving a silicon crystal to create a (100) surface each exposed atom would have two dangling bonds if bulk terminated as shown in Fig. 5.2 (a). However, small nuclear shifts allow dimerisation as pairs of dangling bonds on adjacent surface atoms combine to form a surface dimer σ-bond and a π-bond [4]. Lower in energy this 2x1 surface reconstruction forms spontaneously; see Fig 5.2 (b). This rearrangement can occur in such a way that the surface atoms move along a path that minimizes the induced local strain, without a significant topological distortion that would require breaking of silicon-silicon bonds, and without an activated supply of additional silicon adatoms. Many experiments and calculations have been devoted to resolving whether these dimers are symmetric or asymmetric (buckled), and although contention still surrounds the topic the majority of results point toward buckled dimers, which are believed to further lower the surface energy by a Jahn-Teller or Pierls distortion [1].

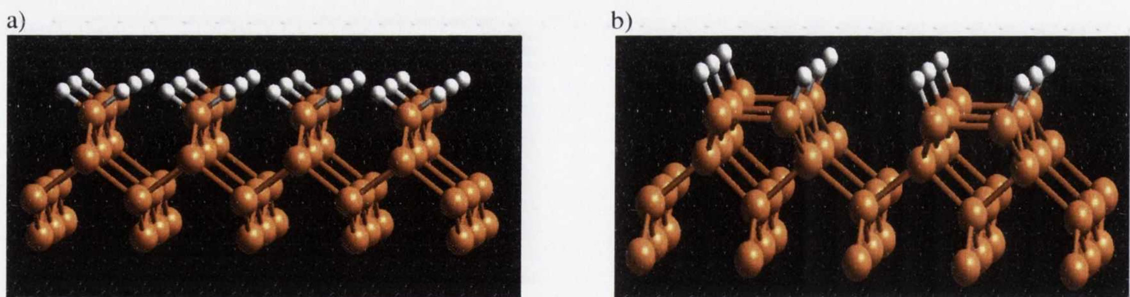

Fig. 5.2: a) When the silicon crystal is cleaved along the (100) plane, each surface Si atom has two dangling bonds. This surface is energetically unstable and spontaneously reconstructs to form a 2x1 surface of dimer rows; b) Si(100)-2x1 surface- the number of dangling bonds on the surface is halved as a result of this reconstruction. The case of symmetric dimers is shown in this figure.

The Si(111) surface rearrangement is much more complicated. The 7x7 surface reconstruction is the lowest energy structure for the Si(111) surface [1, 5]. The unit cell of

this reconstructed surface contains 19 dangling bonds compared to the 49 dangling bonds corresponding to a bulk terminated surface [5]. This structure can be formed by a number of methods, for example, by heat treatment above 950 ^{o}C of mechanically and chemically polished Si(111) wafers, by argon ion bombardment followed by a similar, but shorter, annealing process or by low temperature annealing of cleaved Si(111) samples [5]. Following activated surface transport a complex 7x7 reconstruction exists consisting of surface dimers, adatoms, and stacking faults [5, 6]. The considerable movement of atoms from their normal lattice positions in the unreconstructed surface to the positions in the 7x7 structure results in this surface being highly strained [1].

Despite the fact that silicon-based microelectronic devices are formed exclusively on the (001) crystallographic plane, the Si(111) surface has enjoyed a great deal of interest [7]. The intense study of this surface has been motivated by several factors [7]:

- It has an intriguing 7x7 reconstruction whose atomic structure defied structural analysis for many years.
- For STM investigations, the large unit cell and unusually large corrugation make it easy to image, while the comparative insensitivity to surface contamination makes it easier to prepare.
- The now known structure of this complicated surface reconstruction provides a rich array of chemically non-equivalent atoms, resulting in a rich variety of chemically interesting and spatially inhomogeneous reaction processes.

For the above reasons the majority of our investigations to date; using our novel system for combined scanning tunnelling microscopy (STM) and surface stress measurements [8, 9], have been performed on this fascinating surface reconstruction. However, a fundamental understanding of the nature of this surface reconstruction is necessary before examining more complex issues. Consequently, this chapter examines the detailed atomic structure of the Si(111)-7x7 reconstruction and discusses important features associated with this intricate rearrangement. In addition, a brief discussion regarding reactivity on this surface will also be presented.

5.1. Dimer-Adatom-Stacking Fault Model [1, 5]

The 7x7 structure of the Si(111) surface has been studied thoroughly over a period spanning approximately 25 years, and many models have been proposed to describe this complicated structure. The concept of adatoms in the outermost layer was first proposed by *Harrison* many years ago [5, 10]. Following this, key experiments involving constant momentum transfer averaging low-energy electron diffraction [5, 11] and ion-scattering spectroscopy [5, 12, 13] revealed non cubic stacking in the selvedge. In 1983, a monumental step towards the determination of a suitable model for this structure was achieved by *Binnig et al.*, when they obtained the first STM picture of this surface [5, 14]. This image displayed triangular units with deep holes at vertices and smaller holes along the perimeters of the triangles. Consequently, this led *Himpsel* [5, 15], *McRae* [5, 16], and *Bennett* [5, 17] to develop independent models in which the 7x7 unit cell is separated into two equal triangles with different stacking arrangements. A key contribution was made by *Himpsel* [5, 15] and *McRae* [5, 16], who showed that rebonding of silicon atoms across the boundary between faulted and unfaulted triangular regions results in two dimers, a ring of twelve atoms and two rings of eight atoms in exact agreement with features in the earlier STM image [5, 14]. Finally, *Takayangi et al.* pieced together a model using transmission electron diffraction results [6]. Currently, this model (the so called dimer-adatom-stacking fault (DAS) model) is generally accepted as the best model to describe the atomic arrangement of the Si(111)-7x7 surface reconstruction.

As the name implies the DAS model is very complicated. It involves large displacements of atoms within a (111) double layer and the introduction of twelve adatoms per unit cell on top. The DAS model is displayed in Fig. 5.3, while Fig. 5.4 presents the build-up of the structure layer by layer. The bulk terminated Si(111) surface which has one dangling bond per surface atom is shown in Fig. 5.4 (a). The bottom layer of the DAS double layer; i.e. the dimer layer, is virtually a typical layer of atoms, with each atom saturating one dangling bond of the bulk layer below (Fig. 5.4 (b)). However, one atom is missing at each corner of the 7x7 unit cell, thus creating corner holes. In addition, strings of dimers exist, both along the edge and between the two triangular halves/subunits of each 7x7 unit cell. The dimer atoms have two dangling bonds each,

while the remaining atoms in the dimer layer have three dangling bonds apiece. These dangling bonds are saturated by the atoms of the upper layer of the double layer. This layer is referred to as the restatom layer; see Fig. 5.4 (c). To facilitate saturation of all dangling bonds in the dimer layer, the rest layer atoms must occupy stacking fault sites within one of the two triangular subunits. The resulting surface has 42 dangling bonds per 7x7 unit cell. It is not possible to saturate all of these dangling bonds using typical Si units. The best possible solution is six adatoms in each subunit, which occupy sites in a local 2x2 structure as depicted in Fig. 5.4 (d). The dangling bonds on the remaining three restatoms are left untouched. Adatoms can be divided into two classes according to their position within subunits; corner adatoms reside at the corners of each subunit next to the corner holes, while centre adatoms are located at the centre of subunit edges. The DAS structure has 19 dangling bonds per unit cell and is the most energetically favoured arrangement for the Si(111) surface [1, 5, 7].

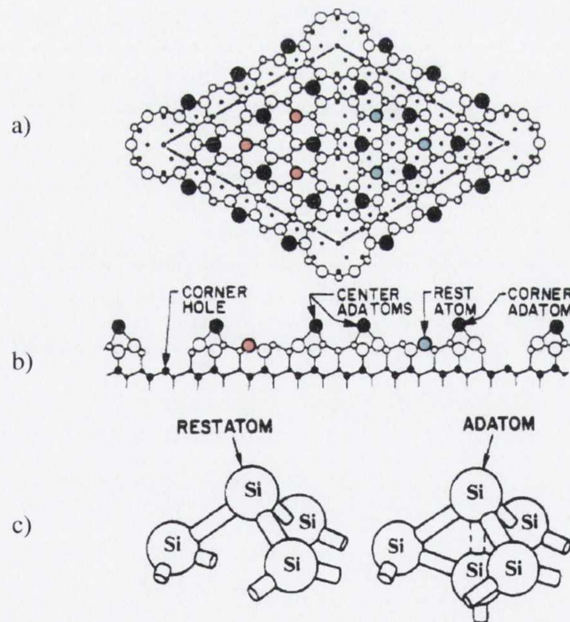

Fig. 5.3: DAS model of the 7x7 reconstruction- a) top view: atoms at increasing distances from the surface are represented by circles of different size. The filled circles denote the adatoms, while the red and blue circles represent the restatoms in the faulted and unfaulted half, respectively; b) side view: cut along the long diagonal of the unit cell. Atoms in the plane of the cut are shown with larger circles than those behind this plane; c) details of the bonding configurations at restatom and adatom sites [1].

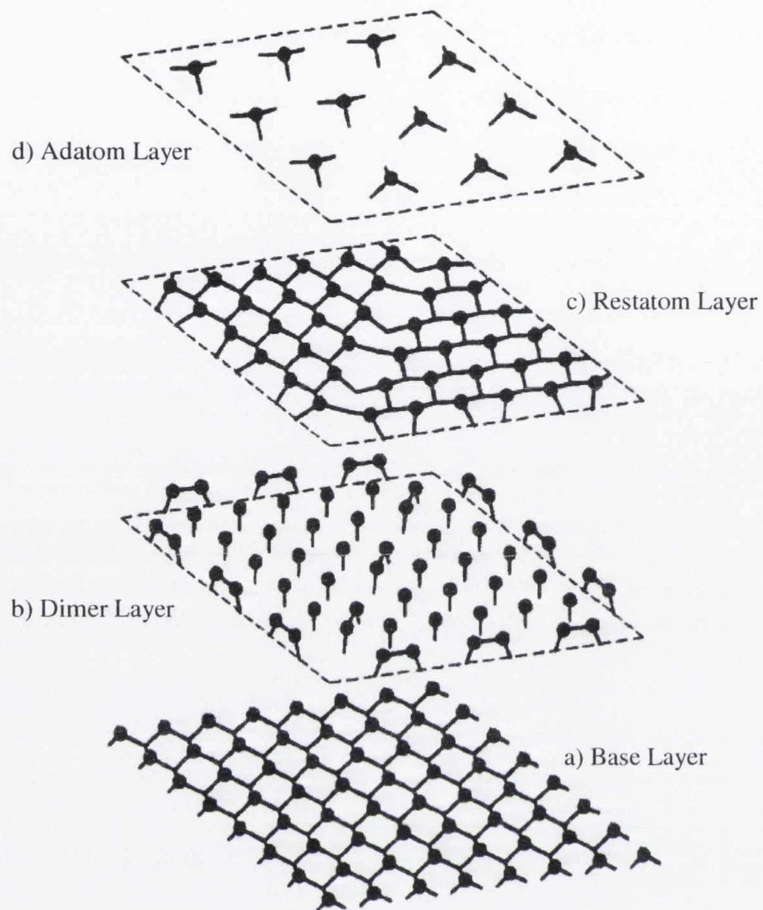

Fig. 5.4: Layer by layer reconstruction of the 7x7 reconstruction- a) 1x1 unreconstructed surface (terminated by a double layer); b) addition of the bottom layer of the reconstructed double layer, i.e. the dimer layer; c) addition of the second layer of the reconstructed double layer, i.e. the restatom layer; and d) introduction of the Si adatoms. The dashed lines show the outline of the 7x7 unit cell for each layer drawn in the plane of the underlying layer [1].

5.2. Electronic Structure [7]

As depicted in Fig. 5.4, the complex structure of the Si(111)-(7x7) surface presents several chemically distinguishable types of surface atoms. The adatoms in the faulted and unfaulted halves are intrinsically different and within each half unit the three corner adatoms are different from the remaining three centre adatoms. In addition, there are seven rest atoms, one of which is at the bottom of a deep corner hole. Figure 5.5 shows that these differences are readily evident in STM images. This results from the fact that the chemically inequivalent Si atoms also possess different electronic state densities [7, 18, 19]. By measuring the tunnelling current as a function of voltage while imaging the surface, it is possible to perform atomic-resolution surface spectroscopy and to directly image the spatial distribution of electronic states of the Si(111)-(7x7) surface [7, 18, 19]. Figure 5.5 (a) displays a topographic image of the Si(111)-(7x7) surface (with one unit cell outlined). At this bias the outer adatom layer and the corner holes of the 7x7 structure are clearly observed. Fig. 5.5 (b) shows an STM image probing the electronic state density at 0.35 eV below the Fermi level. In this regime the six adatoms nearest each corner hole appear brighter than those not adjacent to a corner hole. In addition, the six adatoms in the faulted half (constituting the right half of the unit cell in Fig. 5.5 (b)) are brighter than those in the unfaulted half. Thus, there are four types of chemically-inequivalent adatoms (corner faulted, corner unfaulted, center faulted, and center unfaulted), with the corner adatoms in the faulted half having the highest density of electronic states near the Fermi energy [7, 18, 19]. A differential current image at -0.8 V bias reveals three regions of high current between the six adatoms in each half of the unit cell, exactly where the DAS model has dangling bonds on the atoms in the layer beneath the adatoms; see Fig. 5.5 (c). In addition, high current regions are also observed in the centre of the corner holes, indicative of the dangling bonds present on the base layer. Finally, at bias voltages near -2.0 V (Fig. 5.5 (d)), the STM can reveal the locations of the backbonds between the Si adatoms and the underlying Si layer.

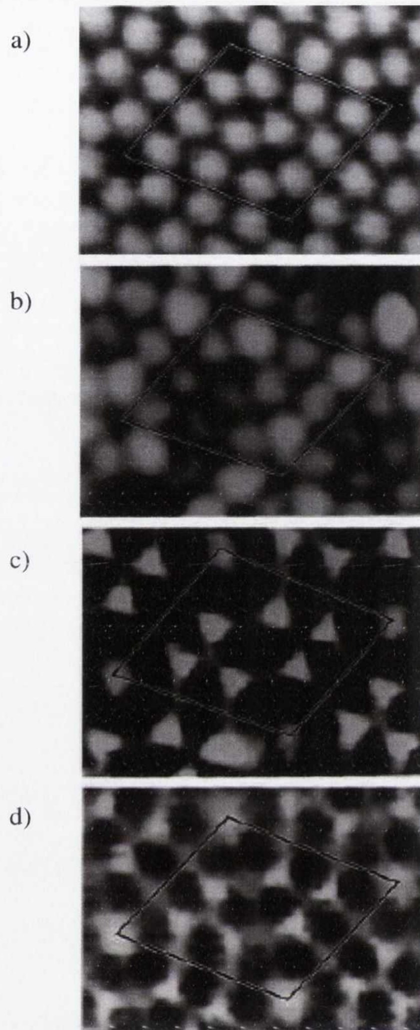

Fig. 5.5: STM and current imaging tunnelling spectroscopy (CITS) measurements of the Si(111)-(7x7) surface, showing the surface topography and spatial location of different surface states: a) topographic image, acquired with V_s= 2 V; b) dI/dV map showing the adatom state at 0.35 eV below E_F; (c) dI/dV map showing the rest atom state at 0.8 eV below E_F; and d) dI/dV map showing the backbond state at 1.7 eV below E_F [7].

5.3. Inherently Strained Structure [1, 20, 21]

Strain is an important element of the 7x7 reconstruction. Due to the considerable movement of atoms from their usual lattice positions in the unreconstructed surface to the new positions in the 7x7 structure results in this surface being inherently strained. As can be seen in Fig. 5.1 the basic building blocks of the silicon lattice are six-membered Si

rings in the chair conformation analogous to one conformation of the cyclohexane molecule [1]. On the other hand, inspection of the DAS model reveals five membered rings on both sides of the dimers (Fig. 5.4 (b)) and three adjacent four membered rings at each adatom site (Fig. 5.6 (a)) [1]. In spite of this the 7x7 structure is very stable and the transformation from a 2x1 cleaved surface is irreversible [22]. In addition, the 7x7 structure is maintained even after deposition of amorphous Si [23]. This led *Ohdomari* to consider the *possibility* of stabilisation by insertion of a fractional coverage of oxygen atoms in one of the adatom back-bonds, eliminating two of the three highly strained four-membered rings (Fig. 5.6 (b)) [1, 22]. It is well known that commercial Si crystals contain a considerable amount of oxygen and in the model of *Ohdomari* during annealing this oxygen diffuses to the surface, where it accumulates due to the desorption barrier [1, 22]. Cluster calculations by *Verwoerd* and *Osuch* showed that the oxygen modified structure would indeed be very stable [1, 23].

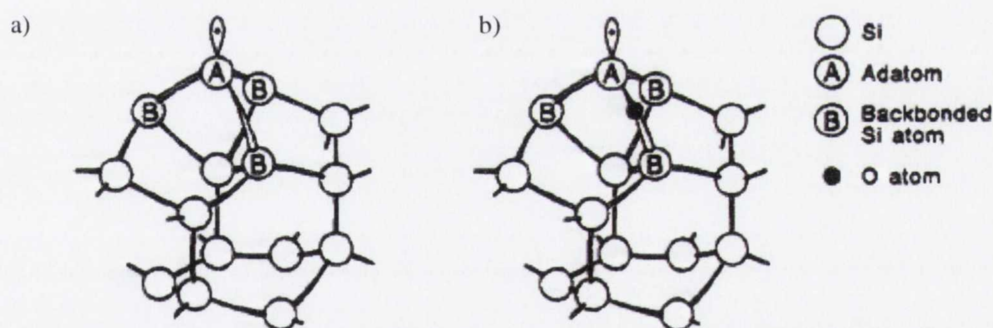

Fig. 5.6: Close-up of strained structures on the 7x7 surface; a) atomic configuration around a large corner hole in the DAS model, where three adjacent four membered rings are clearly visible at the adatom site; b) configuration around a large corner hole in the DAS model after an oxygen atom is inserted into one of the adatom backbonds. This eliminates two of the three four membered rings and results in a drastic decrease in total energy [1, 22].

To date, extensive theoretical and experimental studies have been conducted to decipher the exact origins and nature of strain within the 7x7 reconstruction and to determine the intrinsic surface stress of this convoluted arrangement of surface atoms [20-26]. Several authors have suggested the relief of the surface stress may be the driving

force for the 7x7 reconstruction on the Si(111) surface [16, 27-30]. A calculation conducted by *Pearson et al.* showed a large compressive stress at the Si(111)-1x1 surface [21, 28, 29, 31]. In this picture, the 7x7 dimer walls function to relieve the compressive stress. However, this calculation is based on a highly approximate empirical potential which is of questionable validity for Si [21]. More realistic calculations, i.e. self-consistent density functional calculations using the local-density approximation, were conducted by *Vanderbilt* [20, 21]. Here, stress tensors are calculated for unfaulted and faulted 1x1 and 2x2 adatom models; see Table 5.1 below [20].

Si Structure	**Surface Stress [eV/(1x1 cell)]**
1x1	-0.54
1x1 (Faulted)	0.11
2x2 Adatom	1.66
2x2 Adatom (Faulted)	1.89

Table 5.1: Calculated stresses for the Si(111) surface. Negative stress values correspond to a compressive stress, while positive values indicate a tensile condition [20].

The 1x1 ideal surface is under a small compressive stress. When adatoms are introduced onto the surface, a relatively large tensile stress is induced [20]. Finally for both 1x1 and adatom covered surfaces the presence of a stacking fault adds a small tensile stress [20]. *Vanderbilt* interpreted these results as follows [20]:

- The 1x1 surface has a compressive stress as a consequence of the fact that each topmost atom has only one electron in its dangling bond. By hybridising with an element of sp^2 character each atom can potentially lower its energy. Nonetheless, each atom cannot flatten completely because the perpendicular lattice constant is fixed. It does lie somewhat flatter than the bulk however, having a bond angle of 114 ° and bond lengths of 2.29 A.
- The small tensile character associated with the stacking fault may be explained by visualising the axis formed by atoms 6 and 10 in Fig. 5.7. In the ideal surface the

bond between atoms 6 and 3 and the bond between atoms 10 and 15 are staggered. In the case of the faulted surface these bonds are eclipsed, which results in a repulsive interaction due to the *Pauli Exclusion Principle* [20, 32, 33]. This results in the topmost atom rising up with angles of 112°, thus introducing a tensile stress.

- Adatom covered surfaces are intrinsically tensile due the unnatural bonding topology of the adatom cell. The adatom and the second layer atom beneath it (atom 6) are forced apart either by Coulomb repulsion or by the energy gained by relieving the unnatural bond angle of the first layer atoms. Although these atoms repel one another, they try to maintain their natural bond lengths with the atoms in the first layer. This causes a tensile stress and pulls the first layer atoms closer together.

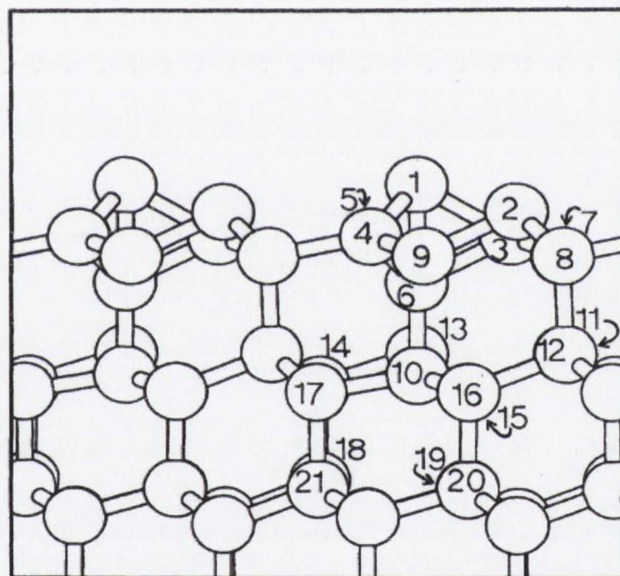

Fig. 5.7: A side view of the relaxed 2x2 adatom covered unfaulted Si(111) slab [20].

In light of these results, the island regions of the 7x7 DAS model, which are faulted and unfaulted 2x2 adatom structures, are found to be under considerable tension. The dimer domain walls of the DAS model are able to relieve compression but not tension, because they tend to pull in neighbouring material, i.e. they are under tension themselves [21]. Therefore, the intrinsic stress of the 7x7 ensemble is expected to be tensile in nature [20, 21]. Consequently, it appears unlikely that the relief of the small

compressive stress of the Si(111)-1x1 surface is the driving force for reconstruction. Moreover, alternative models to explain the motivating force for the reconstruction based on dangling bond reduction and/or adatom formation are available [21, 34-36].

5.4. Chemical Reactivity [1, 7, 37, 38]

The understanding and control of silicon surface reactions is of great importance in the production of silicon based microelectronic devices [1]. As continued reduction in the size of semiconductor devices takes place, surface chemistry will assume an even greater role [1]. Although not as relevant for technological applications, the Si(111)-(7x7) surface provides a rich variety of inhomogeneous reactive surface sites due to its complex reconstruction and will no doubt be a model system for years to come [7]. To date, the study of many types of dangling bonds of the Si(111)-7x7 surface has received much attention because dangling bonds are a main factor in controlling chemical adsorption [39]. However, this is not the only decisive factor in controlling the reaction path. Reactions at adatom and restatom sites are not only influenced by the electronic structure of the dangling bonds, but also by the mechanics of the structural units, i.e. the rich assortment of weak and strained backbonds. For example, in the case of adatoms, the strain can be relieved by breaking the backbond and attaching species at either end (e.g. atomic hydrogen [40]), or by inserting atoms (e.g. oxygen [22]) so as to enlarge the size of the original four-membered Si ring [37]. In addition, reactions at specific sites within the 7x7 unit cell can influence reactions at neighbouring sites; this is due to the fact that atomic reaction processes can potentially induce local changes in electronic structure and/or mechanical character [37].

Due to abundant experimental studies on the topic of reactivity [1, 7, 37], it is possible to make some generalisations about the chemistry of Si(111)-7x7 surface. One important observation is that the surface reconstruction clearly plays an important role in the overall chemistry of the surface. The same factors which are responsible for creating the reconstruction, namely, that the Si surface energy is minimised when as many Si atoms as possible have achieved four-fold coordination, is also ultimately responsible for

most of the variations in chemical reactivity [7]. In addition, the atoms at surfaces are highly strained, and many of the observations reported can be described in terms of a competition between optimisation of overall coordination and the minimisation of strain resulting from non-ideal bond lengths and/or bond angles [7]. Most chemical systems (e.g. atomic hydrogen, O_2, H_2O, SiH_4, GeH_4, Ge_2H_6, etc.) show a preference for reacting at specific sites within the 7x7 unit cell [7]. In some cases (such as oxygen) the reaction probabilities can be understood based on the local electronic state densities of the different adatom sites: corner adatoms in the faulted half of the unit cell have the highest state density and act as the most nucleophilic reaction site [1, 7, 37]. Yet, other preferences (e.g. atomic hydrogen) involve selective reactivity with bonds exhibiting different degrees of bond strain [7, 40]. Additionally, some reactions (such as SiH_4) appear to be controlled by the nature of the dangling bonds on the restatom and corner hole sites [7]. For a more comprehensive discussion regarding reactivity trends on the Si(111)-7x7 surface, the reader is directed to excellent reviews by *Waltenburg* and *Yates* [1], *Hamers* and *Wang* [7], and *Avouris* [37]. In addition, a largely successful theoretical approach to observed reactivity trends on the Si(111)-7x7 surface based on the chemical concepts of local softness and electronegativity is provided by *Brommer et al.* [38].

References:

[1] H. Neergaard Waltenburg, and J. T. Yates, Chemical Reviews **95**, 1589 (1995).

[2] D. Haneman, Reports on Progress in Physics **50**, 1045 (1987).

[3] J. A. Kubby, and J. J. Boland, Surface Science Reports **26**, 61 (1996).

[4] C. M. Aldao, and J. H. Weaver, Progress in Surface Science **68**, 189 (2001).

[5] V. G. Lifshits, A. A. Saranin, and A. V. Zotov, *Surface Phases on Silicon-Preparation, Structures and Properties* (Wiley & Sons, Chichester, United Kingdom, 1994).

[6] K. Takayanagi *et al.*, Surface Science **164**, 367 (1985).

[7] R. J. Hamers, and Y. Wang, Chemical Reviews **96**, 1261 (1996).

[8] T. Narushima, N. T. Kinahan, and J. J. Boland, Review of Scientific Instruments **76**, 095113 (2005).

[9] T. Narushima, N. T. Kinahan, and J. J. Boland, Review of Scientific Instruments **78**, 053903 (2007).

[10] W. A. Harrison, Surface Science **55**, 1 (1976).

[11] H. Huang *et al.*, Physics Letters A **130**, 166 (1988).

[12] R. M. Tromp *et al.*, Solid State Communication **44**, 971 (1982).

[13] R. J. Culbertson, L. C. Feldman, and P. J. Silverman, Physical Review Letters **45**, 2043 (1980).

[14] G. Binnig *et al.*, Physical Review Letters **50**, 120 (1983).

[15] F. J. Himpsel, Physical Review B **27**, 7782 (1983).

[16] E. G. McRae, Physical Review B **28**, 2305 (1983).

[17] P. A. Bennett *et al.*, Physical Review B **28**, 3656 (1983).

[18] R. J. Hamers, R. M. Tromp, and J. E. Demuth, Physical Review Letters **56**, 1972 (1986).

[19] R. J. Hamers, R. M. Tromp, and J. E. Demuth, Surface Science **181**, 346 (1987).

[20] R. D. Meade, and D. Vanderbilt, Physical Review B **40**, 3905 (1989).

[21] D. Vanderbilt, Physical Review Letters **59**, 1456 (1987).

[22] I. Ohdomari, Surface Science **227**, L125 (1990).

[23] W. S. Verwoerd, and K. Osuch, Surface Science **256**, L593 (1991).

[24] I. K. Robinson *et al.*, Physical Review B **37**, 4325 (1988).

[25] I. Stich *et al.*, Physical Review Letters **68**, 1351 (1992).

[26] R. E. Martinez, W. M. Augustyniak, and J. A. Golovchenko, Physical Review Letters **64**, 1035 (1990).

[27] J. C. Phillips, Physical Review Letters **45**, 905 (1980).

[28] E. G. McRae, Surface Science **147**, 663 (1984).

[29] E. G. McRae, Surface Science **163**, L766 (1985).

[30] T. Ichikawa, and S. Ino, Surface Science **136**, 267 (1984).

[31] E. Pearson *et al.*, Journal of Crystal Growth **70**, 33 (1984).

[32] E. B. Wilson, Advances in Chemical Physics **2**, 367 (1959).

[33] J. P. Lowe, Journal of Chemical Physics **45**, 3059 (1966).

[34] D. Vanderbilt, Physical Review B **36**, 6209 (1987).

[35] J. E. Northrup, *in Proceedings of the Eighteenth International Conference on the Physics of Semiconductors edited by O. Engstrom* (World Scientific, Singapore, 1987).

[36] G. Qian, and D. J. Chadi, Journal of Vacuum Science and Technology B **4**, 1079 (1986).

[37] P. Avouris, The Journal of Physical Chemistry **94**, 2246 (1990).

[38] K. D. Brommer *et al.*, Surface Science **314**, 57 (1994).

[39] S. Ihara, T. Uda, and M. Hirao, Applied Surface Science **60-61**, 22 (1992).

[40] J. J. Boland, Advance in Physics **42**, 129 (1993).

Chapter 6

System Development for Combined Scanning Tunneling Microscopy & Surface Stress Measurements to Elucidate the Origins of Surface Forces [1, 2]

In the case of adsorption on solid-state surfaces, induced surface stresses arise primarily from differences in atomic size and electronegativity, in addition to changes in surface morphology and defect formation [3]. It is expected that the role of these induced stresses will become increasingly important as the scale of surface features is reduced and surface effects dominate [4, 5]. As a consequence of this, we have developed a new combined system to investigate the underlying origins of forces on solid state surfaces from the viewpoint of atomic surface structure [1]. This system consists of two main parts: the measurements of force based on sample displacements and detailed atomic resolution observations of the surface morphology. The former involves a large cantilever sample and capacitive detection method that provides sufficient resolution to detect changes of a few meV/atom or pN/atom at surfaces. For the latter, a scanning tunneling microscope (STM) was incorporated to observe structural changes occurring on the surface of the same cantilever sample. However, such measurements are not trivial due to the architecture of the cantilever. To achieve our goal, it was necessary to address two major difficulties: a) self-oscillation of the cantilever sample which reduces the stability of the STM observation and b) sample heating. Following the implementation of our novel approach to tackle these challenges, the atomic scale structural origins of forces on surfaces can be elucidated [1, 2]. This combined system provides us with structural, dynamical and interactional information and is proving to be extremely useful in understanding and improving reaction processes on surfaces. In addition, our system is also equipped with a *sample pusher* which can be used to study the effects of artificially applied stress on processes at the atomic level. In this chapter, the details of our novel measurement system will be presented, including a discussion into the technical challenges encountered during the development process, along with a demonstration of the system performance.

6.1. Experimental Design and Challenges

A cantilever sample is the simplest structure available to measure sample bending. This bending is induced by forces acting at the surface region. However, to achieve atomic scale resolution via STM on the cantilever used to measure stress we are faced with several significant challenges. One such challenge concerns the stability of STM observation on the cantilever sample. A conventional STM sample is clamped at both ends. Consequently, highly resolved STM imaging can be performed displaying atomic features. However, oscillation of the cantilever sample due to its structural design, i.e. natural resonance, affects the quality of the observation. In general, a simple solution to suppress this oscillation is to use a thick sample. On the other hand, to measure sample bending, a thinner sample is preferable. It is therefore imperative to carefully choose the dimensions of the cantilever sample for simultaneous STM and stress measurements.

Another major challenge relates to sample heating. Most sample heating methods are based on the premise that both ends of the sample are clamped. Silicon surfaces, for example, are predominantly heated using both ends of the sample as contact electrodes, and allowing a current to be passed through the sample. However, this type of direct heating method is not possible for a cantilever sample. To overcome this, we adopted different heating methods depending on whether heating was required *before* or *during* measurements. For sample heating before measurements, i.e. sample preparation including surface cleaning and annealing, a novel method using bimetallic strips was developed [2]. The bimetallic strips are used to make electrical contacts to allow current to pass through a defined region of the sample. With this method, we can control temperatures of the sample up to approx. 1400 K. Another method, which we also successfully implemented for sample heating before measurements, involves electron bombardment [6]. This method is very well established and used in many cases, for example, to remove impurities from highly refractory metals and thermal desorption spectroscopy [6]. For sample heating during measurements, it is critical to have no physical contact with the sample, and as a result, some indirect heating method is required. This method is also constrained by the fact that it cannot have any major influence on the sample which would inhibit STM and stress measurement capabilities.

Consequently we use an infrared indirect heating method that allows us to statically heat-up the sample to approx. 950 K. In addition it is worth noting that the current sample holder design does not allow in-chamber sample loading or exchange, thus necessitating *in-situ* sample heating within a complex and spatially-restricted environment; namely on the STM stage. This limitation therefore demands extreme caution when carrying out all heating procedures to protect the numerous delicate components that comprise the STM head from accidental damage.

6.1.1 Sample Bending Detection

When a sample surface undergoes any type of reaction or surface modification, the sample bends due to forces induced by this process and is detected via deflection of the cantilever sample. From this deflection, the forces acting in the surface region can be estimated. The deflections are typically not large, and in the case of atomic scale forces the deflection is typically on the order of a few nanometers. In order to measure such minute deflections, and hence to have greater force resolution, we have to carefully consider a method to detect this sample bending. Several methods are available to detect the deflection of the cantilever sample. *Optical techniques* include an optical cantilever bending method [7-9], similar to that used in an atomic force microscopy (AFM) [10] and interferometery [11]. In addition, *electrical techniques*, such as STM [3, 12, 13] and capacitance methods [3] are also available.

Each method has advantages and disadvantages. The optical cantilever bending method has a good detection limit (typically about 2×10^{-4} N/m in total stress change) and is well established [7-9]. However, this method is preferable for small micron scale cantilevers because the change of angle at the free end is detected to quantify sample deflection. On the other hand, the electrical techniques mentioned above are more practical for large cantilevers, as the change of position at the free end is detected to measure the deflection. This is also advantageous as it frees us from the awkwardness of fabricating small cantilever samples. Nonetheless, such electrical techniques are not easily measured in strong electric and magnetic fields or in charged environments such as plasmas and ionic solutions. The STM method, on the other hand, can detect cantilever

deflections as a variation in the tunnel gap and observe atomic structure simultaneously [9]. However, with this method it is difficult to obtain a comparable detection limit to that of the optical cantilever bending method, because, in principle, thermal drift and/or the unknown shape of STM tip induces uncertainty in measurements. Typically the STM method achieves a resolution of approx. 1×10^{-1}- $1x10^{-2}$ N/m in total stress change [9]. In contrast, the capacitance method which uses a well defined reference electrode, unlike the STM method, has a superior detection limit of $\pm6.9\times10^{-3}$ N/m in total stress change [14]. This stress value corresponds to an energy change of approx. 1- 10 meV/atom at the surface. In order to achieve a good detection limit with the use of large cantilever samples, we adopted the capacitance system developed by *Sander* and *Ibach* to quantify sample bending [14].

6.1.2 Visualisation via STM

In order to observe surface structures on a cantilever surface that is used to measure sample bending, movements of the cantilever must be recognized and managed. During surface modification, two types of movement are important- the first, due to the natural oscillation of the cantilever sample itself, while the other is induced by forces acting at the surface region. To detect sample deflection, it is beneficial to use a cantilever sample which is as long and thin as possible, since surface modifications will result in larger displacements at the free end. However, difficulty arises regarding structural observations with this set-up due to the natural oscillation of the cantilever sample itself, as illustrated in Fig. 6.1. Without suppressing this inherent movement, atomic structural observation may not be possible.

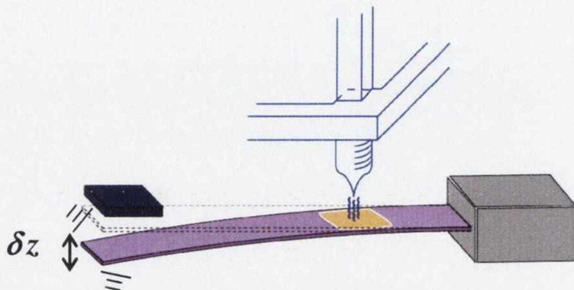

Fig. 6.1: Schematic diagram demonstrating the natural oscillation of a cantilever sample which results in a free end deflection, δz. This natural movement leads to STM difficulties and must be suppressed for successful operation.

Thus, it is necessary to minimize movement due to the natural resonance via tailoring of the cantilever dimensions. The deflection density, $\sqrt{(\partial/\partial f)(\delta z)^2}\Big|_{f=f_0}$, of the cantilever sample at the oscillation peak, as shown in Fig. 6.2, can be obtained from the following theoretical expression

$$\sqrt{(\partial/\partial f)(\delta z)^2}\Big|_{f=f_0} = \sqrt{2k_BTQ/\pi kf_0} \qquad \text{... (6.1)}$$

where, δz, f, f_0, T, k, k_B and Q represent the displacement of the cantilever sample at the free end, the frequency of the self-oscillation, the peak frequency of the self-oscillation, the temperature, the spring constant, the Boltzmann constant and the quality factor of the cantilever sample, respectively [15]. Assuming a Gaussian distribution at $f = f_0$ and by using the definition of the quality factor, $Q \equiv f_0/\Delta f$, we can approximate the root mean square of the displacement

$$\delta z_{rms} \approx \sqrt{2k_BTQ/\pi kf_0}\sqrt{f_0/Q} = \sqrt{2k_BT/\pi k}\,. \qquad \text{... (6.2)}$$

This estimate provides us with valuable information concerning the deflection induced by the self-oscillation. In reality, the peak-to-peak amplitude, δz_{p-p}, should be calculated to quantify the actual displacement at the free end

$$\delta z_{\text{p-p}} = 2\sqrt{2}\delta z_{\text{rms}} \approx 4\sqrt{k_BT/\pi k}\,. \qquad \text{... (6.3)}$$

From $\delta z_{\text{p-p}}$, it is found that the spring constant and the temperature dictate the movement. Therefore, $\delta z_{\text{p-p}}$ is proportional to $\left(t/l\right)^{-3/2} w^{-1/2}$ at constant temperature, since the spring constant, $k = Ewt^3/4l^3$, where w, t, l, and E are width, thickness, length and Young's modulus of the cantilever sample, respectively. This implies that if w and l are known, we can suppress the movement due to the self-oscillation by choosing an appropriate value of t, thus allowing atomic scale structures to be observed.

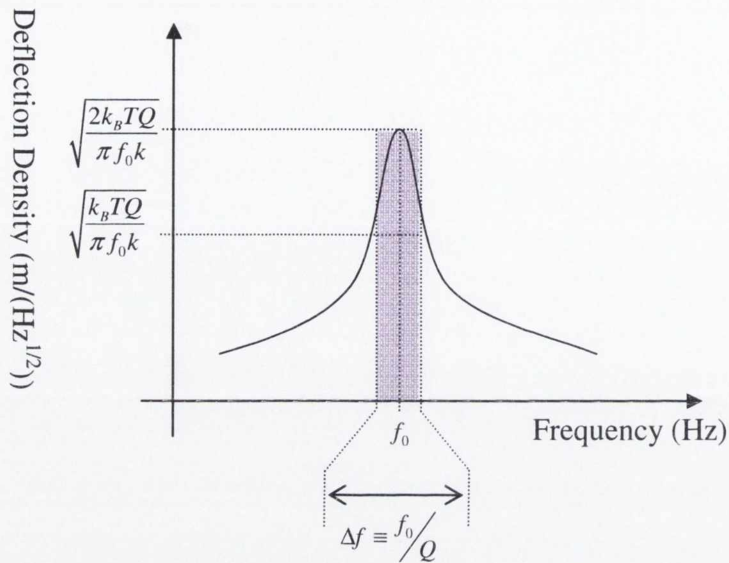

Fig. 6.2: Illustration of the deflection density versus frequency profile for a cantilever sample assuming a Gaussian distribution about the peak frequency.

In general, however, the observed STM topographical signal for a cantilever sample contains both atomic scale structure and self-oscillation features. As both features are independent, i.e. no energetic interaction, this can be described with a simple topographical summation in real space as shown in Fig. 6.3.

Outline of atomic scale structure

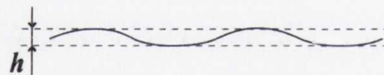

+

Movement due to self oscillation

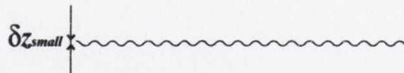

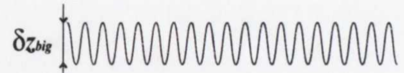

Observable signal

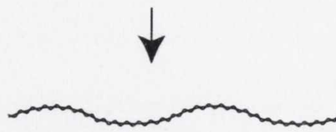

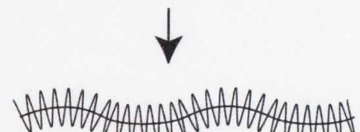

Fig. 6.3: Schematic diagram representing the observable STM topographical signal for a cantilever sample. The signal consists of a mixture of the outline of the atomic structure to be observed and movement induced by the self oscillation. If the movement is sufficiently small, original atomic scale structure can be rebuilt from the signal by use of a fast Fourier transformation (FFT) filter.

In Fig. 6.3, we assume that there are two self oscillation conditions, $\delta z_{\mathrm{small}}$ and δz_{big}, where $\delta z_{\mathrm{small}} < h < \delta z_{\mathrm{big}}$, and h is the height of the atomic scale structure. As a result, the observable STM topographical signal is constantly modified by the natural movement of the cantilever. Consequently, to acquire highly resolved STM images, we have to suppress $\delta z_{\mathrm{p\text{-}p}}$.

Figure 6.4 displays the expected displacement at free end, $\delta z_{\mathrm{p\text{-}p}}$, of a Si(111) cantilever sample induced by self oscillation as a function of sample thickness. Here, the dimensions of the sample are assumed to be 50 mm long and 10 mm wide so as to mimic the cantilever sample used by *Sander* and *Ibach* for their capacitive measurements [14].

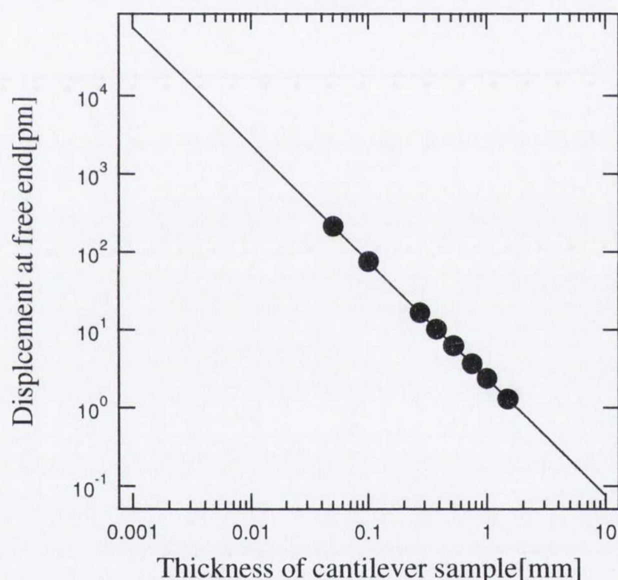

Fig. 6.4: Expected displacement at free end of a Si(111) cantilever sample induced by self-oscillation as a function of thickness. Dimensions of the sample: 50 mm long and 10 mm wide. Each dot represents thicknesses of 0.05, 0.10, 0.275, 0.380, 0.525, 0.750, 1.00 and 1.50 mm, respectively.

The well-known Si(111)-7×7 reconstruction is a nice example to test the performance of our system. The step height of the surface is 0.5 nm. The basis vector length is 2.69 nm and the height of an adatom protrusion is approx. 50 pm. To resolve these adatoms on the Si(111)-7×7 surface, it is required that $\delta z_{\mathrm{p\text{-}p}}$ be smaller than the 50 pm protrusions, which are shown in Fig. 6.5.

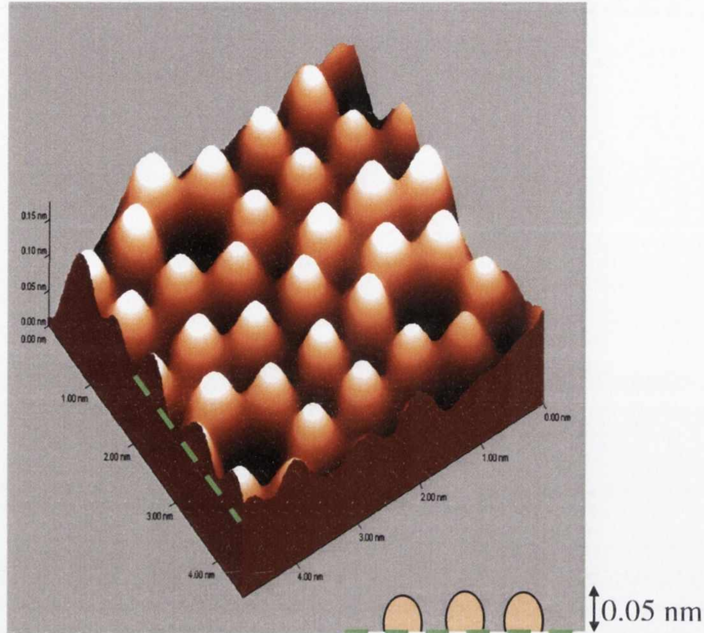

Fig. 6.5: 3-dimensional view of the surface adatoms on the Si(111)-7x7 reconstruction. In order to resolve these adatom features via STM it is imperative that the deflection of the cantilever sample is smaller than the 0.05 nm adatom protrusions.

For this condition we estimated the critical thickness of the cantilever to be 0.13 mm ($k = 8.4$ N/m). In the case of a 0.1 mm thick cantilever sample ($k = 3.7$ N/m), the estimated value for $\delta z_{\text{p-p}}$ is 75 pm. Since this case corresponds to δz_{big} in Fig. 6.3, it would prove difficult to resolve the adatoms on the Si(111)-7×7 surface. To resolve these adatoms sufficiently, $\delta z_{\text{p-p}}$ should be approx. 10 times smaller than the protrusions, thus representing δz_{small} in Fig. 6.3. This condition corresponds to a thickness of approx. 0.5 mm. For example, a 6.25 pm displacement at the free end can be estimated for a 0.525 mm thick cantilever sample ($k = 539.7$ N/m). Therefore, we can expect to resolve the adatoms on the Si(111) surface using a cantilever sample that is thicker than 0.525 mm. Thus far, displacements at the free end of the cantilever were discussed in relation to STM observation. However, for our system, it is preferable to use the free end region of the sample to detect sample bending, as displacements are greater at this point. As a result we chose the centre of the cantilever for surface modification and structural observation via STM. STM at this region has the added advantage of reducing the estimated value of $\delta z_{\text{p-p}}$, resulting in improved STM resolutions. As previously mentioned, our novel

system is equipped with a sample pusher which is used to artificially stress the cantilever sample and study the influences of induced stresses on reaction processes. However, the pusher has another important role; on loading the cantilever sample, the natural oscillation is considerably reduced, which permits high resolution imaging of cantilever samples with thicknesses much lower than 0.525 mm. The details of the pusher will be discussed in a subsequent section.

6.1.3 Design Concepts

Our system is intended to simultaneously measure sample bending and observe surface structure via STM. To realize this, the design of the sample holder is critical for accurate performance. Figure 6.6 presents a schematic of our system. The component to detect sample bending includes a cantilever sample, a reference electrode and a clamping base. The additional component consists of an STM which images the central area on the cantilever sample which is accessible to reaction and surface modification. Sample deflection can be measured by monitoring the change of capacitance between the cantilever sample and the reference electrode. From the measured capacitance value, displacement at free end of the cantilever sample can be calculated allowing the actual deflection to be estimated. Structural observation on the cantilever sample via STM can be performed before, during or after such measurements.

Figure 6.7 represents a 3-dimensional CAD (computer aided design) image of our actual cantilever sample holder. A cantilever sample with dimensions $50\times10\times0.525$ mm^3 is typically used. To form the cantilever structure, we first prepare a rectangular shaped sample with dimensions $60\times10\times0.525$ mm^3. Following this one end is fixed in the clamping base, i.e. the $10\times10\times0.525$ mm^3 region. A modification or reaction across the entire front surface of the cantilever sample is necessary for measurement and interpretation of forces acting at the surface region. However, uniform reaction or modification of a 50×10 mm^2 surface area would prove to be extremely difficult and result in large amounts outgassing during the flash procedure. Therefore the centre 10×10 mm^2 area was chosen to meet this criterion. Passivation of the silicon sample is achieved by exploiting the native oxide layer which covers the entire surface region.

However in order to create a clean 10×10 mm^2 Si surface, which acts as the effective modification area, regionalized heating is required. The heating methods used (namely bimetallic and electron bombardment heating methods) will be discussed in an ensuing section. The centre of this area is located 15 mm from the fixed end of the cantilever sample.

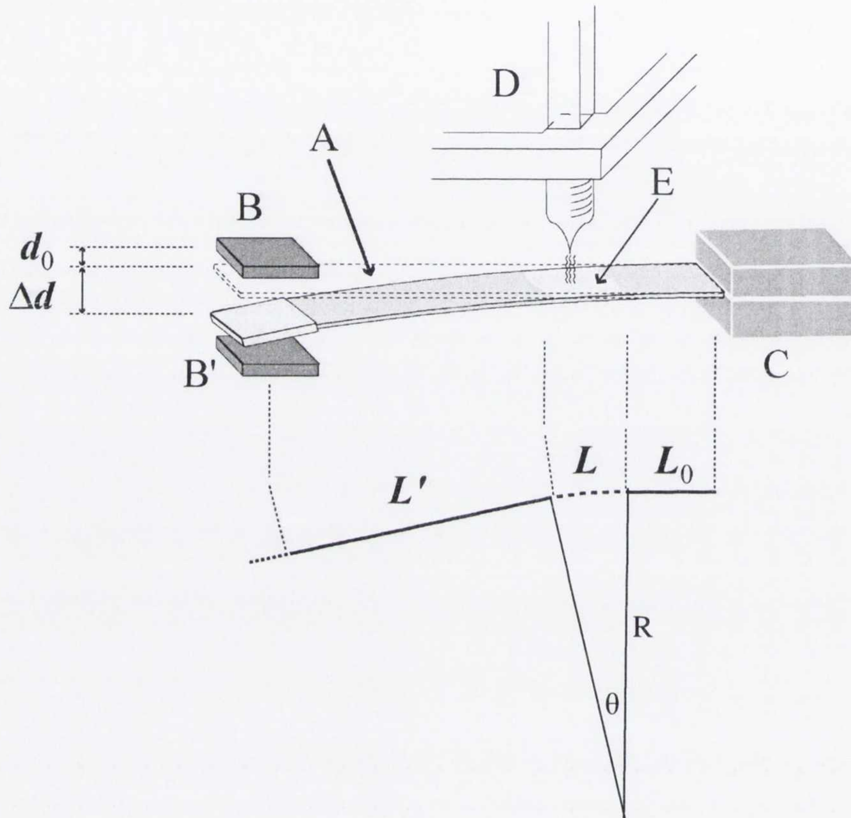

Fig. 6.6: System for measurement of sample bending and structural observation. The detection component for sample bending consists of a cantilever sample (A), a reference electrode (B) and a clamping base (C). The additional component for structural observation consists of a cantilever sample (A) and an STM (D) which observes the effective modification area (E). Sample bending is induced by atomic scale modifications which occur only in region E. This region, with axial length, L, is located between the fixed end region (length, L_0), and the free end region (length, L'). In our system, the values of L_0, L and L' are 10, 10 and 25 mm, respectively. Note that the L' length terminates at the centre of the reference electrode. Although capacitance measurements between one reference electrode and the sample are basically sufficient, the additional reference electrode guaranteed secure displacement monitoring. To avoid involving a parasitic capacitance change when using high resistance semiconducting samples, an electrical by-pass is also present; please see Appendix B for an explanation. It consists of a flexible metallic wire (not shown here) that is connected to a 10x10 mm^2 Ta foil which tightly encapsulates the free end.

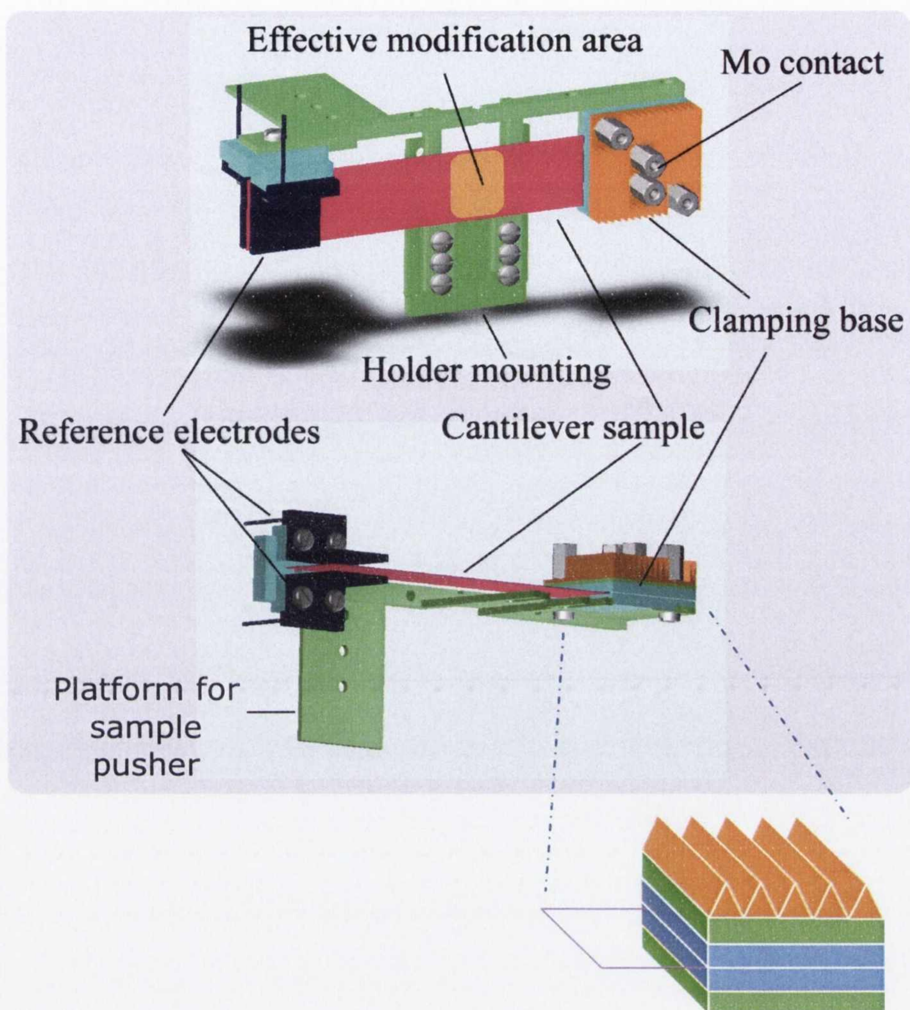

Fig. 6.7: A 3-dimensional CAD image of our actual cantilever sample holder. Each color represents different materials: green, light blue, navy blue, orange and pink correspond to super invar, quartz, molybdenum, copper and silicon, respectively.

The choice of materials for our special sample holder is very important. These materials should be suitable for use in an ultrahigh vacuum (UHV) system [16]. In addition, all components in contact with the silicon sample should be nickel and iron free to prevent surface contamination [6]. Most components of the sample holder are made from super invar, because it has a very low thermal expansion coefficient. This material is therefore suitable for stable STM and sample bending measurements, showing only small instabilities due to high temperature effects and/or temperature fluctuations. Quartz is also known to have a low thermal expansion coefficient. For that reason, super invar and quartz are used for the conducting and insulating parts, respectively. This

combination has an added advantage for the clamping component of the sample holder. Here, not only is the use of low thermal expansion materials important in minimizing undesired effects, but matching these thermal expansion coefficients is equally important to avoid interface stress as in a bimetallic strip [2]. In fact, super invar and quartz have thermal expansion coefficients of 0.4×10^{-6} and 0.5×10^{-6} °C^{-1}, respectively. The clamping base (including the fixed end) was formed with a sandwich structure of quartz and super invar, i.e., super invar – quartz – silicon – quartz – super invar. However, to apply electric potential to the silicon sample for STM (and stress measurements when using low resistance samples), a plate spring contact made from molybdenum is employed. Mo prevents metal contamination of the sandwich structure. In addition, a copper heat sink is added to one side of this sandwich structure, to radiate away excess heat and therefore allow thermal equilibrium to be quickly established.

At the free end, two reference electrodes are set to detect the capacitance values between the sample and the each reference electrode. We assume that this configuration forms a simple parallel plate capacitor. Each electrode is supported by a quartz base. Operationally, one of the electrodes is required to measure the displacement, while the other serves as a back-up of the measured displacement since this electrode experiences opposite changes in capacitance. The distance between these two electrodes is 2 mm. The cantilever sample is located in between these electrodes and thus the distance between the cantilever sample and each electrode is less than 1 mm. Each electrode has a 10×10 mm^2 surface area and the exact centre position of the electrode is situated 45 mm from the fixed end. Both electrodes are made from molybdenum, to prevent metal contamination of the sample in the event of contact. Furthermore, to avoid measurement of a parasitic capacitance when using high resistance semiconducting samples, an electrical by-pass electrode is attached to the silicon. The by-pass permits a bias to be applied to the free end of the sample only. This short-cut consists of a flexible metallic wire that is directly connected to a 10×10 mm^2 Ta foil sleeve which tightly slides over the free end region of the sample. The Ta foil does not contaminate the sample. However, when low resistance semiconducting samples are used, the by-pass can be omitted. Details regarding use of the by-pass are discussed in Appendix B.

Using the sample holder mounting displayed in Fig. 6.7, allows the set-up to be fitted to a conventional STM unit. We chose a room temperature STM, namely the *Omicron UHV STM-1* [17] which was described in Appendix A. The imaging of a surface requires mechanical stability of the tip, the sample, and their holders. Mechanical isolation from the external environment is also critical. Conventional STM systems are carefully designed with regard to these requirements. Specifically, the STM-1 has a special spring suspension system with eddy-current dampening, which ensures excellent vibration isolation. Such isolation is preferable not only for STM observation but also for sample bending detection. With regard to the STM-1 system, the tip is mounted tightly on a tripod scanner, which consists of a triple tube arrangement that is fixed to the STM stage. However, due to the construction of our novel sample holder, the region to be scanned is located 9 mm above the original conventional STM location. To compensate for this height difference, this hitherto inaccessible region was initially accessed using purposely fabricated tip holders, which are taller than standard arrangements; see Appendix C. However, atomic scale images were not achieved at that time, due to excess noise levels induced by the poor structural rigidity of these tall structures. Consequently, it was necessary to raise the scanner assembly to facilitate stable, high resolution imaging using conventional tip holders. To achieve this, the position of the STM scanner was raised using a 2 mm thick UHV grade stainless steel plate arrangement. This arrangement is shown in Appendix C. The internal UHV current-to-voltage converter (I.V.C) was also relocated to accommodate this change in scanner location. In addition, mechanical stabilising braces were fabricated for our special sample holder, in order to anchor the arrangement rigidly on the Omicron STM stage. This added stability, greatly enhances the structural rigidity of the tunneling junction and is a simple but vital component in helping to achieve atomic resolution images.

Our sample holder is also equipped with a device for pushing the cantilever sample. There are several mechanical schemes one might consider to artificially stress a sample. The simplest is bending of the cantilever sample by applying a small force at the free end. This produces uniaxial strain varying linearly along the length of the sample and so there is a constant strain gradient. One could observe the surface properties as a function of strain by observing at different places along the cantilever with a fixed

deflection at the free end or by looking at a fixed place as a function of loading. This allows separating the effects of strain from those of a strain gradient. The value of the strain from the elastic theory for the loaded beam is $\varepsilon_{surf}(x) = 3zt(\ell - x)/2\ell^3$, where $\varepsilon_{surf}(x)$ is the surface strain at a distance x from the clamped end, ℓ and t are the sample length and thickness, and z is the displacement of the loaded end. Our pushing scheme for applying artificial stress to the surface region is illustrated in Fig. 6.8. To push the sample, a linear inertial slider, namely an *Omicron MS5* [17], is used. This device bolts rigidly onto the sample holder at the specified location displayed in Fig. 6.7. This slider is fully UHV compatible, light (approx. 25 g) and bakeable to 180 °C. It has a total travel range of 5 mm in both forward and back directions, while providing 40 nm step displacements of the cantilever sample at a minimum. A specifically designed quartz module couples conveniently onto this slider arrangement and is used to contact the sample when applying an artificial tensile or compressive load to the surface region. Quartz is a suitable material for this purpose as it is an electrically isolating material, thus allowing unimpeded STM and capacitance measurements to be conducted under loading conditions. Furthermore, quartz does not contaminate the silicon surface on contact.

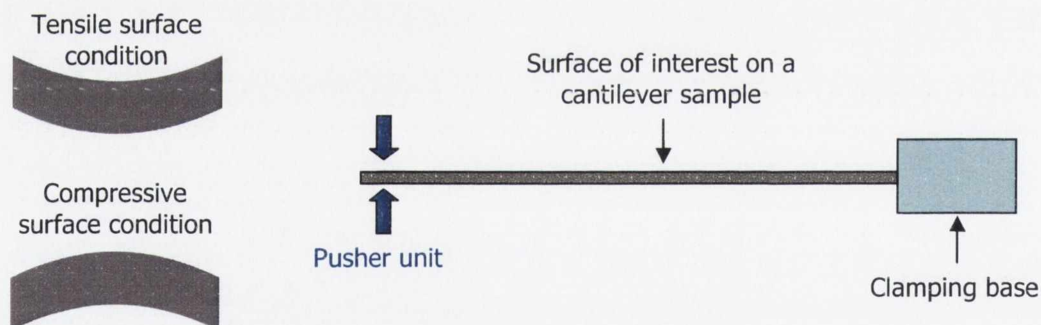

Fig. 6.8: Schematic diagram illustrating how a sample pushing unit can be used to generate tensile and compressive stress conditions at the surface of a cantilever sample. This pusher unit is used to study the effects of artificial stress on reaction processes at the atomic level. In addition, the pusher unit is also used to reduce the natural oscillation of the cantilever sample on contact, thus improving STM resolution.

For our experiments it is imperative to use thin cantilever samples that are polished on a single side only. This measure ensures that atomic scale processes on the

polished surface are the dominant contributors to sample bending. Having a rough surface on the back side of the cantilever sample minimises parasitic bending effects due to reaction processes on this surface, since stress does not accumulate as effectively over a coarse area [3, 18-20]. While it is not possible to totally eliminate parasitic influences using this approach, our experiences to date using various surface morphologies show that its influence is largely negligible. Therefore, we are only interested in events on the polished side where stress accumulates efficiently and atomic structure can be investigated via STM. (An alternative approach to eliminate parasitic bending effects would involve passivation of the back side surface with a non-reactive overlayer; however, such approaches are not trivial from our experience and carry their own inherent issues). Figure 6.9 (a-d) presents photographs of our developed system portraying some of the aforementioned components in our experimental set-up.

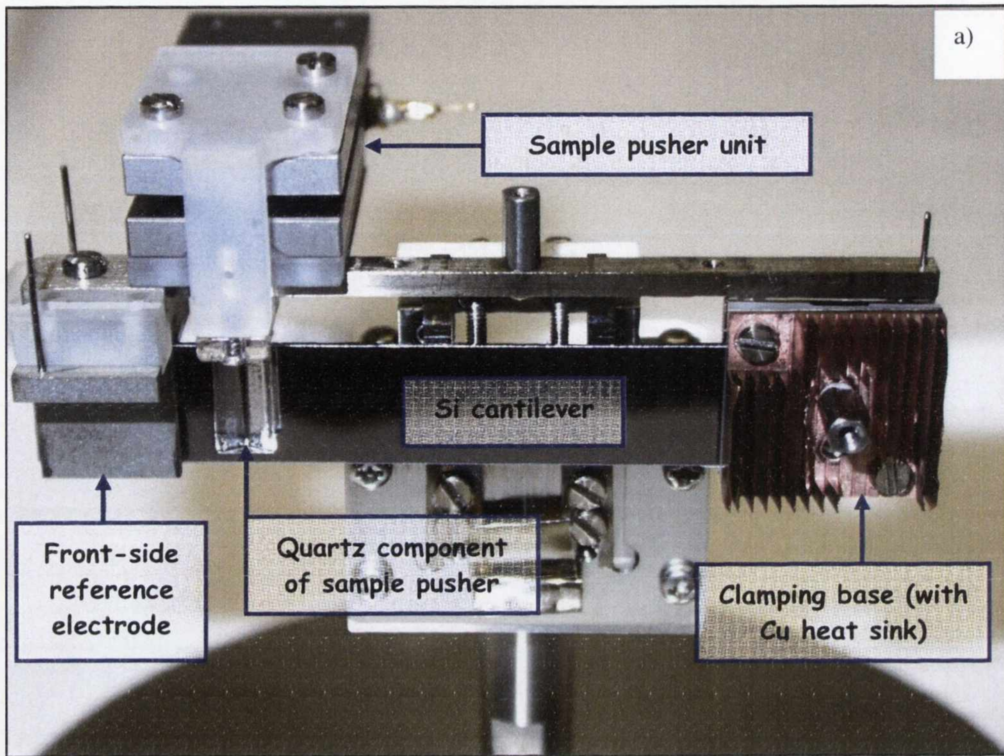
a)
Sample pusher unit
Si cantilever
Front-side reference electrode
Quartz component of sample pusher
Clamping base (with Cu heat sink)

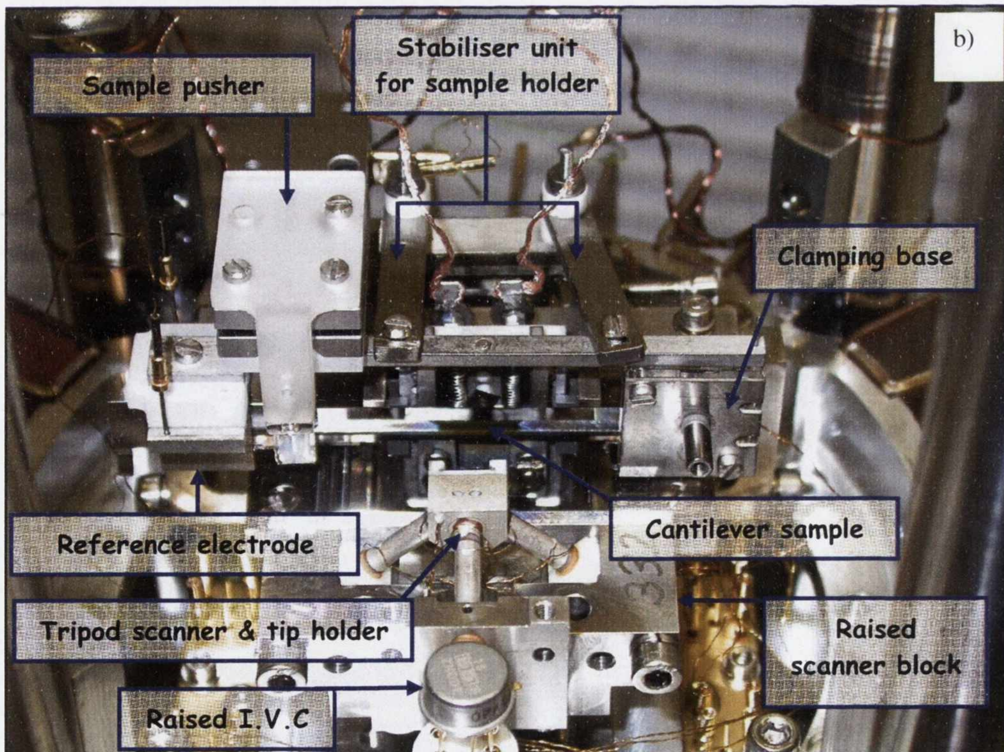
b)
Sample pusher
Stabiliser unit for sample holder
Clamping base
Reference electrode
Cantilever sample
Tripod scanner & tip holder
Raised scanner block
Raised I.V.C

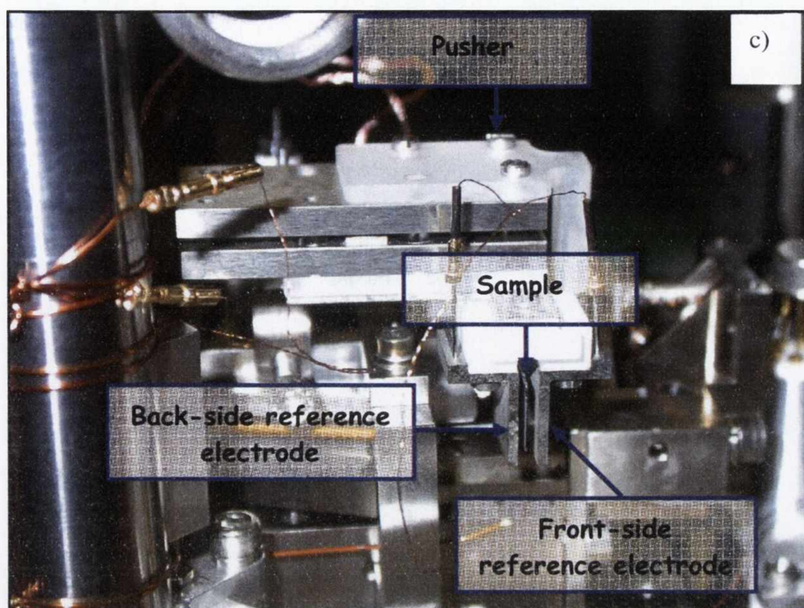

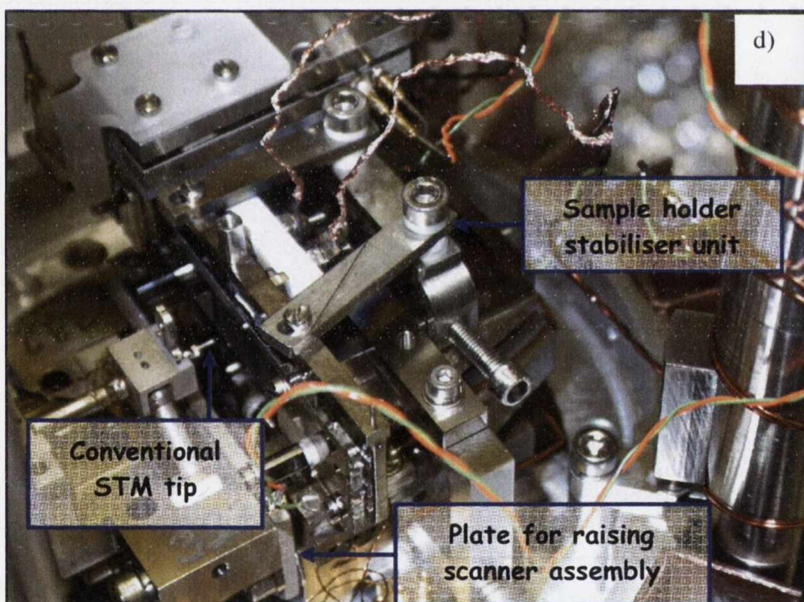

Fig. 6.9 (a-d): Photographs of our developed system: consists of a cantilever sample holder designed by us and an Omicron UHV STM-1. (It should be noted that the Cu heat sink is only necessary when conducting high temperature studies to minimise unwanted influences from the clamping region during measurements).

6.1.4 Determination of Sample Bending

As previously mentioned, sample bending can be detected capacitively. Here, we will discuss a conversion method from capacitance values to deflections and forces. Initially, a pair of parallel plates which have a spacing, d_0, and equivalent surface areas, S, under UHV conditions result in a capacitance value, $C(d_0) = \varepsilon_0 S / d_0$. When there is a spacing variation from d_0, namely Δd, the change in capacitance is given by,

$$\Delta C(\Delta d) \equiv C(d_0 + \Delta d) - C(d_0) \cong \frac{\varepsilon_0 S}{d_0^2} \Delta d \qquad \ldots (6.4)$$

where, ε_0 is the dielectric constant for a vacuum and assuming $\Delta d << d_0$. Fig. 6.6 displays a small displacement at the free end, Δd, from the initial spacing, d_0. Along the longitudinal direction of the cantilever, the lever part can be divided into three regions, L_0, L and L'. The effective modification area, i.e. the region L, is located between the fixed end region, L_0, and free end region, L'. It should be noted that the L' region terminates at the centre of the reference electrode as displayed in Fig. 6.6. Hence, the small displacement at the free end originates only from the region L, while the regions L_0 and L' do not display any deflection.

To quantify the deflection by means of the displacement, Δd, it is necessary to establish the radius of curvature, R, for the region L. Let L and l represent the arc and its chord, respectively, of the circle segment with central angle, θ, and radius, R. Subsequently, the displacement is given by,

$$\Delta d = l \sin\frac{\theta}{2} + L' \sin\theta \cong \left(\frac{L^2}{2} + LL'\right)\frac{1}{R} \qquad \ldots (6.5)$$

The above approximation is valid, assuming that, $l \cong L$, which is true when $\theta << \pi / 2$.

In order to estimate the forces contributing to the sample bending, we use the Stoney-Hoffman Equation [21, 22],

$$h \cdot \sigma = \frac{Et^2}{6(1-\nu)} \frac{1}{R} \qquad \dots (6.6)$$

where, ν, σ and h represent Poisson's ratio, the force per unit area along the longitudinal direction of the cantilever and the effective thickness of the atomically strained layer, respectively. Finally, from equations 6.4, 6.5 and 6.6 we obtain an equation converting the capacitance change to force change induced at the surface region,

$$h \cdot \sigma(\Delta d) = \frac{t^2}{6} \left\{ \frac{1}{L^2/2 + LL'} \right\} \frac{E}{(1-\nu)} \frac{\varepsilon_0 S}{C(d_0)^2} \Delta C(\Delta d) \qquad \dots (6.7)$$

From equation 6.7, it is evident that in order to have the capability to detect atomic scale forces, a precise means of sensing capacitance changes is vital. To achieve this we use an ANDEEN-HAGERLING AH 2550A capacitance bridge [23]. The AH 2550A enables us to detect extremely small changes in the capacitance value, between 0.5- 0.8 aF. With this detection resolution and considering a typical set-up for our system, i.e. $t = 525\times10^{-6}$ m, $L = 1.0\times10^{-2}$ m, $L' = 2.5\times10^{-2}$ m, $S = 10^{-4}$ m^2, ε_0=8.854×10^{-12} C^2/N·m^2 and $E/(1-\nu)|_{\mathrm{Si(111)}} = 2.29\times10^{11}$ N/m [24], the theoretical detection limit for the displacement at the free end of the cantilever sample and the force induced are estimated to be 0.71 Å and 2.48×10^{-3} N/m, respectively. In estimating these values we used a value of $C(d_0) = 3.0$ pF as an initial capacitance value (this $C(d_0)$ value typically varies between 2.5 and 3.5 pF depending on the clamping condition). In reality, our capacitance resolution including noise, is slightly reduced, i.e. ±1.9 aF, which will be statistically deduced later, giving values of ±1.87 Å and ±6.55×10^{-3} N/m, for the displacement and force detection limits respectively. Assuming an effective thickness for the strained layer of $h = 0.1\, or$ 0.5 nm provides us with a strain energy detection limit of ±8.2 or ±1.6 meV/atom, when all force in the effective modification area is assigned to surface strain.

It is important to note these values are much smaller than those associated with bonding energies, which are of the order of a few eV. In addition, sample bending is basically caused by lateral force. In the case of Si(111), the force per atom detection limit along the $[1\bar{1}0]$ direction corresponds to ±6.82 or ±1.37 pN/atom for $h = 0.1$ *or* 0.5 nm, respectively. This is almost comparable with the force detection limit in non-contact atomic force microscopy (nc-AFM). Hence, our system is adequate to study the origins of forces in atomic scale structures and phenomena on surfaces.

6.1.5 Heating a Cantilever Sample

Sample heating presented a serious challenge to us in the development of our novel system for a number of reasons:

- The architecture of the cantilever sample hinders conventional direct current heating as the sample is clamped at one end only
- Regionalised heating of a small area is desired for large cantilever samples to: a) minimise outgassing from the sample during flashing; b) reduce power input requirements for the heating process; and c) create a clean surface region which can then be uniformly modified on exposure to reactive species (uniform surface modification is an essential ingredient for the accurate application of the Stoney-Hoffman equation [21, 22], however, in some instances, this can prove difficult to accomplish for clean surfaces over a large surface area)
- To study high temperature reaction processes, the adopted heating method for this purpose should not impede STM or capacitance measurements
- The sample and its holder reside in a delicate and sensitive environment, i.e. on the STM stage, which is susceptible to damage during heating
- In order to maintain adequate UHV conditions during heating, outgassing from the sample holder and surrounding components on the STM stage must be suppressed
- The present sample holder design does not support in-chamber sample loading or exchange, hence, if a problem arises within the UHV chamber, the chamber must be

vented for repairs, and a time consuming bake cycle is required to re-establish UHV conditions

As a result, during the design and implementation stages for sample heating, it was imperative to ensure that adequate measures were in place to achieve our desired goals and prevent damage to sensitive components in the vicinity of the sample holder. Fortunately, after overcoming these difficulties we now have the capability to routinely perform successful heating of a cantilever sample in UHV.

To heat our cantilever sample, different methods of sample heating are employed. For sample preparation *before measurements*, very high temperature regionalised heating is required. At this stage, physical contact with the cantilever sample is permitted if necessary. To achieve this goal, we have developed two independent heating methods, namely, direct current heating using bimetallic strips [2] and more recently electron bombardment. These methods allow us to prepare a well defined clean region from oxide covered cantilever samples. On the other hand, to study high temperature reaction processes (i.e. *during measurements*) physical contact with the cantilever sample is completely forbidden for heating. As a result, only indirect heating methods are acceptable. There are typically two techniques available- electron bombardment and radiative heating [6]. With regard to our system, the former method prevents STM and capacitance measurements from being conducted due to the presence of a large electric field that is required to accelerate electrons. In contrast, the latter method is electrically static. To employ this method the incident radiation has to be directed solely towards the cantilever sample surface in order to heat up the modification area effectively and to conduct UHV experiments. To this end, we employed an infrared heating system with a quartz light guide. During all heating procedures it is imperative to install a shield at the tripod scanner location to prevent contamination of the sample surface due to outgassing from a constituent rubber material; see Appendix D. Now let us look at the exact details of each of these heating methods.

6.1.5.1 Simple Controlled Heating Method for a Free-Standing Cantilever Sample using Bimetallic Strips [2]

In this section, our novel technique to heat up a free-standing cantilever sample using bimetallic strips will be introduced. A bimetallic strip is an actuator derived from thermal forces. Each strip is made by bonding two materials together with distinct and different thermal expansion coefficients. The strip will bend when heated or cooled from the initial reference temperature because of the incompatible thermal expansions of the materials that are bonded together. It will return to its initial reference shape once the applied thermal stress is removed. Bimetals are commonly used as temperature sensors, thermostats, etc. In our original design for sample heating, two bimetallic strips are heated using a filament, causing them to deflect towards the cantilever sample. Physical contacts with the sample are made under appropriate conditions. A current can then be passed through the cantilever sample using these contact points, causing resistive heating of the sample. Using this technique a 10×10 mm^2 region of the sample can be heated-up by placing two bimetallic strips at the back side of the effective modification area of the cantilever sample with a spacing of 10 mm between them. In the case of a Si cantilever sample, it is possible to flash the sample with the above mentioned method. Following the flash all contacts between the sample and strips are broken as desired. With this method, we can establish repeated controlled contacts that allow the free standing sample to be heated to temperatures over 1400 K. Now let us examine the finer details associated with our novel bimetallic heating system.

In order to make electrical contact, the bimetallic strips must be constructed from conductive materials and should not induce any significant outgassing during heating under UHV conditions. In addition, a good combination of materials with substantially different thermal expansion coefficients must be used to form the bimetal. Finally, it is also advantageous to choose soft materials, i.e. materials with small Young's moduli, to have large effective motions of the bimetallic strip, thus allowing it to operate at lower temperatures. Taking these considerations into account, a combination of Ta and stainless steel grade 304 (SUS304) was deemed to be the most promising choice amongst ordinary materials for UHV, which are listed in Table 6.1.

Materials	α [K^{-1}]	E [GPa]
Mo	4.8×10^{-6}	329
Ta	6.3×10^{-6}	186
W	4.5×10^{-6}	411
SUS304	17.3×10^{-6}	196
Si	2.6×10^{-6}	129.5 for <100> 168.0 for <110> 186.5 for <111>

Table 6.1: Thermal expansion coefficient α at 273 K and Young's modulus E of ordinary materials used in UHV [25-27].

To quantify the motion of the bimetallic strip (which is shown in Fig. 6.10) induced by a temperature change, it is necessary to estimate the deflection at the free end. The deflection of the bimetallic strip due to a change in temperature, ΔT, can be derived from the balanced equation of forces,

$$a\alpha_1 E_1 \Delta T \int_{e-h-t}^{e-h} dy + a\alpha_2 E_2 \Delta T \int_{e-h}^{e} dy = a\int_{e-h-t}^{e-h} \varepsilon_1 E_1 dy + a\int_{e-h}^{e} \varepsilon_2 E_2 dy, \qquad \dots (6.8)$$

and the balanced equation of moments,

$$a\alpha_1 E_1 \Delta T \int_{e-h-t}^{e-h} y dy + a\alpha_2 E_2 \Delta T \int_{e-h}^{e} y dy = a\int_{e-h-t}^{e-h} \varepsilon_1 E_1 y dy + a\int_{e-h}^{e} \varepsilon_2 E_2 y dy, \qquad \dots (6.9)$$

where, e describes the distance between the top plane of layer 2 and a plane which shows no expansion or shrinkage in it, i.e. the neutral plane. By introducing this neutral plane,

the origin for the y direction can be set at this plane. In addition, the curvature of the bimetallic strip can be determined from the strain, ε, since $\varepsilon = y/R$. Then, solutions for the neutral plane, e, and the curvature of the bimetallic strip, $1/R$, can be obtained, i.e.

$$e = h + \frac{E_1 t^3 + 3E_2 h^2 t + 4E_2 h^3 + 4\mu\alpha_2 E_2 h\left(E_1 t^3 + E_1 h t^2 - E_2 h^2 t - E_2 h^3\right)}{2E_2 h(h+t)\left\{-3 + 4\mu\alpha_2\left(E_2 h + E_1 t\right)\right\}}, \quad \ldots (6.10)$$

$$\frac{1}{R} = \frac{2\Delta T\left(t\alpha_1 E_1 + h\alpha_2 E_2\right)}{E_1 t(2e - 2h - t) + E_2 h(2e - h)}, \quad \ldots (6.11)$$

where, $\mu \equiv \frac{3}{4}\frac{1}{t\alpha_1 E_1 + h\alpha_2 E_2}$. Therefore, the deflection of bimetallic strip, δ, can be obtained using the relation $1/2R = \delta/L^2$, where L is length of bimetallic strip.

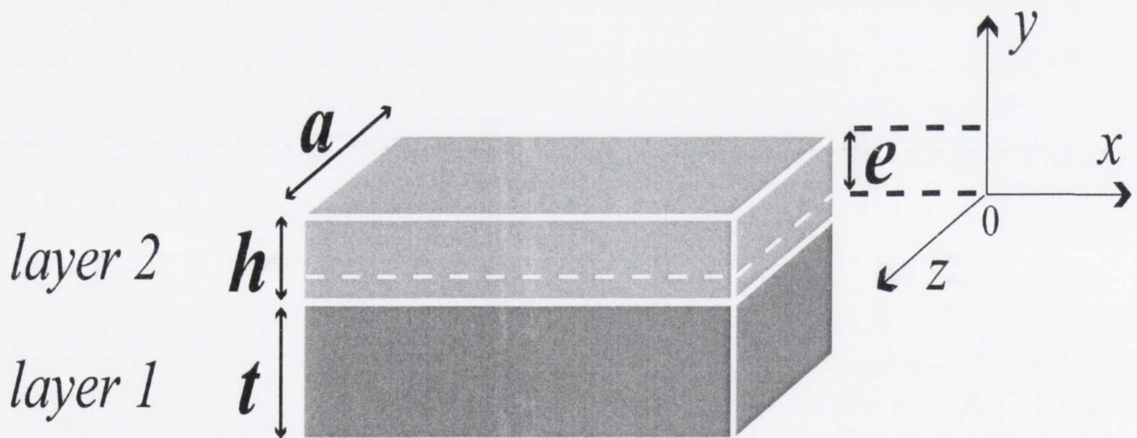

Fig. 6.10: Bimetallic strip- the width of the bimetallic strip is a and the thickness of layer 1 and 2 are t and h. Young's moduli and thermal expansion coefficients of each layer are E_1, E_2, α_1 and α_2, respectively.

To heat the bimetallic strip in order to induce bending, radiative heating from a filament is used. To obtain a filament with a long life-time, we use a finely wound

filament obtained by breaking a commercial halogen 50 W light bulb (12 V, OSRAM: 64440). Figure 6.11 (a) shows the temperature increase of the bimetallic strip which is located at a distance of 3 mm from the filament. Via radiation from the filament we should in principle be able to heat up the bimetallic strip to around 500 °C. However, due to heat loss via thermal diffusion and thermal radiation from the bimetallic strip itself increasing the input power above 10 W does not produce an effective increase in the temperature of the bimetallic strip. The most effective temperature increase with filament current is observed up to approximately 250 °C. On the other hand, a lower operational temperature is preferable to avoid damage to the sample and possible outgassing from surrounding materials. Hence, the bimetallic strip employed operates below 250 °C and results in a controlled reproducible contact with the substrate.

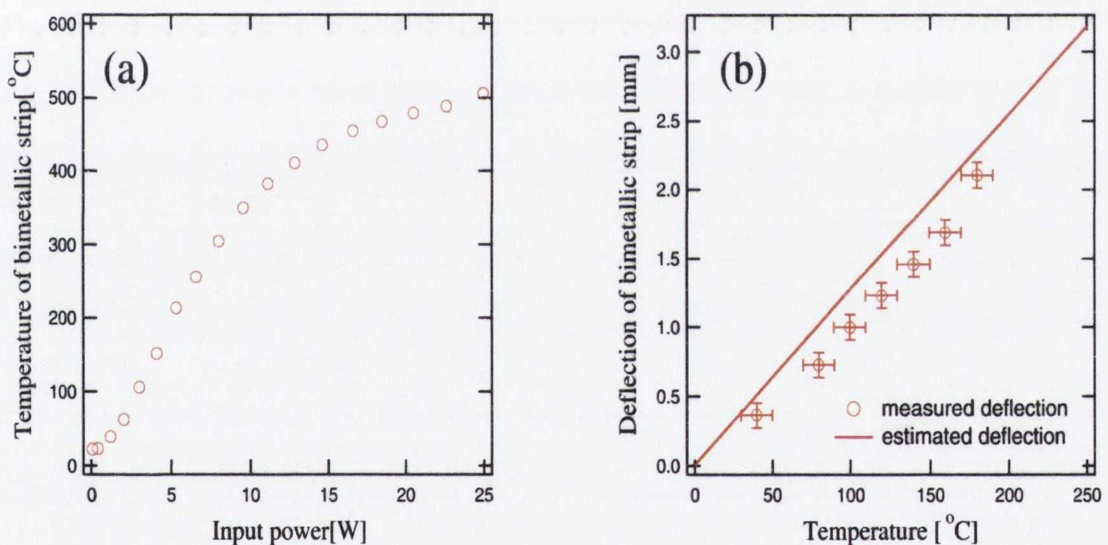

Fig. 6.11: a) Temperature increase of a bimetallic strip heated by radiation from a 50 W filament; b) measured and estimated deflection of the bimetallic strip. The bimetallic strip was located at a 3 mm distance from the filament. The deflection at the free-end was measured using a 20 mm long bimetallic strip. The estimation was conducted using equation 6.11 and $1/2R = \delta/L^2$.

In general, a thin bimetallic strip is superior for achieving significant deflection, as is evident from equation 6.11. However, a bimetallic strip that is too thin is not suitable for passing a large current. This is due to the fact that resistive heating at the

contact can dramatically increase the temperature in the strip itself and it becomes impossible to control the deflection. To avoid this, a bimetallic strip which is 20 mm long, 3 mm wide, with a total thickness of 0.25 mm is used. This strip was fabricated from 0.15 mm thick Ta and 0.10 mm thick SUS304 sheets. To assemble the bimetallic strip, the Ta and the SUS304 pieces were fixed rigidly together by spot welding. Figure 6.11 (b) shows the deflection of this bimetallic strip, which can be estimated by $\delta = 0.0127\Delta T$ [mm] from equation 6.11. The actual measured deflection is also shown in Fig. 6.11 (b). A significant deflection is clearly seen under gentle heating conditions. The slopes of the estimated and measured deflections as a function of temperature show good agreement, although the observed deflection is between 9- 29 % less than that of the estimated value. We believe that this difference is the result of a non-uniform interface between the respective components of the bimetallic strip due to the spot welding procedure.

In order to make electrical contact to the sample using the bimetallic strip, we have to consider suppressing the contact resistance so that we can pass significant current without unwanted local heating at the contact point. To do so, two major points need to be considered. First, in order to achieve a stable electrical contact, good mechanical contact is required. Second, in order to reduce contact resistance, a large surface area contact is necessary. In the case of a free-standing sample such as a cantilever, the problem is further complicated because stable electrical contact can be lost due to the inherent flexibility of the sample itself. Figure 6.12 shows a schematic of the heating system we developed for our cantilever sample. The Ta side of the bimetallic strip is placed facing the unpolished side of the cantilever sample allowing contact to be made with the sample when the temperature of the bimetallic strip is increased. For our system, the dimensions of the cantilever sample are typically $50 \times 10 \times (0.280\text{-}0.525)$ mm^3 as previously mentioned. The filament used to heat the bimetallic strip is placed at a 3 mm distance from the strip. The movable part of the bimetallic strip which has an L-shape is 20 mm long and 3mm wide.

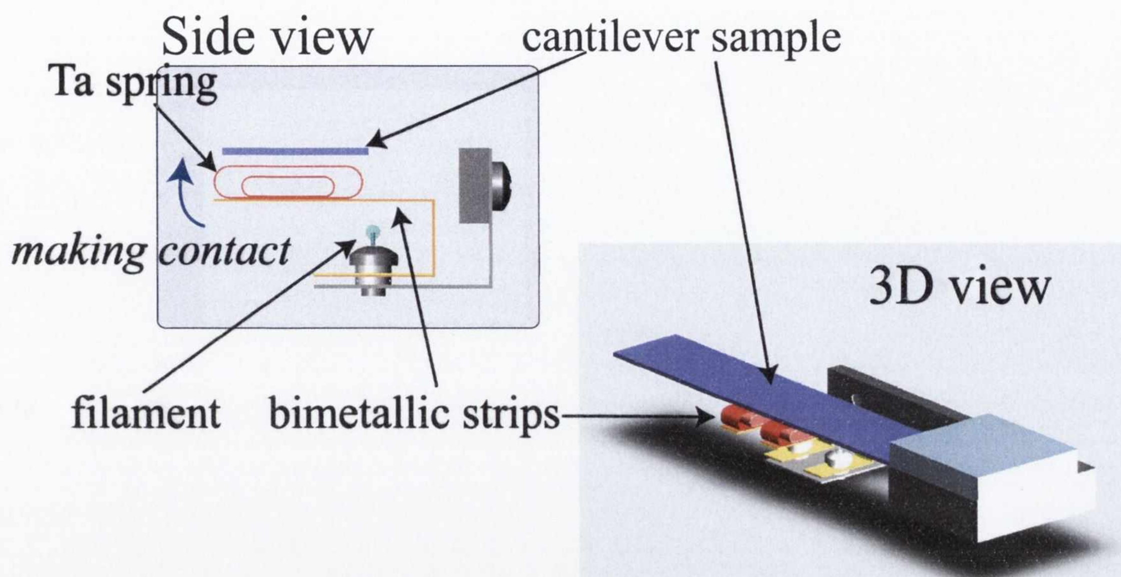

Fig. 6.12: A heating system for a cantilever sample with use of bimetallic strips. This system consists of a cantilever sample, two bimetallic strips, a filament and a base for the sample and the heating system. The side view illustrates how each bimetallic strip has a double looped spring to have stable electrical contact.

Upon heating, the bimetallic strip bends towards the sample and establishes contact. However, stable electrical contact is difficult to achieve due to the intrinsic rigidity of the strip and the fact that typically there is only a single point of contact between the strip and the substrate. This not only affects uniformity of the heated area on the sample surface but causes excessive local heating at the contact point. To eliminate this problem we added a strip of Ta that was looped twice into an oval-shaped plate spring and attached to the Ta side of the L-shaped bimetallic strip (see side-view of Fig. 6.12). We set the distance between the sample and the outer fold of the spring to be less than 1 mm. The dimensions of the outer loop of the Ta spring are 10×3×1.8 mm, while those of the inner loop are 6×3×1.2 mm. Each spring has the same thickness of 0.025 mm. The outer spring loop has a larger surface area and radius of curvature than that of the inner spring loop and this outer loop makes contact directly to the sample when the bimetallic strip is heated. This set-up permits stable electrical contact to be achieved (a single loop design did not allow us to establish reproducible contacts). With this combination of an outer and inner spring loops we achieve excellent reproducibility without contact failures. The double looped spring design has another advantage. Instead

of heating the cantilever sample by passing a current between the clamping element and the bimetallic strip it is possible to use two separate bimetal strips. This is achievable because the double loop design allows each spring to absorb excess forces occurring naturally upon contact. As a result, we can control the area heated-up by using multiple bimetallic strips by passing a current between them, while compensating for the difference in their deflections. In our set-up, we use two bimetallic strips, each with the double looped spring design. The distance between the two strips is set to be 10 mm.

To demonstrate the performance of the two bimetallic strips with the double looped spring design, the steps involved in the preparation of a clean Si(111)-7x7 surface are detailed in Appendix E. With this arrangement, we have the facility to successfully and repeatedly prepare a well defined clean area from oxide covered cantilever samples as temperatures up to 1400 K are easily achievable. This method is easier to implement than a movable contact involving a piezo element. Moreover, by carefully tailoring our heating system it is possible to eliminate induced stresses in the cantilever substrate itself, while at the same time ensuring excellent electrical contacts. This method provides us with a new tool to make controlled mechanical and electrical contact to free standing samples and expands the range of systems for which temperature dependent studies can be performed. In fact, such controlled regionalised contacting opens up a window of opportunity for potential commercial applications, which resulted in the filing of a patent application to the Irish Patent Office in Sept. 2005; please see Appendix F.

While our bimetallic heating method is successful in heating and preparing clean Si surfaces under UHV conditions some shortcomings also exist. Firstly, prolonged use occasionally causes deformation of the contacting springs, which reduces their force absorbing character. This can result in an undesirable stress being applied to the sample during heating and under extreme circumstances sample fracture can occur. Secondly, migration of contaminants from the bimetals to the sample surface can also occur following extended use. We believe that the spot weld sites which bind each bimetal together act as the source of this contamination. Finally, large currents are required (typically >6 A) to heat the desired 10x10 mm^2 sample area on contact. Therefore, the current carrying wires become extremely hot during the flash procedure and outgas significantly. While it is possible to prepare a clean Si(111)-7x7 surface in this

environment, preparation of the more reactive Si(100)-2x1 surface would prove problematic. Unfortunately, thicker wires cannot be used to reduce the amount of outgassing during the flash cycle, as these stiffer wires would jeopardise our STM capability by transmitting vibrations to the sample holder.

6.1.5.2 Localised Heating of a Cantilever Sample via Electron Bombardment

Due to the aforementioned issues associated with our bimetallic heating method, we developed an alternative means of heating the sample at a defined region. Ideally this heating procedure should be indirect, i.e. not involve physical contact with the sample, of which there are typically two methods available- radiative heating and electron bombardment [6]. The radiative heating method is sometimes a better choice, as it eliminates unwanted effects on sample properties and/or damage to the surface region caused by energetic electrons [6, 28, 29]. On the other hand, with radiative heating, it is difficult to achieve temperatures exceeding 1000 K without minimal heat dissipation, because of the power requirements of the light source. Moreover, there are difficulties associated with effectively coupling the light into the vacuum chamber. Consequently, we adopted the electron bombardment technique, ensuring that the impacting electrons collide with the rear of the sample only. This avoids any unwanted effects from the energetic electrons at the surface region of interest. A schematic of our basic set-up is displayed in Fig. 6.13.

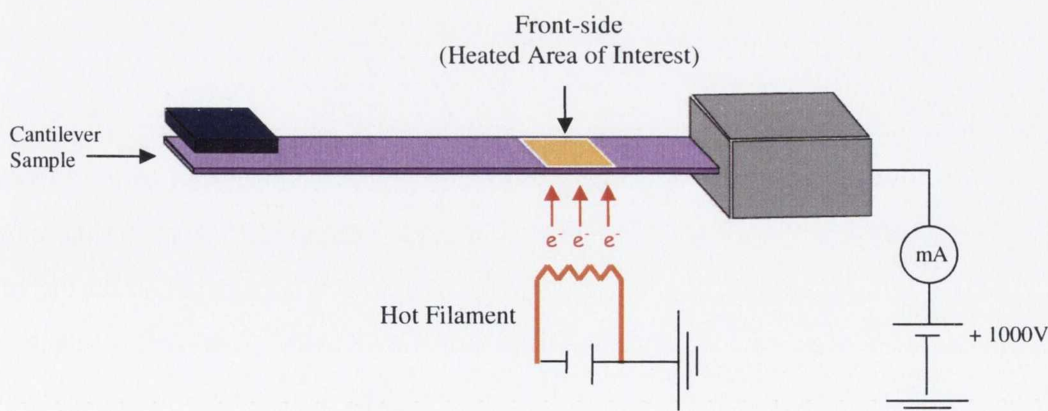

Fig. 6.13: Schematic diagram illustrating electron bombardment of a cantilever sample, which produces a locally heated region. The impinging electrons strike the back-side of the sample.

During electron bombardment a filament (typically tungsten) is heated to a temperature where it can source an electron current via thermionic emission [30]. A high voltage is then applied between the filament and the sample, such that electrons bombard the sample resulting in heating [30]. As a result, temperatures much greater than 1400 K can be achieved. Consequently, clean silicon surfaces can be successfully prepared using this method, in addition to clean metal surfaces which demand very high temperatures [6]. Now let us examine this process in greater detail.

Thermionic emitters are widely used in surface science experiments as sources of electrons. Thermionic emission from a resistively heated filament is the flow of electrons from the surface caused by thermal excitation overcoming the electrostatic forces restraining the charge carriers [30]. The emission of electrons in the absence of an applied field follows the Richardson-Dushman equation

$$J = AT^2 e^{\frac{-\phi}{kT}} \qquad \ldots (6.12)$$

where, J is the emitted current density, T is the temperature, ϕ is the work function of the metal, and k is the Boltzmann constant [6]. The proportionality constant, A, known as Richardson constant, is given by

$$A = \frac{4\pi mk^2 e}{h^3} = 1.20173 \, x10^6 \text{ A m}^{-2}\text{K}^{-2} \qquad \ldots (6.13)$$

where, m and e are the mass and charge of the electron, and h is Planck's constant [6]. Due to the exponential dependence of J on T, the current density increases rapidly with temperature when kT is less than ϕ. In the presence of an electric field resulting from an applied bias voltage, a modification to equation 6.12 is required to describe the current density; the current emitted by the hot filament into the vacuum depends on the metal thermionic work function, and this function is lowered from its normal value by the presence of images forces and by the applied electric field. This enhancement is given by the field-enhanced thermionic emission equation:

$$J(E_S, T, \phi) = AT^2 e^{\frac{-(\phi - \Delta\phi)}{kT}}$$

$$\Delta\phi = \sqrt{\frac{e^3 E_c}{4\pi\varepsilon_0}} \qquad \ldots (6.14)$$

where, E_c is the electric field strength and ε_0 is the vacuum permittivity [30]. This equation is reasonably accurate for electric field strengths lower than approx. 10^8 V m^{-1}, in which range the enhancement is known as the *Schottky-effect* [30].

Various coatings on thermionic emitters are used to reduce the work function, permitting the thermionic emitter to operate at lower temperatures while delivering the same current density as an unmodified emitter at higher temperatures [6]. For various reasons, ThO_2 coatings on W or Ir surfaces exhibit the most favorable properties for use in UHV [31]. In addition to W wire thoriated with surface coatings of ThO_2, it is also possible to purchase W wire alloyed with Th at the 1- 2% level [32, 33]. With this small addition of thorium the work function is reduced from 4.54 eV to approx. 2.96 eV [6]. These wires display a greatly enhanced thermionic emission, compared with pure W as a result. Figure 6.14 represents the calculated current densities for both pure and thoriated tungsten wire estimated using equation 6.14. Another important reason for using thoriated thermionic emitters is to reduce the operating temperature for electron emission to levels that involve negligible evaporation of the metal. At the higher emission current densities for pure W, significant evaporation will occur, whereas thoriated tungsten emitters involve negligible evaporation rates under typical operating conditions [6]. For the above reasons alloyed Th-W filaments are employed by us as efficient providers of electrons at more favourable operational temperatures. This is very important for improved UHV conditions as it minimises outgassing from the filament and its surroundings during heating.

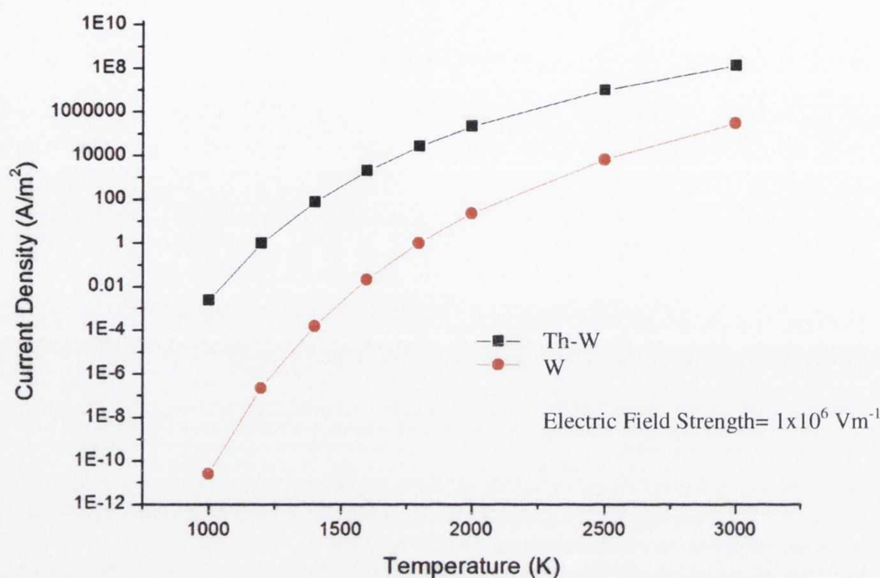

Fig. 6.14: Calculated current densities as a function of temperature for both pure and thoriated tungsten. A tremendous enhancement of electron emission is achieved as a result of lowering the work function via alloying tungsten wire with small amounts of thorium (typically 1- 2%).

Thoriated filaments are made by adding 1 or 2 per cent thorium oxide to the tungsten before it is sintered and drawn into shape. For this reason high emissions are ordinarily not obtained from thoriated filaments until they have been heated to a very high temperature. A flashing of the filament at 2800 K for 3 minutes is a sufficient preliminary treatment [34]. This process reduces the thorium oxide to thorium metal which remains distributed at a very low concentration throughout the filament. The heating to such a high temperature, however, removes all the thorium from the surface via evaporation. Therefore, if the temperature of the filament is lowered and the emission is measured, it is found to be the same as that from a pure tungsten filament at the same temperature [34]. To *activate* the filament, thorium metal needs to be brought to the surface by diffusion from the interior. This occurs at an appreciable rate only at temperatures above 1900 K. On the other hand, above 2200 K sufficient evaporation of thorium occurs. The best temperature range for activating the filament is therefore between 2000- 2100 K [34]. In this range, thorium moves to the surface along grain boundaries and migrates over the surface where it forms a monatomic layer which has a

lower work function than clean tungsten [35]. After the filament has been brought to an active state, it will remain in this condition once the temperature is kept below 2100 K, and provided the vacuum is sufficiently high and free from oxidizing species. The activation procedure is a critical step for us in achieving efficient electron emission under low filament conditions. The required filament condition to achieve the desired temperature for the activation process can be estimated using Fig. 6.15. However, it should be noted that this estimate does not take radiative heating from nearest neighbour turnings of the filament into account. Therefore, the actual temperature of the filament is believed to be slightly higher than the estimated value. Alternatively, an optical pyrometer can also be used for this purpose [6].

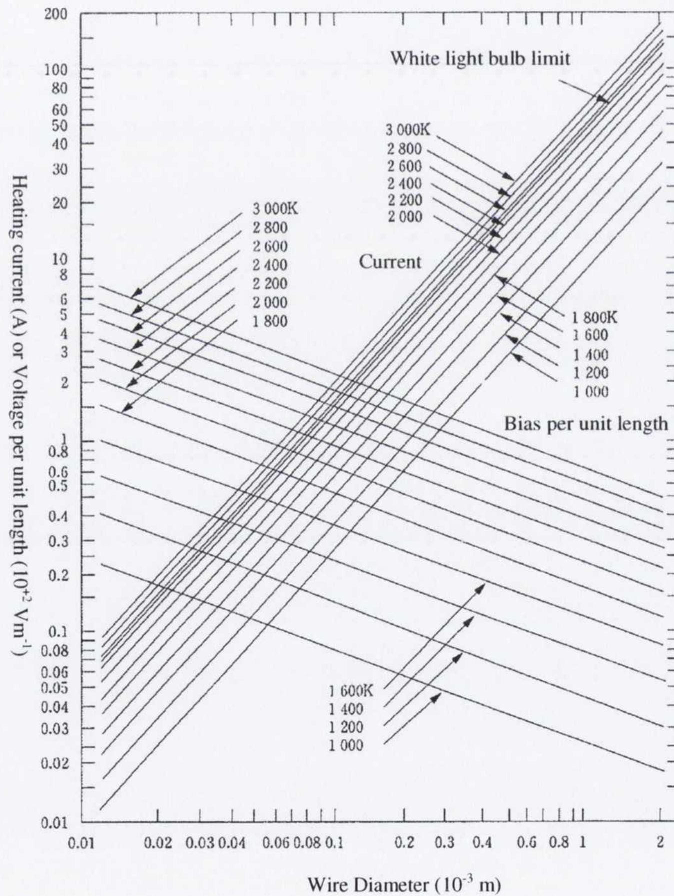

Fig. 6.15: Relationship between the filament current (or voltage per unit length), wire diameter and filament temperature for a thoriated tungsten filament in vacuum [36].

In the presence of inert gases etc., the filament may become deactivated by positive ion bombardment, where the positive ions acquire high velocities as a result of high sample voltages [37]. In some cases thoriated tungsten filaments are carburised to reduce the rate of thorium evaporation and also to reduce the susceptibility to deactivation by ion bombardment [38, 39]. However, it should be noted that carburised filaments are much more brittle than an uncarburised ones. Therefore, we did not look to fabricate carburised filaments. However, occasionally a reactivation process for alloyed Th-W filaments is required to rejuvenate thorium levels at the surface.

Our basic design for electron bombardment of the cantilever sample is shown in Fig. 6.16 (a-d). It consists of a T-shaped Macor® [40] block which is fixed rigidly to the sample holder plate, where it acts as a scaffold for two alloyed Th-W filaments. Macor® is a machineable glass-ceramic and is often used in high-temperature and/or high vacuum environments due to its excellent electrical and thermal characteristics and low outgassing rate [40, 41]. It is light, stable at high temperatures, electrically and thermal insulating and has a low thermal expansion coefficient at elevated temperatures [40, 41]. Its low thermal expansion coefficient ensures that its shape changes minimally during heating. Due to the above properties, Macor® possesses the desired requirements to act as suitable frame for our filaments. The filaments are made from tungsten wire alloyed with 1% thorium, which is 0.15 mm in diameter. Each filament was fabricated by us by wrapping the wire uniformly around a suitable threaded rod, in such a fashion that their ends could be mounted at the desired locations without producing strain in the coils themselves. This is important and ensured that the coils did not become distorted during initial heating. Each filament is approximately 8 mm long, with a coil diameter of 2 mm. The inter-filament distance is 6 mm, while the filament-sample distance at the back side of the cantilever sample is set at 2 mm. The filaments are connected in series (securely and under a strain free condition) using M1 molybdenum nuts and threaded rods, thus permitting the construction of an electrical circuit enabling current flow through the filaments. By passing a current through the filaments (typically within the 1.5–2.0 A range) and applying a high voltage (1000 V) to the sample, electrons are emitted from the filaments and are accelerated towards the sample surface causing heating of a 10x10 mm^2 region. This heat is sufficient to overcome the bond energy of silicon dioxide, thus

resulting in elimination of the oxide layer. However, in order to improve the uniformity of heating and prevent hot spots on the sample surface during bombardment, the sample width is typically reduced from 10 mm to 6 mm. Fortunately, this amendment has no serious implications for our STM or stress measurement capabilities; see Appendix G. With this method temperatures > 1400 K are achievable over a 10x6 mm^2 area, resulting in the preparation of extremely clean Si(111)-7x7 surfaces under low outgassing conditions. The experimental procedure for this process is described in Appendix H.

a)

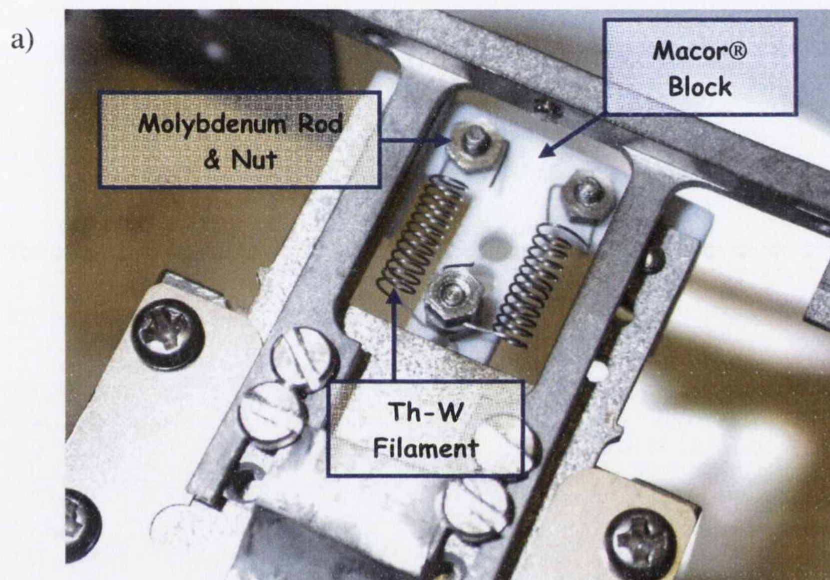

b)

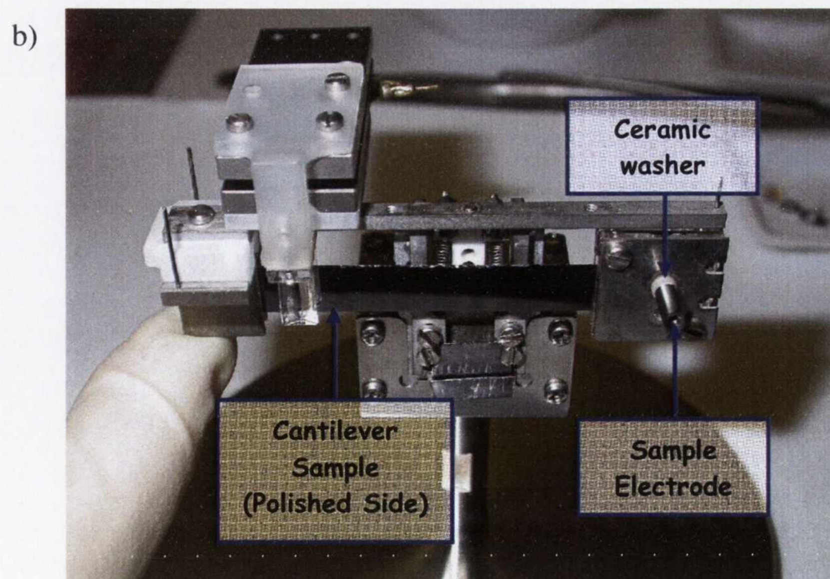

c)

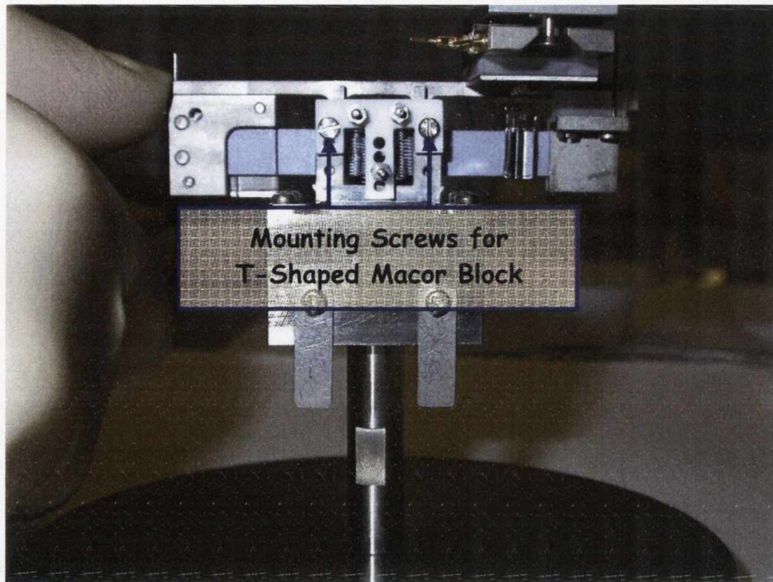

d)

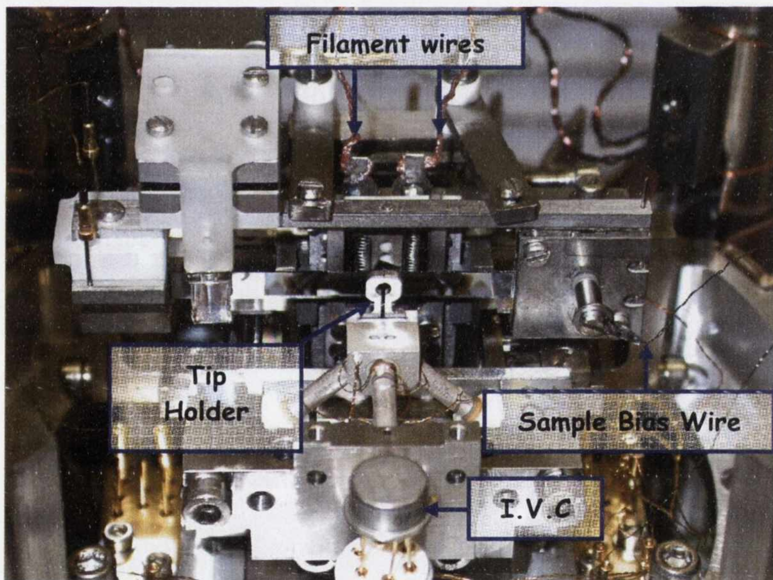

Fig. 6.16: Photographs of our developed electron bombardment system: a) two Th-W filaments are fixed to a Macor® block support using Mo rods and nuts, and act as the source of thermionic electrons; b) the cantilever sample is electrically isolated from the sample holder using a suitable ceramic washer, allowing a large bias voltage to be applied to the sample only; c) the Macor® block arrangement is mounted securely to the back side of the sample holder via purposely tapped holes, thus permitting the desired region of the cantilever sample to be heated effectively; d) the entire set-up is located within a complex and spatially restricted environment, demanding extreme caution during the bombardment process (for example, it is imperative to: i) ground all electrically sensitive components in the vicinity of the sample during the application of large bias voltages and ii) never leave the tip in place during bombardment as this may incur an electrical arc from the sample to the sharp tip, consequently damaging the vulnerable I.V.C).

6.1.5.3 Heating a Cantilever Sample Using an Infrared (IR) Radiation Source & Quartz Light Guide

For sample heating during measurements it is imperative that the adopted heating technique has no physical contact with the sample during operation. It is also critical that the selected method does not impede STM and capacitance measurements. To this end we have chosen a commercial heating system based on infrared radiation [42]. Infrared radiation is electromagnetic radiation with wavelengths between approximately 750 nm and 1 mm (see Fig. 6.17). When infrared radiation strikes a material and is absorbed, heating of the material occurs. The electromagnetic wave range of infrared radiation is subdivided into near, intermediate and far wavelengths. The near infrared radiation has the same properties as visible light with respect to radiation, condensation, reflection, transmission and refraction [42]. Our adopted infrared heating system is so designed that it skillfully utilises such properties [42]. It can introduce infrared radiation to the exact location of a sample placed in UHV.

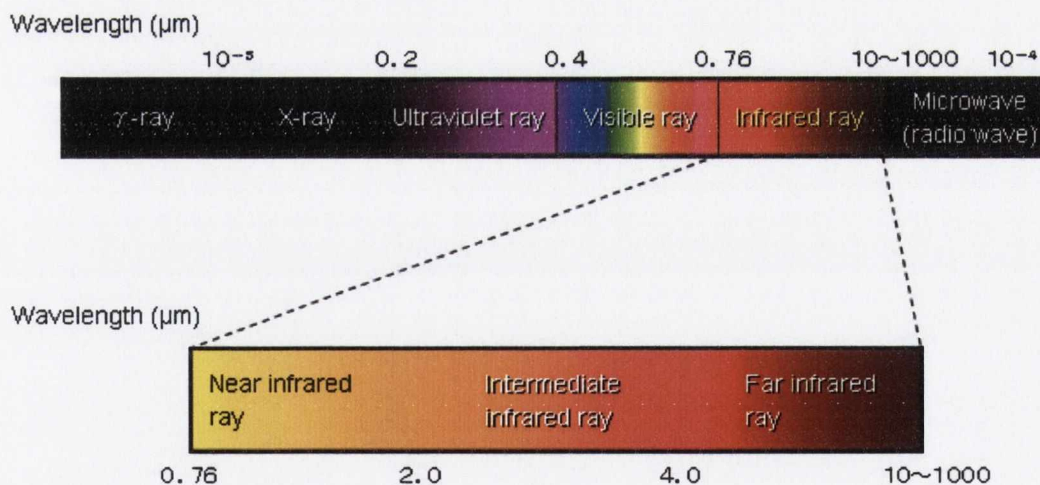

Fig. 6.17: Wavelength distribution of electromagnetic waves [42].

The infrared heating system is composed of a high power 3 kW infrared source (with an emitted distribution range between 700-3000 nm and a peak intensity of 900 nm), a spheroid reflection mirror, and a quartz light guide. As shown in Fig. 6.18, an infrared

lamp which serves as the heat source is placed at F1, i.e. the 1st focus of the gold spheroid mirror [42]. Infrared radiation emitted from the energised lamp hits the gold spheroid mirror and is reflected and collected at the 2nd focus, F2 [42]. A transparent quartz light guide is installed at this position and collected infrared rays are led into the light guide. Some infrared rays undergo straight transmission, while others are directed towards the effective modification area of the cantilever sample by total internal reflection through the light guide [1, 42]. As a result, temperature increase at the sample surface can be achieved. This system permits: a) clean rapid heating of the sample without heating the peripheral areas; b) no generation of noise or electrical induction; c) sample heating in UHV.

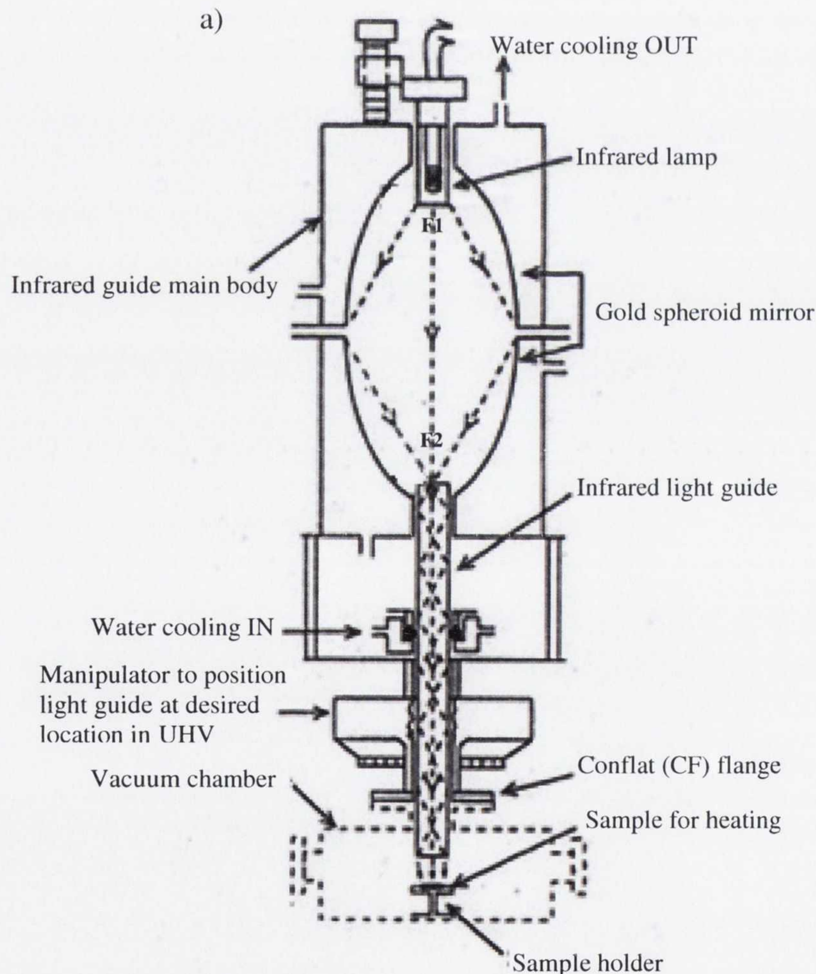

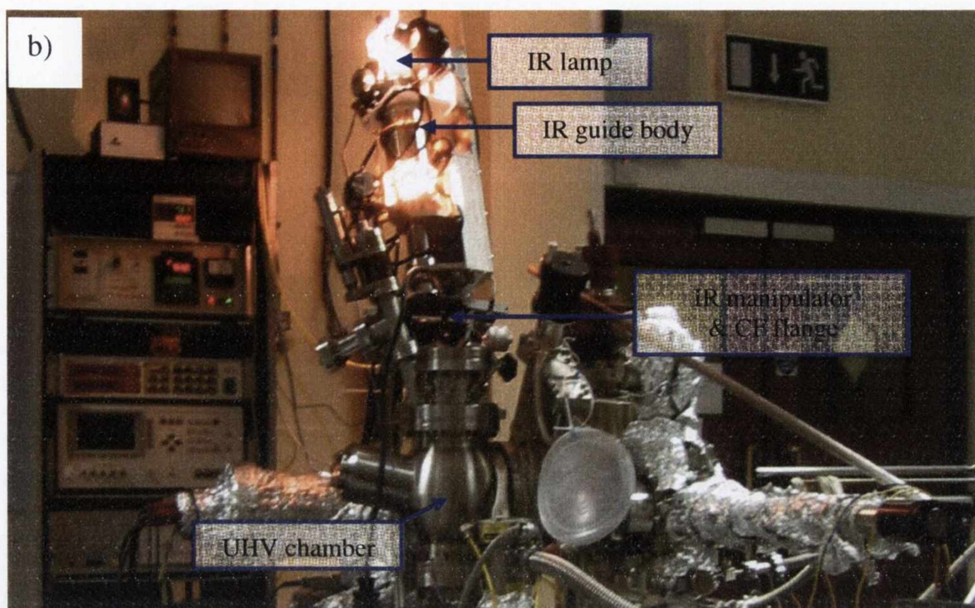

Fig. 6.18: Configuration of the infrared heating system: a) schematic diagram [42]; b) external-view during heating process; c) specifically designed support structure for the infrared heating unit to facilitate unimpeded STM and capacitance measurements.

Due to space limitations in the vicinity of the STM and the cantilever sample holder (shown in Fig. 6.19), measures had to be taken to appropriately direct light from the light guide towards the sample surface. To overcome this we utilised refraction effects due to a sharp end. This demanded fabrication of a specifically designed light guide. The sharp

end has an off cut 30° from its cross section and the light guide stands at a 20° offset angle from the vertical direction. This set-up provides us with an $8 \times 10.4\ mm^2$ heated area at the effective modification region (assuming a sample width of 10 mm).

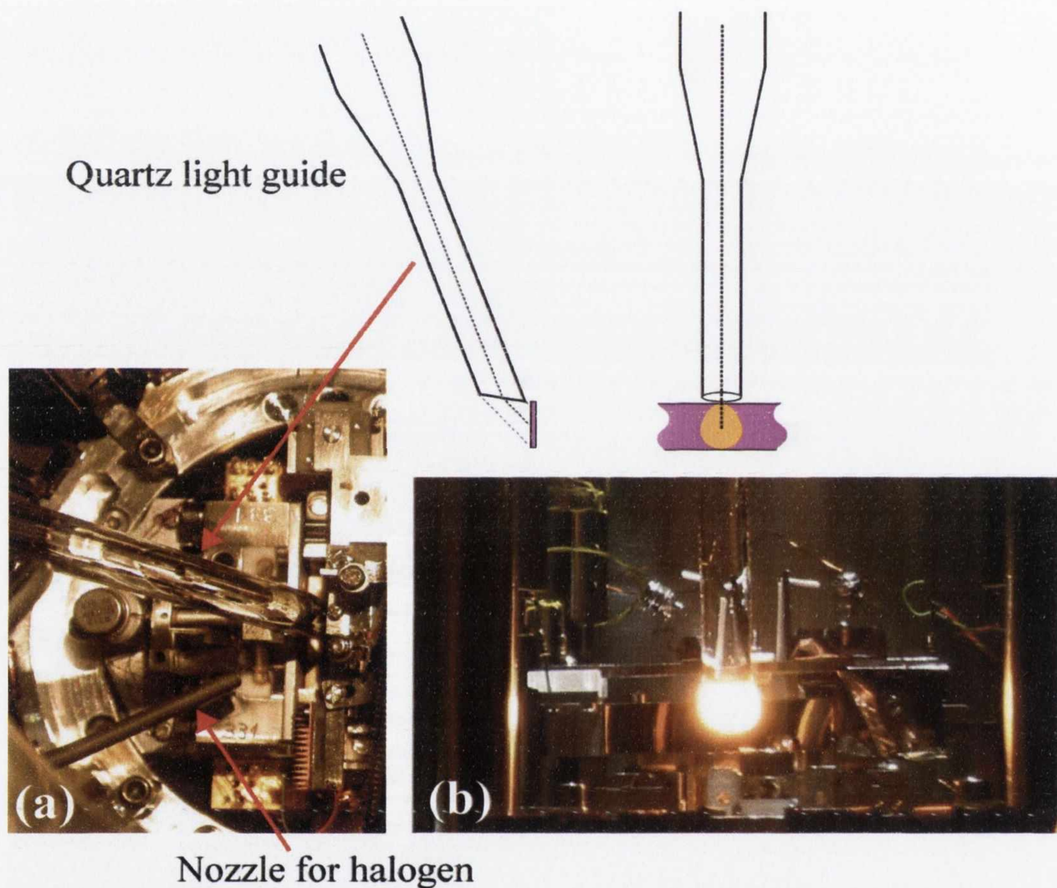

Fig. 6.19: Set-up for effective infrared heating of a cantilever sample. Pictures (a) and (b) display views both from above and from the front-side of the cantilever sample holder, respectively. To introduce infrared light into the system via the infrared light bulb, a quartz light guide is used. The wide and narrow parts of the light guide have 20.6 and 8 mm diameters, respectively. The sharp end has an off cut 30° from its cross section and the light guide stands at a 20° off set angle from the vertical direction. By use of refraction through the sharp end, the infrared light can be directed towards the effective modification area.

Although a 3 kW infrared bulb is employed, only a small proportion of this power is transferred to a Si cantilever sample in the form of heat. Firstly, power loss along the length of the light guide occurs [42, 43]. Secondly, reflection of infrared radiation at the Si surface and transmission through the sample leads to further power dissipation;

see Fig. 6.20. Furthermore, absorbed radiation is not entirely harnessed as heat. When a material is illuminated, photons induce electronic excitations. The photon is destroyed in the process and the absorbed radiant energy is transformed to electric potential energy. This absorbed energy may be re-emitted by the electrons as radiant energy via a number of de-excitation processes, or may be dissipated to the rest of the material, i.e. transformed into heat [44, 45]. The absorption process is further complicated by a temperature dependence [46]. Despite the above mentioned losses it is possible to heat the effective modification area of a 525 micron thick Si sample to approx. 950 K. We estimate that 10-15 W of power is delivered to the surface region to achieve this temperature (this estimation includes heat dissipation effects at the sample surface as a result of thermal diffusion and black-body radiation). While this temperature limit is not sufficient to prepare clean surfaces from oxide covered samples, it is suitable to study a wide range of high temperature surface reactions. (It should be noted that attempts were made to prepare clean silicon surfaces from hydrogen terminated samples [47] using the infrared radiation source). Moreover, the non-contact and non-electrical nature of the method permits heating during STM and capacitance measurements. Metal cantilever samples can also be heated in this way. However, metals are almost 100 % reflective in the infrared region [45]. Consequently, heating a metal surface to high temperatures using infrared radiation may not be very effective.

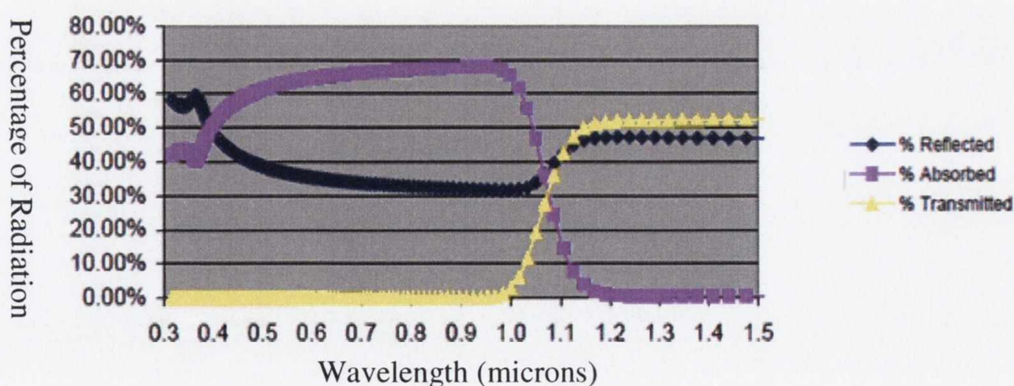

Fig. 6.20: Percentage of radiation reflected, transmitted and adsorbed for a 600 micron thick silicon sample. Our light source has a distribution range between 700-3000 nm with a peak intensity of 900 nm. In order to minimise loss due to transmission, a metal plate is placed at the back side of the cantilever to reflect transmitted radiation back into the sample [42, 48].

6.2. STM imaging on the Cantilever Sample

In order to discuss the quality of STM imaging on the cantilever sample, let's observe a clean Si(111)-7×7 reconstructed surface. The clean Si(111)-7×7 surface was prepared using the bimetallic strips heating method [2]. During sample cleaning, the base pressure in the UHV chamber was lower than 1.0×10^{-10} Torr. The Si(111) cantilever sample used was cut from a single-side mirror polished 5 inch wafer which was p-type boron doped, with a thickness of 525±10 μm and a resistivity of 5–18 Ω cm. The wafers were supplied by Shin-Etsu Chemical Co., Ltd. Figure 6.21 displays a typical STM image of a Si(111)-7×7 surface observed on the cantilever sample using our unique set-up.

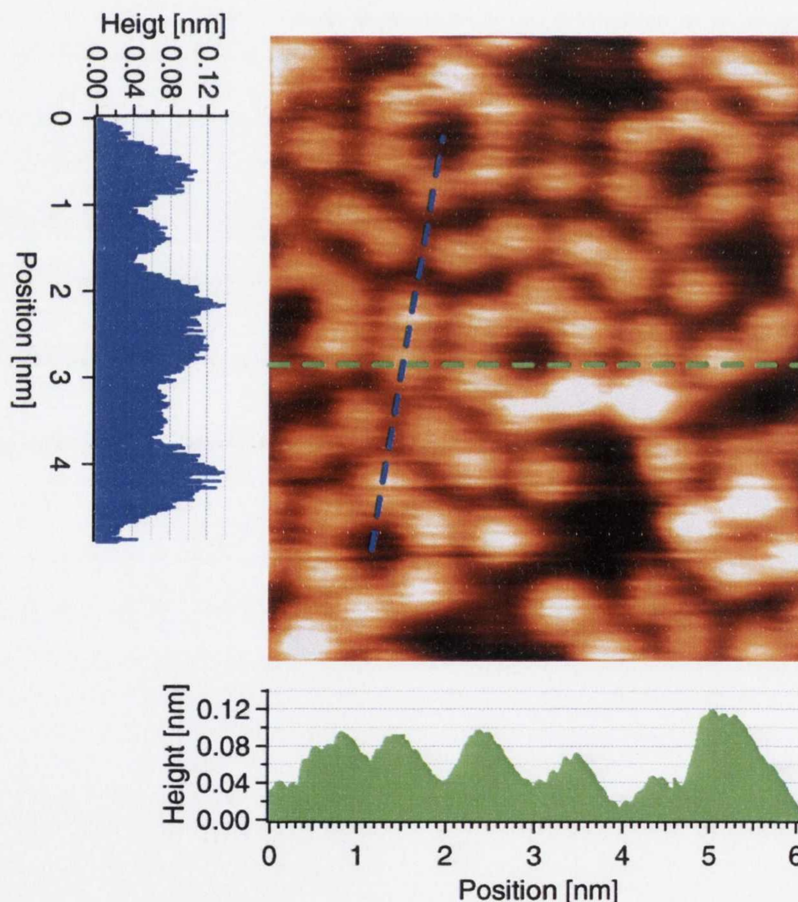

Fig. 6.21: A typical STM image of the Si(111)-7×7 surface taken on a free standing cantilever sample. This image was achieved with a sample bias of +0.7 V and a tunnelling current of 0.01nA. The image size is 6.2×7.2 nm^2. This image was scanned from left to right. The green and blue dashed lines represent cross sections along different scan lines.

From this image, each adatom site is clearly resolved and some reacted sites can also be easily recognised. However, there are approx. ±4 pm noise fluctuations in the image cross section shown by the green dashed line in Fig. 6.21, while the blue dashed line displays ±7.5 pm noise fluctuations. These noise levels may be due to induced electrical effects and/or the STM tip. Another potential source is the natural oscillation of the cantilever sample itself. Nonetheless, although there are ways to improve the quality of the imaging technique, at present it is more than sufficient to observe and discuss atomic scale structures and phenomena on Si(111)-7x7 surfaces.

As previously mentioned, our system is equipped with a sample pusher. Its primary role is to study the effects of artificially applied stress on atomic-scale reaction processes. However, it can also be utilised to reduce the natural oscillation amplitude of the cantilever sample, thus permitting improved imaging capability and the providing the capacity to image thinner samples that cannot otherwise be imaged due to issues with natural resonance. Figure 6.22 below displays a high resolution image obtained on a 280 micron thick cantilever sample under a gentle loading condition using the sample pusher.

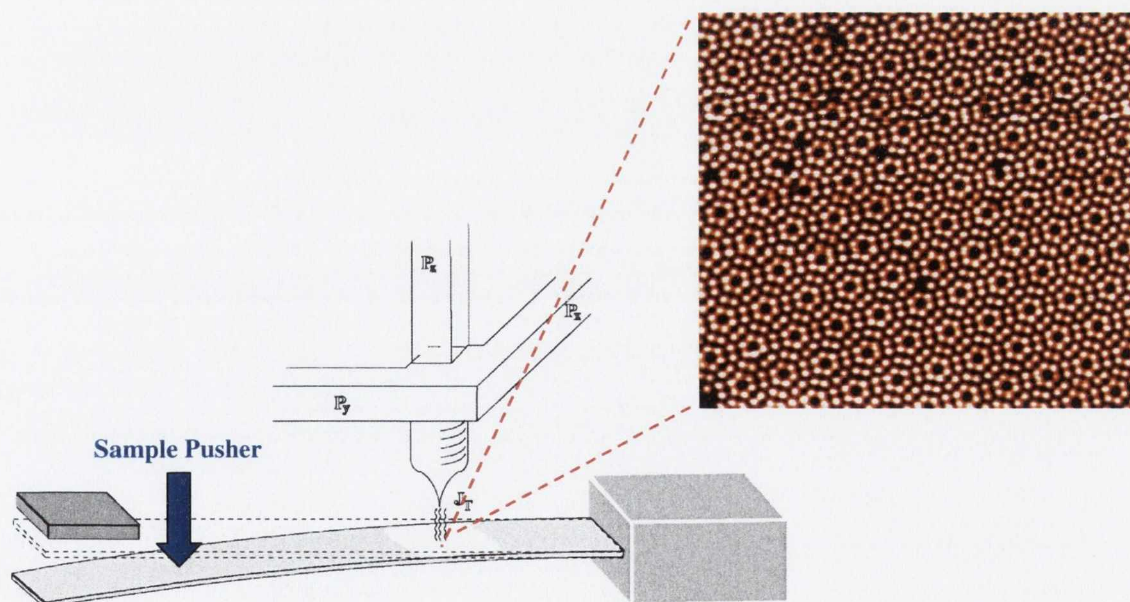

Fig. 6.22: High resolution STM image of a Si(111)-7×7 surface taken on a 280 micron thick cantilever sample. Gentle loading of the cantilever sample using the sample pusher reduces the oscillation amplitude, thus permitting atomic level imaging. This image was taken with a sample bias of +1.0 V and tunneling current of 0.06 nA.

We are the first group to achieve true atomic resolution images in UHV on a cantilever sample using STM. We credit this achievement to our careful design considerations and original ideas. Nevertheless, it should be noted that the scheme of performing STM on a cantilever sample was pioneered by *Binnig*, *Quate* and *Gerber*, in the development of the worlds first Atomic Force Microscope (AFM) [49]. However, in this case the STM was not used to image the cantilever sample, but rather monitor the displacement induced by atomic scale forces experienced by another probe at an insulating surface. The original design by *Binnig*, *Quate* and *Gerber* is displayed in Fig. 6.23.

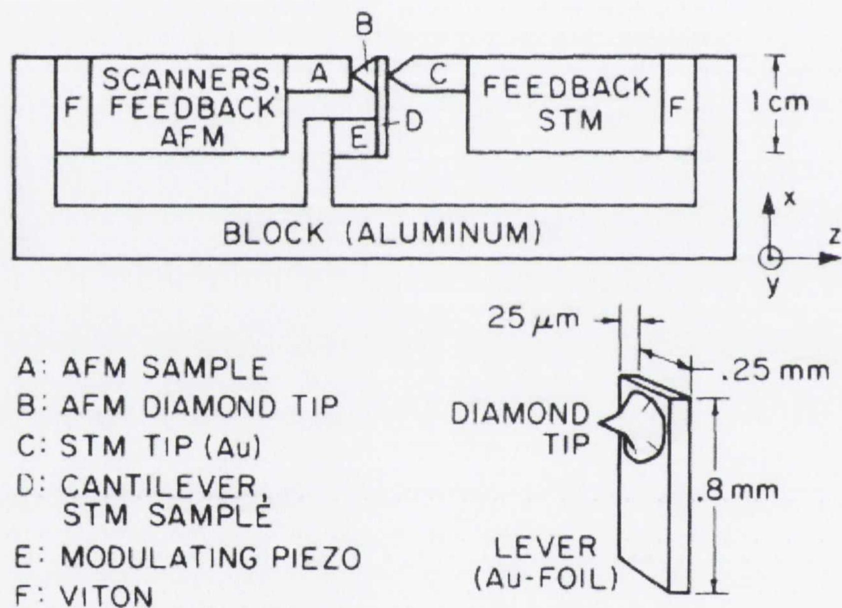

Fig. 6.23: Experimental set-up developed by *Binnig*, *Quate* and *Gerber* in which an STM is used to monitor the displacement of a cantilever sample in the developed of the first AFM [49].

In addition, relatively recently *Bach et al.* performed STM on a cantilever sample located in an electrochemical solution [3, 12, 13]. In this work, the bending of the cantilever was detected by STM, which also served as a means to observe surface structure (Fig. 6.24). Nonetheless, true atomic resolution images were not achieved in this study, in contrast to our achievement. Moreover, when a cantilever is placed in solution its oscillation

amplitude is dampened, thus facilitating STM observation; unfortunately we do not have this luxury.

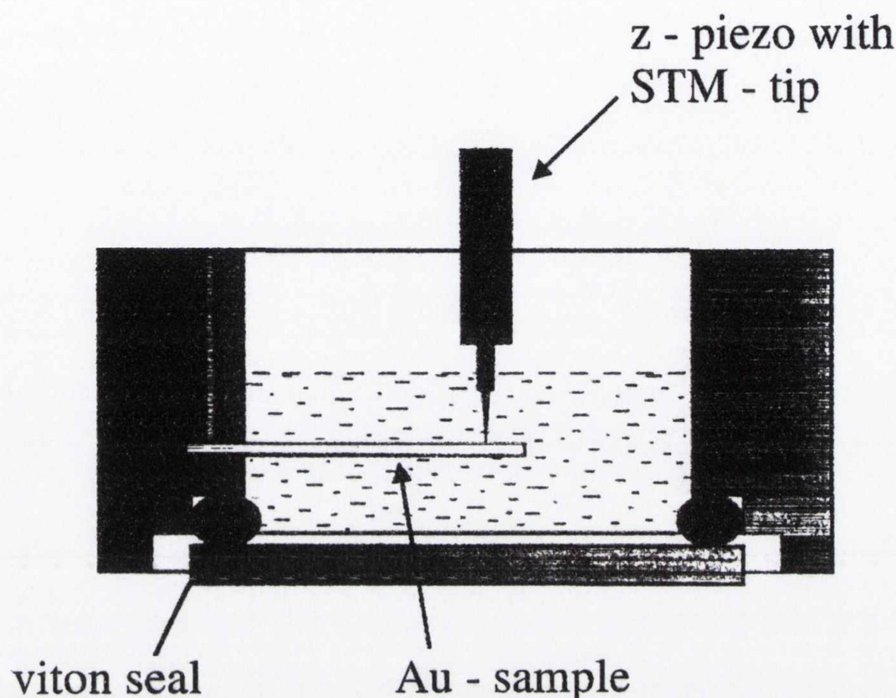

Fig. 6.24: Example of an electrochemical cell for STM studies on a solid-electrolyte interface which allows simultaneous measurement of the bending of the cantilever sample (i.e. surface stress measurements) when the electrode potential is varied [3, 12, 13].

6.3. Capacitance Measurements: Detection Limit & Stability

In order to discuss the forces acting at the surface region, not only are precise capacitance measurements essential, but mechanical, electrical and thermal stability also play pivotal roles. Figure 6.25 displays a typical time evolution of the capacitance change which was achieved roughly 4.5 hours following a flash procedure. Analysis indicates that we have minuscule thermal drift; approximately -0.39×10^{-7} pF/sec. This thermal drift effect diminishes greatly over time following the flash procedure as depicted in Fig. 6.26. Typically, we conduct exposures to clean sample surfaces 4-10 hours following the flash cycle. As a result, the thermal drift effect does not disguise any deflections due to the reaction. Comparing our value for the thermal drift (4.5 hours after the flash) with the value of -2.8×10^{-7} pF/sec estimated from a previous report [14], we see that our thermal

drift affect is 86 % smaller. Our high thermal stability can be attributed to the careful choice of materials for our special sample holder set-up. This result is important since small thermal drift is essential for reliable long time capacitance measurements. In addition, we can estimate the electrical stability by subtracting the thermal drift effect. Consequently, the average capacitance value and variance were calculated as $\mu = 2.5179901$ pF and $\sigma_v = 1.9\times10^{-6}$ pF , respectively. Statistically speaking $\pm\sigma_v$ around μ corresponds to accidental error. Although this is value is slightly inferior to the ideal detection limit of (0.5-0.8) $\times10^{-6}$ pF for the capacitance bridge, it has almost ideal resolution. Consequently, while strictly keeping the environment thermally and electrically quiet, we have the capability to perform stable high resolution capacitance measurements. (Aside: The basic workings of the capacitance bridge, as well as a discussion into measures to ensure accurate measurements are presented in Appendix I).

Fig. 6.25: Time evolution of the capacitance change. The red solid line was drawn using linear curve fitting and represents a miniscule slope due to thermal drift. The cantilever sample dimensions in this case are (50x10x0.525 mm^3).

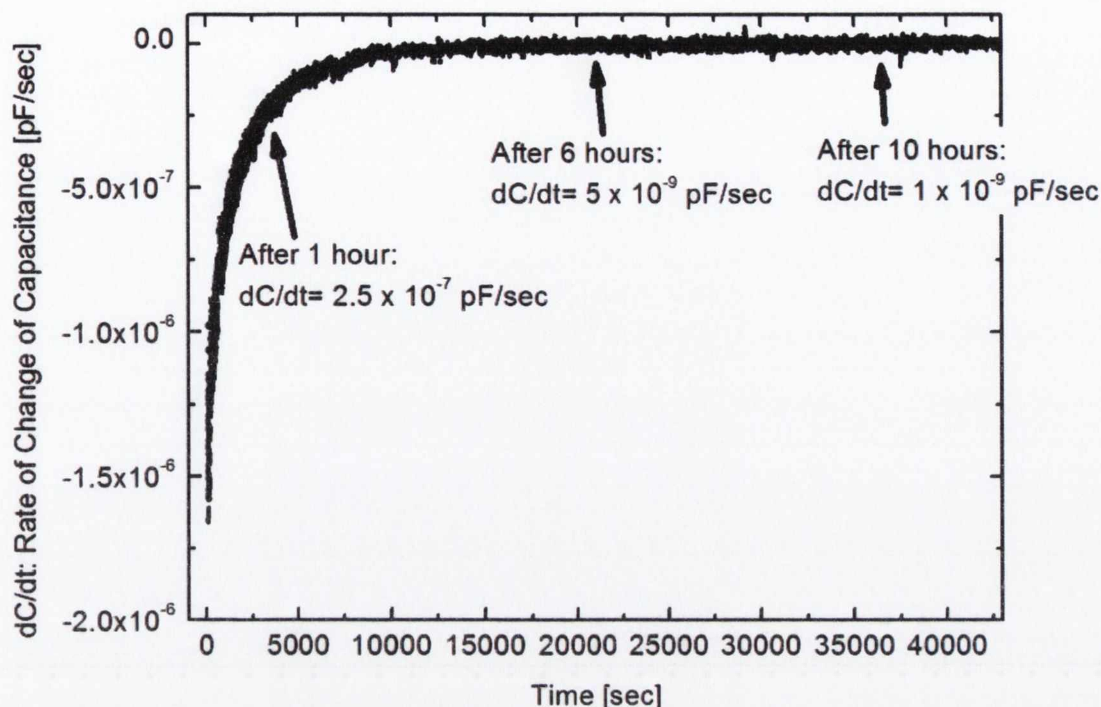

Fig. 6.26: Graph representing the rate of change of capacitance with time (dC/dT) at different stages following a typical flash procedure. Time t= 0 sec represents the time (directly after the flash) at which capacitance measurements were initiated.

6.4. Accurate Determination of the Axial Lengths: L_0, L & L'

One of the largest sources of error in quantifying surface stress changes due to reaction processes lies with the accurate determination of L_0, L and L' (see Section 6.1.4). In order to correctly apply Stoney's equation it is assumed that these quantities are known and have no variance over the surface area of the cantilever sample. In reality however this is very difficult to achieve, as the boundaries of the reaction zone deviate slightly from their desired locations as a consequence of the initial flash procedure. Typically, a reasonable estimate of L_0, L and L' can be attained via our STM capability (and by observing the temperature gradient across the sample surface during flashing). However, the accurate determination of these values is hindered due to scan range limitations of the STM assembly (see Appendix A). To this end AFM can be applied. Even on exposure of the cantilever sample to atmospheric conditions, clear evidence of

the heated region remains when viewed using this microscopic technique; see Fig. 6.27. This approach allows us to survey the entire heated region and accurately quantify L_0, L and L'. Typically, L_0 = 10 mm ±1 mm, L = 10 mm ±1 mm and L' =25 mm ±1 mm.

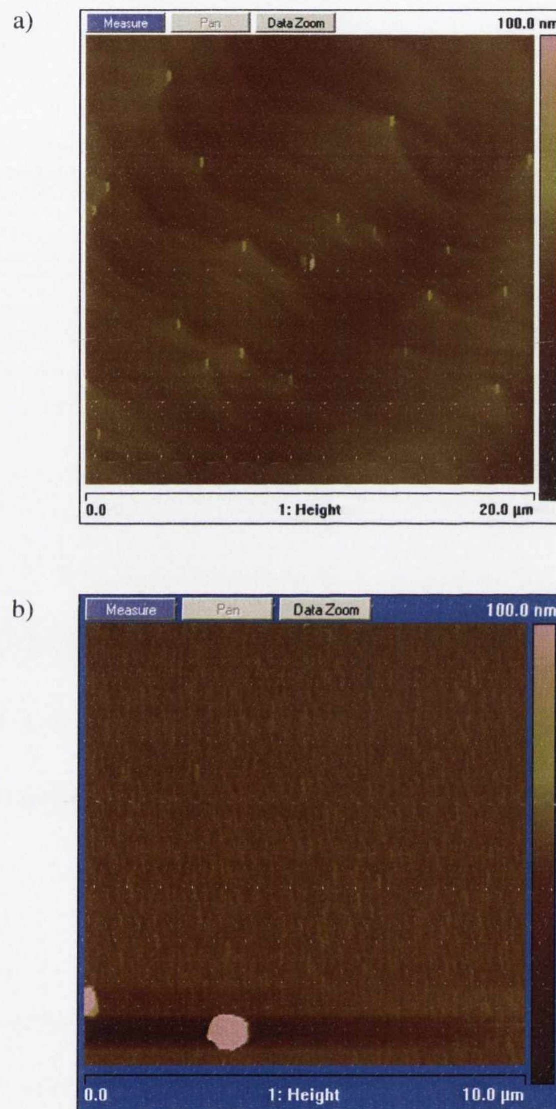

Fig. 6.27: a) AFM image displaying a section of the heated region on the cantilever sample after it was removed from the UHV chamber. Evidence of Si(111)-7x7 step structures are clearly visible; b) The boundary of the heated region is signified with a smooth covering of native oxide.

6.5. Investigations to Date

To date we have carried room temperature exposure of clean Si(111)-7x7 surfaces to various reactive species at room temperature. In each case, structural and stress evolutions were measured using our newly developed set-up (Fig. 6.27). As a result we found that:

- Different reactive species result in different surface stress evolutions (excellent sensor)
- Each stress evolution is rich in detail and specific to the atomic scale processes that occur
- STM is an indispensable tool in helping to deduce the atomic scale structural origins of the measured surface stress signatures

Our current focus is on the room temperature oxidation of the Si(111)-7x7 surface. The results obtained are discussed at length in chapter 7. (Room temperature exposures to bromine and atomic hydrogen were also performed).

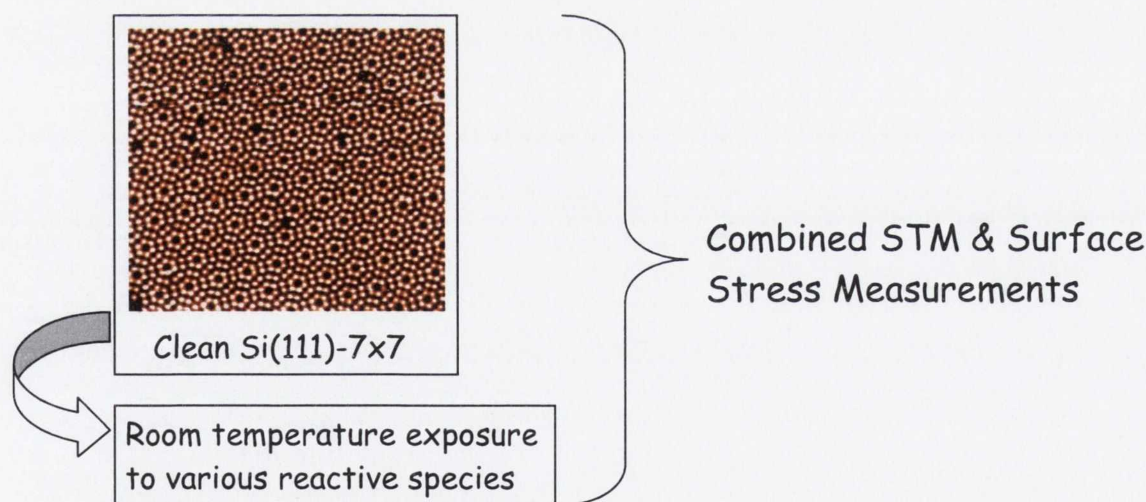

Fig. 6.28: We have exposed clean 7x7 surfaces to various reactive species at room temperature and performed combined STM and stress measurements using our novel system. This combined system provides us with structural, dynamical and interactional information and is proving to be extremely useful in understanding and controlling reaction processes on surfaces.

References:

[1] T. Narushima, N. T. Kinahan, and J. J. Boland, Review of Scientific Instruments **78**, 053903 (2007).

[2] T. Narushima, N. T. Kinahan, and J. J. Boland, Review of Scientific Instruments **76**, 095113 (2005).

[3] H. Ibach, Surface Science Reports **29**, 195 (1997).

[4] C. F. Herrmann, D. Chen, and J. J. Boland, Physical Review Letters **89**, 096102 (2002).

[5] M. Fouchier, and J. J. Boland, Physical Review B **57**, 8997 (1998).

[6] J. T. Yates, *Experimental Innovations in Surface Science: A Guide to Practical Laboratory Methods and Instruments* (Springer, Newark, 1997).

[7] A. Kurokawa *et al.*, Japanese Journal of Applied Physics **43**, 281 (2004).

[8] T. Narushima *et al.*, Applied Surface Science **159-160**, 25 (2000).

[9] T. Narushima *et al.*, Applied Physics Letters **79**, 605 (2001).

[10] T. Fukuma *et al.*, Review of Scientific Instruments **76**, 053704 (2005).

[11] M. Helm *et al.*, Applied Physics Letters **87**, 064101 (2005).

[12] C. E. Bach *et al.*, Physical Review Letters **78**, 4225 (1997).

[13] H. Ibach *et al.*, Surface Science **375**, 107 (1997).

[14] D. Sander, and H. Ibach, Physical Review B **43**, 4263 (1991).

[15] T. R. Albrecht *et al.*, Journal of Applied Physics **69**, 668 (1991).

[16] J. F. O'Hanlon, *A Users Guide to Vacuum Technology* (Wiley & Sons, Hoboken, New Jersey, 2003).

[17] *Omicron Nanotechnology GmbH, Limburger Str. 75, 65232 Taunusstein, Germany.*

[18] R. Desikan, I. Lee, and T. Thundat, Ultramicroscopy **106**, 795.

[19] M. Godin *et al.*, Langmuir **20**, 7090 (2004).

[20] P. Zahl, P. Kury, and M. Horn von Hoegen, Applied Physics A: Materials Science & Processing **69**, 481 (1999).

[21] G. G. Stoney, Proceedings of the Royal Society of London, Series A **82**, 172 (1909).

[22] R. W. Hoffman, *"Mechanical Properties of Nonmetallic Thin Films" in Physics of Nonmetallic Thin Films by S. Dupuy & A.A. Cachard* (Plenum Press, New York, 1976).

[23] *Model AH 2550A, Andeen-Hagerling, Inc., 31200 Bainbridge Road, Cleveland, Ohio 44139-2231* (www.andeen-hagerling.com/ah2550a.htm)

[24] W. A. Brantley, Journal of Applied Physics **44**, 534 (1973).

[25] www.webelements.com.

[26] *Rika-Nenpyou edited by National Astronomical Observatory of Japan* (Maruzen, Tokyo, 1993).

[27] http://www.mmc.co.jp/nfac/hpm/okegawa/OHP/products/teiboutyou/gijyutsu9.html.

[28] G. K. Wertheim, Physical Review **110**, 1272 (1958).

[29] D. E. Hill, Physical Review **114**, 1414 (1959).

[30] http://en.wikipedia.org/wiki/Thermionic emission.

[31] P. A. Redhead, J. P. Hobson, and E. V. Kornelsen, *The Physical Basis of Ultrahign Vacuum* (American Institute of Physics, New York, 1993).

[32] I. Langmuir, Physical Review **22**, 357 (1923).

[33] R. G. Murray, and R. J. Collier, Review of Scientific Instruments **48**, 870 (1977).

[34] I. Langmuir, Journal of the Franklin Institute **217**, 543 (1934).

[35] R. O. Jenkins, and W. G. Trodden, British Journal of Applied Physics **10**, 10 (1959).

[36] W. H. Kohl, *Handbook of Materials and Techniques for Vacuum Devices* (American Institute of Physics, New York, 1995).

[37] K. H. Kingdon, and I. Langmuir, Physical Review **22**, 148 (1923).

[38] M. R. Andrews, Physical Review **33**, 454 (1929).

[39] S. Dushman, Reviews of Modern Physics **3**, 190 (1931).

[40] http://www.corning.com/docs/specialtymaterials/pisheets/Macor.pdf.

[41] http://en.wikipedia.org/wiki/Macor.

[42] *Model GVH398 (modified), Thermo-RIKOH, Thermo RIKO Co., Ltd., Tokyo, Japan* (http://www.kagaku.com/thermo/index_e.html).

[43] http://www.lightsearch.com/resources/lightguides/lightloss.html.

[44] http://en.wikipedia.org/wiki/Absorption_(electromagnetic_radiation).

[45] M. Fox, *Optical Properties of Solids* (Oxford University Press, Oxford, United Kingdom, 2001).

[46] E. H. Sin, C. K. Ong, and H. S. Tan, Physica Status Solidi (a) **85**, 199 (1984).

[47] V. G. Lifshits, *Surface Phases on Silicon: Preparation, Structures & Properties* (John Wiley & Sons Ltd., Chichester [England], 1994).

[48] http://www.virginiasemi.com/pdf/Optical%20Properties%20of%20Silicon71502.pdf.

[49] G. Binnig, C. F. Quate, and C. Gerber, Physical Review Letters **56**, 930 (1986).

Chapter 7

Unit Selective Oxidation of the Si(111)-7x7 Surface & the Influence of Artificially Applied Stress

The reaction of oxygen with silicon surfaces is of great fundamental and technological interest. For many years, extensive experimental and theoretical work addressed this important process [1-6]. These effects have been largely motivated by the necessity to grow high quality oxide layers for the microelectronics industry [7-9]. Understanding this reaction process becomes increasingly important as device dimensions are reduced [10, 11]. As a consequence of device miniaturisation, silicon oxide layers have to be scaled down to thicknesses of only a few atomic layers [6]. The initial oxidation of silicon surfaces has been investigated thoroughly to gain an atomic-scale understanding of the oxide formation process [6]. Despite this effort, fundamental questions still remain concerning the actual atomic structure, the electronic properties and the step-by-step kinetics of the initial oxidation stages [1-6]. It has been proposed that surface stress measurements may prove useful in elucidating these and related issues [12-15]. To this end we have employed our newly developed system combining both surface stress measurement and Scanning Tunnelling Microscopy (STM) capabilities [16, 17]. The former measurement is based on the displacement of a large cantilever sample during the reaction process, while the latter permits direct observation of the atomic structure on the same cantilever. One may expect a large adsorbate-induced surface stress from the insertion of oxygen atoms into the Si-Si bonds which is the prevailing adsorption mechanism [1-6, 12]. In this chapter, we present results of a combined study of the room temperature oxidation of the Si(111)-7x7 surface. We show that the initial oxidation involves two compressive stress stages with different growth signatures. The atomic scale origins of the measured surface stress evolution will be discussed and supported via complementary STM data. In particular, we demonstrate that the initial rapid rise in compressive stress is associated with selective oxidation of the faulted-half units of the 7x7 reconstruction [18]. Preliminary results relating to the effects of an artificially applied stress as a means to alter the unit selectivity during the oxidation

process will also be presented and discussed. This study is a collaborative venture with Prof. Kazushi Miki, a distinguished member of the National Institute for Material Science (NIMS), Tsukuba, Japan, who performed early STM and X-ray Photoemission Spectroscopy (XPS) experiments. These studies prompted us to investigate this interesting process using our combined stress-STM system.

7.1. Introduction to the Initial Oxidation of the Si(111)-7x7 Surface

The reaction of molecular oxygen with the Si(111)-7x7 surface is rather complex and non-uniform and the exact mechanism is still not fully understood [1, 5, 6]. Although a great deal of effort was devoted to the atomic-level understanding of the reaction process, it is still under debate whether the initial adsorbed state of oxygen is molecular or dissociative [1-6, 19]. Frequently, adsorption induced chemical and geometrical complexity has greatly hindered experimental and theoretical identification of the oxidation products [20]. Thus, many structural and spectroscopic issues still remain unresolved [20]. Such difficulties may arise due to the influence of reaction induced surface strain [13, 15].

The Si(111)-7x7 surface has three kinds of reactive adsorption sites, consisting of adatom, restatom, and corner hole sites [19]. The adatom site was found to be the most reactive towards O_2 molecules; the Ultraviolet Photoelectron Spectroscopy (UPS) peak corresponding to the adatom dangling-bond state is readily quenched and the oxygen-induced changes in STM images occur primarily at the adatom site [2, 21-25]. In the case of oxidation on Si(111)-7×7 surfaces by means of molecular oxygen, recent High Resolution Electron Energy Loss Spectroscopy (HREELS) and STM experiments have shown that spontaneous dissociation of the oxygen molecule occurs at the surface adatoms even at 82 K [6, 26, 27]. This result is consistent with Density Functional Theory (DFT) calculations which found that the molecular state is unstable on Si(111)-7x7; an oxygen molecule spontaneously dissociates without any activation barrier [20, 21]. At 82 K, one of the dissociated oxygen atoms forms a bond with the surface dangling bond of the adatom structure, while the other atom is inserted into the adatom backbond [6, 26, 27]. This chemical configuration is referred to as an 'ad-ins'

structure. In turn, this feature can be transformed into an 'insx2' structure by annealing over 200 K [6, 20]. In this case both dissociated atoms are inserted into adatom backbonds (the on-top O atom migrates into an adjacent backbond by thermal activation) and the dangling bond is re-generated. This transformation can also be induced at 82 K via atomic manipulation using an STM tip [26]. Since 'ad' oxygen atoms result in weaker bonding than 'ins' oxygen atoms, the 'ad-ins' state turns out to be less stable than that of the 'insx2' state by 1.3 eV, and there exists a low-barrier (~0.15 eV) transformation pathway to the stable 'insx2' configuration; i.e. the 'ad-ins' configuration is metastable [20]. Therefore, following recent theoretical and experimental studies, it is now the general consensus that the initial oxidation product on Si(111)-7x7 is the 'ad-ins' structure at approx. 80 K which converts into the stable 'insx2' structure at higher temperatures (> 200 K) [6]. With the addition of another oxygen molecule to either of the above mentioned configurations, an 'ad-ins×3' structure results [6, 21, 28-31]. Here oxygen atoms are arranged in a tetrahedral arrangement forming a SiO_4 structure. Each of the aforementioned configurations are displayed in Fig. 7.1. The resulting atomic-oxygen products can explain quantitatively the "molecular" interpreted features reported in previous experimental studies [1-6, 20, 21]. This is the most recent reliable scenario regarding the initial oxidation of the surface adatoms.

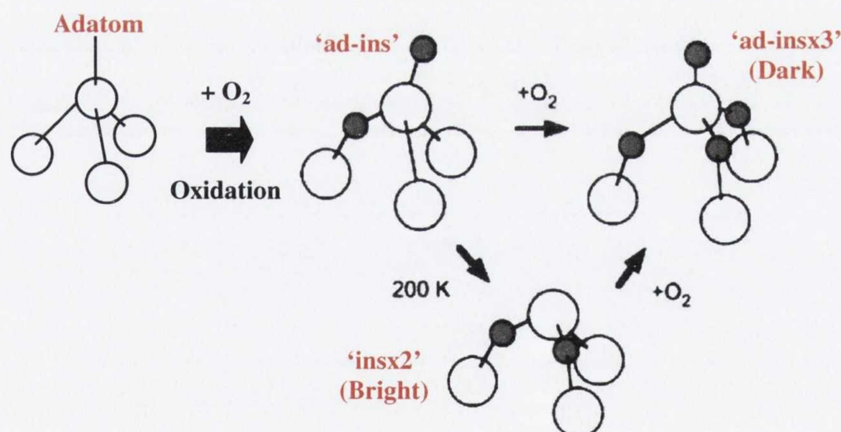

Fig. 7.1: Schematic model of the oxidation reaction on Si(111)-7x7. The open and gray circles indicate the Si and O atoms, respectively. The initial product at 82 K is of the 'ad-ins' feature which transforms to the 'insx2' structure at 200 K. It has been proposed that the successive reaction with further O_2 produces the 'ad-insx3' structure. It should also be noted that the ad-ins structure can be transformed into an 'insx2' arrangement via manipulation using the STM tip at 82 K [6, 26, 27].

The backbond reactions break the threefold symmetry of the surface adatoms. During the initial oxidation stage (i.e. >0.1-0.2 L oxygen exposure) structural inhomogeneities are induced [32]. This makes it difficult to interpret further oxidation steps via numerous structural, spectroscopic, and theoretical methods [1]. As a result the majority of studies to date regarding the initial oxidation of Si(111)-7x7 have focused only on adatom reactions [1-5]. In order to understand subsequent phases of the oxidation process, influences from other constituent structures such as stacking faults, dimer strings and other dangling bonds at restatoms and corner holes need to be considered. The structural inhomogeneity observed during the oxidation process may be explained by atomic scale mechanical strain resulting from successive oxygen insertions into the complex Si(111)-7×7 surface structures. The strain introduces structural non-uniformity, modifies the surface properties and may in turn influence subsequent reactions. Therefore, it is also very important to examine the detailed evolution of strain during the reaction. The resultant strain if detected with sufficient resolution and accuracy can indirectly capture information regarding changes in local chemical and geometrical configurations. This is possible since such changes introduce a certain amount of distortion due to the surrounding surface elasticity. Hence, combining strain measurements with structural observations will prove helpful in studying and interpreting all stages of the initial oxidation process. The aim of this work is to shed light on the intrinsic oxidised structures and resulting strain effects during the initial oxidation of Si(111)-7×7 surfaces at room temperature through a complementary study comprising of STM and surface stress measurements.

7.2. Unit Selective Oxidation: Experimental Results & Discussion

Oxidation experiments were carried out using two separate STM systems. One is a variable temperature (VT) ultrahigh vacuum (UHV) STM which is used for detailed structural observation (in Japan) [33]. The other is our modified STM which permits simultaneous surface stress measurements [16]. For this purpose, a room temperature UHV STM is used as a basic model; see chapter 6 for details.

A series of empty-state STM images of the Si(111)-7×7 surface structures oxidised at room temperature as a function of oxygen exposure are shown in Fig. 7.2. These measurements were conducted by our Japanese colleagues using the conventional VT STM [33]. The exposures depicted in Fig. 7.2 (a)-(f) represent $n \times 0.045$ L exposures, where $n = 1, 2, \ldots, 6$ respectively and 1 L= 1.0x10^{-6} Torr.sec. Each exposure involved the introduction of oxygen gas to a pressure of 7.5x10^{-10} Torr for 60 seconds. The images were observed at the same position. The STM tip was retracted to a spacing of 150 nm from the sample surface at each oxygen exposure to avoid shadowing effects from the STM tip. During the initial stage of oxygen exposure, three kinds of adatom features exist, namely, normal ('NF'), bright ('BF') and dark ('DF') adatom features. These features are represented by (yellow and orange), (aqua and blue) and green arrows, respectively in Fig. 7.2 (a). These features are transformed into two distinct states following an additional 0.045 L exposure as displayed in Fig. 7.2 (b). Let's firstly look at the transformation of bright adatom features, 'BF'. These features can be basically assigned to 'insx2' configurations, because 'ad-ins' structures are not achievable at room temperature as previously mentioned [20, 21, 26]. As a result, additional oxygen insertion may form 'ad-ins×3' arrangements thus forming dark adatom features, 'DF' [20, 21, 26]. By following this simple scenario, it is possible to explain the path of the yellow, orange and aqua arrows in Fig. 7.2 (a) to (b), applying the transitions 'NF'→'ad-ins×3', 'NF'→'insx2' and 'insx2'→'ad-ins×3', respectively. To explain the additional transformations of green and blue features, it is necessary to consider the transitions, 'ad-ins×3'→'NF' and 'insx2'→'NF', respectively. However, these transitions should not be physically achievable at room temperature, because they indicate an oxide reduction reaction. It is therefore necessary to discuss reactions with other dangling bonds at restatom and corner hole sites, in addition to strain effects induced by the oxidation process. In fact, interesting hopping of adatoms can also be occasionally seen as indicated by the pink arrows in Fig. 7.2, while Fig. 7.3 provides a clearer view of this interesting room temperature process. Progressing through images (a)-(d) in Fig. 7.3, it is evident that one of the adatoms in a faulted-half unit hopped into an inter-adatom position between original adatom sites. This position may be achievable by switching backbonds of the adatom with restatom dangling bonds. However, as adatoms are strongly bound

with three covalent bonds to the rest layer, thermal bond breakage and migration should not occur at room temperature. Therefore, this hopping may be spontaneously caused by accumulated mechanical strain due to the oxidation process. Following this it returned to the original adatom position and finally vanished. In general, for such discussions, assistance is required from other spectroscopic techniques such as HREELS, Fourier Transform Infrared Spectroscopy (FT-IR) and XPS. However, these highly sensitive techniques are not suitable for disordered systems under large strain fields.

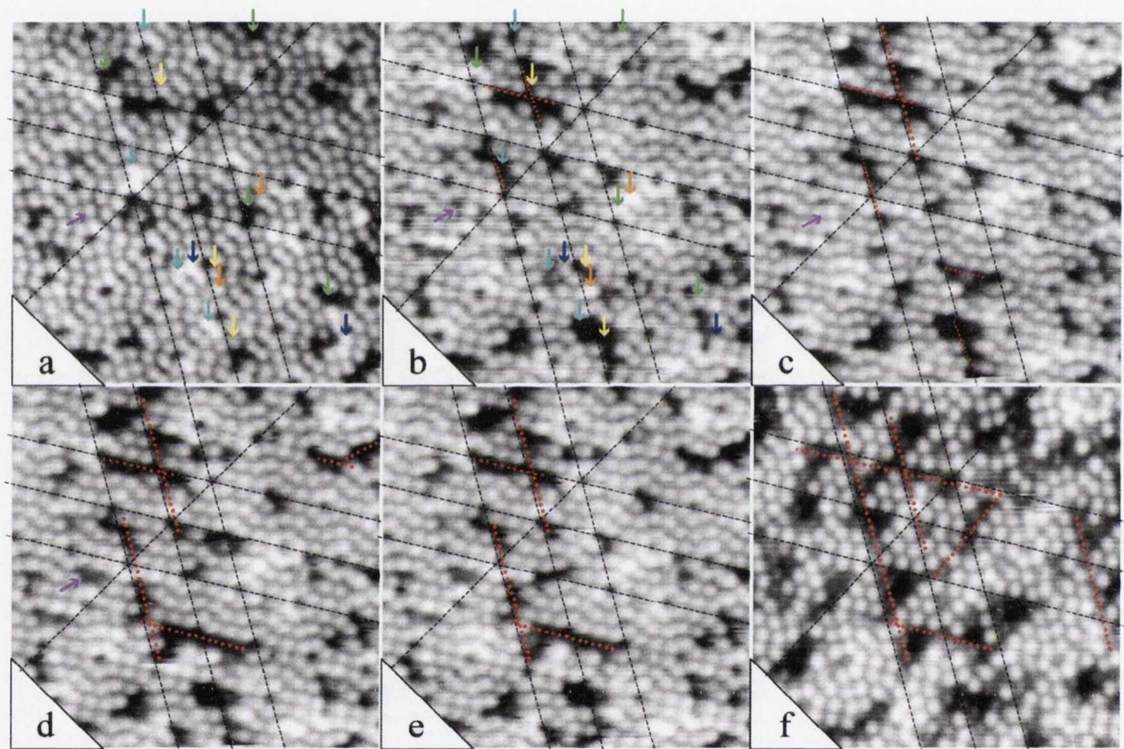

Fig. 7.2: Sequential STM images of Si(111)-7×7 surface structures oxidized at room temperature and observed using the VT-UHV-STM. All images were taken at V_{sample} = +1.0 V and cover a 20×20 nm^2 area. The oxygen exposures are (a) 0.045 L, (b) 0.09 L, (c) 0.135 L, (d) 0.18 L, (e) 0.225 L and (f) 0.27 L, respectively. Each colour corresponds to different adatom features. Normal adatom features ('NF') are indicated with yellow and orange arrows in (a), which transform into dark ('DF') and bright ('BF') features in (b), respectively. Similarly, 'BF' (aqua and blue) are transformed into 'DF' and 'NF', while 'DF' (green) are changed into 'NF' and 'BF'. Pink arrows indicate room temperature adatom migration. Red dashed lines are a visual guide to display chain propagation of 'DF' [18, 33].

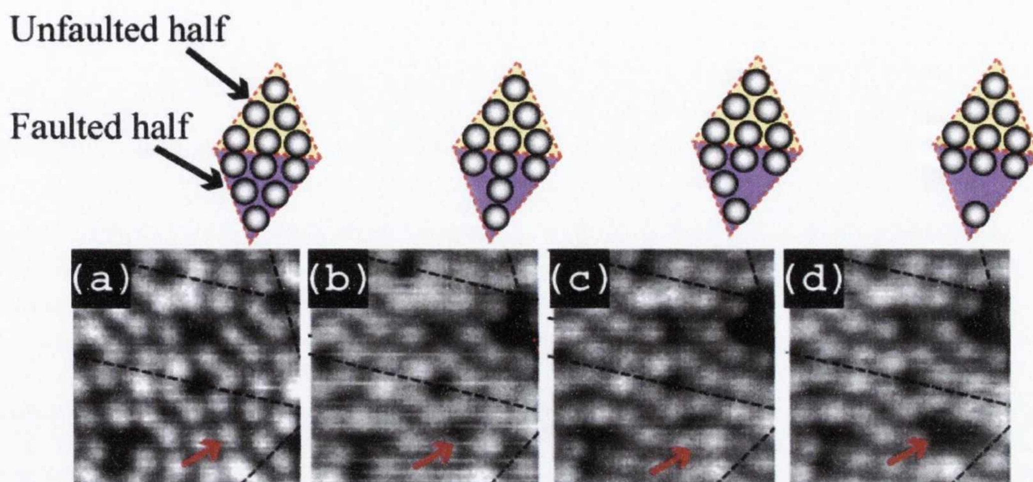

Fig. 7.3: This figure shows movement of a surface adatom. Images (a)-(d) were observed after oxygen exposures of 0.045, 0.09, 0.135 and 0.18 L, respectively. The red arrow indicates the position of the moving adatom. The dashed lines were drawn along the edge of the unfaulted-half units as a visual guide to observe the transition [18, 33].

As the oxidation process proceeds, the number of dark adatom features increases. During initial oxygen adsorption, the site selectivity of the reaction was reported to be (0.27:0.07:0.53:0.13) at 298 K [2] and (0.04:0.16: 0.55:0.25) at 5 K [27] for the unfaulted corner (A), unfaulted center (B), faulted corner (C) and faulted center (D) adatom sites, respectively. This selectivity was determined by counting the number of reacted adatoms from a 20×20 (=400) nm^2 image. Our Japanese colleagues conducted similar counting experiments by use of 120 unit cells which contains 1440 adatoms and has an area of 757.6 nm^2 [18, 33]. This estimation is therefore more statistically accurate. Consequently, a site selectivity of (0.23:0.19:0.27:0.31) at 1.8% coverage (26 reacted adatoms) and (0.15:0.13:0.33:0.39) at 9.9% coverage (142 reacted adatoms) was obtained. In contrast to previous reports, no reaction preference exists between corner and center adatom sites, although approx. a 3:1 reaction preference between faulted and unfaulted regions still remains. Following further oxidation, this trend was almost similar (see Fig. 7.4). This implies that the stacking condition of the 7x7 surface is a key factor for the site selectivity observed during the oxidation process. Furthermore, similar investigations were also conducted using ozone which had a purity of 93 % [18, 33]. In this case approx. 700 unit cells were examined. As a result, a suppression of the reaction selectivity between units

was observed (approx. 2:1) across all oxidation regimes. This may be due to the presence of reactive atomic oxygen species derived from ozone molecules [34]. Hence, spontaneous dissociation of molecular oxygen at the surface may be an influential step in establishing the reaction selectivity between units.

On average, transitions to dark adatom features dominate the initial oxidation process [24, 32, 35]. Chain propagations of dark features are clearly visible as indicated by the red dashed lines in Fig. 7.2. This may result due to the modification of local bonding configurations and charge densities caused by insertion of oxygen at nearby sites. This modification introduces strain around reacted sites. The strain can weaken the local structural stability and thus promote reactions at neighboring sites. In fact a similar nucleation effect was reported by *Leibsle et. al* [36] and *Tokomoto et al.* [35]. Finally, at a surface coverage of approx. 0.5 monolayer (ML), a significant feature was observed as shown in Fig. 7.5 [18, 33]. This feature consists of many triangular structures which are comprised of unfaulted units. These structures are realised by complete reaction of the faulted-half regions. This strongly suggests that the faulted-half unit is far more reactive than its unfaulted counterpart. Since there is no stacking fault, the unfaulted unit has a less strained structure [37, 38] and is therefore potentially more resistant to chemical attack. It should also be noted that electronic structural differences between both units may also play an important role [2, 39, 40].

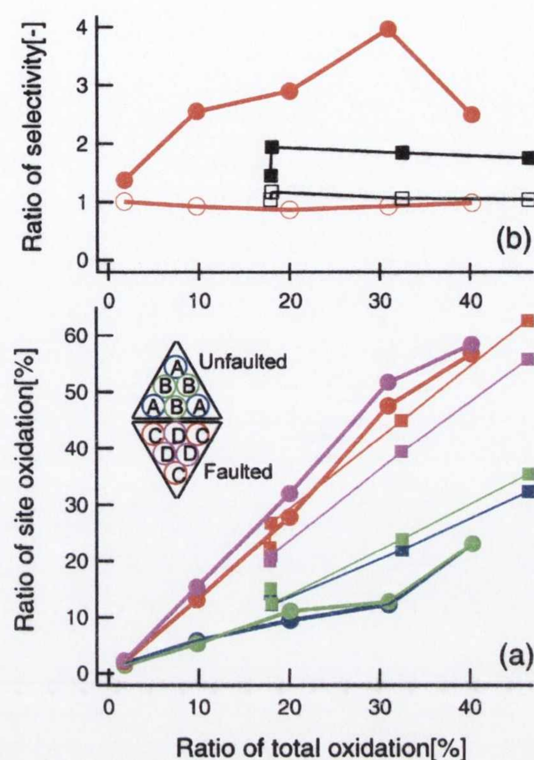

Fig. 7.4: The oxidation ratio at each reacted adatom site (a) and the reaction selectivity between units and between corner and center adatoms (b) as a function of the total oxidation ratio. The results for molecular oxygen (O_2) and ozone (O_3) are indicated with circles and squares, respectively. In (a), each reacted adatom site of the unfaulted corner (A), unfaulted center (B), faulted corner (C) and faulted center (D) adatom sites are shown in blue, green, red and pink, respectively. In (b), closed and open markers represent the ratio of selectivity between units and that between corner and centre adatoms, respectively [18, 33].

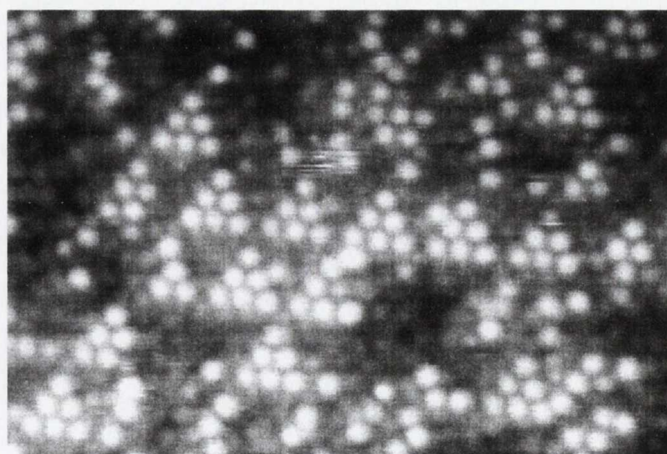

Fig. 7.5: Unit selective oxidation of the Si(111)-7×7 surface. This image was observed with V_{sample}= +1.0 V. Most unreacted adatoms occur at unfaulted units. The unfaulted units were identified by observing filled state images of the clean Si(111)-7x7 surface [18, 33].

In order to directly examine strain as a result of the initial oxidation process, we also performed combined STM and stress measurements on a cantilever sample using our newly developed system [16, 17]; a brief reminder of the unique configuration is provided in Fig. 7.6 below.

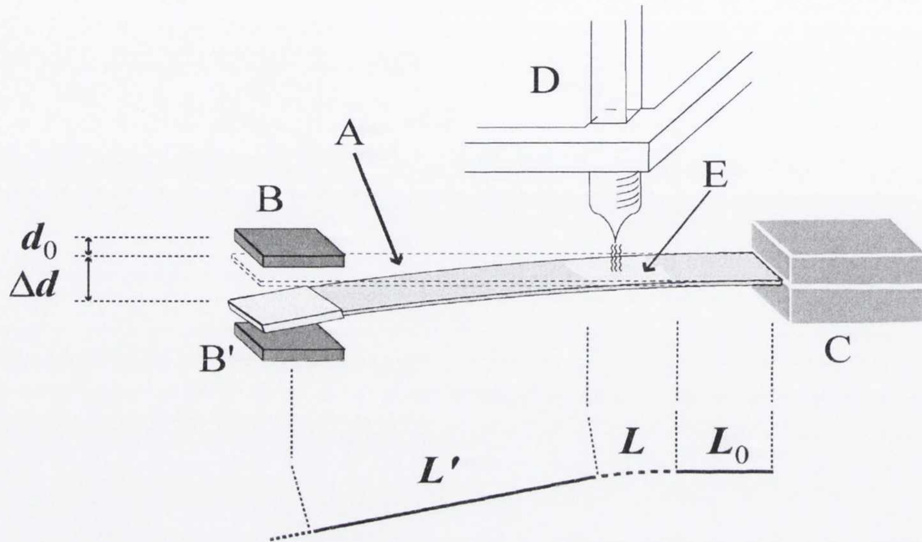

Fig. 7.6: Our experimental set-up for surface stress measurement and structural observation via STM. The detection component for sample bending consists of a cantilever sample with typical dimensions 50×10×(0.280-0.525) mm^3 (A), a reference electrode at the front side (B) (back side (B')) and a quartz clamping base (C). The rectangular shaped sample is cleaved from a one-side mirror polished Si(111) wafer. This measure ensures that atomic scale processes on the polished surface are the dominant contributors to sample bending. Having a rough surface on the back side of the cantilever sample minimises parasitic bending effects due to reaction processes on this surface, since stress cannot accumulate as effectively over a rough area. Therefore, we are only interested in events on the polished side where stress accumulates and atomic structure can be investigated via STM. The component for structural observation consists of part (A) and an STM (D) which observes the effective modification region (E). This region, with axial length, L, is located between the fixed end region (length, L_0), and the free end region (length, L'). Therefore, all deflections are originated at region E only. In our system, the values of L_0, L and L' are 10, 10 and 25 mm, respectively. Note that the L' length terminates at the centre of the reference electrode. Although capacitance measurements between one reference electrode and the sample are basically sufficient, the additional reference electrode guaranteed secure displacement monitoring. To avoid involving a parasitic capacitance change, an electrical by-pass is present when using high resistance semiconducting samples. It consists of a flexible metallic wire (not shown here) that is connected to a 10x10 mm^2 Ta sleeve (0.025 mm thick) which tightly encapsulates the free-end. This by-pass is not necessary when low resistance samples are used.

Let us firstly examine the capacitance evolution during oxygen exposure to a 280 μm thick cantilever sample which was *n*-type phosphorus doped with a resistivity of 800-1200 Ω.cm. Due to the resistive nature of the cantilever sample it was imperative to have a by-pass unit present at the free end to avoid measurement of a parasitic capacitance effect (see Appendix B). A clean Si(111)-7×7 surface was created at a 10×10 mm^2 area only, which is indicated as the effective modification region, E, in Fig. 7.6. To achieve this result a novel technique which we developed was used, namely, regionalized direct current heating using bimetallic strips [17]. The base pressure of our UHV system was $<6.0\times10^{-11}$ Torr. Oxygen exposures were achieved by backfilling the UHV chamber with a fixed pressure of oxygen. The oxygen pressure was measured using a cold cathode ion gauge [41] or by observing the ion current of the preparation-side ion pump on the system. While some studies have reported an influence of hot filaments on the oxidation process others have shown a negligible effect [10, 11]. For safety we leave all our hot filaments off during all oxidation processes. In addition, only the preparation-side ion pump was operated during oxygen introductions (while the STM-side equivalent was switched off); this measure was performed to avoid ionisation of oxygen molecules in the vicinity of the sample. Oxidation of the clean 7x7 surface region was performed at room temperature by introducing O_2 gas to a pressure of 6.0×10^{-9} Torr by means of a variable leak valve. Capacitance measurements were performed using the back side reference electrode. The acquired capacitance evolution as a function of oxygen exposure is displayed in Fig. 7.7 [18].

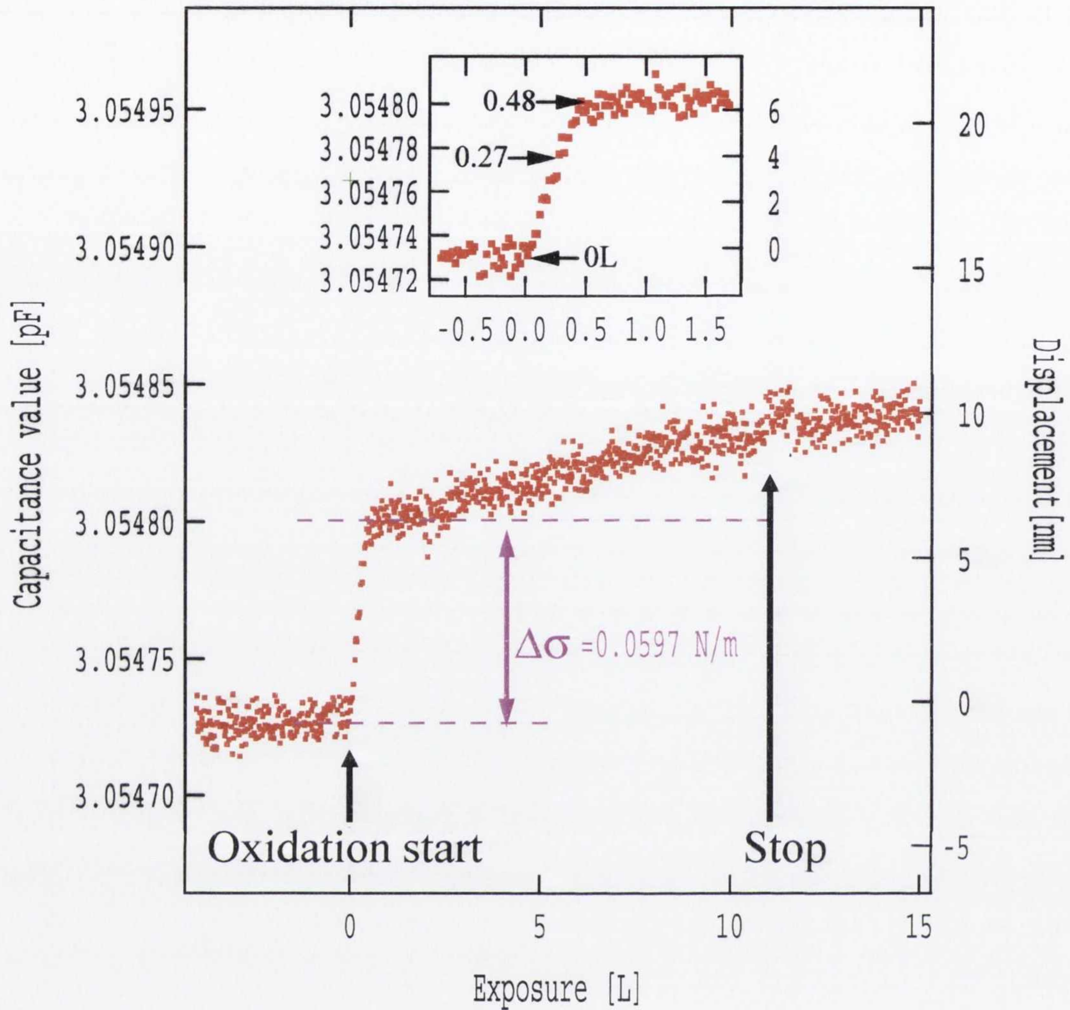

Fig. 7.7: Evolution of capacitance (and displacement) at the free end of the cantilever sample as a function of oxygen exposure (1L= 1.0×10^{-6} Torr.sec). The capacitance values were measured using the back side reference electrode. From these measurements, surface stress values can be estimated. Oxygen gas was introduced to an exposure of 11 L. After terminating the oxidation process the capacitance evolution returned to the thermal drift line, however, this progression was not instantaneous as residual oxygen remains in the chamber for a short period before being completely pumped. Inset displays the initial detailed behaviour up to 1.5 L. Each arrow in the inset indicates oxygen exposures corresponding to the images shown in Fig. 7.8. For this measurement a by-pass unit was employed due to the resistive nature of the cantilever sample used [18]. (Front electrode measurements showed identical compressive stress behaviour).

On commencing oxidation a rapid increase in the capacitance value was observed. This increase in capacitance corresponds to surface expansion, i.e. a compressive surface

stress condition. The growth rate became much less significant at an oxygen exposure of approximately 0.45 L and showed a constant rate thereafter until oxidation was ceased. The rate difference between both stages was huge; approx. 43 times (fast and slow stages had gradients of 0.112 and 0.00259 nm/sec, respectively). Furthermore, from careful examination of the initial behaviour, see inset Fig. 7.7, a purely monotonic increase in capacitance was resolved exhibiting no fine features. The change in surface stress at an exposure of 0.45 L; which represents the boundary between fast and slow stages, was calculated to be 0.0596 N/m. Here, it should be noted that the capacitance evolution may have captured information relating to 'atomic-scale' chemistry, as it displayed a characteristic two stage oxidation process at very low exposure. This result suggests that there are two dominant reaction phases during the initial oxidation of the Si(111)-7x7 surface at room temperature. As the origin of the two stages, a change in reactivity, a saturation of surface dangling bonds and a structural transformation involving volume expansion are possible candidates. But, if this behaviour is simply caused by the saturation of surface dangling bonds, the border between stages should be observed at a 1 ML coverage. However, the oxygen exposure of 0.45 L is too small to result in this surface coverage. Therefore, a richer oxidation mechanism is expected. Nevertheless, the exact origin of this two stage feature cannot be fully explained without observing atomic structure.

In order to investigate this, a series of STM images were recorded on the same cantilever surface and are shown in Fig. 7.8 [18]. (It should be noted that each image was acquired following the generation of a clean Si(111)-7x7 surface and introducing oxygen gas to the desired dosage level). At an oxygen exposure of 0.27 L, reacted adatom sites were clearly visible and triangular features; similar to those shown in Fig. 7.5, started to emerge on the surface. Again these triangular structures resulted from preferential oxidation of the faulted-half units (the location of the faulted portion of the unit cell was confirmed from occupied state images of the clean 7x7 surface). When the oxygen exposure reached 0.48 L (i.e. the onset of the slow stage in the capacitance evolution) the presence of these triangular features was much more pronounced. At this point the vast majority of faulted-half adatoms had reacted, leaving the distinctly less reactive unfaulted-half units. These unfaulted adatoms reacted very gradually as time evolved,

which was determined by additional STM observations on the cantilever at exposures >0.48 L. In fact, experiments conducted using the conventional VT STM revealed that several triangular features can persist up to exposures >10 L [18, 33]. Therefore, it is evident that the triangular structures are formed by selective oxidation of faulted-half units, while the transition between both stages in the capacitance evolution was caused by completion of the faulted-half reaction [18]. The faulted-half adatoms react readily on initial exposure and are represented by the fast stage of the capacitance curve, while the slow stage revealed the gradual oxidation of the less reactive unfaulted-half adatoms. The capacitance evolution was measured up to a maximum exposure of 11 L. Up to this point the vast majority of the faulted-half adatoms had reacted, but the very slow oxygen uptake at the unfaulted-half regions meant that a 1 ML feature was not detected in the capacitance evolution. (We are currently conducting capacitance measurements at higher oxygen exposures to determine when all surface adatoms have reacted). A summary of the correlated structural and stress evolutions is provided in Fig. 7.9.

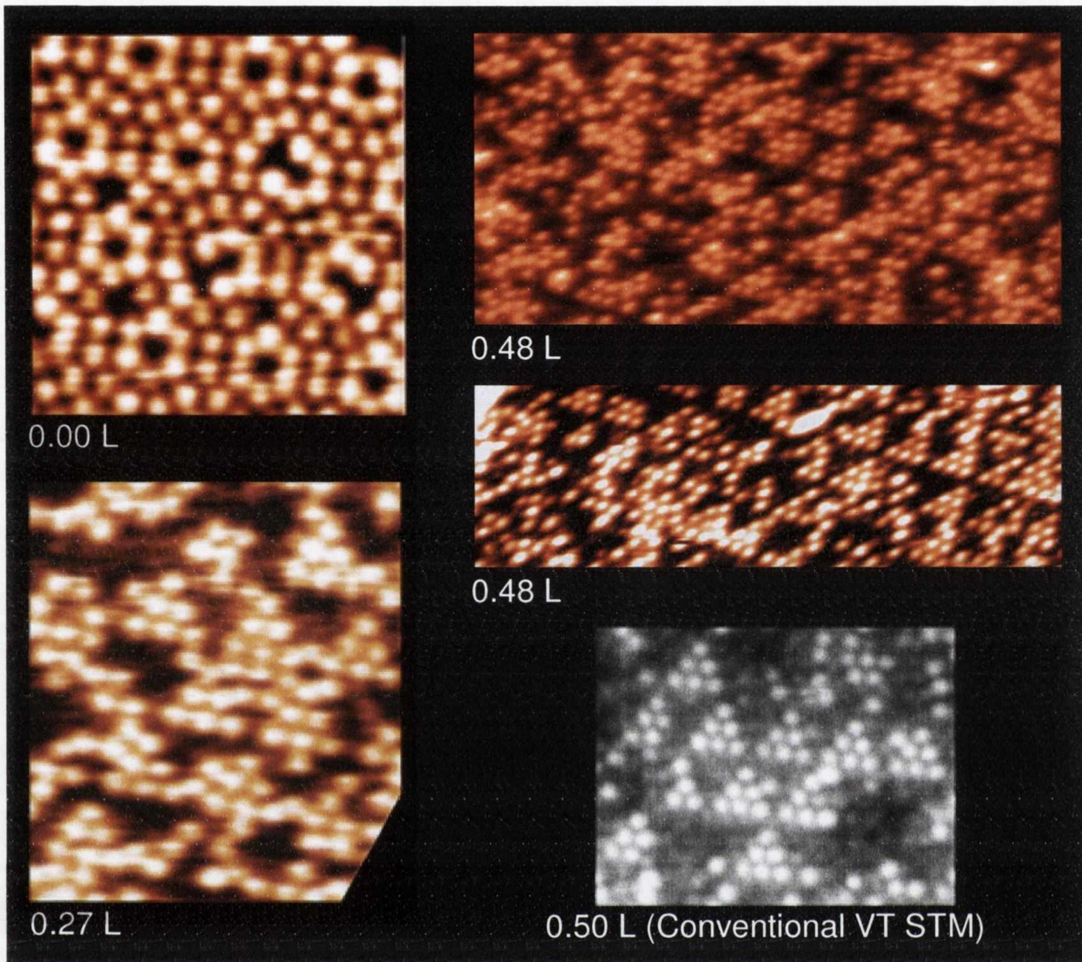

Fig. 7.8: A series of STM images of the Si(111)-7x7 surface as a function of oxygen gas exposure, namely, 0, 0.27, and 0.48L, respectively. All images were observed '*on the cantilever sample*' with sample biases between +0.8 and +1.0 V. Each image corresponds to the condition indicated by the arrow in the inset of Fig. 7.7. As a reference, a typical image observed using the conventional VT STM is also shown [18, 33].

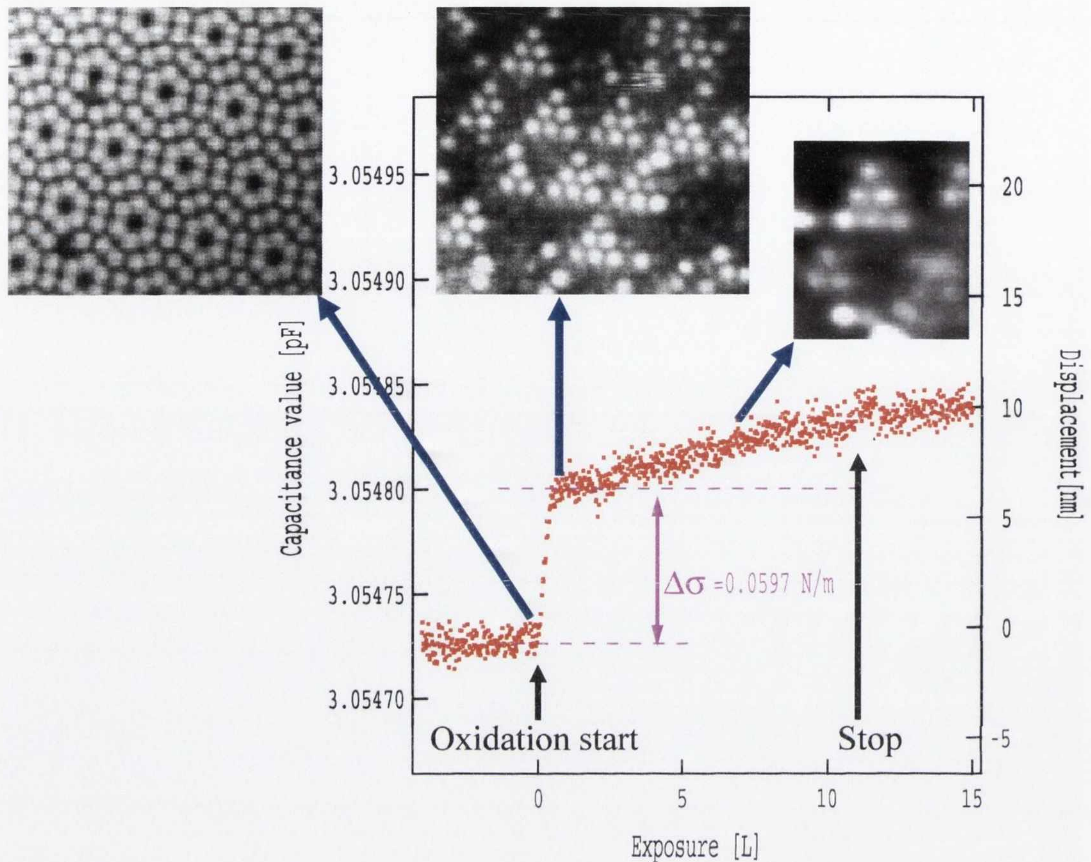

Fig. 7.9: Combined STM and surface stress studies reveal that the initial rapid rise in compressive stress is associated with selective oxidation of the faulted-half units of the 7x7 reconstruction, while the gradual evolution results from the slow oxidation of the chemically resistant unfaulted-half regions [18, 33].

Recently, the capacitance change on oxygen exposure was also investigated for a 280 μm thick low resistance sample (*n*-type phosphorus doped with a resistivity 0.008-0.012 Ω.cm). Using this configuration the by-pass unit was not necessary. In addition, a new heating method was adopted to prepare the initial clean 7x7 surface, namely, localised electron bombardment of the cantilever sample. In order to ensure uniformity of heating during the flash procedure, the width of the cantilever sample was reduced from 10 mm to 6 mm. This adaptation had no serious implications on our STM and surface stress measurement capabilities; see Appendix G. Capacitance measurements were made on oxygen exposure using the back side reference electrode. The resultant capacitance evolutions as a function of time for two different exposure conditions are displayed in Fig. 7.10, and indicated a compressive surface stress condition in each

case [18]. Each evolution displayed the same characteristic two stage feature (with fast and slow stages) that was observed in Fig. 7.7 for the high resistance sample. Furthermore, following the cessation of the oxidation process, both evolutions promptly returned to the thermal drift line.

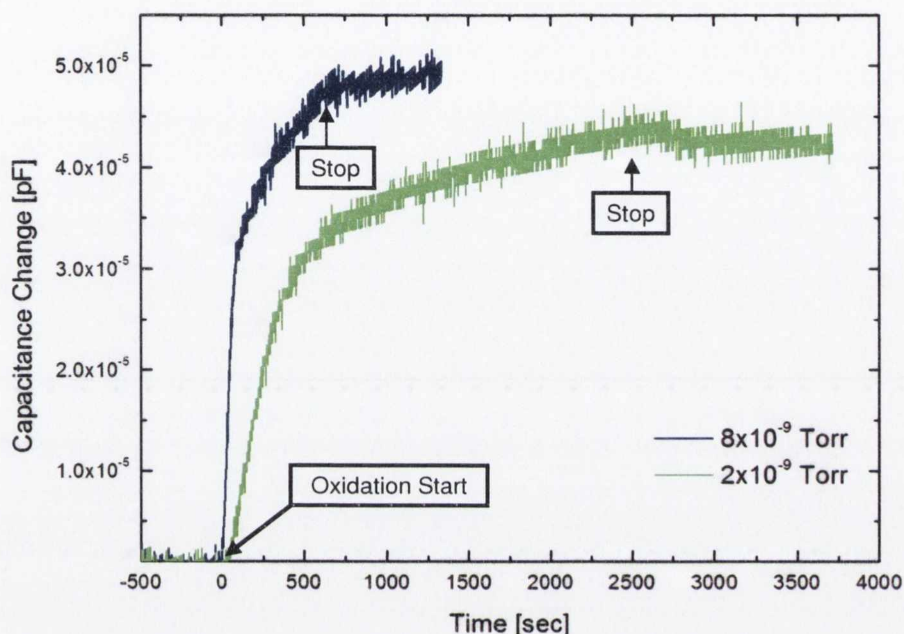

Fig. 7.10: Capacitance evolutions for a low resistance sample (0.008-0.012 Ω.cm) under two different exposure conditions, namely $8x10^{-9}$ Torr and $2x10^{-9}$ Torr. These measurements were taken using the back side reference electrode. Each evolution indicated a compressive surface stress condition, and had two clear detachable periods similar to Fig. 7.7 [18].

As anticipated the transition point between fast and slow stages occurred at different time stamps for the two pressure conditions used, with the turning point occurring earlier for the high pressure exposure. This particular measurement also served as a validation test to ensure that we were detecting a true sample deflection due to atomic scale reaction processes; surface dangling bonds of the faulted-half units should saturate quicker at higher exposure pressures. Interestingly, when the time axis of Fig. 7.10 was converted to Langmuir it was found that both curves aligned almost identically as shown in Fig. 7.11. (It should be noted that the subtle variation between these curves most likely resulted

from slight differences in the sizes of the clean areas produced on flashing using the electron bombardment technique. We are currently in the process of automating this heating process which will help in defining more consistent areas on flashing).

Although Fig. 7.11 strongly resembles the features observed in Fig. 7.7 (for the high resistance sample with accompanying by-pass unit) several differences are evident. Firstly, in Fig. 7.11 it is more difficult to identify the precise transition point between fast and slow stages, as an intermediate regime seems to be present. For the chemical system under investigation, this intermediate regime is intuitively anticipated as the reaction of faulted-half adatoms progresses. We believe that this phase in the capacitance evolution resulted from a slow-down in the reaction rate of the faulted-half adatoms due to: a) a decrease in the number of available sites in these reactive half units; and b) strain induced steric hindrance effects inhibiting subsequent reaction processes; such occurrences are supported by numerous experimental studies [10, 42-47]. Furthermore, adsorbed oxygen atoms have been shown previously to be electron withdrawing [10, 48]. Consequently, a partial negative charge density accumulates in the near-surface region of the faulted-half regions where the oxygen-silicon bonds are formed [10]. As oxidation proceeds, electrostatic repulsion between these oxygen adatoms may cause the activation barrier for oxygen chemisorption to increase as a function of oxygen coverage at the faulted regions. The slow down in the reaction rate of the faulted units was verified by our STM observations on the same cantilever sample, and we are confident that the intermediate regime in the capacitance evolution represents this period in the oxidation process, owing to the abovementioned processes. We believe that Fig. 7.7 did not visibly detect this intermediate phase due to an inferior capacitance resolution at that time. From the data presented in Fig. 7.11, as well as accompanying STM information, we determined that the vast majority of the faulted-half adatoms reacted following an oxygen exposure of approx. 0.5-0.6 L, thus forming the characteristic triangular features. Again comparing Fig. 7.7 and Fig. 7.11 it is evident that larger cantilever deflections; and therefore estimated surface stress values, were obtained on oxidation of the low resistance sample. We believe that this disparity is a result of the different heating methods employed in preparing the initial clean surface in each case. The bimetallic heating method produced a 7x7 surface with a greater presence of carbide contamination and a greater density of

steps (resulting in smaller terrace widths) when compared with the clean surface formed by the electron bombardment technique. Therefore, stress does not accumulate as effectively over this area during the oxidation process, and as a result smaller deflections can be expected. In addition, the likely introduction of surface dislocations due to slight pushing of the cantilever sample during bimetallic heating is not ideal. This occurrence is not conducive to stress propagation as these defects act as relaxation sites for accumulated stress. Another likely factor contributing to the observed differences in cantilever deflections relates to slight variations in the area of the clean region produced by both flashing techniques; in general, the larger the clean area produced, the larger the free end deflection on reaction. In Fig. 7.7 the onset of the slow stage in the capacitance evolution occurred at a lower oxygen exposure when compared with that of Fig. 7.11. Yet again we associate this occurrence with the heating method used. During heating by way of the bimetallic set-up, large outgassing of the current carrying wires occurred during flashing since a high current was required to prepare the desired clean area (5-6 A). As a result a higher defect density existed on the surface prepared by this method relative to the virtually defect free surface produced by the electron bombardment technique; i.e. the number of reacted faulted-half adatoms per unit cell increased. (It is worth noting that the defects formed during flashing using the bimetallic method seemed to be more susceptible to the faulted–half units). Consequently, the slow stage in the capacitance evolution emerged at a lower oxygen exposure in Fig. 7.7, as a smaller quantity of oxygen molecules is required to form the distinctive triangular features. Finally, in Fig. 7.7 the rate difference between the fast and slow stages of the capacitance evolution was estimated to be 43 times. However, from Fig. 7.11 we estimated this difference to be approx. 20 times. We expect that this discrepancy is due to the increased presence of defect sites formed by the bimetallic heating method. *Leibsle et al.* [36] and *Tokomoto et al.* [35] showed that defect sites (as well as oxidised sites) act as nucleation sites for the oxidation process and consequently facilitate oxygen uptake by acting as 'catalyst' sites. We therefore assign the observed rate disagreement to a quicker uptake of oxygen molecules in the fast stage of Fig. 7.7. For the above reasons we deem that the results presented in Fig. 7.11 are more representative of the actual stress evolution during the oxidation process. However, we expect that similar data to that presented in Fig 7.11 can

be obtained using the high resistance sample (with accompanying by-pass unit) when combined with the electron bombardment heating technique and our recently improved capacitance resolution. We plan to confirm this occurrence in the future and are very confident of the effectiveness of the by-pass unit for accurate deflection measurements when high resistance samples are used (silicon or otherwise).

Capacitance measurements during oxygen exposures were also conducted using the front side reference electrode. These measurements were imperative to ensure that we were detecting a true sample deflection due to atomic scale strain and not some parasitic effect. For a legitimate sample deflection, the detected increase in capacitance using the back side reference electrode should be accompanied by a capacitance decrease when measured using the front side equivalent. A typical front side electrode measurement during oxygen exposure to a clean region of a low resistance sample (prepared via the electron bombardment method) is shown in Fig. 7.12 [18]. As anticipated a decrease in capacitance was observed which again corresponded to a compressive surface stress. It is evident from this result that all features observed are similar to those obtained in Fig. 7.11 under analogous conditions. This result demonstrates conclusively that we are detecting a true deflection due to atomic scale strain. The capacitance evolution for the high resistance sample with by-pass arrangement shown in Fig. 7.7 was also confirmed using the front side reference electrode. Previous reports published by other groups concerning capacitance based stress measurements lacked this validation [12, 15]. Hence, our simple but vital incorporation of an additional reference electrode is of huge importance as it acts as an integrity test for all acquired stress evolutions. Another integrity test available to us involves loading the cantilever sample using the sample pusher, and then conducting oxygen exposures to a clean area. Under the loaded condition no change in capacitance was observed as expected. (If a parasitic component was present its influence should be visible even under the loaded condition).

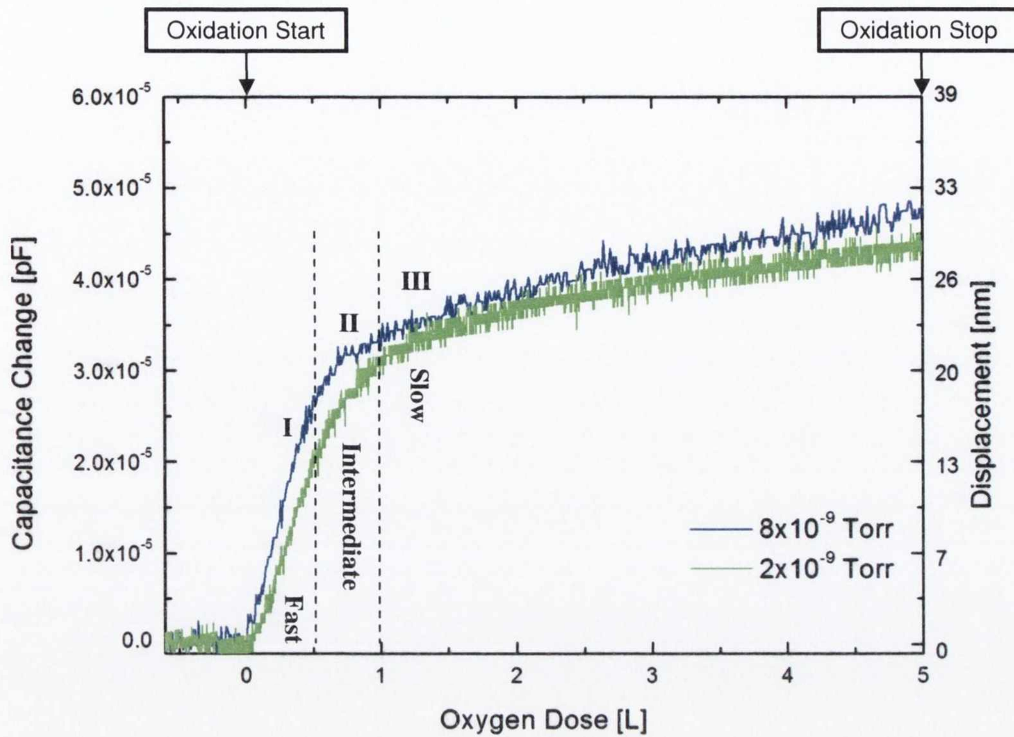

Fig. 7.11: Capacitance evolutions as a function of exposure for a low resistance sample (0.008-0.012 Ω.cm) under two different exposure conditions, namely $8x10^{-9}$ Torr and $2x10^{-9}$ Torr. In this plot fast, intermediate and slow evolution periods are clearly evident [18].

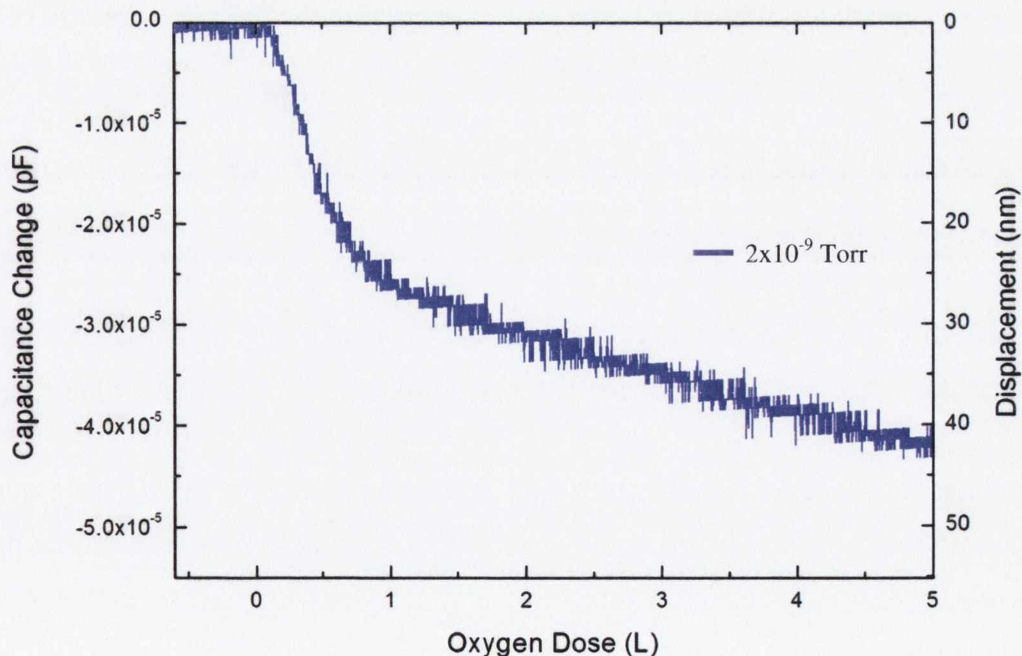

Fig. 7.12: Capacitance evolution for a low resistance sample (0.008-0.012 Ω.cm) using the front side reference electrode. This result endorses the validity of our measurement as a defection sensor as the opposite capacitance trend was obtained in Fig. 7.11. This proves conclusively that we are detecting a true sample deflection as a result of atomic-scale reaction processes and not some parasitic effect [18].

From the data sets presented in Fig 7.11 and Fig. 7.12, we deduced that the onset of the slow stage of the capacitance evolutions occurred at an exposure of approx. 0.55 L. This exposure induced on average a surface stress change of 0.190 N/m. At this stage almost all faulted-half adatoms have reacted resulting in the triangular structures when observed via STM, and corresponded to a surface coverage of approx. 0.5 ML. The observation of a slow down in oxygen uptake at a surface coverage of approx. 0.5 ML is not uncommon as reported by *Stockhausen et al.* [49], *Gupta et al.* [10], and *Carosella* and *Comas* [11]. They too saw a relatively rapid uptake of oxygen below this coverage followed by a more gradual uptake thereafter. It must be noted that our surface stress behaviour is absolutely distinct from the study of *Sander* and *Ibach* [12]. They also reported a compressive stress for the adsorption of oxygen on the Si(111)-7x7 surface at room temperature by use of a capacitance measurement, however, no two-stage feature was detected in their case. In addition, their compressive stress value was reported as 7.2 N/m per ML. This stress value is a great deal larger than our measured result (even on extrapolation to 1 ML), and does not make physical sense for a room temperature process. We also achieved a similar result to that presented by *Sander* and *Ibach* when measurements were conducted on high resistance samples in the absence of the electrical by-pass arrangement. We therefore believe that some parasitic effect was detected in their measurements. Moreover, they provided no supplementary information to verify that they were observing a true sample deflection. It should also be noted that the triangular features observed in our study are most prominent when imaged at a sample bias of +0.8-1.0 V. As a result we believe that other reports regarding the initial oxidation of the Si(111)-7x7 surface at room temperature did not reveal these characteristic features as the vast majority of observations to date were conducted at +2.0 V or at negative sample biases [2, 32, 35]; from our experience these bias conditions are not conducive to revealing the triangular features. However, *Hasagawa et. al.* did report seeing nominal triangular features on the surface at sample bias of +2 V [32]. Nevertheless, the limited number of triangular features observed was not consistent with selective oxidation of the faulted-half units.

Assuming that all of the stress at the time of the slope change in the capacitance evolutions was uniformly generated by the strains in the top four surface layers (0.392 nm

thick) of the faulted-half units, it can be deduced that each faulted-half atom accumulated strain energy of ~121 meV. Compared with average bonding energies for Si-Si and Si-O-Si (~4 eV), this value is too small to result in bond breakage, but should be sufficient to modify bonding configurations. Indeed, *Leibsle et al.* reported seeing changes in position registry in their STM study relating to the initial oxidation process at room temperature [36]. In our STM investigations, surface modification was also observed as is evident in Fig. 7.3. Additionally, phase transitions are visible in Fig. 7.13; this occurrence was observed using the VT STM at an oxygen exposure of ~1 L [18, 33]. Structures which look like the unfaulted-half unit of a 9×9 or 11×11 reconstruction are evident. This may be accomplished through transformations of faulted units of the 7×7 reconstruction via the release of locally accumulated strain. Furthermore, most adatoms in these structures are unreacted, even though they occupy a large surface area. This suggests that the unfaulted regions of any 7×7, 9×9 or 11×11 reconstruction are oxidation resistant, due to their inherent structural stability caused by the absence of a stacking fault.

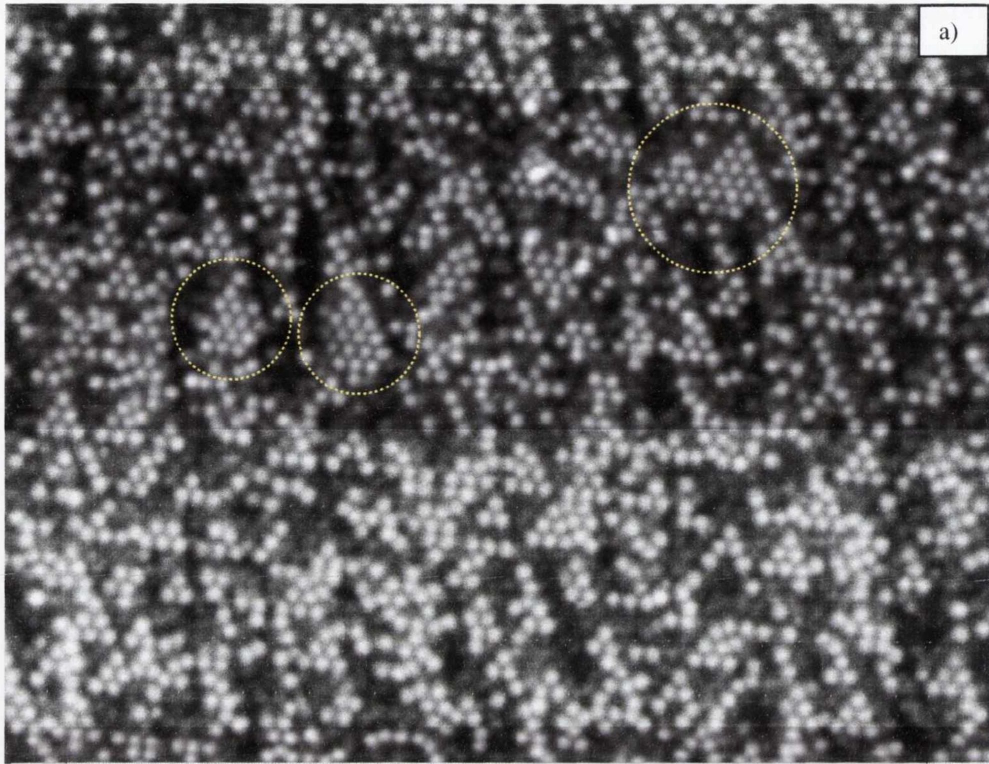

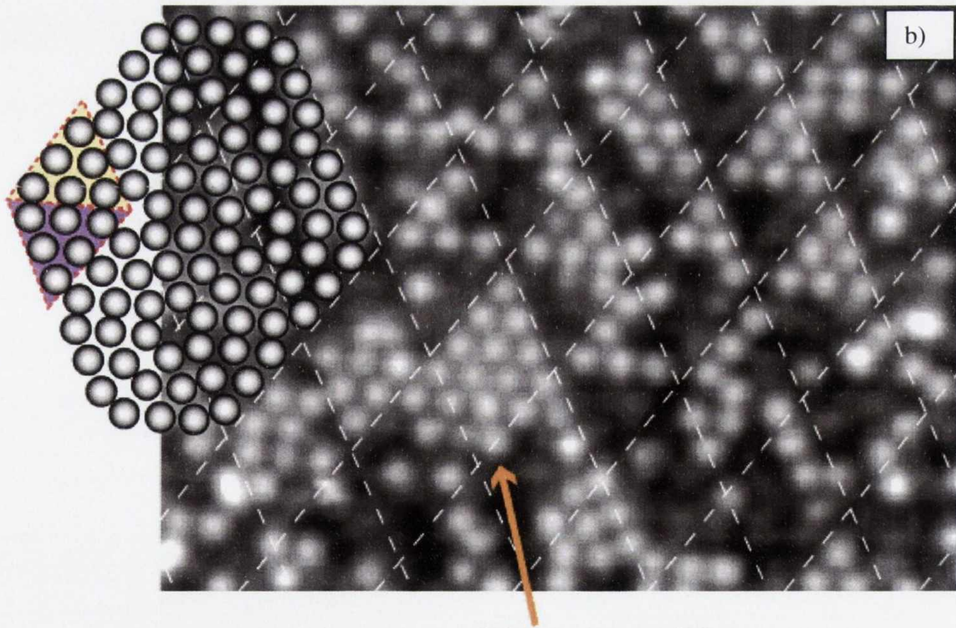

Fig. 7.13: a) Phase transitions induced by the initial oxidation process. The exposure was ~1 L. The yellow circles indicate the positions where phase transitions occurred. The sample voltage was +1 V; b) Closer view of a phase transition event [18, 33].

In recent studies using HREELS [6, 26, 27], STM [27] and theoretical calculations [20, 21], a full picture of the exceptionally early stage of the oxidation process (corresponding to exposures <0.2 L) has been revealed. Although these results covered reactions at adatom sites involving one or two oxygen molecules, experiments could not be accurately extended following this period owing to surface inhomogeneity induced by atomic scale strain. In contrast, for thick oxide film formation (100~1000 nm thick) on Si surfaces, intrinsic compressive stresses (approx. 0.1-0.4 GPa) were measured in the case of (111), (100), (110) and (311) orientations [47, 50, 51]. The lower values were obtained by post-annealing or oxidising at higher temperatures. If our measured compressive surface stress of approx. 0.190 N/m at the end of fast stage of the capacitance evolution is caused by the top four surface layers (0.392 nm thick) for example, the specific stress value can be evaluated as 0.484 GPa. This value is in good agreement with that for thick oxide film growth. This is not surprising as a study by *Stohr et al.* (using Extended X-ray Adsorption Fine Structure (EXAFS)) showed that the O-Si bond length at the adsorption stage (1.65 ± 0.03 Å) to be almost the same as in the bulk SiO_2 (1.61 Å) [52]. Contrary to our result, *Sander* and *Ibach* reported a much larger compressive stress of 7.2 N/m per ML as previously mentioned [12]. This value corresponds to a stress value of 18.4 GPa if the top four atomic layers are again responsible for the observed surface stress signature. This value is extremely large and reinforces our belief that they are detecting a parasitic effect. Therefore, our presented result is the first accurate report into the surface stress induced during the initial oxidation of Si surfaces.

The adsorption of oxygen on Si(111)-7x7 has been extensively studied using a large variety of surface analysis techniques, and the values obtained for the initial sticking coefficient have been as diverse as the techniques themselves [1]. For oxygen exposure to Si(111)-7x7 at room temperature, the initial sticking coefficient, $\theta_{7\times7}$, was reported by several groups to be smaller than 0.2 [1]. However, such estimations were based on exceptionally large oxygen exposures. In contrast, by considering surface structures at lower oxygen coverage's using LEED as well as Auger Electron Spectroscopy (AES), a larger $\theta_{7\times7}$ was obtained (~0.4), and a saturation coverage of ~0.6 ML was observed [49]. Nevertheless, since it is difficult to differentiate between

faulted and unfaulted-half units using results from LEED and AES (these techniques average information over large areas), and taking their exposure condition into account (within the slow stage of our capacitance evolutions), we expect that the initial sticking coefficient is in all probability underestimated [49]. In addition the direct determination of absolute oxygen coverage using these techniques is difficult [10]. On examination of our STM data, exposures in the range 0.5-0.6 L (representing the 'very' initial stage of the oxidation process) resulted in a surface coverage of ~0.5 ML, and displayed the aforementioned triangular features as a result of predominant oxidation of the faulted-half units. This suggested that the initial sticking coefficient is in fact very close to unity, with a strong reaction preference for the faulted-half units. To be more specific, when each adatom is fully occupied with two oxygen molecules forming 'ad-ins×3' structures [6, 20, 26, 27], 24 oxygen molecules are required to cover the 12 adatom sites in the 7×7 unit cell (many investigations have shown that the adatom reaction is the predominant step during the initial oxidation process [1]). Considering the typical definition of $1L \equiv 4\times10^{14}$ molecules/cm^2·sec and the Si(111) surface density of 7.8×10^{14} atoms/cm^2 [1], 0.96 L is obtained as the necessary exposure condition to saturate the 12 adatom sites (assuming a sticking coefficient of 1). Hence, because half of this value is comparable to the value obtained by STM to induce this 0.5 ML coverage, we conclude that the initial sticking coefficient is indeed very close to unity [18]. However, for oxygen exposures >0.5-0.6 L, STM images indicated that the reaction rate is diminished substantially; i.e. there was a considerable decrease in the sticking coefficient. Our accompanying capacitance evolutions are consistent with this interpretation, as the transition point between fast and slow stages was obtained at an exposure of approx. 0.55 L. If we assume an initial sticking coefficient of 1 for the fast stage in the capacitance evolutions, we can estimate the corresponding value during the low stage, using the rate difference between both periods. Based on a ratio of the stress-exposure gradient in these two regimes, a value of ~0.05 was obtained, which is comparable to the values presented in reference [1] for large oxygen exposures. The above analysis demonstrates how atomic scale chemical processes can be accurately detected via macroscopic surface stress measurements.

The Si(111)-7×7 surface is an energetically stabilised superstructure, as this reconstruction reduces the number of surface dangling bonds [3]. The considerable movement of atoms from their normal lattice positions in the unreconstructed surface to the positions in the 7x7 structure results in this surface being highly strained [3]. Consequently, the 7×7 unit cell is not a geometrically favoured structure but a locally strained arrangement; this suggests that the 7x7 structure has the potential to be modified into a less strained arrangement on triggering via surface reactions. Specifically, the 7x7 surface is under an intrinsic tensile surface stress due to the surface reconstruction [3, 37, 38]. *Gibson* established using high-energy transmission electron diffraction that, provided electron beam exposure is avoided during oxygen dosing, a stable and well ordered Si(111)-7x7:O surface persists up to an exposure of ~10^5 L [53]. In addition, *Leibsle et al.* [36] and *Tokomoto et al.* [35] in their STM investigations into the oxidation process deduced that the 7x7 surface is preserved for oxygen exposures up to 30 L. For our oxygen exposures (5-11 L) our STM results are consistent with the above findings. Therefore, it is not surprising that we did not to see any major attribute in our capacitance evolutions which is associated with a complete release of this intrinsic surface stress, as the reconstruction is maintained under our exposure conditions. (However, for reactions involving surface etching (i.e. reactions with halogen species), we have observed a characteristic capacitance feature which is associated with this event). As previously mentioned many structural changes occur on this surface but the primary effect is bonding of oxygen atoms in adatom backbonds. This has been predicted by *Ohdomari* to significantly lower the energy of the 7x7 surface because of the creation of 5-memebered rings at the adatom positions [53-55]. The clean surface has only 4-membered rings at the adatom sites, and is such a strained configuration that it is never seen for amorphous Si [53-55]. Cluster calculations by *Verwoerd* and *Osuch* showed that the oxygen modified structure would indeed be very stable [3, 56]. These results reinforce the point that the 7x7 reconstruction is preserved on oxidation at room temperature for our oxygen exposures, and points to the stabilisation of this surface on reaction by lowering the intrinsic strain energy of the adatom sites.

The electronic structure and strain heterogeneities between the half units of the 7x7 reconstruction have the potential to exhibit interesting chemical reactivity effects

[3, 40] as exemplified in this study. From the viewpoint of electronic structure, chemical reactivity differences between the faulted and unfaulted-halves was theoretically discussed for reactants which act as electron acceptors with respect to the Si surface (e.g. oxygen, hydrogen and halogens) [39]. As a result a reaction preference for the faulted-half region was obtained for Si(111)-7x7 [39]. This arises primarily from the difference in electron density associated with the faulted and unfaulted-halves of the 7x7 cell. For example, *Hamers et al.* observed a filled adatom dangling bond state at ~0.3 eV below the Fermi energy on the clean 7x7 surface, that appears more intense in Scanning Tunneling Spectroscopy (STS) images (i.e. has a higher density of states) on the faulted versus the unfaulted-half of the unit cell [2, 40]. *Pelz* and *Koch* observed that this faulted-half region is more susceptible to chemical attach by oxygen species, suggesting that the site preference is directly related to differences in the adatom electronic local density of states (LDOS) of both halves; i.e. greater electron density of the faulted regions favours the reaction at these locations [2]. The LDOS argument is consistent with a "harpooning" mechanism. Based on combined results from high resolution spectroscopic techniques [57, 58] it was suggested that during the initial stage of oxygen interaction with silicon surfaces a chemisorbed O_2^- like species is formed, whose spontaneous dissociation at room temperature leads to the aforementioned oxidation products [59]. As pointed out by *Avouris et al.* [22], the formation of this O_2^- intermediate quite naturally explains the site selectivity of oxygen adsorption in STM experiments [59]. The bonding of O_2 on Si(111) involves considerable charge transfer from the Si dangling bonds to the oxygen $2\pi^*$ level [59]. In analogy to a gas phase "harpooning" reaction, an oxygen molecule approaching the surface is therefore expected to stick predominantly at those sites which have high electron density above the surface [59]. These are the faulted-half regions of the 7x7 unit cell as previously stated. If the barrier to reaction of the unfaulted-half regions at room temperature is dominated by electronic effects at the surface, STM examination of the "harpooning" phenomenon as a function of substrate doping may show reactivity variations [25]. For example, in our case the results presented were for n-type Si samples, however, if the surface region is p-type doped a reduction of the electron population of the adatom dangling bond states may occur [25], thus potentially altering the observed unit selectivity. We hope to test this

hypothesis in the near future. In our studies a similar reaction preference for the faulted-half units was obtained but, it is difficult to totally attribute the origin of the unit selective oxidation with this electronic argument, as the influence of different strain energies between the respective units may also play an important role. Theoretical calculations have shown that the faulted-half of the 7x7 unit cell is under a greater tensile stress when compared with that of the unfaulted region [37, 38]. Therefore, the faulted-halves may be more vulnerable to reactions inducing volume expansion by compensating for the volume reduction (i.e. tensile stress) associated with the original 7x7 reconstruction. On the other hand, in the unfaulted-half unit, additional mechanical expansion is required to insert oxygen atoms into the adatom backbonds. This atomic scale effect may also in part explain the unit selective oxidation of the faulted-half units. Moreover, it must be recognised that during the reaction process, significant local modifications from the original structure will occur that will produce changes in the LDOS available for reaction at nearby unreacted sites, not to mention the incorporation of significant mechanical strain. However, at this juncture it is not possible to establish whether electronic and/or strain effects play the dominant role in the observed unit selectivity.

7.3. Probing the Origin of Unit Selectivity

To help decipher the origin of the unit selectivity, our collaborators conducted XPS and molecular beam experiments which involved controlling the incident translational energy of oxygen molecules by use of a supersonic beam ranging from 0 to 2 eV [18, 60]. The dependence of the reactivity on the kinetic energy yields a clue as to whether the unit selectivity is dominated by the electronic structure or the mechanical condition of the surface. The kinetic energy of the incident O_2 molecules can be controlled by changing the O_2, He and/or Ar gas mixing ratios with the oxygen delivery nozzle temperature set at a specific value (namely 300 K or 1400 K). In each experiment the oxygen dose was fixed at 6.5 L so that the difference in the XPS signal provides a measure of the dependence of the sticking coefficient on the incident kinetic energy. Fig. 7.14 shows the O-1s XPS intensity as a function of the incident energy of the

molecular oxygen [18, 60]. For low translational energies in the range from 0.04-0.7 eV, triangular features were present at the surface as confirmed by the VT STM [18, 33] and the XPS signal remained essentially constant indicating a constant sticking coefficient. On increasing the incident energy above 0.7 eV the O-1s XPS intensity gradually increased and above 1.3 eV ultimately saturated at a value that is double the original level. This likely indicates that both faulted and unfaulted-halves were oxidised at these higher translational energies; this occurrence was indeed verified by our colleagues using the VT STM [18, 33].

On careful examination of the intensity behaviour, a simple gradual change was observed. If the reaction was dominated by electronic effects, a steeper intensity increase after exceeding some threshold activation energy is anticipated (even if the Gaussian energy profile for the molecular beam is taken into account). In contrast, if this gradual change is due to mechanical origins (for example the stiffness of the various surface bonds) higher incident energy should be more advantageous to physically expand and penetrate the surface lattice and in doing so promote subsequent reactions. From this speculation, unit selective oxidation of the faulted-half units appears to be influenced by mechanical effects at the surface region. However, this cannot be conclusively stated at present and further investigations are required to fully elucidate the exact origin of the observed unit selectivity in our experiments to date.

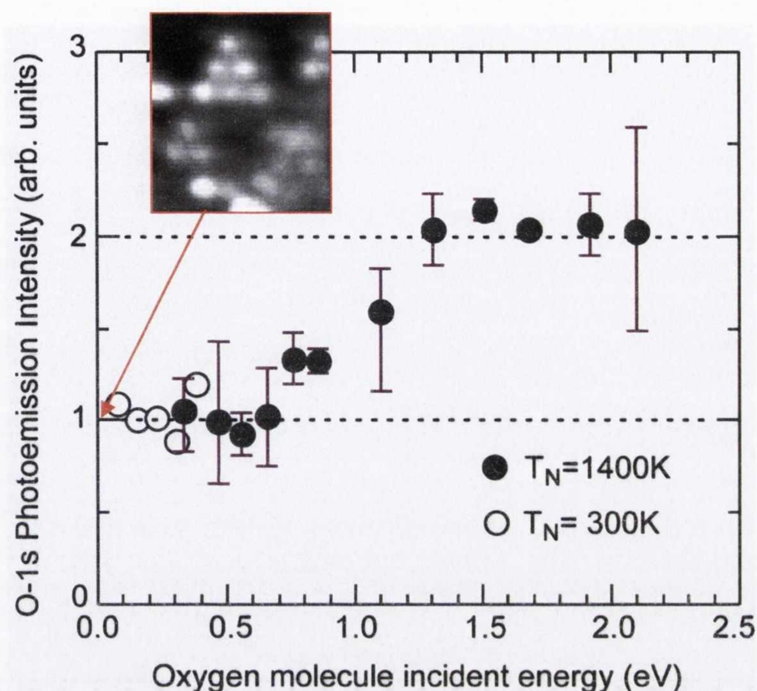

Fig 7.14: O-1s normalised photoemission intensity for the initial oxidised Si(111)-7x7 surface as a function of oxygen molecule incident translational energy. The oxygen dose for each data point presented was 6.5 L. T_N denotes the nozzle temperature [18, 33, 60].

7.4. Effects of Artificial Applied Stress on the Oxidation Process

It is apparent from both theory and experiments that surface stress is an important ingredient in the physics and chemistry of surfaces. However, it is also useful to be able to apply an artificial stress to the surface in order to study its effect on atomic scale processes [61, 62]. Such investigations are not only important from a fundamental point of view, but will also be of huge significance for microelectronic device manufacture particularly as device dimensions are reduced and surface effects dominate. Furthermore, these studies may provide illuminating insights into the role of wafer mounting during industrial processing steps; the wafer gripping condition may induce artificial surface stresses thus influencing the reaction outcome. Applying an external force to bend the sample seems to be the best way to study the intrinsic effect of stress on the adsorption properties of various gases. Consequently, our novel system for combined STM and surface stress measurements is equipped with a sample pusher which is used to artificially stress the cantilever sample and study the influences of induced stresses on reaction

processes. There are several mechanical schemes one might consider to artificially stress a sample. The simplest is bending of the cantilever by applying a small force at the free end. To realise this we use a linear inertial slider which is capable of generating both tensile and compressive surface stress conditions of varying magnitudes; see Fig. 7.15. This tool is proving to be a very important component of our system and offers exciting research opportunities for the future.

Quite recently we have commenced investigations into the influences of artificially applied stress on the room temperature oxidation of Si(111)-7x7. Such investigations are required to: a) explore the possibility of removing the observed site selectivity on exposure to a pre-stressed surface; and b) examine the prospect of tuning the reaction processes (i.e. adsorption sites and kinetics) using applied stress as the control parameter. To date, only large artificial stresses were applied to the cantilever sample in order to examine the feasibility of this method in perturbing the atomic scale events. While we are not in a position to offer any decisive outcomes at present, our preliminary results provide a useful insight into the role of artificial stress on the oxidation process.

Fig. 7.16 (a) displays surface structures observed following a 0.5 L oxygen exposure to a free standing cantilever sample at room temperature. From this image triangular features are clearly visible (as a result of unit selective oxidation of the faulted-half units) and a surface coverage of ~0.5 ML exists. The STM results obtained (under identical exposure conditions to abovementioned arrangement) for two pre-stressed cantilever configurations, namely strongly tensile and strongly compressive, are displayed in Fig. 7.16 (b) and Fig. 7.16 (c), respectively. A similar stress magnitude was applied to the cantilever in each case; i.e. $\sim 10^4$ times the free end deflection induced by the oxidation process to the free standing arrangement. On inspection of both results it is evident that the triangular features are not as distinguishable in these images when compared to the image obtained under the stress free condition. This suggests that the atomic scale reaction processes may be influenced by the applied stress at the surface region. Now let us briefly examine each pre-stressed result individually. (It should be noted that the following discussion is based on 'perceived surface changes on visual observation' as time restraints did not permit more detailed investigations, therefore this

discussion is somewhat speculative. A complete accurate discussion would require counting experiments to deduce exact changes at the surface region and numerous STM observations to build a statistically accurate picture; we are currently performing these tasks).

Fig. 7.16 (b) represents the surface features following oxidation under a tensile condition. Here, it is apparent that triangular features still exist, however a suppression of the faulted-half reaction appears to have occurred when compared with Fig. 7.16 (a). This resulted in fewer observable reacted sites on this surface and a reduced prominence of the triangular features. This may be a consequence of the fact that the unit cells were compacted on application of the tensile surface stress, thereby making it sterically more difficult for oxygen atoms to become incorporated into adatom backbonds of the faulted-half regions, reducing the reaction rate as a result. The effect of an applied compressive stress is displayed in Fig. 7.16 (c). Again, an apparent decrease in the quantity of reacted sites was observed when compared with Fig 7.16 (a). In addition, triangular features were far less discernible on this surface. The applied compressive stress seemed to remove the majority of the site selectivity in this case. At this time, expansion of the surface region on application of the artificial stress potentially made it more amenable for oxygen atoms to become incorporated into adatom backbonds of both half units, as additional energy to expand the surface region on oxygen incorporation was not required.

The above discussions did not take account of changes in the surface electronic structure; this too is expected to play an important role in the observed atomic scale processes and will need to be investigated in the future. This perturbment may have resulted in the apparent decrease in the reaction rate for both pre-stressed conditions as well as site selectivity effects. In addition, we are applying large strain fields to the surface region which are not necessarily ideal for exhibiting the most remarkable changes in the observed reaction processes. Consequently, we hope to shortly commence similar investigations as a function of applied stress under much lower pre-stressed conditions. It is early days in these studies and we look forward to shedding valuable light on the effects of artificially applied stress on the oxidation process in the not so distant future.

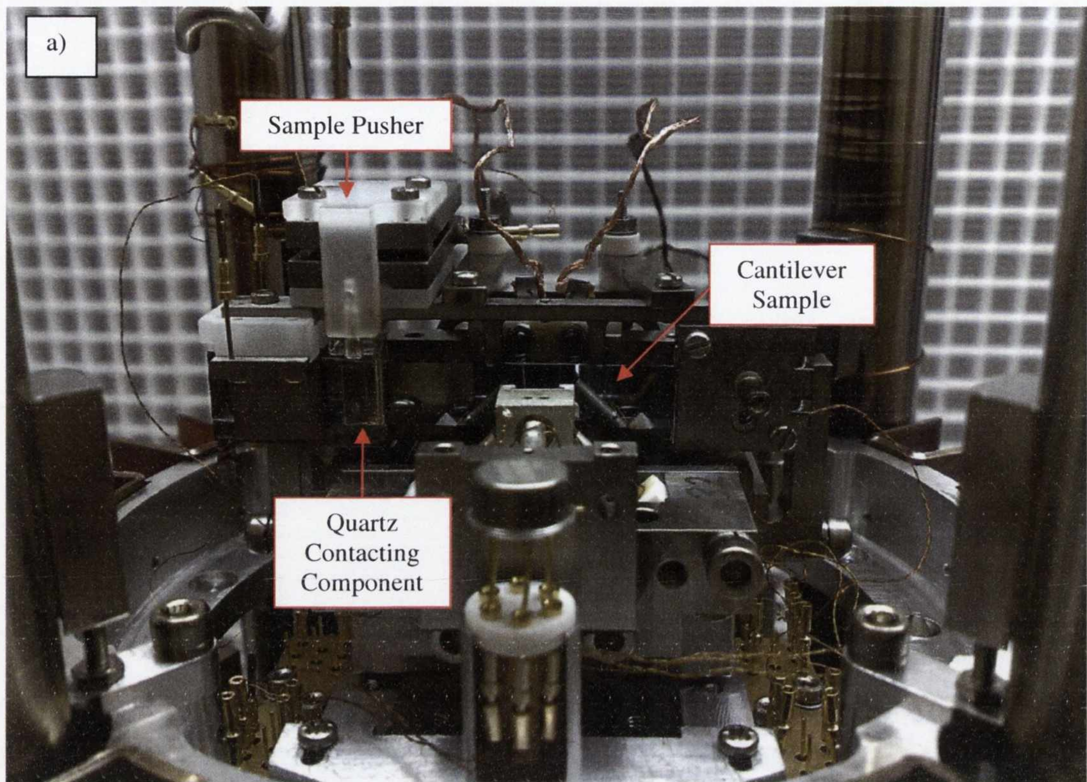

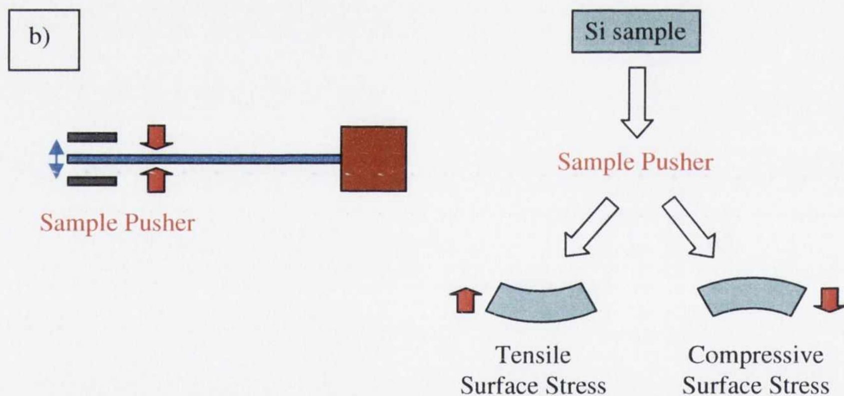

Fig 7.15: Our system is equipped with a sample pusher which can be used to study the effects of artificially applied stress on processes at the atomic level- a) Photograph illustrating the sample pusher. To push the sample a linear inertial slider is used. It has a total travel range of 5 mm in both forward and back directions, while providing 40 nm step displacements at a minimum. A specifically designed quartz module couples conveniently onto this slider arrangement and is used to contact the sample when applying an artificial stress. Displacements of the cantilever sample on loading can be monitored capacitively; b) schematic diagram illustrating how the pusher unit can be utilised to generate a tensile or compressive stress conditions at the surface of the cantilever.

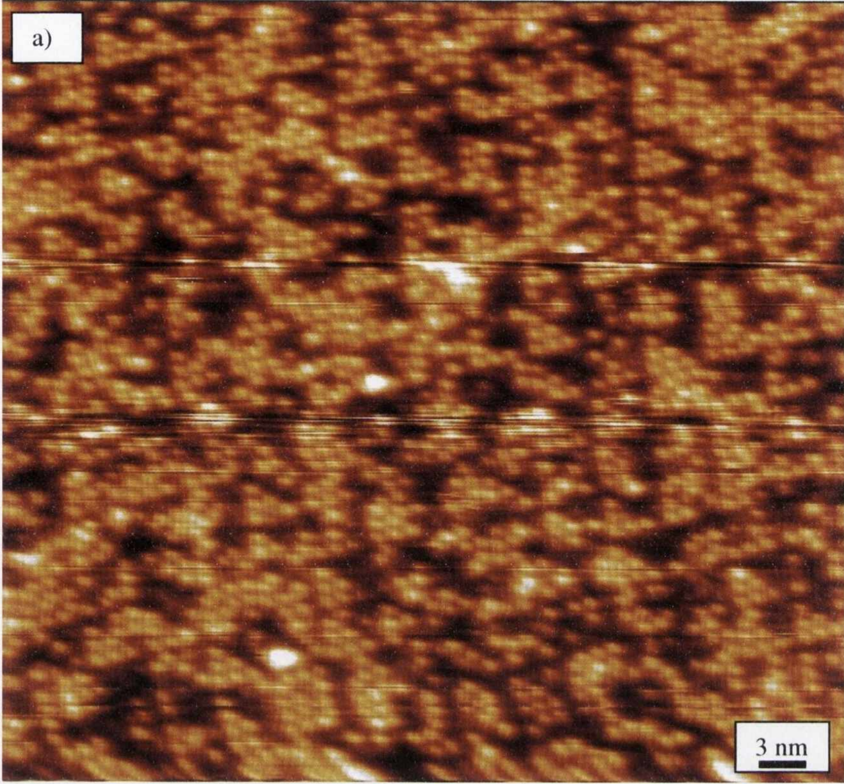
a)
3 nm

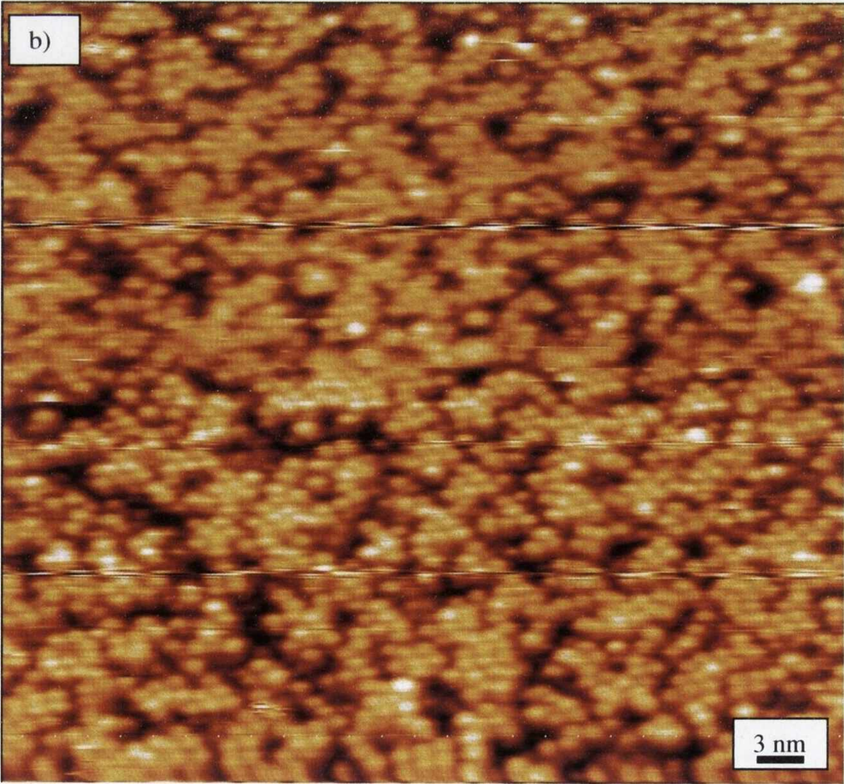
b)
3 nm

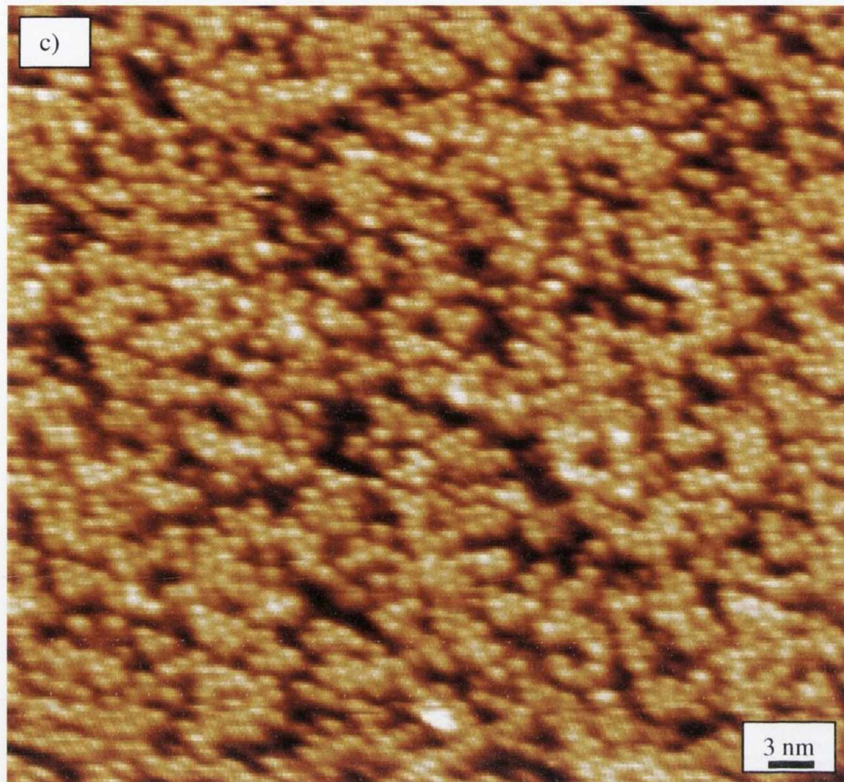

Fig 7.16: STM images taken on the cantilever sample following a 0.5 L room temperature oxygen exposure to- a) a free standing cantilever sample; b) a cantilever sample under a large tensile surface stress; and c) a cantilever sample under a large compressive surface stress. All images were acquired with a +1V sample bias [18].

References:

[1] V. G. Lifshits, *Surface Phases on Silicon: Preparation, Structures & Properties* (John Wiley & Sons Ltd., Chichester [England], 1994).

[2] J. P. Pelz, and R. H. Koch, Physical Review B **42**, 3761 (1990).

[3] H. Neergaard Waltenburg, and J. T. Yates, Chemical Reviews **95**, 1589 (1995).

[4] R. J. Hamers, and Y. Wang, Chemical Reviews **96**, 1261 (1996).

[5] T. Engel, Surface Science Reports **18**, 93 (1993).

[6] H. Okuyama, Y. Ohtsuka, and T. Aruga, The Journal of Chemical Physics **122**, 234709 (2005).

[7] P. Balk, *The Si-SiO_2 System, Vol. 32 of Materials Science Monographs* (Elsevier, Amsterdam, 1988).

[8] R. B. Fair, *Microelectronics Processing: Chemical Engineering Aspects* (American Chemical Society, Washnington, D.C., 1989).

[9] E. A. Irene, CRC Critical Reviews in Solid State and Materials Sciences **14**, 175 (1988).

[10] P. Gupta *et al.*, Physical Review B **40**, 7739 (1989).

[11] C. A. Carosella, and J. Comas, Surface Science **15**, 303 (1969).

[12] D. Sander, and H. Ibach, Physical Review B **43**, 4263 (1991).

[13] D. Sander, Solid State and Material Science **7**, 51 (2003).

[14] C. F. Herrmann, D. Chen, and J. J. Boland, Physical Review Letters **89**, 096102 (2002).

[15] H. Ibach, Surface Science Reports **29**, 195 (1997).

[16] T. Narushima, N. T. Kinahan, and J. J. Boland, Review of Scientific Instruments **78**, 053903 (2007).

[17] T. Narushima, N. T. Kinahan, and J. J. Boland, Review of Scientific Instruments **76**, 095113 (2005).

[18] To be published.

[19] K. D. Brommer *et al.*, Surface Science **314**, 57 (1994).

[20] S.-H. Lee, and M.-H. Kang, Physical Review Letters **82**, 968 (1999).

[21] S.-H. Lee, and M.-H. Kang, Physical Review B **61**, 8250 (2000).

[22] I. W. Lyo *et al.*, The Journal of Physical Chemistry **94**, 4400 (1990).

[23] J. P. Pelz, and R. H. Koch, Journal of Vacuum Science and Technology B **9**, 775 (1991).

[24] P. Avouris, I.-W. Lyo, and F. Bozso, Journal of Vacuum Science and Technology B **9**, 424 (1991).

[25] F. Bozso, and P. Avouris, Physical Review B **44**, 9129 (1991).

[26] H. Okuyama, T. Aruga, and M. Nishijima, Physical Review Letters **91**, 256102 (2003).

[27] H. Okuyama, T. Yamada, and T. Aruga, Japanese Journal of Applied Physics **44**, 5362 (2005).

[28] B. Schubert, P. Avouris, and R. Hoffmann, The Journal of Chemical Physics **98**, 7593 (1993).

[29] B. Schubert, P. Avouris, and R. Hoffmann, The Journal of Chemical Physics **98**, 7606 (1993).

[30] G. Comtet *et al.*, Physical Review B **65**, 035315 (2001).

[31] H. W. Yeom, Physical Review B **66**, 157301 (2002).

[32] T. Hasegawa *et al.*, Surface Science **312**, L753 (1994).

[33] Experimental work conducted in NIMS, Tsukuba, Japan under the leadership of Prof. Kazushi Miki. Contributors: Dr. Tetsuya Narushima, Mr. Kazunori Aoki, and Mr. Takashi Onizawa.

[34] T. Narushima *et al.*, Surface Science **601**, 1384 (2007).

[35] H. Tokumoto *et al.*, Journal of Vacuum Science and Technology A **8**, 255 (1990).

[36] F. M. Leibsle, A. Samsavar, and T. C. Chiang, Physical Review B **38**, 5780 (1988).

[37] R. D. Meade, and D. Vanderbilt, Physical Review B **40**, 3905 (1989).

[38] D. Vanderbilt, Physical Review Letters **59**, 1456 (1987).

[39] K. D. Brommer *et al.*, Surface Science **314**, 57 (1994).

[40] R. J. Hamers, R. M. Tromp, and J. E. Demuth, Physical Review Letters **56**, 1972 (1986).

[41] J. F. O'Hanlon, *A Users Guide to Vacuum Technology* (Wiley & Sons, Hoboken, New Jersey, 2003).

[42] G. Hollinger, and F. J. Himpsel, Journal of Vacuum Science and Technology A **1**, 640 (1983).

[43] C. M. Garner *et al.*, Journal of Vacuum Science and Technology **14**, 372 (1977).

[44] G. M. Guichar *et al.*, Surface Science **58**, 374 (1976).

[45] R. J. Jaccodine, and W. A. Schlegel, Journal of Applied Physics **37**, 2429 (1966).

[46] J. K. Srivastava, and E. A. Irene, Journal of the Electrochemical Society **132**, 2815 (1985).

[47] E. Kobeda, and E. A. Irene, Journal of Vacuum Science and Technology B **5**, 15 (1987).

[48] J. A. Stroscio, R. M. Feenstra, and A. P. Fein, Physical Review Letters **58**, 1668 (1987).

[49] A. Stockhausen, T. U. Kampen, and W. Mönch, Applied Surface Science **56-58**, 795 (1992).

[50] E. Kobeda, and E. A. Irene, Journal of Vacuum Science and Technology B **4**, 720 (1986).

[51] E. Kobeda, and E. A. Irene, Journal of Vacuum Science and Technology B **6**, 574 (1988).

[52] J. Stohr *et al.*, Journal of Vacuum Science and Technology **16**, 1221 (1979).

[53] J. M. Gibson, Surface Science **239**, L531 (1990).

[54] I. Ohdomari, Surface Science **227**, L125 (1990).

[55] I. Ohdomari *et al.*, Journal of Non-Crystalline Solids **89**, 239 (1987).

[56] W. S. Verwoerd, and K. Osuch, Surface Science **256**, L593 (1991).

[57] U. Höfer *et al.*, Physical Review Letters **55**, 2979 (1985).

[58] U. Höfer *et al.*, Physical Review B **40**, 1130 (1989).

[59] P. Bratu, K. L. Kompa, and U. Höfer, Physical Review B **49**, 14070 (1994).

[60] Experimental work conducted in NIMS, Tsukuba, Japan under the leadership of Prof. Masafumi Ohashi and Prof. Kazushi Miki. Contributors: Dr. Tetsuya Narushima, Dr Wataru Yashiro, Dr. Yuden Teraoka, and Dr. Akitaka Yoshigoe.

[61] M. Gsell, P. Jakob, and D. Menzel, Science **280**, 717 (1998).

[62] F. K. Men, W. E. Packard, and M. B. Webb, Physical Review Letters **61**, 2469 (1988).

Conclusion

- We have developed a novel measurement system capable of investigating the underlying origins of surface stress in the context of atomic surface structure.
- This system successfully combines two distinct measurement capabilities for the first time, namely (i) measurement of surface stress based on the displacement of a large silicon cantilever sample; and (ii) atomic resolution observation of the surface structure of the same cantilever.
- The former measurement incorporates a capacitive detection method capable of detecting strain energy changes with meV/atom resolution, while the latter measurement incorporates a scanning tunnelling microscope (STM) capable of observing structural changes occurring on the surface.
- Although non-trivial, the development of this combined measurement system was accomplished through careful electrical, thermal and mechanical design, in addition to tuning of the sample thickness to control the natural oscillation of the cantilever.
- This dual measurement system provides structural, dynamical and interactional information and is proving to be extremely useful in heightening understanding of reaction processes on surfaces.
- In relation to the oxidation process on Si(111)-7x7 at room temperature, we showed that the initial oxidation period involves two compressive stress stages with different growth signatures. The atomic scale origins of the measured surface stress evolution were discussed and supported via complementary STM data. In particular, we demonstrated that the initial rapid rise in compressive stress is associated with selective oxidation of the faulted-half units of the 7x7 reconstruction. The effects of an artificially applied stress as a means to alter the unit selectivity during the oxidation process were also presented and were shown to influence the surface reactivity.
- While our research activities lie predominantly with silicon processing it is important to note that our novel system is extremely versatile and can be applied to a wide range of research topics as outlined in chapter 1.

Appendix A: Standard Design for Scanning Tunneling Microscopy (STM) under Ultra-high Vacuum (UHV)

In chapters 2 and 3, generic discussions concerning STM and UHV were presented. However, no specific details in relation to our conventional system design were provided. To help fill this void, the essential design features (to conduct standard STM measurements under a suitable UHV environment) will now be discussed.

A.1. STM Unit [1, 2]

- A commercial room temperature *Omicron UHV STM-1* is employed as the basic platform for performing our STM measurements; see Fig. A.1.
- The Omicron UHV STM-1 is the benchmark for easy, reliable and high-performance STM measurements in UHV. Advantages associated with this system include: (a) ease of operation; (b) proven internal spring suspension system with eddy current damping provides excellent vibration isolation, thus permitting high resolution imaging even under non-ideal conditions; and (c) an in-vacuum preamplifier (current to voltage converter (IVC)) close to the tip provides lowest noise conditions.

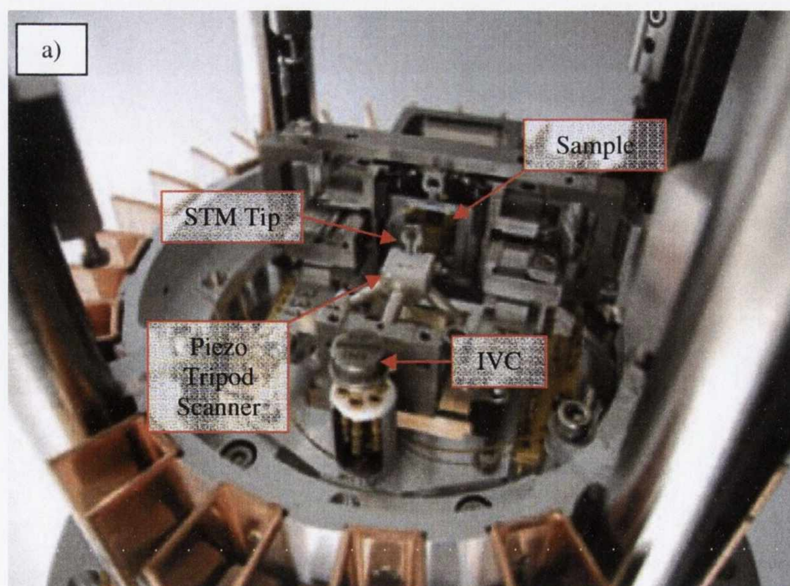

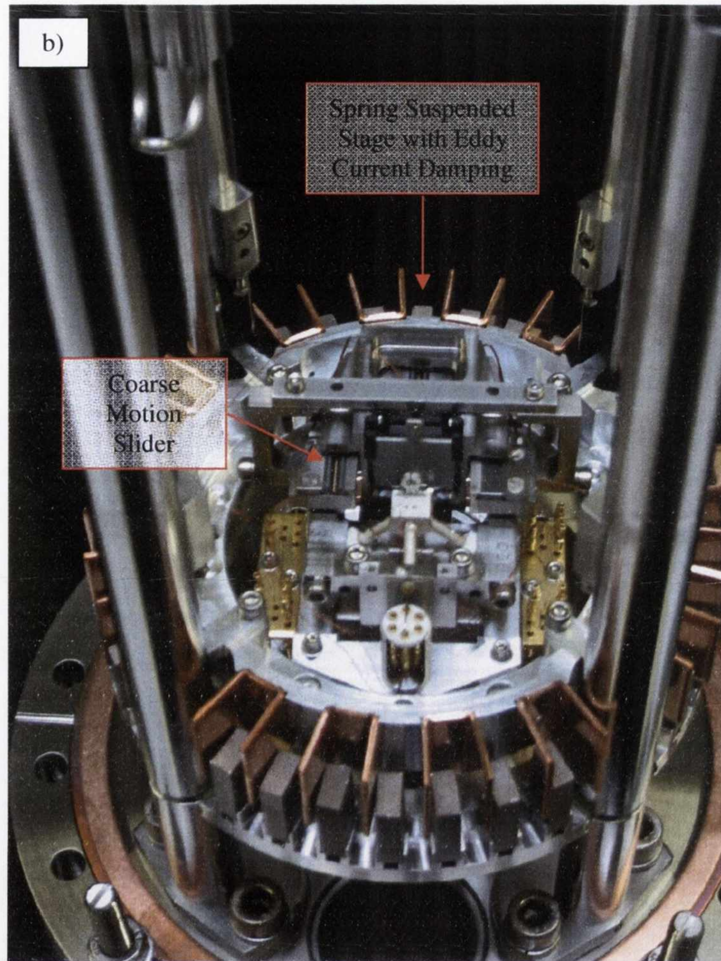

Fig. A.1: a) and b) display alternative views of our employed commercial Omicron UHV STM-1[1].

- The main components include:
  - Tripod scanner (x, y, and z-piezo sensitivities: 9.5 nm/V; maximum scan size 2.3 μm)
  - 2-axes inertial slider for coarse motion sample positioning (x travel: ±5 mm; z travel: 10 mm)
  - STM stage push-pull mechanism (allows the stage to be locked to permit sample and tip transfer or alternatively suspended by the suspension springs to perform high resolution STM imaging)
  - Carousel (additional samples and tips can be stored at this location, which has a total of 8 tip/sample parking positions; see Fig. A.2)

- Long wobble-stick permits sample and tip transfer between the STM stage, the carousel and one of our purpose built transfer rods (described later) within the UHV chamber. Three modes of motion are possible- a) a linear motion; b) an angular motion; c) the pincer grip motion
- Comprehensive control electronics and software allows ease of operation of the STM and data acquisition.

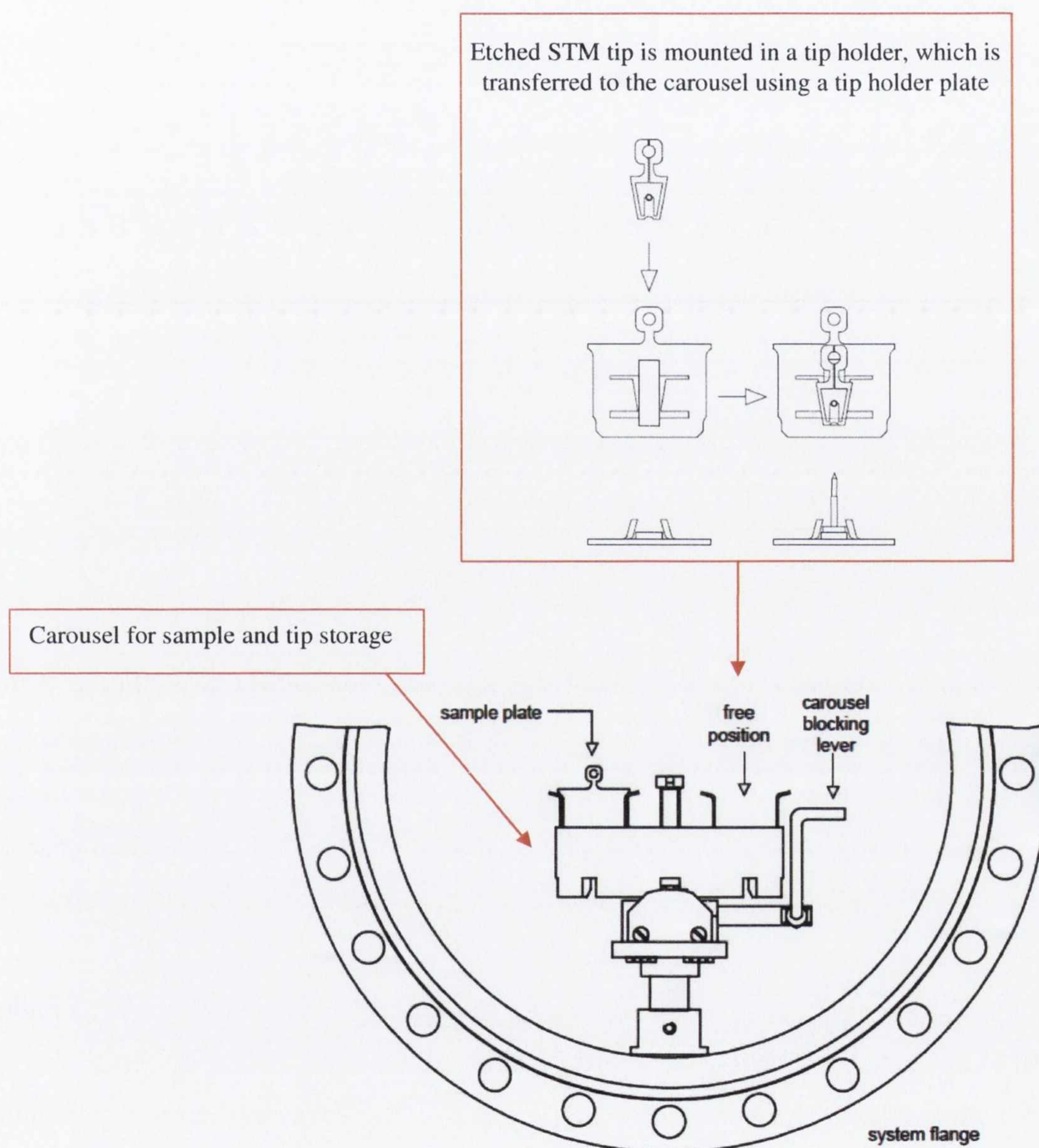

Fig. A.2: Diagram displaying the carousel unit which is used for sample and tip storage [2].

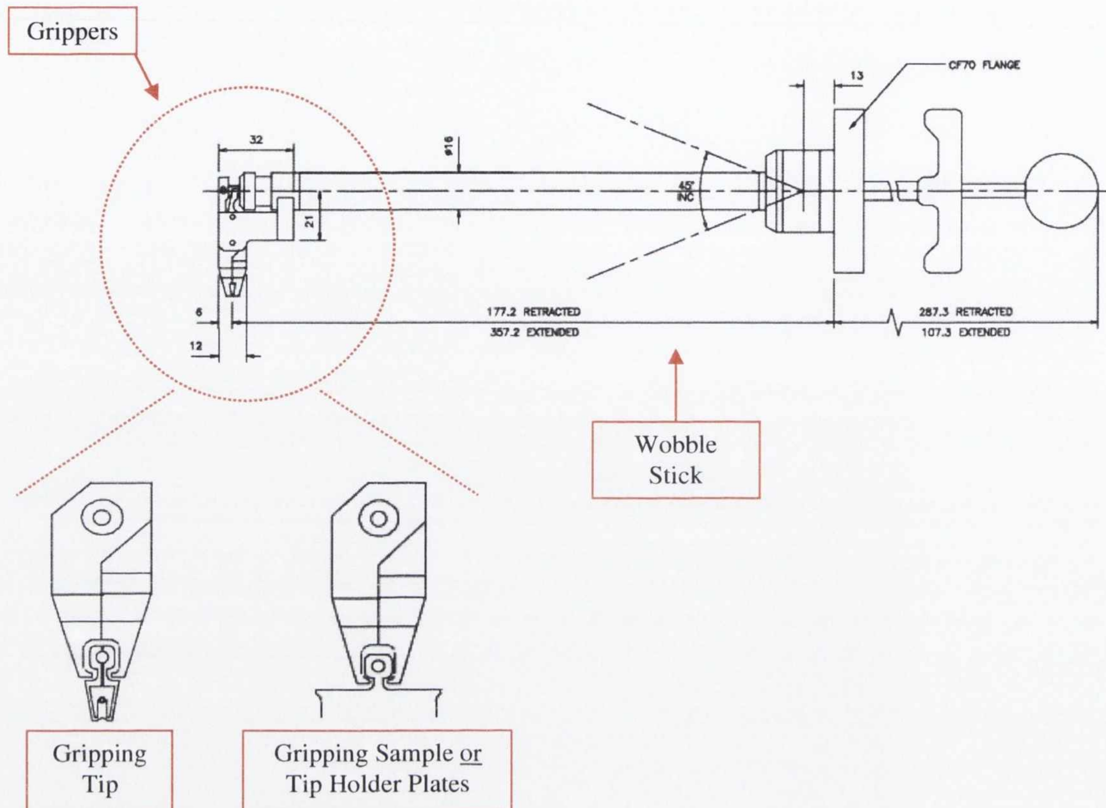

Fig. A.3: Schematic diagram representing of the UHV STM-1 wobble-stick [2].

A.2. Vacuum System

- The main components associated with our vacuum system are displayed in Fig. A.4.
- The vacuum system is comprised of two main chambers, namely, an STM chamber and a preparation chamber. The STM chamber was purchased from Omicron to meet the design and operation requirements for the STM-1 [1]. The preparation chamber already existed in our laboratory [3], and is used to prepare clean sample surfaces and conduct exposures to reactive species if necessity demands.
- The STM and preparation chambers are separated by a 150 mm gate valve to allow simultaneous imaging and sample preparation/exposures.
- Each chamber is pumped with an ion pump (~240 l/sec) combined with a titanium sublimation pump (TSP). The preparation-side is also equipped with a turbo molecular pump and accompanying backing pump, which is used to initially pump down the system or after sample dosing (~170 l/sec).

- The vacuum level is measured in each chamber using ion gauges and logged using a LabVIEW program. A pressure of approx. $5x10^{-11}$ Torr can be achieved in the system following a 48 hour bake at ~150 ^{O}C.
- Additionally a quadrupole mass spectrometer (QMS) is present to perform leak checks and to measure the quality of the vacuum (mass range: 1- 200 amu).
- A purposely designed magnetic transfer rod allows tip and sample introduction from atmosphere into the system (preparation-side) by means of a separately pumped load-lock chamber and gate valve arrangement. Pumping of the load-lock is achieved using a turbomolecular pump/rough pump assembly, while an ion-gauge monitors the load-lock pressure. (Baking of the load-lock before loading is typically required).

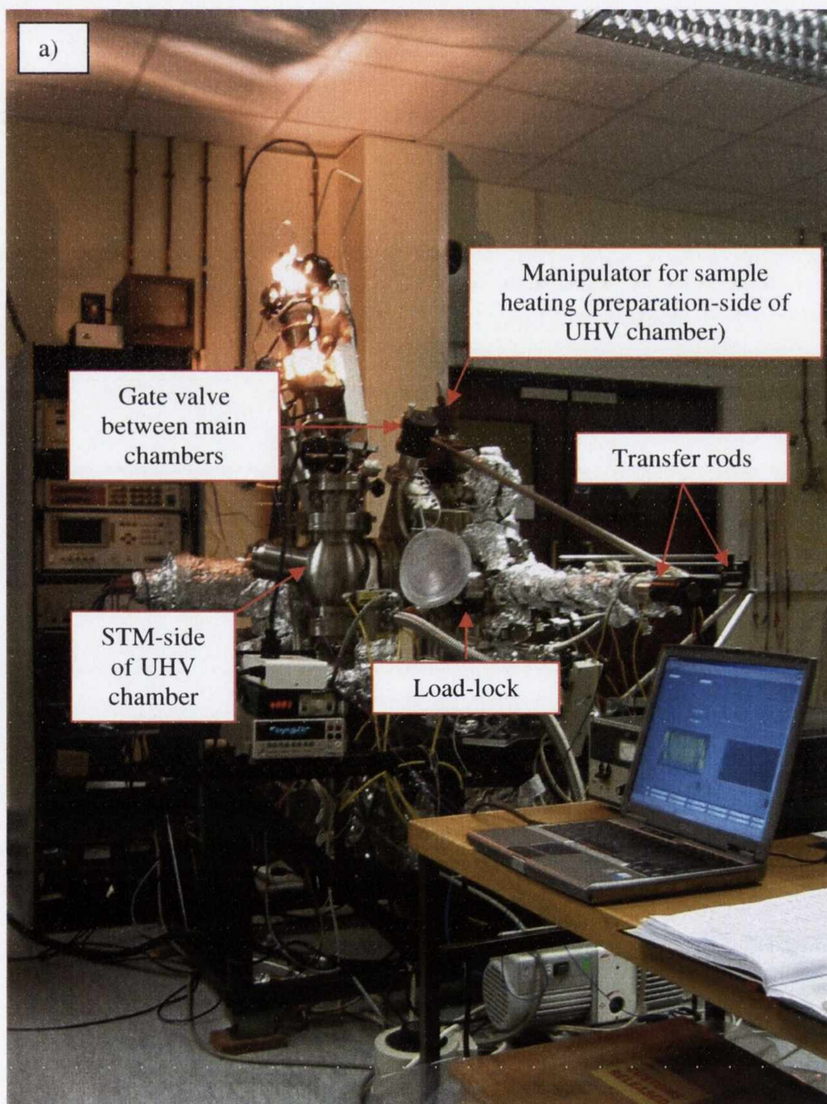

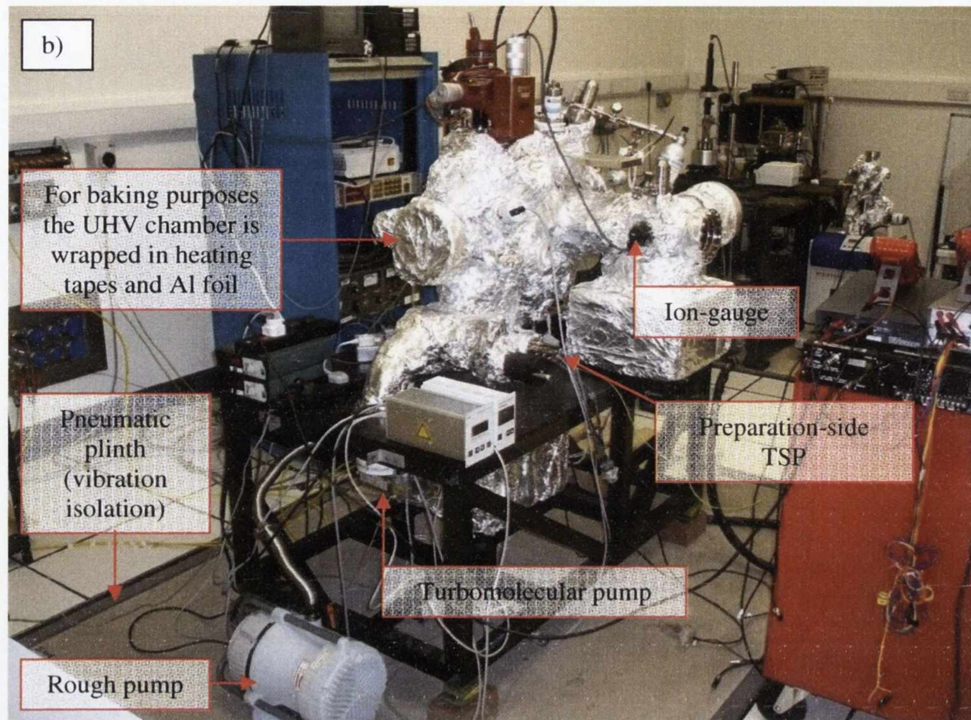

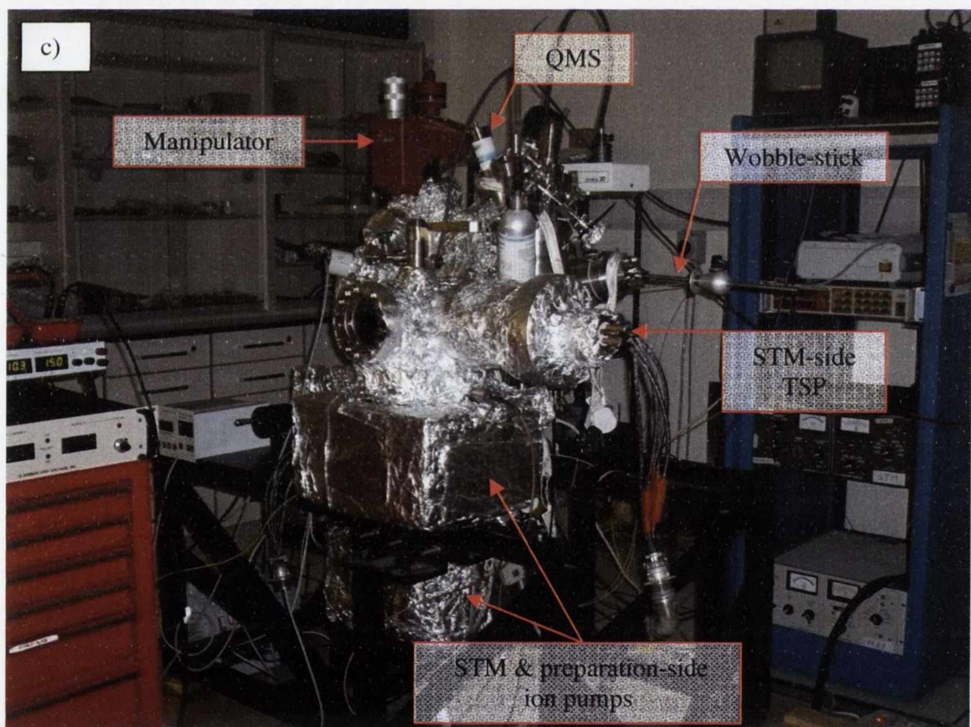

Fig. A.4: Photographs a) to c) display the main components of our chamber design to perform STM measurements under UHV conditions. Slightly different chamber arrangements are apparent from these images due to a recent laboratory move; photographs b) & c) represent the current arrangement in our new state-of-the-art laboratory located in the CRANN building (no load-lock or transfer rods presently attached).

A.3. Manipulator for Sample Preparation

- As previously mentioned samples and tips can be introduced from the load-lock to the preparation-side of the UHV chamber using a transfer rod. Transfer to the STM chamber can then be completed with the assistance of a second transfer rod arrangement.
- In the case of Si samples, however, direct current heating in UHV is typically conducted to remove the oxide layer, thus producing a clean surface reconstruction which can subsequently be observed via STM.
- To this end, we have designed a specific unit that permits direct current sample heating when positioned on a vertical manipulator arm within the preparation chamber; see Fig. A.5. (This unit also acts as the transportation vessel for sample and tip holder plates when coupled with the magnetic transfer rods). The manipulator can be moved (within limits) in all three spatial directions and is rotatable.
- Additionally, the manipulator can potentially be used to position clean sample surfaces in front of specific ports in the preparation chamber to conduct exposure and deposition procedures, as well as temperature programmed desorption experiments if required.

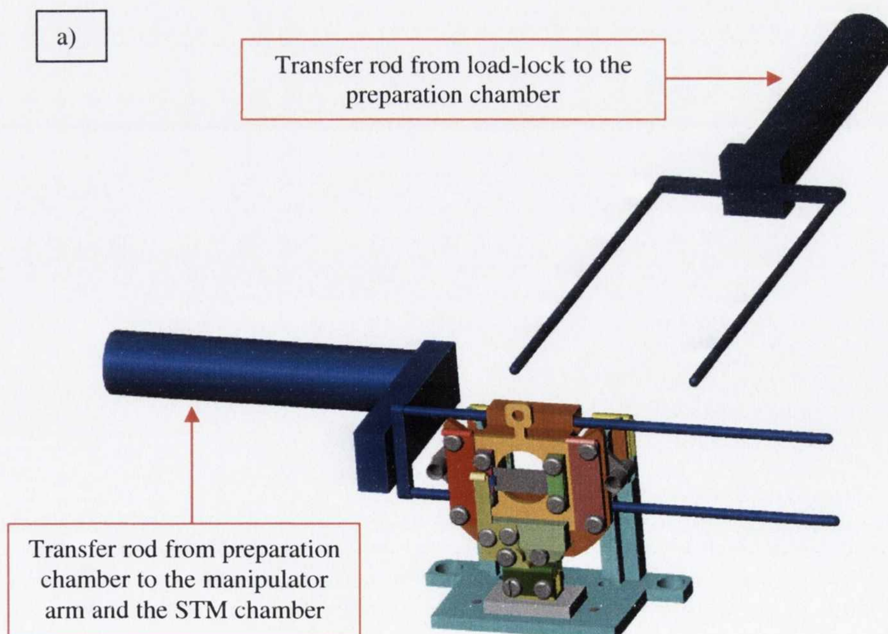

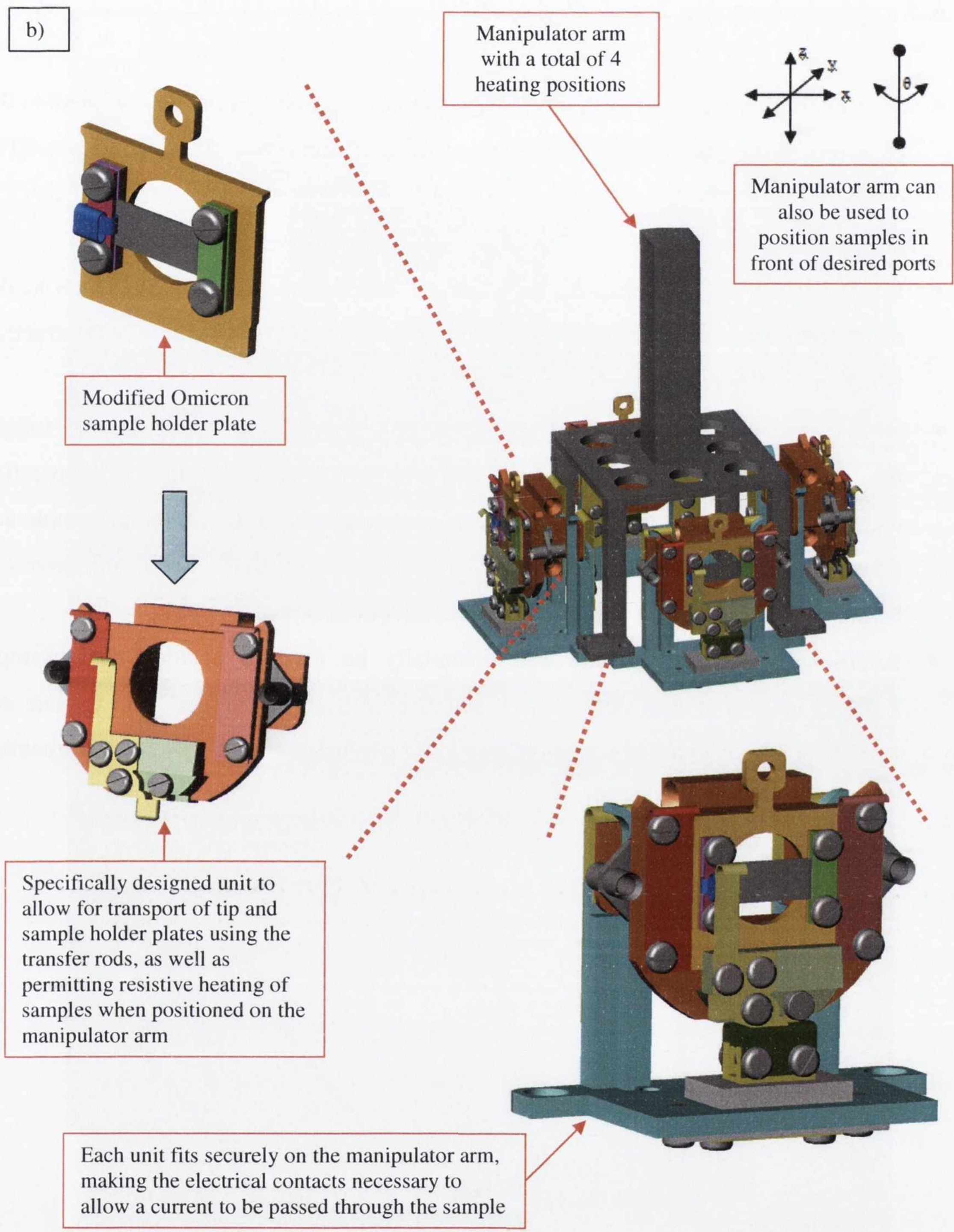

Fig. A.5: Schematic- a) Transfer rods are used to transfer samples and tips from the load lock to the STM chamber and/or the manipulator arm; b) A purposely designed unit (fabricated from suitable materials) allows direct current heating of Si samples when positioned on the manipulator arm using the transfer rods.

A.4. Si(111)-7x7 Surface

- A standard test sample for our UHV STM is the Si(111)-7x7 reconstructions [4]. This surface is reasonably easy to image due to its large unit cell and high corrugation [2].
- However, sample preparation is critical for Si samples since this reconstruction is extremely sensitive to even trace amounts of contaminants e.g. nickel [2].
- To ensure contaminant free samples, nickel-free instruments to cut the Si-wafer and also for mounting the Si-sample are necessary. Si should never be handled with stainless steel tools. Use only molybdenum and/or ceramic coated tweezers. In addition, use only the original supplied Mo wrench for tightening the Mo nuts of the sample holder plate [1].
- A flashing produce according to [5] using our direct current facility in UHV is used to remove oxide layers on S(111) surfaces, thus creating virtually defect free 7x7 reconstructions when observed using our implemented STM; see Fig. A.6 below.

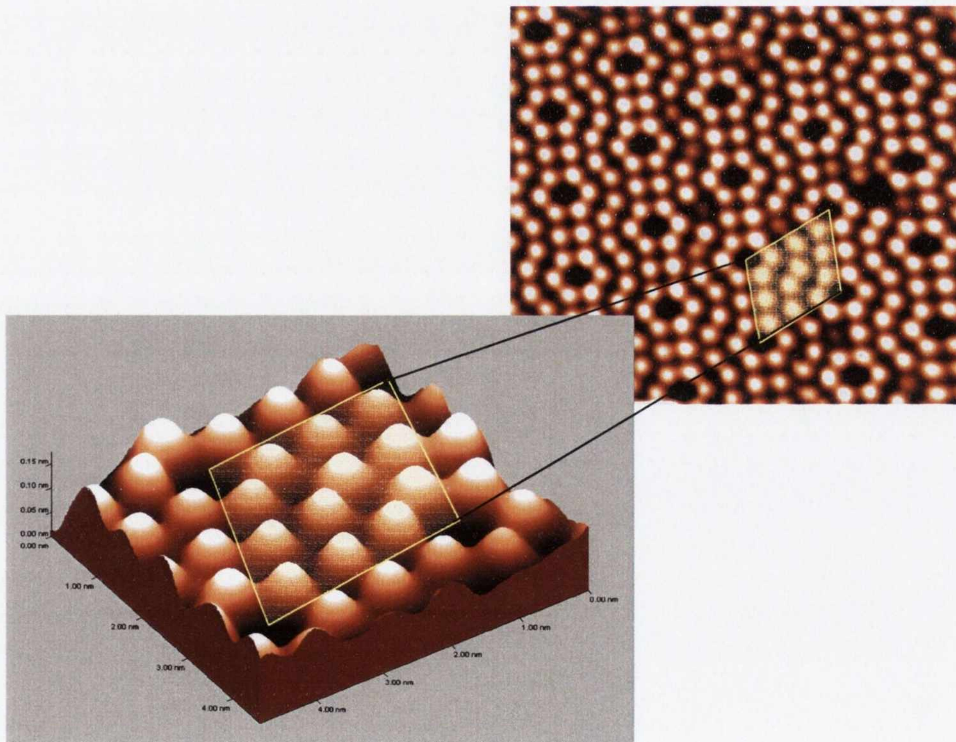

Fig. A.6: STM image of the Si(111)-7x7 surface acquired using our conventional UHV STM set-up. The basis vector length of the unit cell is 2.69 nm and the height of an adatom protrusion is approx. 0.05 nm. This image was acquired with a sample bias of +1 V and a tunneling current of 0.15 nA.

References:

[1] http://www.omicron.de/products/spm/room_temperature/stm_1/media/stm_1_1.pdf.

[2] The UHV STM 1 User's Guide, Omicron Nanotechnology, Taunusstein, Germany.

[3] M. Fouchier, Thesis: Development of an UHV STM, University of North Carolina, Chapel Hill (2000).

[4] H. Neergaard Waltenburg, and J. T. Yates, Chemical Reviews **95**, 1589 (1995).

[5] B. S. Swartzentruber *et al.*, Journal of Vacuum Science and Technology A **7**, 2901 (1989).

Appendix B: Electrical By-pass Unit for Accurate Capacitance Based Deflection Measurements of High Resistance Samples

Our capacitance based set-up for measuring sample bending is displayed in Fig. B.1 and detailed in chapter 6. The detection component for sample bending consists of a cantilever sample (A), a reference electrode (B) and a clamping base (C). Although capacitance measurements between one reference electrode and the sample are basically sufficient, the additional reference electrode (B') guaranteed secure displacement monitoring (i.e. a genuine sample deflection results in a capacitance increase when measured with respect to one reference electrode, and a decrease when measured with respect to the other). Previous reports published by other groups concerning capacitance based deflection measurements lacked such validation [1, 2]. Hence, our simple but vital incorporation of an additional reference electrode is of huge importance as it acts as an integrity test for all acquired stress evolutions. In fact, this set-up proved extremely beneficial in detecting a parasitic effect during experiments involving high resistance samples, which would have otherwise been interpreted as a true sample deflection. To avoid measuring this parasitic capacitance change when using high resistance semiconducting samples, an electrical by-pass unit was introduced. It consists of a flexible metallic wire that is connected to a Ta foil which tightly encapsulates the free end (see Fig. B.1), and is the subject of this appendix.

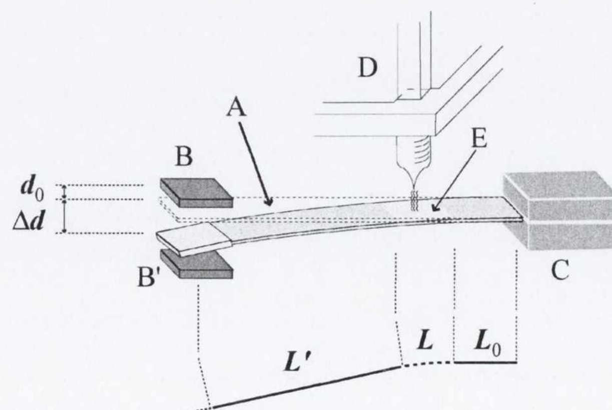

Fig. B.1: Designed system for sample deflection measurement consisting of two reference electrodes to ensure secure displacement monitoring. An electrical by-pass unit is present at the free end when performing experiments using high resistance samples.

B.1. Series versus Parallel Circuit Models [3]

- Real capacitors are not perfect; i.e. they contain loss mechanisms which cause the parallel resistive component of their impedance to be less than the infinite value expected for an ideal capacitor. The leads and plates of capacitors contain some resistance. This appears in series with the actual capacitance. The dielectric material between the plates (in our case vacuum) also contains one or more loss mechanisms that appear in parallel with the actual capacitor.
- A simple model of a real capacitor which contains both the series and parallel resistances is depicted in Fig. B.2 (a).

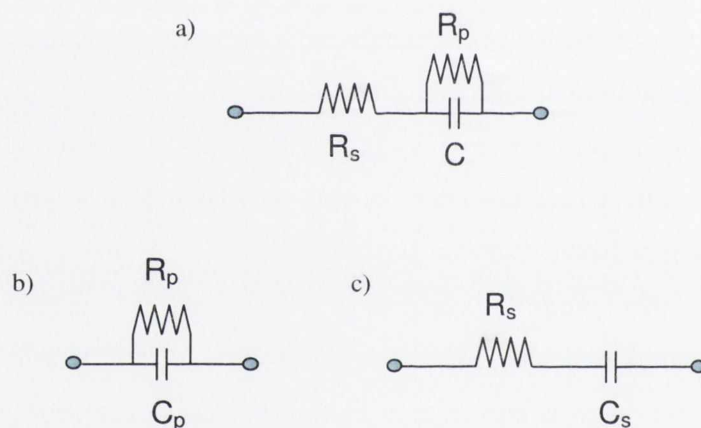

Fig. B.2: a) Capacitor model with both series and parallel resistances; b) capacitor model with loss represented by a single parallel resistor; c) capacitor model with loss represented by a single series resistor.

- The ultra precision capacitance bridge used in our experiments has no way of measuring these two resistances with a single measurement. For each individual measurement the bridge reports either a series resistance or a parallel resistance but not both. Luckily, it is possible to treat both of these resistances as if they were a single parallel or series resistances as depicted in Fig. B.2 (b) and (c), respectively.
- The bridge makes its measurement in the form of parallel capacitance (pF) and parallel loss (loss= $1/R_p$ (nS)), representing the equivalent circuit shown in Fig. B.2. (b). Reference [3] presents a series of equations which demonstrate the close relationship between the measured capacitance and the loss. (In addition, equations

are also presented which allow a series capacitance and series loss to be calculated using the measured parallel equivalents).

- In simple terms, for our capacitance based deflection measurements it is imperative that the effective resistance of the circuit is negligibly influenced by the experimental process; otherwise parasitic capacitance changes are observed which do not represent true sample deflections. Unfortunately, such occurrences can occur when measurements are conducted using high resistance samples as demonstrated below.

B.2. High Resistance Samples- Evidence of Parasitic Effects

A) Light illumination (visible range) effects on capacitance/loss measurements of oxide covered high resistance Si(111) samples (800- 1200 Ω.cm) at room temperature:

- The experimental set-up used for independent measurements involving the front and back electrodes is shown in Fig. B.3. (It is clear from this diagram that the series resistance of the sample is an integral part of the circuit arrangement).

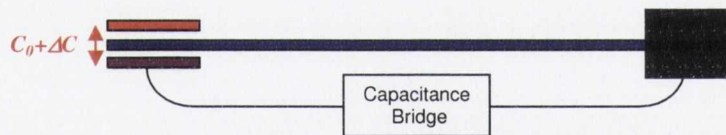

Fig B.3: Measurements are performed using either one of two reference electrodes. One terminal of the capacitance bridge is attached to the front (or back) reference electrode while the other is connected to the clamped end of the cantilever sample.

- On light illumination both front and back electrode measurements displayed an instantaneous capacitance increase (see Fig. B.4 and B.5). This observed effect is not caused by sample deflection as both electrodes showed the same behaviour, and therefore represents a parasitic effect.
- The capacitance increase in each case was accompanied by a simultaneous abrupt decrease in loss. The loss ($=1/R_p$) change is indicative of a resistance change in the equivalent circuit shown in Fig. B.2 (b). Although an increase in the measured

parallel resistance was observed on illumination, this effective change is in all probability induced by a decrease in the series resistance of the sample [3] as a result of photon induced charge carrier excitations [4, 5]. (The observed instantaneous change in loss enforces this argument [4, 5]).

- For a high resistance sample such photon induced excitations can considerably modify the sample conductivity, thereby initiating a capacitance change that is not associated with a true sample deflection. (It is also worth noting that this abrupt event in the capacitance curve can in principle be subtracted as a baseline correction, since the influence remained constant over the illumination period).

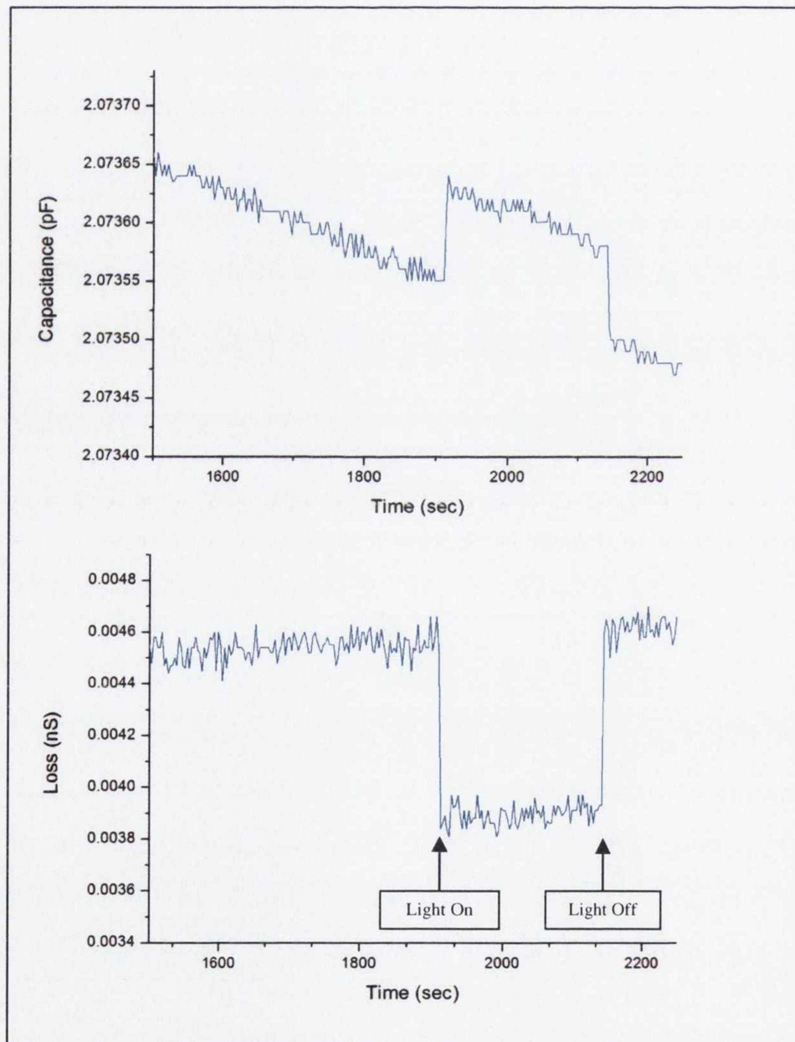

Fig B.4: Capacitance and loss behaviour on light illumination of a high resistance sample (800- 1200 Ω.cm). Measurements were performed using the front side reference electrode.

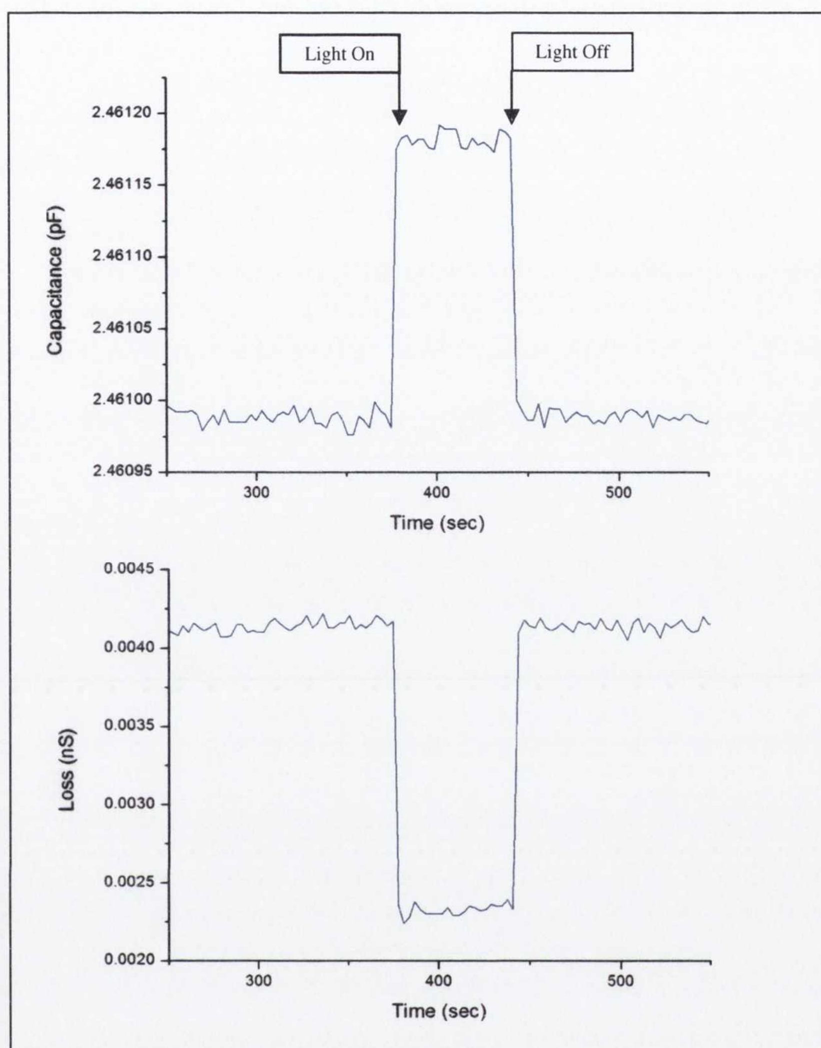

Fig B.5: Capacitance and loss behaviour on light illumination of a high resistance sample (800- 1200 Ω.cm). Measurements were performed using the back side reference electrode. The observed behaviour is very similar to that shown in Fig. B.4. Therefore, a genuine sample deflection was not detected.

B) Capacitance (and loss) measurements during oxygen exposure of clean Si(111)-7x7 surfaces at room temperature using high resistance cantilever samples (800- 1200 Ω.cm):

- A clean region was created on a Si(111)-7x7 high resistance cantilever sample using our novel bimetallic heating method [6]. Following this the sample was allowed to cool to room temperature and oxygen gas was introduced to a pressure of 7.5×10^{-9} Torr. The resulting capacitance and loss evolutions were measured during the exposure period using the back side reference electrode. The results are shown in

Fig. B.6. Following this the experiment was repeated using the front side reference electrode (see Fig. B.7).

- In each case, the introduction of oxygen gas resulted in an observable capacitance decrease as a function of time (with an accompanying loss increase). Consequently, a true sample deflection due to the reaction process is not detected.

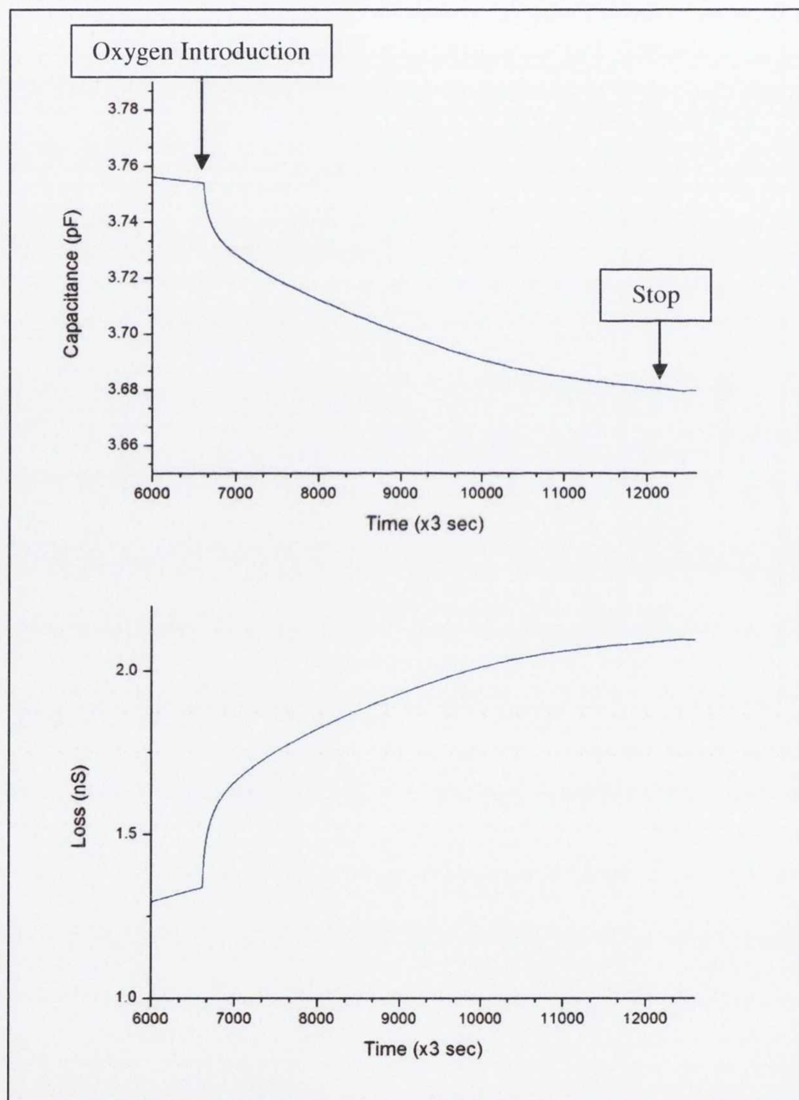

Fig B.6: Capacitance and loss behaviour on oxygen exposure to a high resistance sample (800- 1200 Ω.cm). Oxygen gas was introduced to a pressure of $7.5x10^{-9}$ Torr. Measurements were performed using the back side reference electrode.

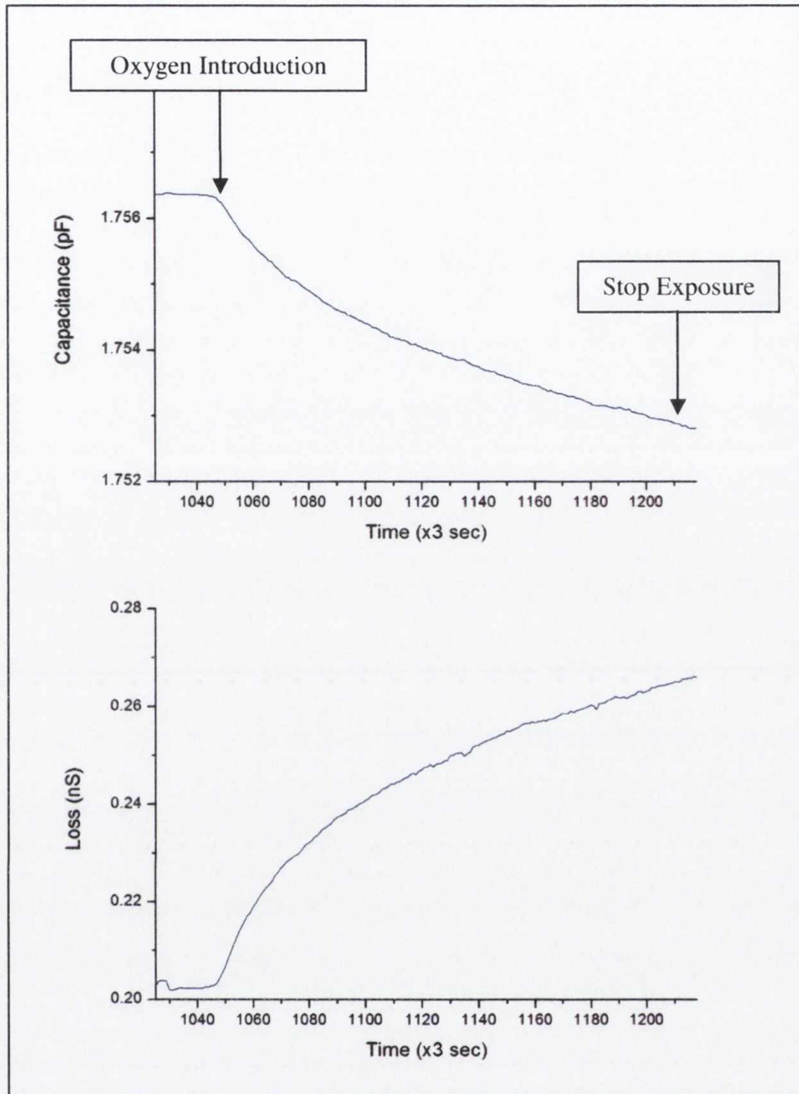

Fig B.7: Capacitance and loss behaviour on oxygen exposure to a high resistance sample (800- 1200 Ω.cm). Oxygen gas was introduced to a pressure of $7.5x10^{-9}$ Torr. Measurements were performed using the front side reference electrode. The observed behaviour is very similar to that shown in Fig. B.6. Therefore, a genuine sample deflection was not detected.

- Again, we assign this parasitic effect to a change in the series resistance of the sample; namely a series resistance increase. The conductivity σ ($\equiv 1/R$) including both bulk (σ_b) and surface (σ_s) contributions is given by $\sigma = \int_0^d [\sigma_s(z) + \sigma_b] dz / d$, where d is the wafer thickness [7]. *Hasagawa et al.* succeeded in measuring the electrical conduction through a surface state band inherent to the 7x7 surface

superstructure [8]. *Hasagawa at al.* also showed that rearrangement of atoms in only one or two atomic layers on the topmost 7x7 surface actually affects the electronic transport properties [8] and demonstrates the close correlation of the electrical properties with atomic structure [7]. We anticipate that as the surface adatoms react with oxygen atoms [9, 10], the surface component of the sample resistance progressively increases due to the removal of carriers from the surface state band. Therefore, the perceived capacitance decrease is almost certainly associated with this event due to their inherent relationship.

- Interestingly, the trend in capacitance shows a sharp decrease followed by a more gradual evolution. Although this trend does not represent a sample deflection it may be indirectly tracking the reaction rate of the surface dangling bonds via changes of the surface conductivity; the majority of adatoms react quickly on oxygen exposure thus reducing the surface conductivity substantially, followed by a more gradual reaction rate until saturation is achieved.
- While the total conductivity of high resistance samples can be considerably modified by light illumination and by surface reaction processes, low resistance samples (~0.01 Ω.cm) are much less sensitive [4, 5]. As a result, these samples do not exhibit observable parasitic capacitance changes, thus allowing accurate deflection measurements to be conducted. Alternatively, high resistance samples can be used for precise measurements of sample bending when coupled with an electrical by-pass arrangement as depicted in Fig B.8.
- The by-pass unit permits a bias to be applied to the free end of the cantilever sample only. When properly constructed the by-pass unit allows the sample resistance to be decoupled from the measurement, thus permitting accurate deflection sensing. This short-cut consists of a very fine flexible metallic wire that is directly connected to a Ta foil which tightly encapsulates the free end region of the sample. The by-pass unit is made from tantalum foil, to prevent metal contamination of the sample. Fig. B.9 presents photographs of this arrangement.

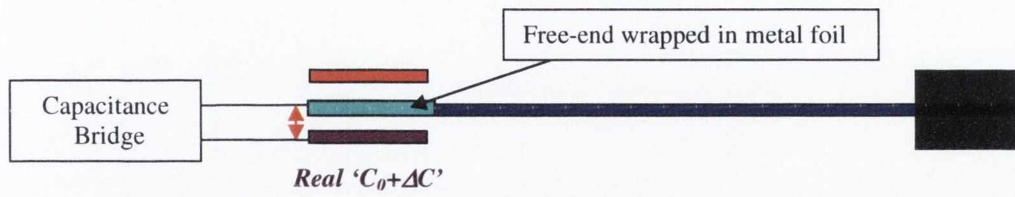

Fig B.8: Schematic diagram representing the by-pass unit arrangement used to accurately measure free end deflections when high resistance samples are used.

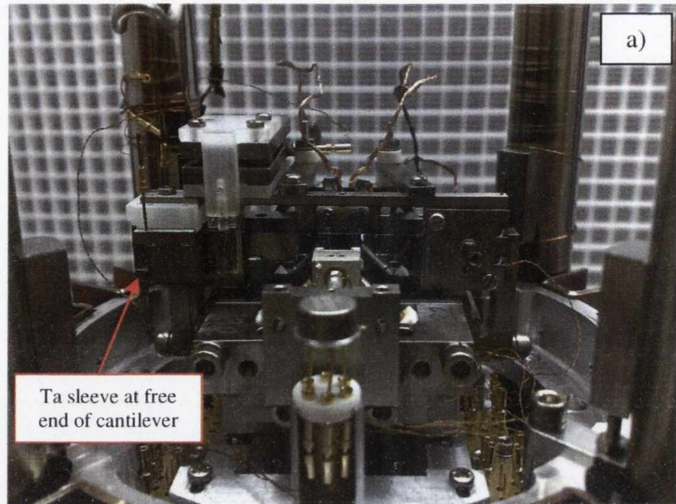

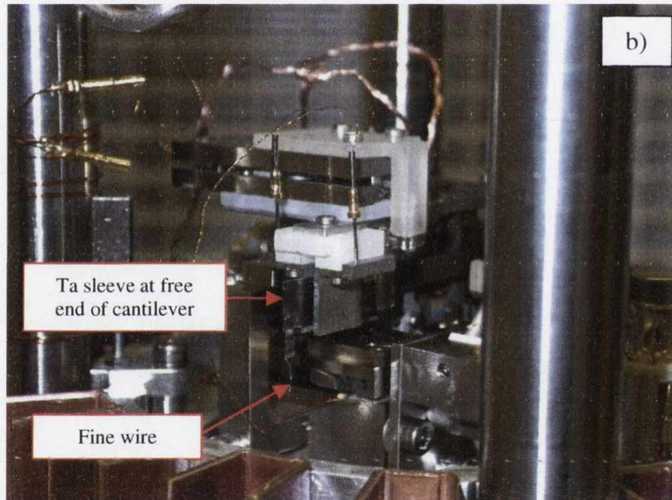

Fig B.9: Photographs a) and b) displaying our by-pass unit which is used for experiments involving high resistance samples.

B.3. Accurate Deflection Measurements

- In this section data is presented which verifies that true sample deflections are detected on light illumination and oxidation of low resistance samples. Furthermore, it should be noted that the observed behaviours are identical to those obtained using high resistance samples with a sleeve accompaniment; consequently for brevity this data is not displayed.

* Light illumination of a low resistance (0.008- 0.012 Ω.cm) oxide covered Si(111) sample at room temperature: Fig. B.10 displays the capacitance and accompanying loss evolutions for a back side reference electrode measurement, while Fig. B.11 represents the equivalent front side measurements.

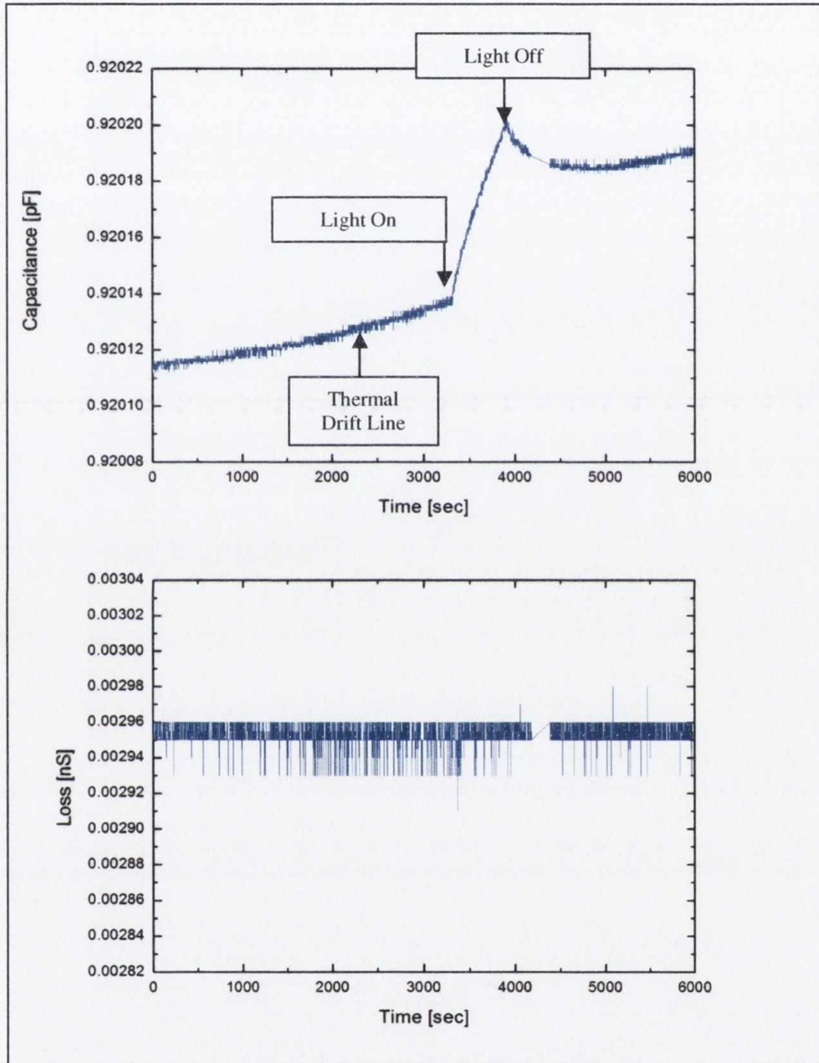

Fig B.10: Capacitance and loss behaviour on light illumination of a low resistance sample (0.008- 0.012 Ω.cm). Measurements were performed using the back side reference electrode.

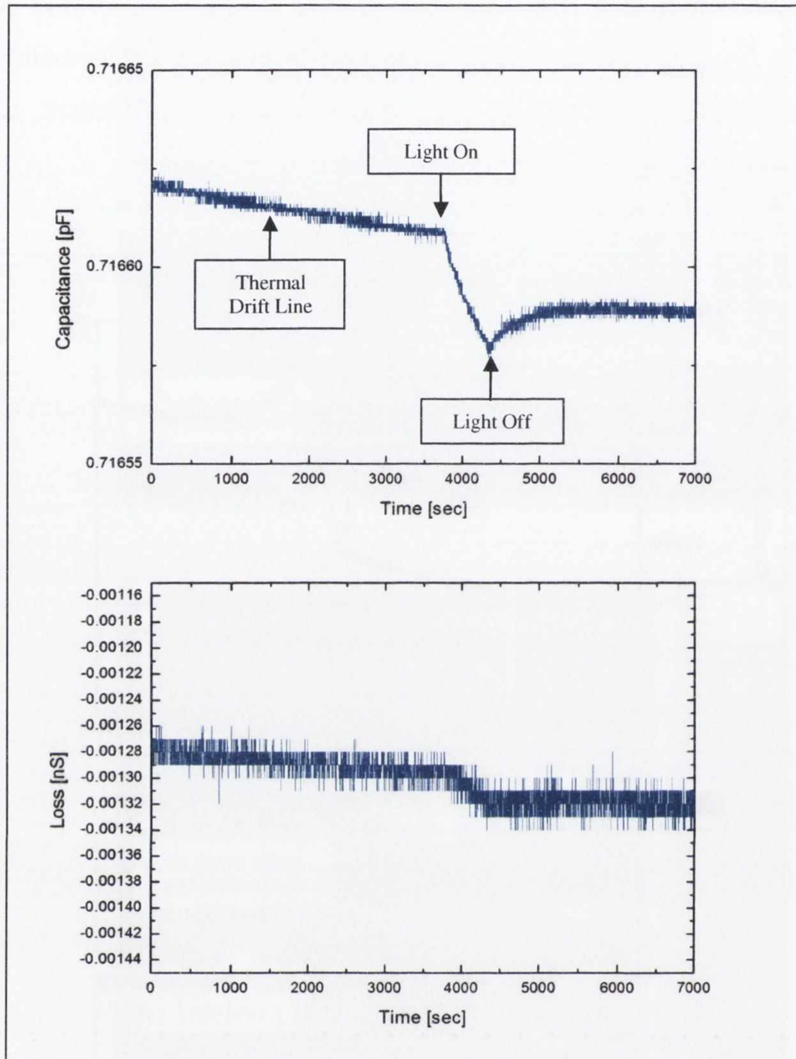

Fig B.11: Capacitance and loss behaviour on light illumination of a low resistance sample (0.008- 0.012 Ω.cm). Measurements were performed using the front side reference electrode. The capacitance trend is opposite to that obtained in Fig. B.10. Therefore, a true sample deflection was detected.

- It should be noted that the light source was not moved during the course of these experiments and was predominantly directed towards the front side of the cantilever sample.
- From Fig. B.10 and Fig. B.11 it is evident that opposite behaviours occurred in the capacitance evolutions when the light source was switched on; i.e. a gradual capacitance increase was detected using the back side reference electrode, while a gradual capacitance decrease was detected for the front side equivalent. This signifies that a genuine sample deflection was detected.
- The observed capacitance behaviour may be assigned to photon induced heating of the cantilever sample. Since the front side of the cantilever was exposed to a greater intensity of incident photons relative to the back side (i.e. radiant energy), this surface underwent greatest expansion, resulting in the cantilever bending towards the back side reference electrode.
- On switching off the light source, both capacitance evolutions gradually returned to the initial thermal drift line, which is consistent with sample bending due to a cooling event.
- Regarding the loss, no remarkable changes were observed in Fig. B.10 and Fig. B.11. This is to be expected as the series resistance of a highly doped sample is negligibly influenced on illumination via visible light [4, 5], thereby avoiding parasitic influences on deflection measurements.
- Capacitance and loss measurements were also performed during oxygen exposures to clean Si(111)-7x7 surfaces using low resistance samples (see chapter 7 for details). Typical results obtained for measurements using back and front reference electrodes are displayed in Fig. B.12 and Fig B.13, respectively.
- It is apparent from these results that a true sample deflection was detected due to atomic scale reaction processes on the surface; an interpretation of these events is provided in chapter 7.
- In conclusion, we have an excellent sensor that is capable of accurately measuring cantilever deflections of low resistance samples. In addition, the by-pass unit opens up the avenue for accurate capacitance based deflection measurements on high resistance cantilever samples (Si or otherwise).

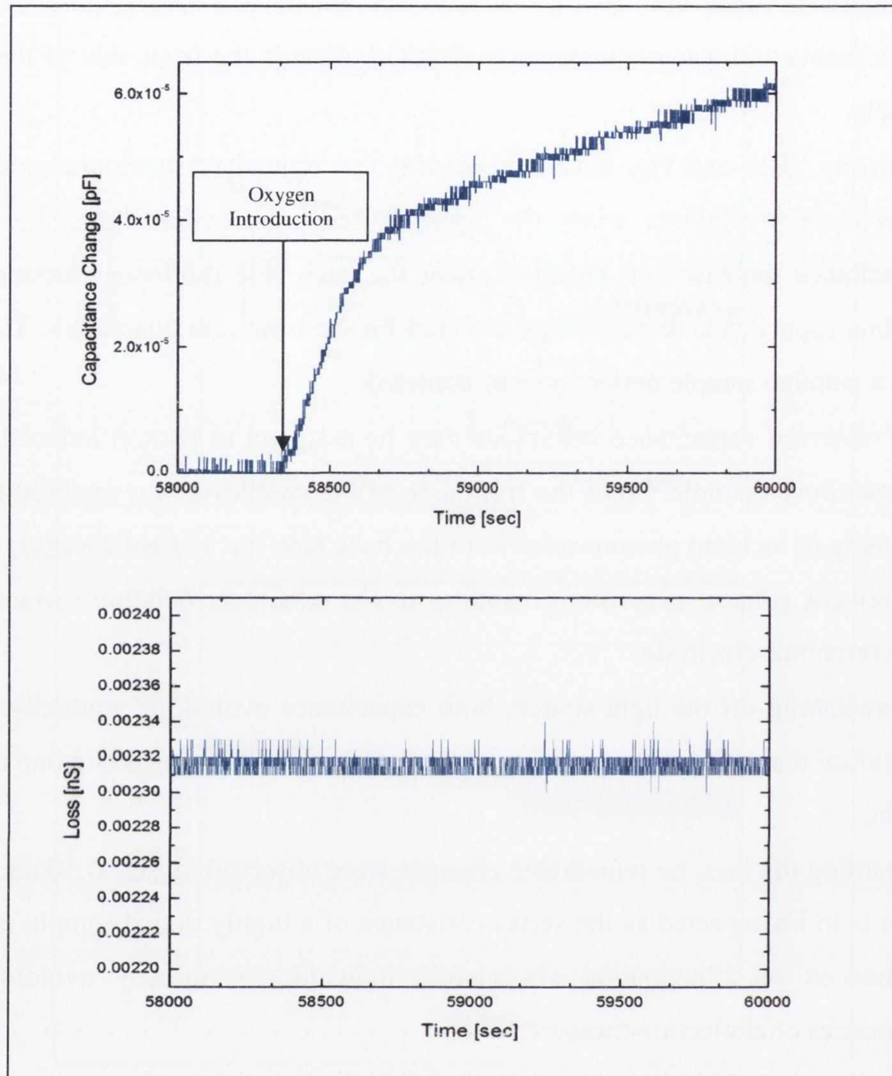

Fig B.12: Capacitance and loss behaviour on oxygen exposure to a low resistance sample (0.008- 0.012 Ω.cm). Oxygen gas was introduced to a pressure of $2x10^{-9}$ Torr. Measurements were performed using the back side reference electrode.

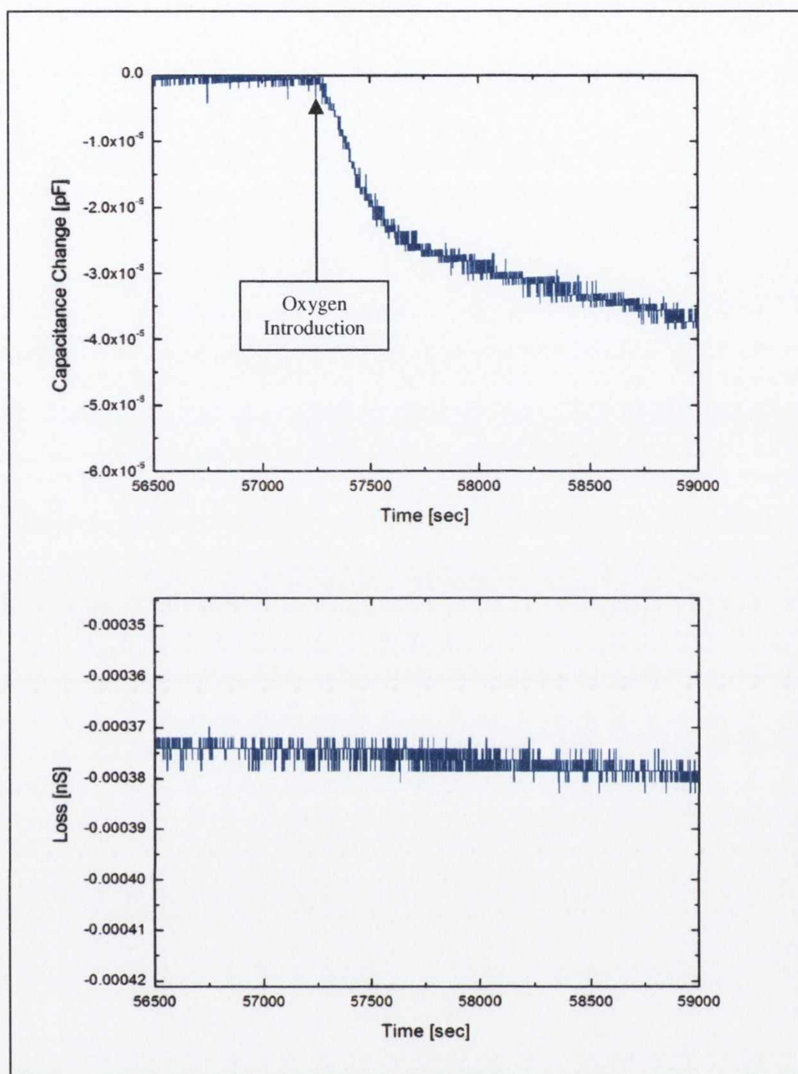

Fig B.13: Capacitance and loss behaviour on oxygen exposure to a low resistance sample (0.008- 0.012 Ω.cm). Oxygen gas was introduced to a pressure of $2x10^{-9}$ Torr. Measurements were performed using the front side reference electrode. The observed capacitance trend is opposite to that obtained in Fig. B.12; therefore a true sample deflection was detected.

References:

[1] H. Ibach, Surface Science Reports **29**, 195 (1997).

[2] D. Sander, and H. Ibach, Physical Review B **43**, 4263 (1991).

[3] User Manual, Model AH 2550A, Andeen-Hagerling, Inc., 31200 Bainbridge Road, Cleveland, Ohio 44139-2231.

[4] J. I. Pankove, *Optical Processes in Semiconductors* (Dover Publications, Inc., New York, 1971).

[5] S. M. Sze, *Physics of Semiconductor Devices* (John Wiley & Sons, New York, 1981).

[6] T. Narushima, N. T. Kinahan, and J. J. Boland, Review of Scientific Instruments **76**, 095113 (2005).

[7] C. S. Jiang, S. Hasegawa, and S. Ino, Physical Review B **54**, 10389 (1996).

[8] S. Hasegawa *et al.*, Surface Review and Letters **5**, 803 (1998).

[9] H. Okuyama, T. Aruga, and M. Nishijima, Physical Review Letters **91**, 256102 (2003).

[10] H. Okuyama, Y. Ohtsuka, and T. Aruga, The Journal of Chemical Physics **122**, 234709 (2005).

Appendix C: Tip Accessing of the Cantilever Sample to Perform STM Measurements

Due to the construction of our special sample holder (see chapter 6), the region to be scanned is located 9 mm above the conventional Omicron STM location. To compensate for this height difference, attempts were made to scan this region using purposely fabricated tip holders which are taller than standard Omicron arrangements; see Fig. C.1. However, these tip structures were not rigid enough to permit atomic resolution imaging of the cantilever surface. Therefore the scanner assembly was raised using a 2 mm thick UHV grade stainless steel plate (Fig. C.2), which allowed: a) conventional tip holders to be used and; b) atomic resolution images to be acquired.

C.1. Tall Tip Structures

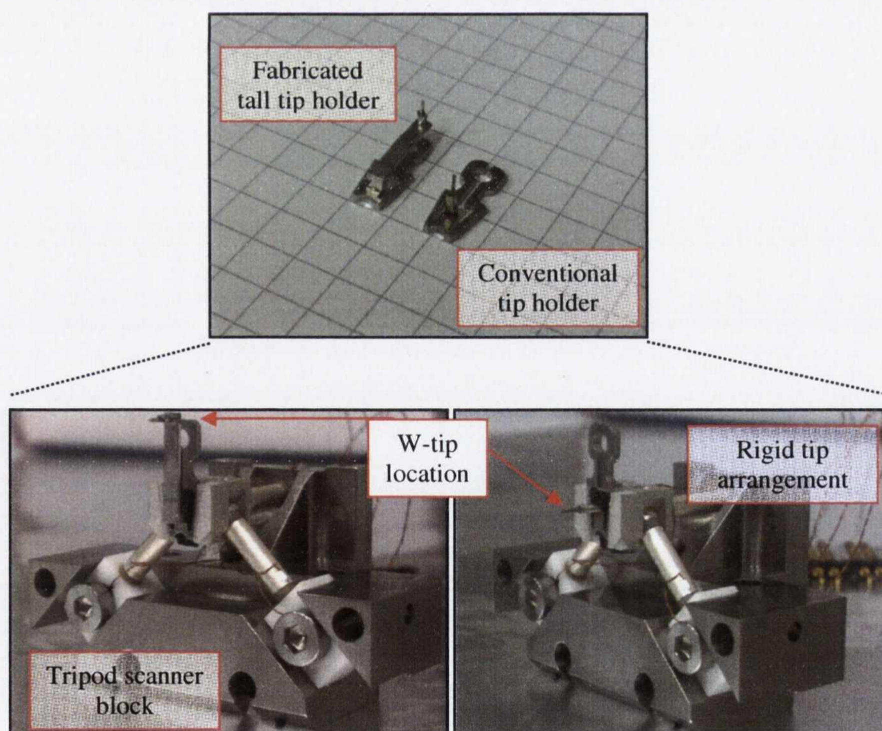

Fig. C.1: Initial attempts were made to scan the inaccessible cantilever sample using purposely fabricated tip holders. However, atomic scale images were not achieved due to poor structural rigidity.

C.2. Raised Tripod Scanner Assembly

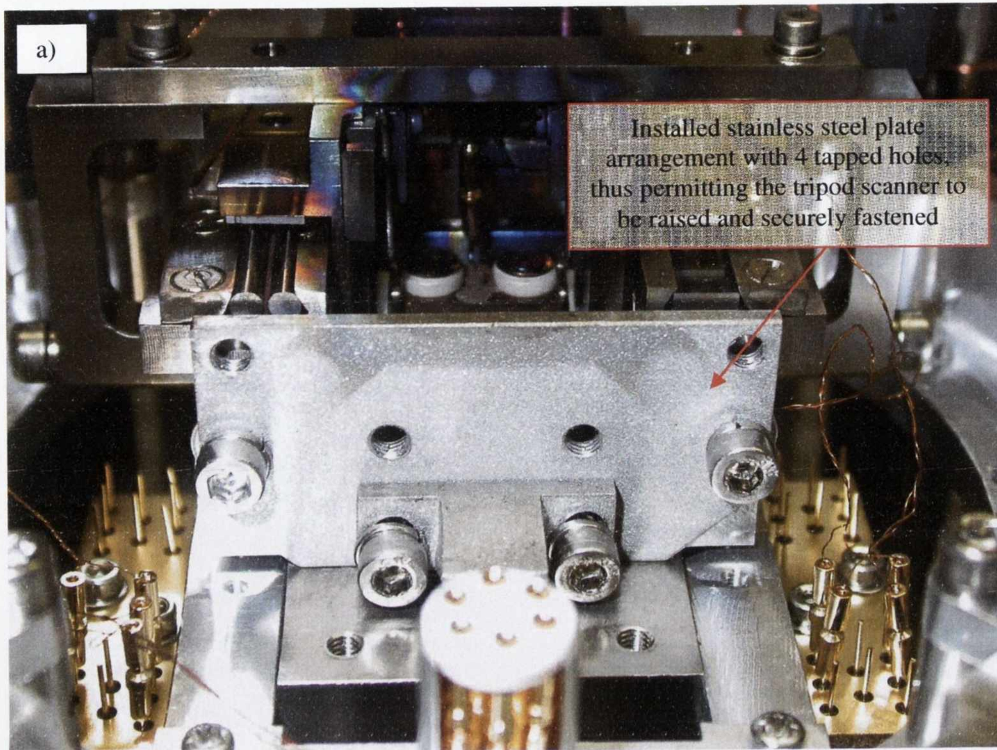

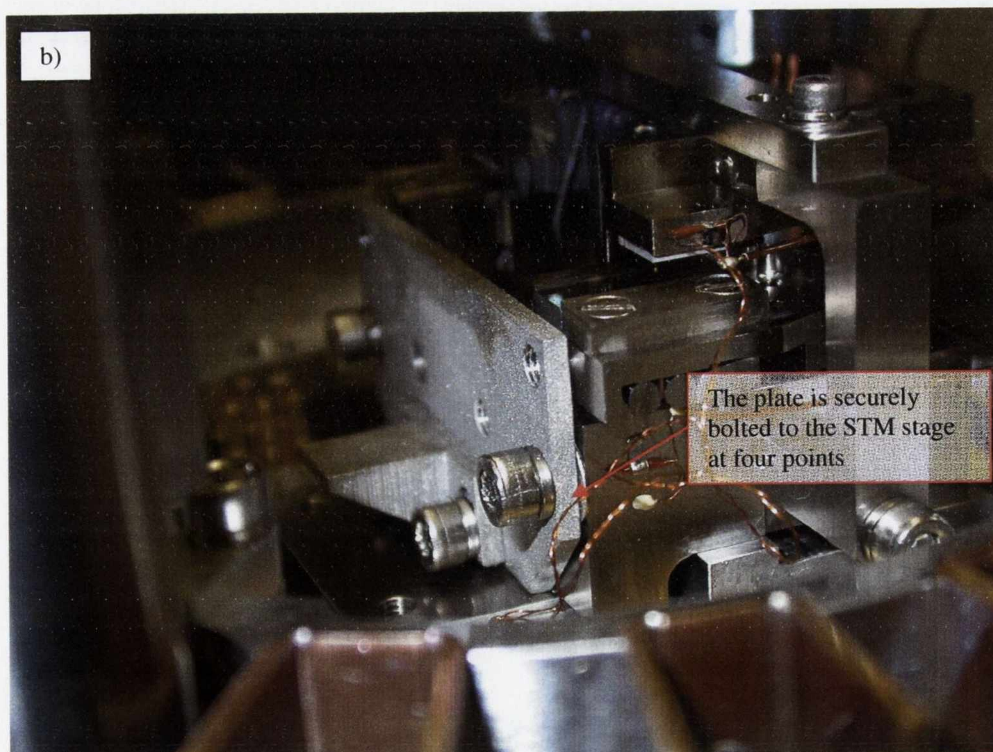

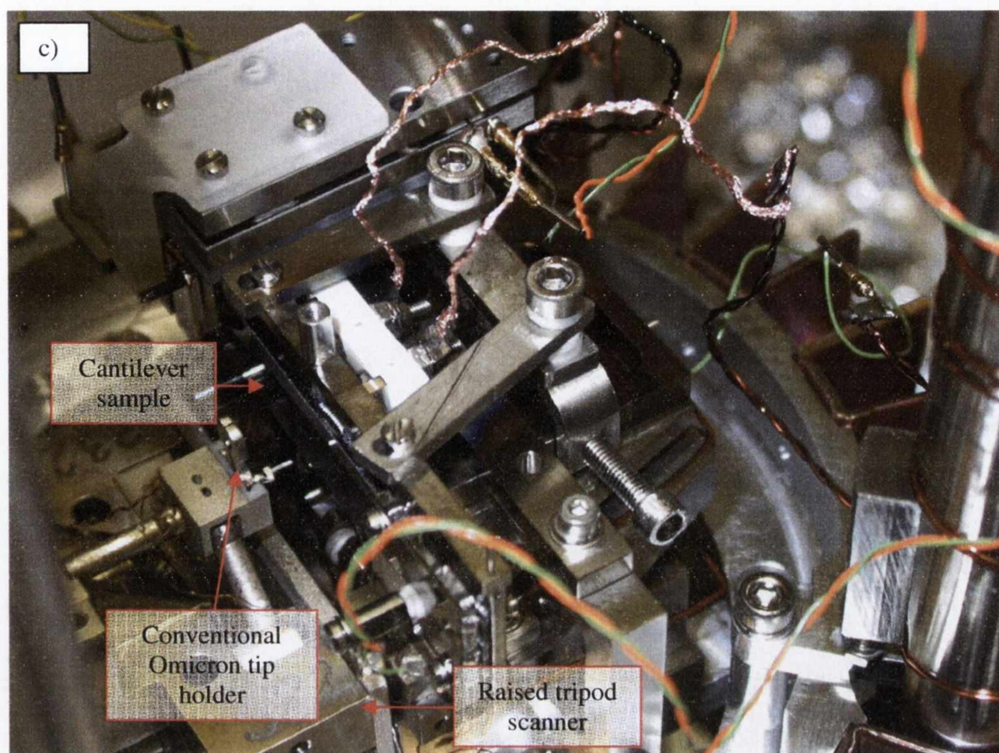

Fig. C.2: A 2mm thick UHV grade stainless steel plate was used to raise and securely fasten the tripod scanner arrangement- a) front view of the plate; b) side view of the plate; c) raised scanner assembly allows the cantilever surface region to be accessed, this permitting atomic resolution imaging using conventional tip holders.

Appendix D: Shield Unit for Sample Heating Methods

The development of sample heating methods capable of preparing clean sample surfaces and investigating high temperature studies was an important task in the implementation of our novel system for combined STM and surface stress measurements. Presently, all heating procedures are conducted on the STM stage. This configuration demands extreme caution when carrying out all heating procedures in order to protect several delicate components from accidental damage. In addition, care must be taken to ensure that outgassing from surrounding parts does not jeopardise the Si surface condition. During all heating procedures, it is necessary to insert a shield unit at the tripod scanner location (namely at the tip insertion position) to prevent contamination of the sample surface due to outgassing from a constituent rubber like material which is in very close proximity to the heated sample surface; this topic is the subject of this appendix.

D.1. Kalrez [1]

- Kalrez is a registered trademark of DuPont Performance Elastomers. This material is black in appearance and is composed of perfluoroelastomer (>75 %), carbon black (<20 %), and accelerators/curatives (<6 %). This material has excellent chemical resistance and offers a wide range of beneficial properties.
- Its primary functions at the tip location of the tripod scanner are to provide secure fixing of the tunneling tip and also to act as a dampening medium for tip vibrations. The Kalrez component of the tripod scanner is displayed in Fig. D.1.
- In conventional STM systems this elastomeric material would not be heated by more than ~150 ^{o}C (due to bake procedure). However, because of our modified arrangement this is no longer true. Sample heating on the STM stage may lead to a sizeable temperature rise of the Kalrez material, as the tip is removed during all heating processes.

- High temperature spikes can degrade the elastomer causing their cross-linking structure to become irreversibly damaged. Additionally, elastomeric degradation under high temperatures (>200 °C) causes outgassing to occur, thereby contaminating the sample surface; see Fig. D.2. (In fact, if heated above 400 °C, HF can evolve as a degradation product).
- To protect against this occurrence during sample heating a shield unit was designed.

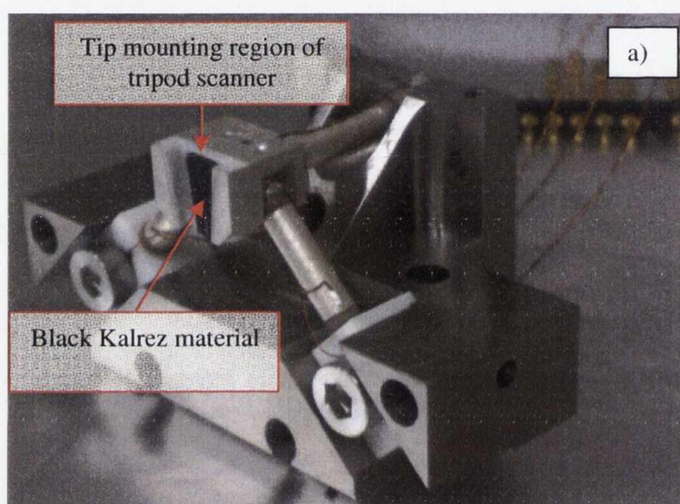

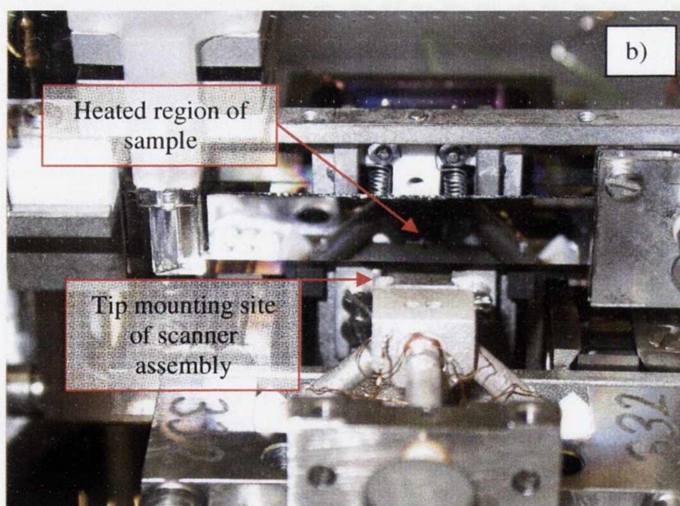

Fig. D.1: a) Photograph displaying the exposed Kalrez material on removal of the STM tip; b) photograph of our novel configuration illustrating the close proximity of the Kalrez to the heated region.

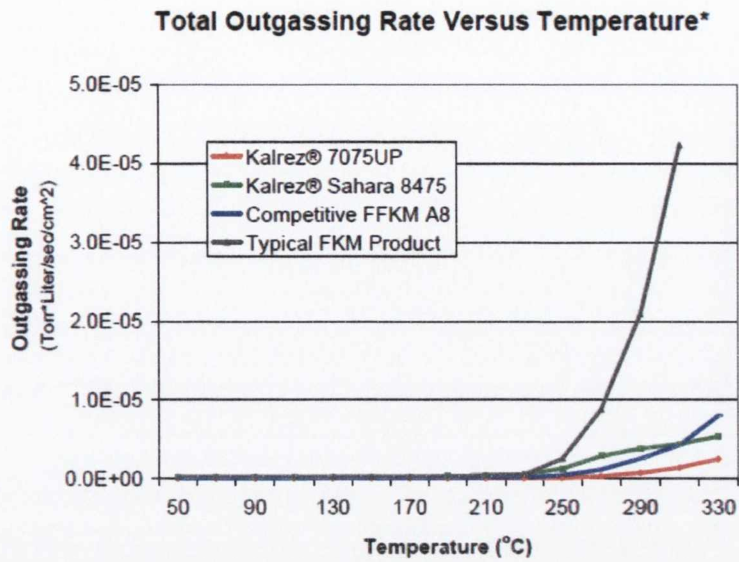

Fig. D.2: Total outgassing rate versus temperature for various Kalrez materials [1].

D.2. Shield Unit

- The shield unit was fabricated from an Omicron tip carrier and Ta foil. The resulting structure is displayed in Fig. D.3.

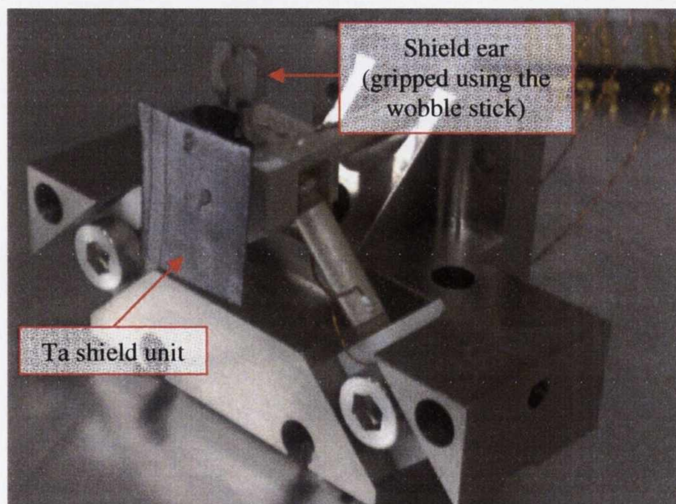

Fig. D.3: Our fabricated shield unit.

- The shield unit prevents radiant energy reaching the Kalrez material by acting as a heat sink and reflective surface. It also protects the piezo tubes of the scanner assembly as they may become depolarised due to excess heating.
- On initial installation of the shield unit a noticeable decrease in outgassing levels during heating was immediately apparent, which resulted in significantly cleaner sample surfaces when viewed via STM.
- The shield unit can be transferred to/from the carousel using the wobble stick (a tip holder plate on the carousel permits this movement).

References:

[1] www.dupontelastomers.com/kalrez.

Appendix E: Bimetallic Heating of a Cantilever Sample

In chapter 6, we introduced a novel method to heat up a free-standing sample such as cantilever using two bimetallic strips (with accompanying contacting springs). Using this approach we can heat a specific region of a Si cantilever sample up to 1400 K, thus removing the oxide passivating layer and exposing a clean surface. This method is simpler to implement than that of a movable contact involving a piezo electric element. Moreover, by tailoring each bimetallic strip with a double looped spring design, it is possible to eliminate stresses in the cantilever substrate itself while at the same time ensuring excellent electrical contacts. The purpose of this appendix is to describe the basic experimental procedure to carry-out a successful flash procedure using this method under ultra-high vacuum conditions.

E.1. Bimetallic Heating Procedure [1]

- The steps involved in the preparation of a clean Si(111)-7x7 surface will now be presented, to demonstrate the effectiveness of our unique heating method. The set-up used is displayed in Fig. E.1 below.

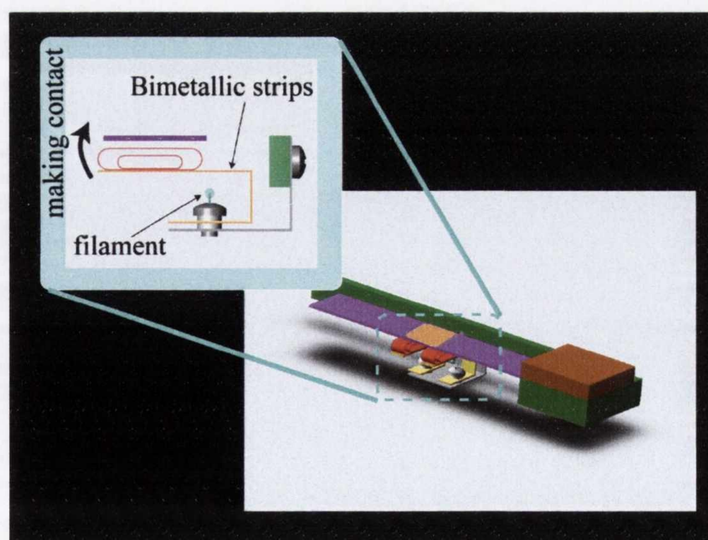

Fig. E.1: The heating system for a cantilever sample with use of two bimetallic strips.

- The Si(111) cantilever samples used are cut from a single-side mirror polished wafers, which are p-type boron doped, with a thickness of 525±10 μm and resistivity of 5.0- 18.0 Ω.cm. The base pressure is typically $<5 \times 10^{-11}$ Torr.
- The flash procedure is described below:
    - ♦ Electrical contact is judged by measuring the change in resistance between each bimetallic strip and the clamped end of the cantilever sample.
    - ♦ For this purpose, a wide-range resistance meter is used which can measure resistances over 100 MΩ (resistance values on initial contact are typically in excess of 10 MΩ).
    - ♦ Prior to passing current through the filament, the resistance values between the sample and each bimetallic strip are checked; both of which should register non-contact under correct design conditions.
    - ♦ On switching on the filament, deflection of each bimetallic strip occurs. When stable, good quality electrical contacts with the sample are formed, a resistance of 0.1-1 MΩ is normally measured between each contact point and the cantilever clamp. (Reliable electrical contacts are typically established with a filament input power of ~4 W, thus permitting resistive heating of the sample).
    - ♦ A current (~6 A) can then be briefly passed (~10 secs) through the cantilever sample via the bimetallic strips to prepare the 7x7 surface. (Note: During the passage of current it is not necessary to maintain the filament current, as heat from the sample is sufficient to preserve both electrical contacts, thereby minimising outgassing).
    - ♦ By monitoring the colour of the Si sample, a temperature of approx. 1400 K should be achieved without difficulty. In addition, a uniformly heated area on the cantilever surface should be observed under correct contacting conditions. (Typical outgassing levels on flashing: $\sim 1 \times 10^{-9}$ Torr).
    - ♦ This flash process is usually repeated up to 3 times (insuring that a suitable time period has elapsed between heating cycles to allow for base pressure recovery). Following the flash the filament is switched off and contacts to the sample are broken as desired.

E.2. Resultant Surface Condition

- Scanning tunnelling microscopy can be used to observe the surface morphology of the heated region of the cantilever sample following flashing [1, 2]. A typical result is displayed in Fig. E.2 below.
- On the atomic scale, we find evidence of well ordered 7x7 domains. Additionally, visible levels of carbon contamination are apparent; imaged as white blobs which pin the surface steps. (We are currently in the process of optimising this set-up to reduce the observed levels of carbon contamination).
- This result clearly demonstrates that our novel heating method can be used to prepare reasonably clean Si(111)-7x7 surfaces on cantilever samples.

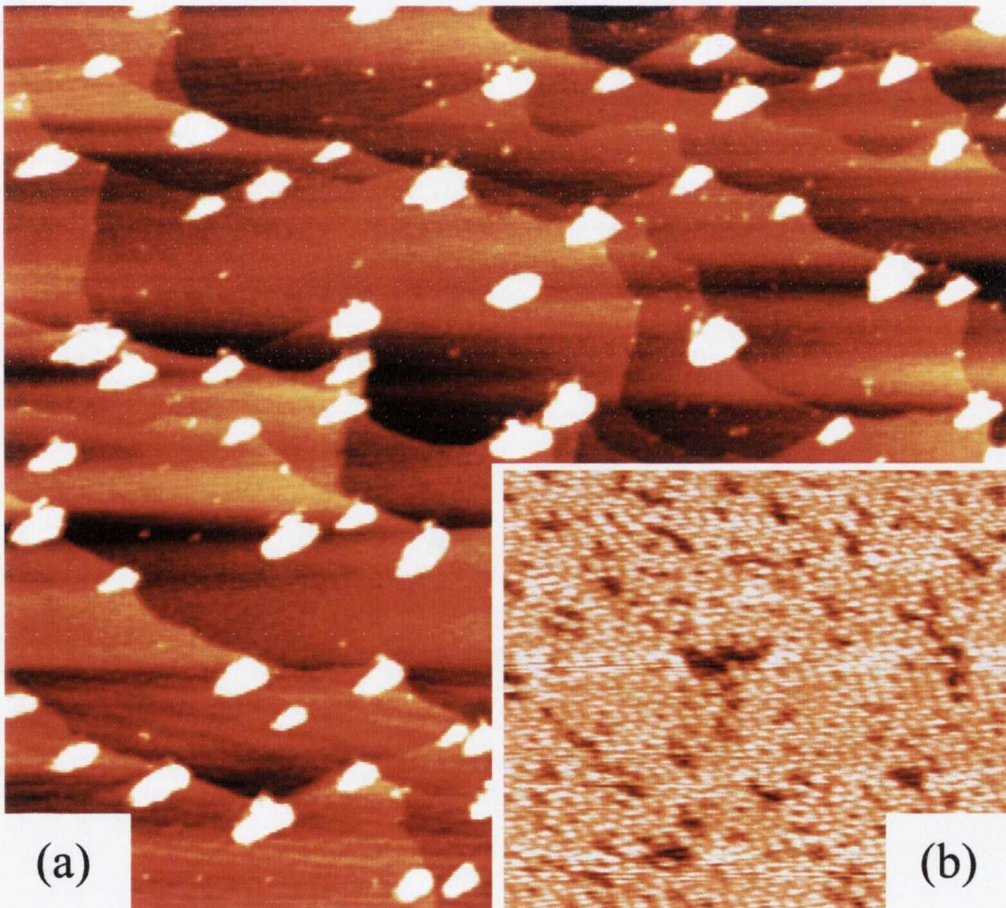

Fig. E.2: This is the famous Si(111)-7x7 surface which was observed on the cantilever sample following flashing using our unique bimetallic heating method. Image scales: (a) 334×273 nm and (b) 15×15 nm.

References:

[1] T. Narushima, N. T. Kinahan, and J. J. Boland, Review of Scientific Instruments **76**, 095113 (2005).

[2] T. Narushima, N. T. Kinahan, and J. J. Boland, Review of Scientific Instruments **78**, 053903 (2007).

Appendix F: Potential Commercial Applications of Our Bimetallic Heating Set-up

In chapter 6, a simple method to heat a free-standing sample such as a cantilever using bimetallic strips was described. The bimetallic strips are used to make controlled electrical contacts on radiative heating of the strips by a W filament [1]. In order to improve the electrical contacts and have good reproducibility, a double looped spring design was employed. Using this method, we can heat-up free-standing samples to 1400 K. In addition, by employing two bimetallic strips with the double looped spring design, regionalised heating of the sample can be achieved. It can be appreciated that bimetallic strips according to the invention are suitable for use in a variety of systems and applications where controlled electrical and/or mechanical contact is required [2]. This appendix summarises some of the potential commercial applications that we envisage.

F.1. Valves (Microelectromechanical systems (MEMS) with micro-actuation)

Microvalves are primarily used in industrial systems that require precision control of gas flow for manufacturing processes, or in biomedical applications such as in controlling the blood flow in artery's. A growing market for microvalves is in the pharmaceutical industry where these valves are used as a principal component in microfluidic systems for precision analysis and separation of constituents. Microvalves operate on the principles of microactuation. As illustrated in the Fig. F.1 the heating of the two electrical contacts attached to the top diaphragm can cause a downward movement to close the passage of flow. Removal of heat from the diaphragm opens the valve again to allow the fluid to flow. The conducting strips may be heated via the passage of current through them following contacting using bimetallic strips. Also, through contact with the diaphragm, predefined amounts of heat may be supplied, allowing for a pulsating microvalve to be created which may have interesting applications. Using a series of strips would provide added functionality and flexibility to the system.

Alternatively the diaphragm may be operated via harnessing the force generated by moving bimetals.

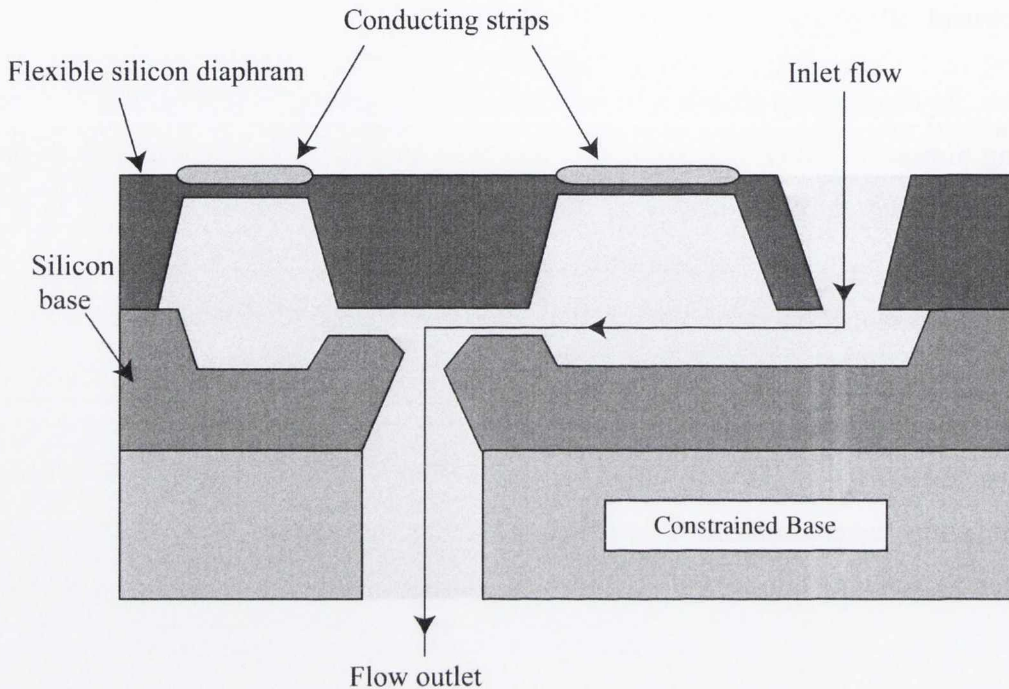

Fig. F.1: The microvalve is operated by heating conducting strips via the passage of current through them following contacting using bimetallic strips. Alternatively the diaphragm may be operated via harnessing the force generated by moving bimetals.

F.2. Pumps (Microelectromechanical systems (MEMS) with micro-actuation)

A simple micropump can be constructed by using the electrostatic actuation of a diaphragm as illustrated in Fig. F.2. The deformable silicon diaphragm forms one electrode of a capacitor. It can be actuated and deformed toward the top electrode by applying a voltage across them. The upward motion of the diaphragm increases the volume of the pumping chamber and hence reduces the pressure in the chamber. This reduction of pressure causes the inlet check valve to open to allow inflow of fluid. The subsequent cut-off of the applied voltage prompts the diaphragm to return to its initial position, which causes a reduction of the volume in the pumping chamber. This reduction of volume increases the pressure of the entrapped fluid in the chamber. The outlet check valve opens when the entrapped fluid reaches a designed value, and fluid is released. A

pumping action can thus be achieved. Contact to the electrodes using bimetallic strips may be used to achieve this pumping action via biasing of the electrodes on contact. Bimetallic strip arrays may also be used to provide additional functionality and flexibility to the pumping system. Alternatively the diaphragm may be operated via harnessing the force generated by moving bimetals.

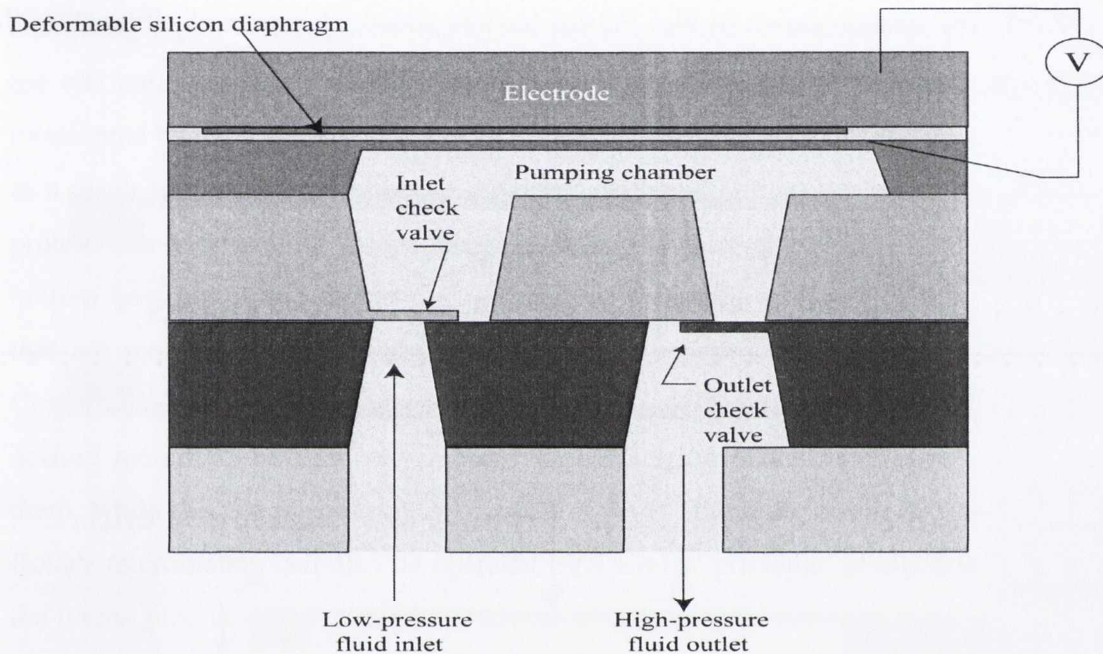

Fig. F.2: Micropump- contact to the electrodes using bimetallic strips may be used to achieve the pumping action via biasing of the electrodes on contact. Alternatively the force generated by moving bimetals can be utilised to achieve the desired pumping effect.

F.3. Grippers (Microelectromechanical systems (MEMS) with micro-actuation)

Referring to Fig. F.3 (a) and (b), grippers for use as micromanipulators or robots in micro-manufacturing processes or microsurgery, incorporating bimetallic strips according to the invention, are illustrated. There are two modes of operation:

A) Application of electrostatic force in which an actuator delivers a desired motion when it is driven by a power source. The electrostatic force generated in parallel charged electrode plates can be used as the driving force for gripping objects. The

electrostatic force between each electrode can be achieved by contacting each electrode with a bimetallic strip and applying a bias between them.

B) Application of physical force- actuation may be achieved via direct manipulation using the motion of the bimetallic strips themselves.

In addition, bimetallic strip arrays provide flexibility of motion, i.e. extra modes of motion. The system shown in Fig. F.3 (b) has the added advantage of eliminating the excessive space that the electrodes occupy in a micro-gripper.

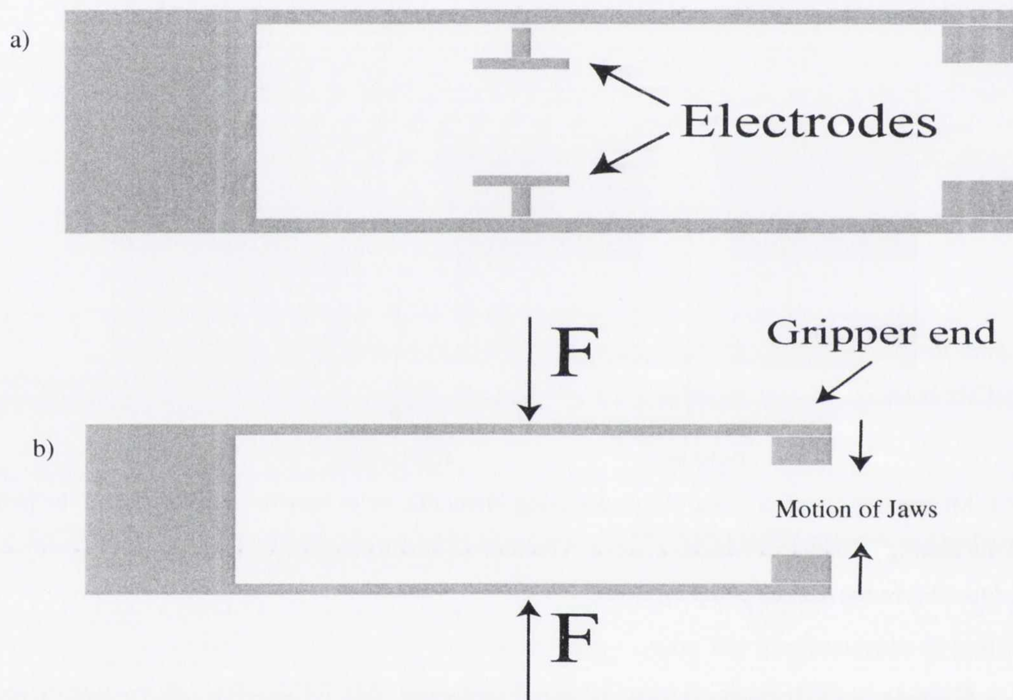

Fig. F.3: Micro-grippers actuated using bimetallic strips- a) each electrode is contacted using a bimetallic strip allowing a bias to be applied between them, thus causing motion of the jaws; b) a force, F, can also be applied to the gripper arms directly by means of heated bimetallic strips.

F.4. Motors (Microelectromechanical systems (MEMS) with micro-actuation)

The actuation forces for motors are primarily electrostatic forces. The sliding force generated in pairs of electrically energised misaligned plates prompts the required relative motion in a linear motor. Fig. F.4 illustrates the working principle for the linear

motion between two sets of parallel base plates. Each of the two sets of base plates contains a number of electrodes made of an electrically conducting material. All of these electrodes have a length *W*. The bottom base plate has an electrode pitch, *W*, whereas the top base plate has a slightly different pitch, say *W+W/3*. The two sets of base plates are initially misaligned by *W/3*, as shown in the Fig. F.4. The bottom plates are set to be stationary, while the top plates can slide in the horizontal plane. Therefore, on electrically energising a pair of electrodes, namely *A* and *A'*, induces movement of the top plate to the left until *A* and *A'* are fully aligned. At that moment the electrodes *B* and *B'* are misaligned by the same amount, i.e. *W/3*. One can then energise this misaligned pair, and as a result prompt the top plates to move by another *W/3* distance toward the left. This process can be continued. In conclusion, with carefully arranged electrodes in the top and bottom base plates and proper pitches, one can create the necessary electrostatic forces that are required to provide the relative motion between the two sets of base plates. Contact to the electrodes, for example *A* and *A'*, using bimetallic strips allows for the desired motion to be achieved through the application of an appropriate bias between them, while the use of an array of bimetallic strips allows for controlled linear motion. Rotary micromotors can also be operated by a similar principle. In addition, harnessing the forces generated by moving bimetals can also be adapted to operate such motors.

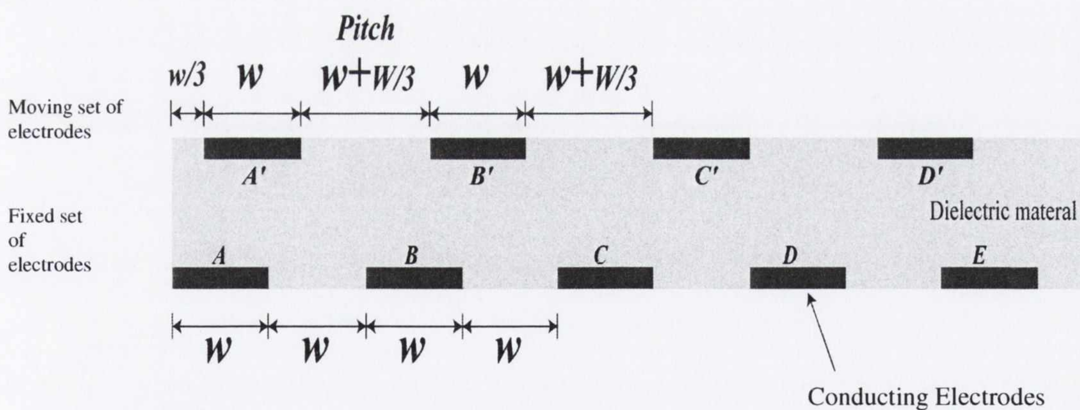

Fig. F.4: Linear motion is induced on contacting conducting electrodes, for example *A* and *A'*, using bimetallic strips and applying an appropriate bias between them.

F.5. Temperature Distribution Controllers

Using an array of bimetallic strips it is possible to create temperature gradients along a sample on contacting, through the passage of different currents between the strips. This is illustrated in the F.5.1.

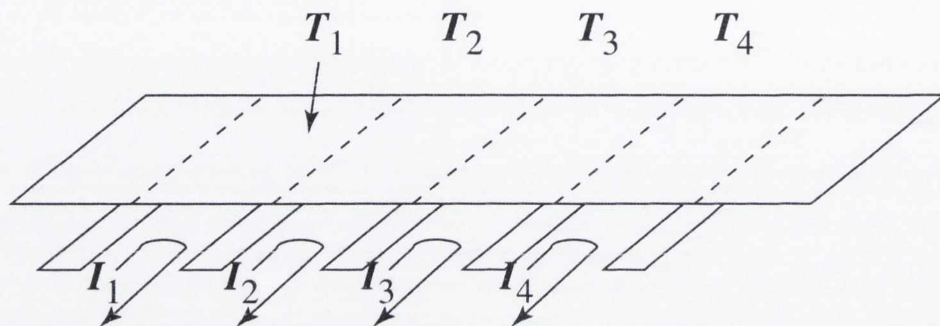

Fig. F.5.1: Using an array of strips it is possible to control the heat distribution along a sample.

This may be used as:

A) A Diffusion Controller-

The diffusion process is the introduction of a controlled amount of foreign material into selected regions of another material. Diffusion is strongly dependent on temperature. A temperature distribution along a sample allows the distribution of species at the surface and in the bulk to be controlled as shown Fig. F.5.2 below:

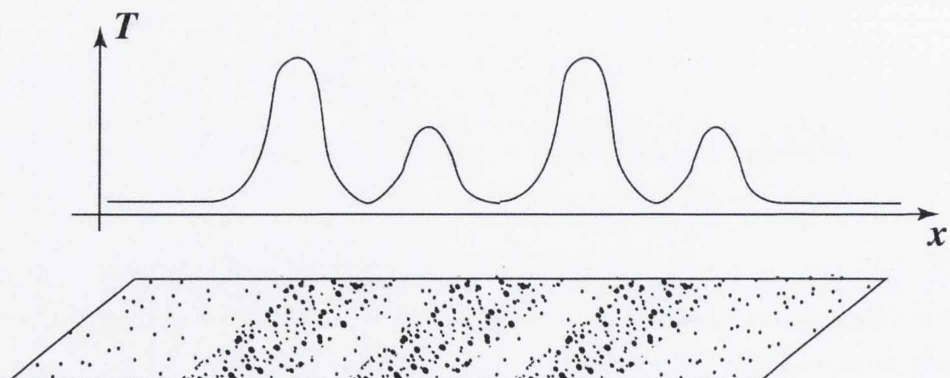

Fig. F.5.2: The distribution of species can be controlled by controlling the temperature at different regions.

B) Reaction Rate Controller-

Reaction rates are also strongly dependent on temperature. Having a temperature distribution along a sample allows the reaction rates to be controlled, e.g. film growth (see Fig. F.5.3).

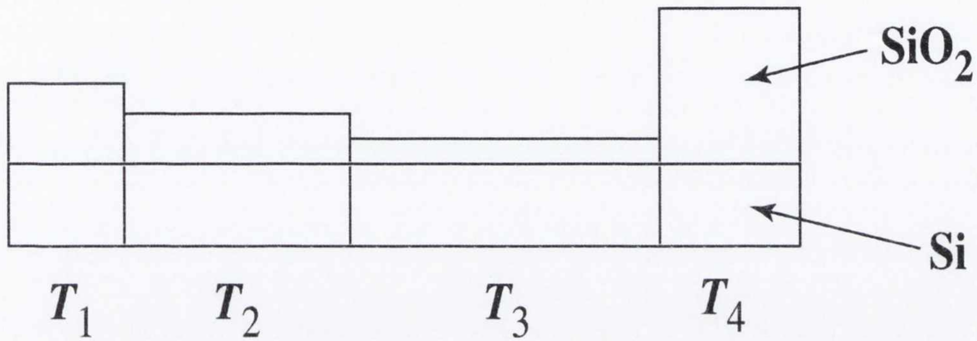

Fig. F.5.3: Film thickness distribution due to temperature gradients.

F.6. Voltage Sources

Certain crystals, such as quartz, deform with the application of an electric voltage. The reverse is also valid, i.e. an electric voltage can be generated across the crystal when an applied force deforms the crystal. This mechanical force may be applied using bimetal strips as illustrated Fig. F.6 below, thus producing a source of potential energy, i.e. voltage.

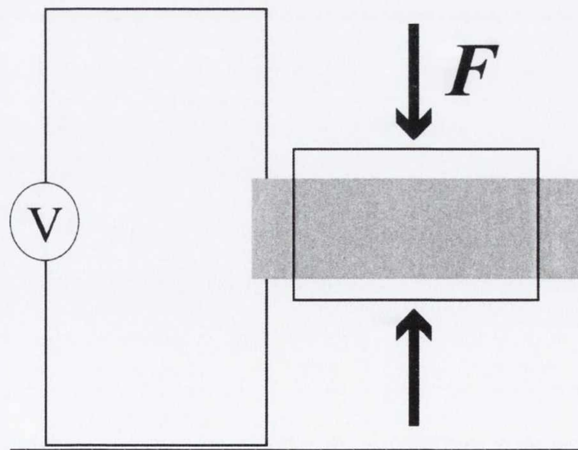

Fig. F.6: Harnessing the forces generated by moving bimetals on heating can be used to provide a source of voltage.

F.7. Regionalised Polarisation Controller

Materials may be polarised on contacting using bimetallic strips by applying a bias between the strips as illustrated in Fig. F.7 below:

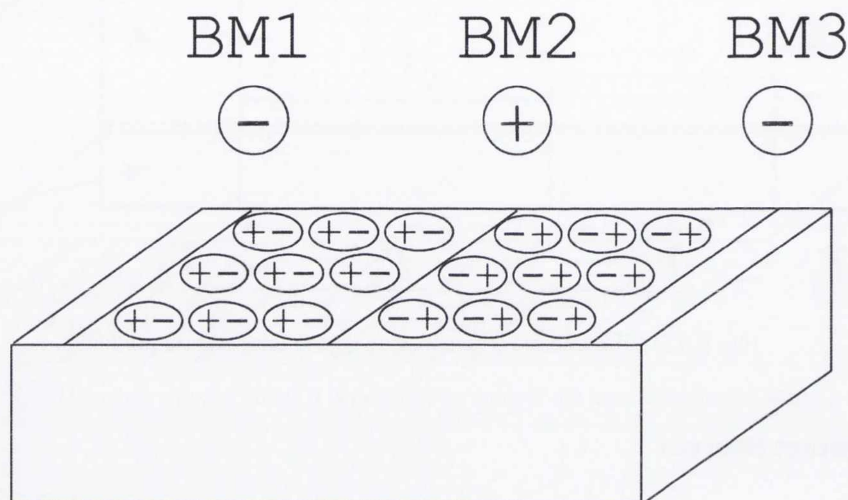

Fig. F.7: Polarisation controller.

An array of bimetallic strips allows selective regions to be polarised. Such selective polarisation would provide interesting optical applications.

F.8. Electrohydrodynamics

Electrohydrodynamics (EHD) deals with the motion of fluids driven by an electric field applied to the fluids. There are two principal applications of EHD: (1) electro-osmotic pumping and (2) electrophoretic pumping. These unique pumping techniques are used to move chemical and biological fluids in channels with extremely small cross sections, ranging from square micrometers to square millimetres at flow rates in the order of cubic micrometers per second. Microfluidics is widely used in the pharmaceutical industry and in biochemistry analysis. Bimetallic strips can be used to make contact with such fluidic cells allowing the required electric fields to be applied. With the use of an array of strips it is possible to generate electric field gradients which may be advantageous for such electrohydrodynamic applications.

F.9. Heat Valve

Through contacting a sample with a bimetal, controlled amounts of heat (Q) may be transferred either from the bimetal to the sample ('normally on', i.e. heat bimetal) or from the sample to the bimetal ('normally off', i.e. don't heat bimetal). This would have interesting biological applications. This provides us with a new method to transfer controlled amounts of heat to or from a sample. Conventional methods can only control the temperature (T). See Fig F.8 below.

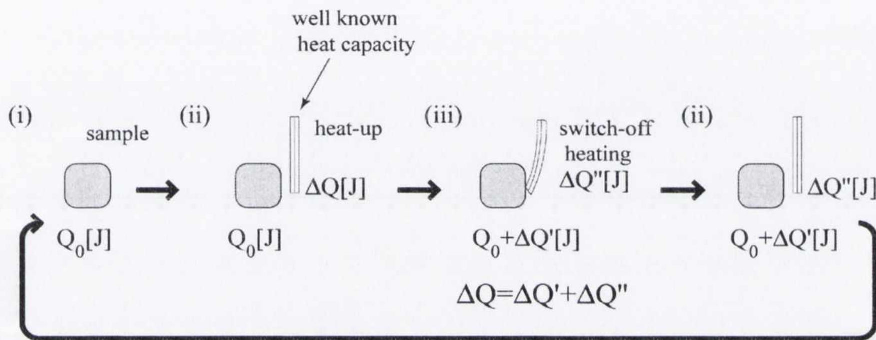

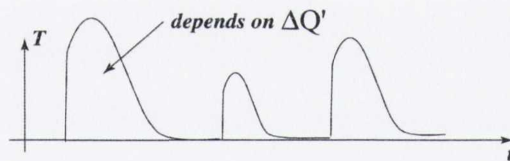

This is a example of 'normally on'. We can apply this idea for the 'normally off'.

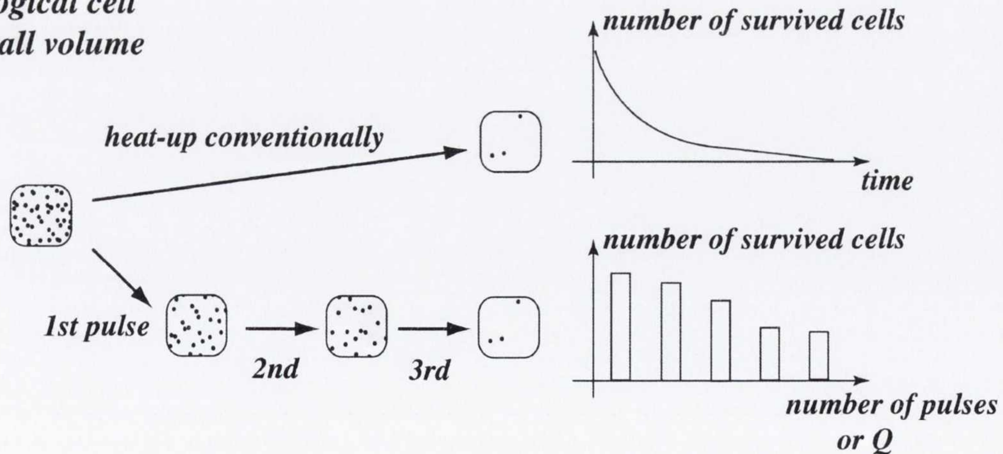

Fig. F.8: Heat valve idea- predefined amounts of heat are transferred from the bimetal to the sample.

F.10. Smart Source

By controlling the heating position using bimetallic strips we can create a 'smart source'. This type of system would have applications for chemical vapour deposition and epitaxy as displayed in Fig F.9.

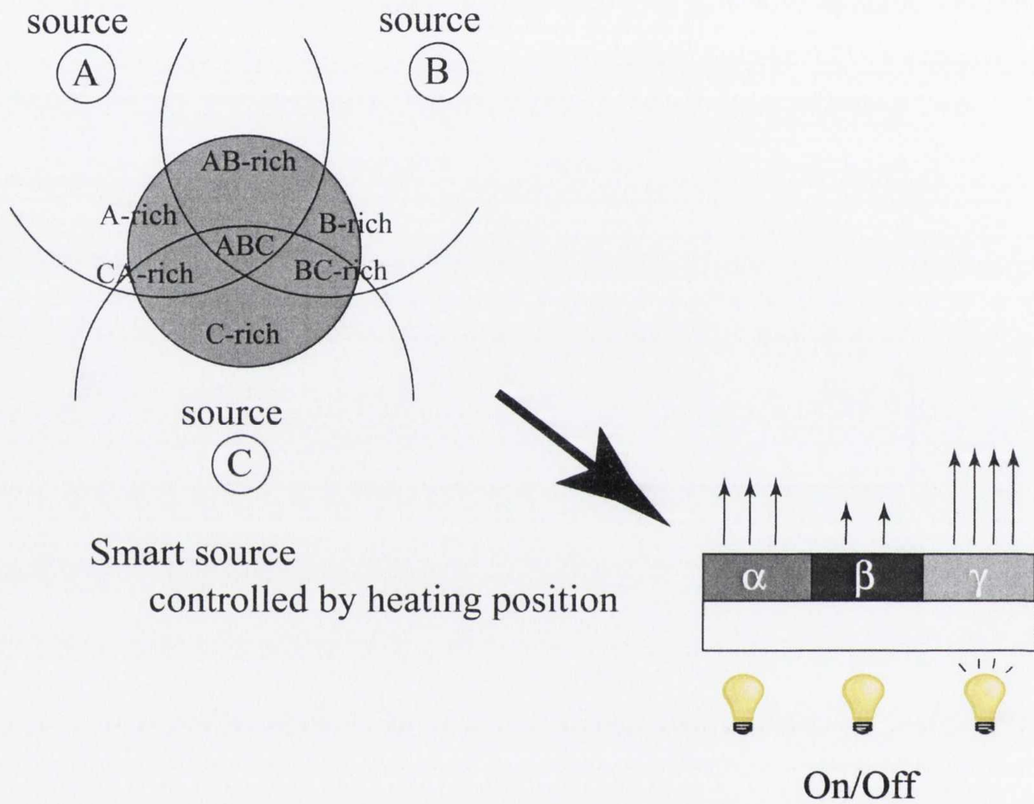

Fig. F.9: Smart source created via controlling heating position

References:

[1] T. Narushima, N. T. Kinahan, and J. J. Boland, Review of Scientific Instruments 76, 095113 (2005).

[2] Patent filed to the Irish Patent Office in Sept. 2005.

Appendix G: Reducing the Sample Width- Implications for STM and Surface Stress Measurement Capabilities

A method to heat a free standing cantilever sample using electron bombardment was introduced in chapter 6. However, in order to improve uniformity of heating and prevent hot spots forming on the sample surface (i.e. melted regions), the sample width is typically reduced from 10 mm to 6 mm. Fortunately, this amendment has no serious implications for our measurement capabilities as demonstrated in this appendix.

G.1. Improving Heating Uniformity during Electron Bombardment

- A cantilever sample with a width of 10 mm demands large input power in order to heat a 10 mm^2 surface area, thus removing the oxide layer.
- However, due to the architecture of the sample (large heat sink) difficulties arise in achieving a uniform temperature gradient across this heated area using the electron bombardment technique. This difficulty is amplified by the fact that a heated filament is hottest at the central filament coil. Therefore, a greater yield of thermionic electrons [1] are liberated from this region (see Fig G.1), inherently resulting in a power input gradient across the desired area; the consequences are displayed in Fig. G.2.

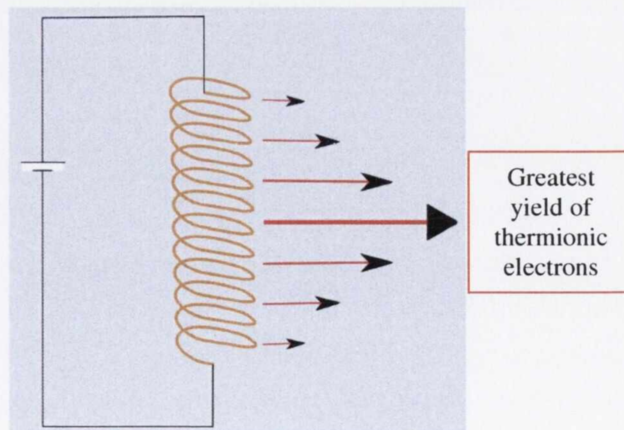

Fig. G.1: A resistively heated filament by nature is hottest at the central coil due to radiative heating from neighbouring coils. This results in a greater yield of thermionic electrons from this region.

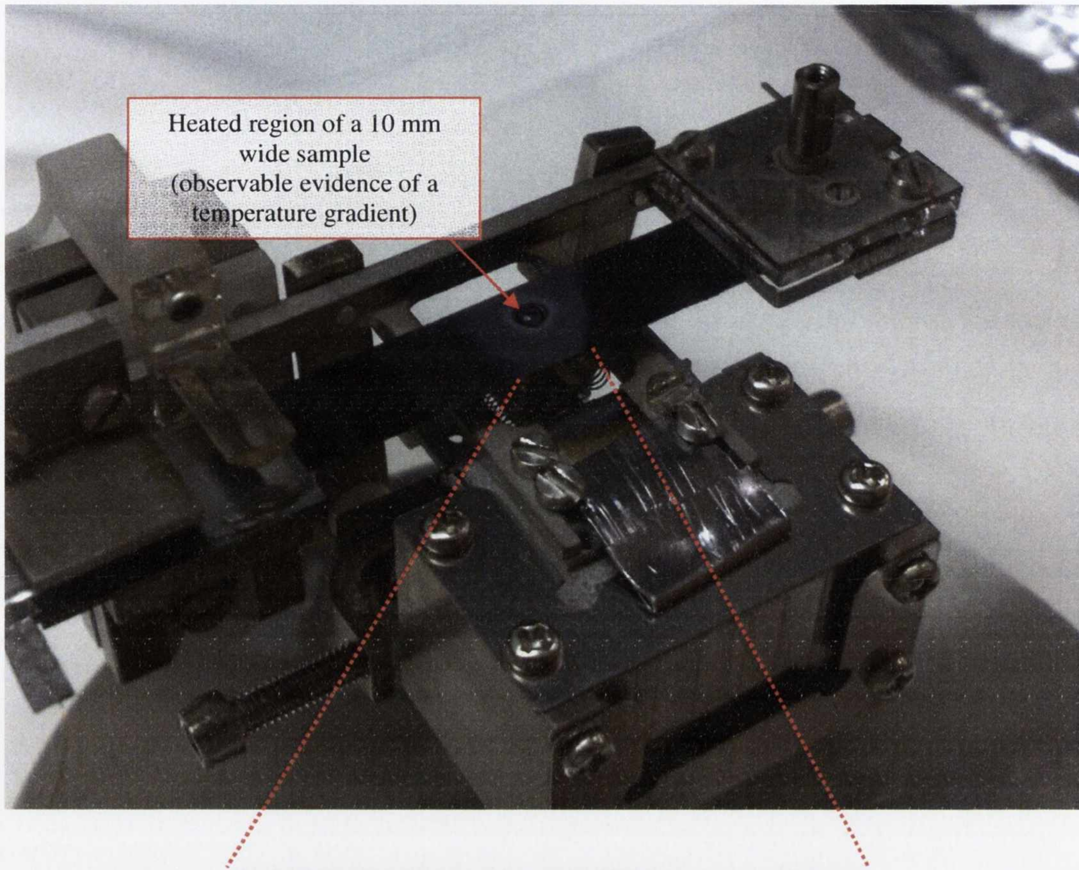

Fig. G.2: Due to the architecture of a 10 mm wide cantilever sample, a large amount of power is required to achieve the desired temperature at the extremities of the heated area. Under these conditions there is a high probability of melting at the central region, due to superior radiative and bombarding power at this zone. This event is not conducive to experiments; however, reducing the sample width improves the situation dramatically.

- One way to improve the heating uniformity and prevent surface melting is to reduce the sample width.
- For our configuration, a 6 mm wide sample has proven to be optimal not only for sample heating, but also in conserving our STM and stress measurement capabilities (as demonstrated in sections G.2 and G.3, respectively). This reduction in width is very effective in producing the desired clean surface area (10x6 mm^2) under lower input power conditions.

G.2. STM Capability- Effect of a Reduced Sample Width

- In order to observe atomic structure via STM on a cantilever sample, the free end deflection needs to be suppressed, as discussed in chapter 6 and depicted in Fig. G.3 below.

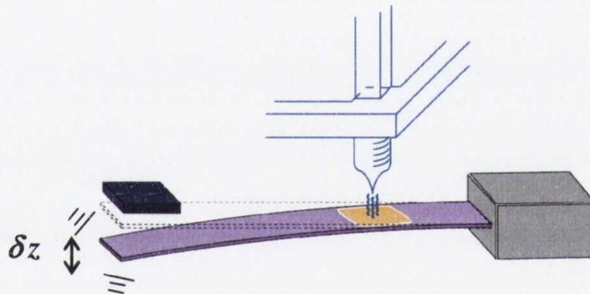

Fig. G.3: Schematic diagram demonstrating the natural oscillation of a cantilever sample which results in a free end deflection, δz. This natural movement leads to STM difficulties and must be suppressed for successful operation.

- The spring constant of a cantilever sample is defined as, $k = \frac{Ewt^3}{4l^3}$, where *w, t, l* and *E* are width, thickness, length and Young's modulus of the cantilever sample, respectively [2]. It is evident from this equation that adjusting the sample width should not have a dramatic influence on the spring constant when compared to cubic influence of the sample thickness and length. The spring constant in turn is related to

the free end deflection, δz_{p-p}, by: $\delta z_{\text{p-p}} = 2\sqrt{2}\delta z_{\text{rms}} \approx 4\sqrt{k_B T / \pi k}$, where T is the sample temperature [2].

- From the above equations we can estimate the free end deflection as a function of sample width (assuming that the sample is at room temperature). Reducing the cantilever width from 10 mm to 6 mm, for a 280 micron thick cantilever of length 0.05 m, results in a free end deflection increase from 0.016 nm to 0.02 nm. This condition is quite sufficient to observe Si(111)-7x7 adatoms via STM, and therefore does not jeopardise our imaging capability. (It should be noted that a slight increase in sample thickness can easily compensate for this free end deflection off-set).

G.3. Stress Measurement Capability- Effect of a Reduced Sample Width

- As previously mentioned, cantilever bending is detected capacitively by assuming that the sample and reference electrode arrangement form a simple parallel plate capacitor. When there is a spacing variation, Δd, from the initial spacing, d_0, the change in capacitance is given by, $\Delta C(\Delta d) \equiv C(d_0 + \Delta d) - C(d_0) \cong \frac{\varepsilon_0 S}{d_0^2} \Delta d$, where, S is the area of each capacitor plate and ε_0 is the vacuum dielectric constant. The change in capacitance is measured using a high precision capacitance bridge and can be related to the surface stress change, $\Delta\sigma$, via the Stoney equation [3].
- Reducing the sample width results in a decrease in our stress detection capability (due to a decrease in the area of the capacitor plates). We estimated that a reduction in sample width from 10 mm to 6 mm results in a decrease in our stress detection resolution of approx. 38.4 % (for a 280 micron thick cantilever sample and assuming a capacitance detection resolution of 1.9 aF). This corresponds to a decrease of approximately a few meV/atom in strain energy, and is more than sufficient to investigate atomic scale interactional forces at surfaces.
- Therefore, reducing the sample width has no serious implications on our stress measurement capability.

References:

[1] http://en.wikipedia.org/wiki/Thermionic_emission.

[2] T. R. Albrecht *et al.*, Journal of Applied Physics **69**, 668 (1991).

[3] G. G. Stoney, Proceedings of the Royal Society of London, Series A **82**, 172 (1909).

Appendix H: Electron Bombardment Heating of a Cantilever Sample

An electron bombardment heating system is also employed for regionalised heating of our cantilever samples and is discussed at length in chapter 6. The basic set-up is shown in Fig. H.1 below.

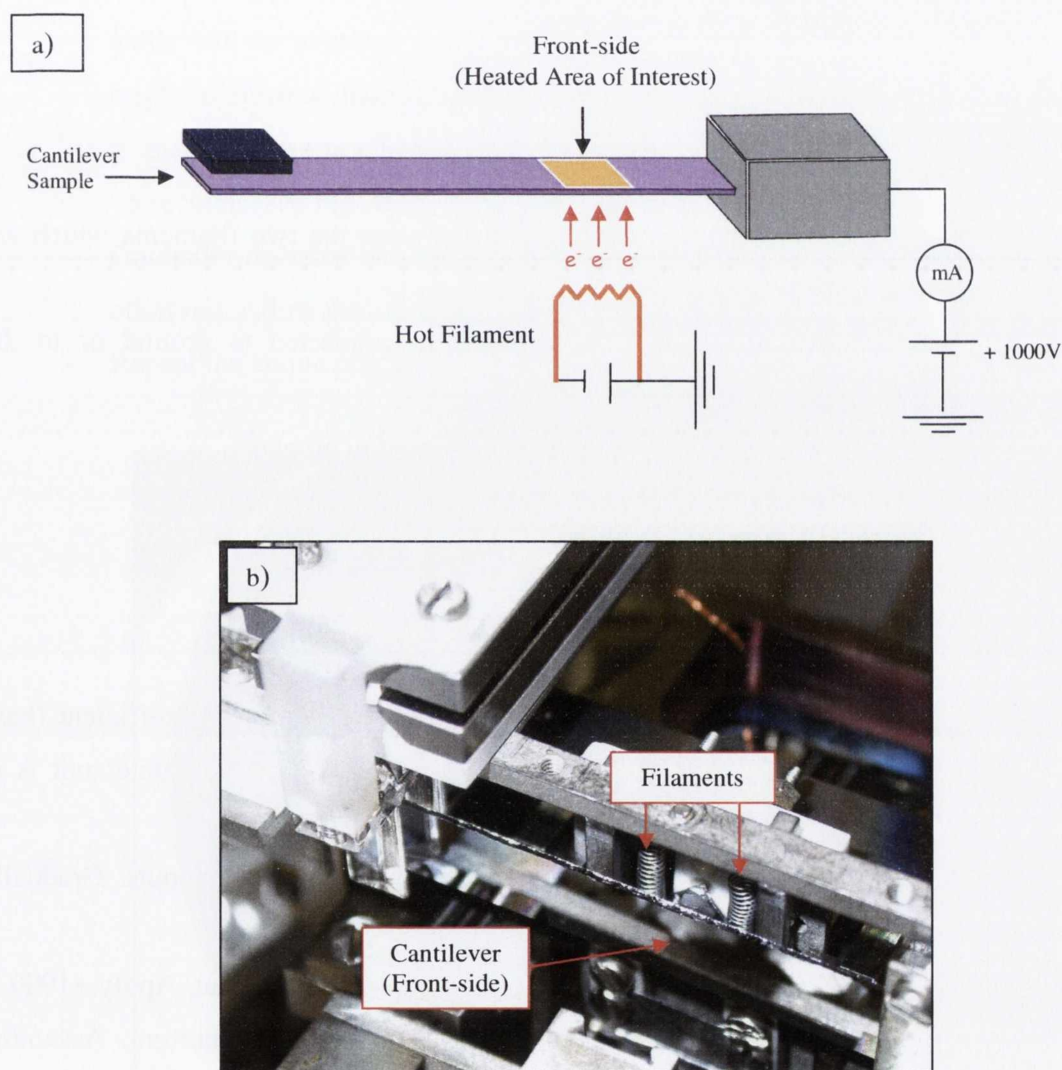

Fig. H.1: a) Schematic diagram illustrating electron bombardment of a cantilever sample, which produces a locally heated region; b) photograph of the basic heating components. The impinging electrons strike the back-side of the cantilever sample.

In short, the set-up consists of a thoriated tungsten filament which can source an electron current via thermionic emission [1, 2]. A high positive voltage can then be applied to the sample such that electrons bombard the surface inducing a heating effect [3]. Using this method, temperatures greater than 1400 K can be easily achieved. Consequently, extremely clean Si(111)-7x7 surfaces can be prepared; the experimental procedure to prepare this surface using the abovementioned method is the subject of this appendix.

H.1. Electron Bombardment Heating

- Basic Operation – Checks

  - Check for an electrically conductive path between the two filaments which are connected in series.
  - Check that the filaments are not electrically connected to ground or to the cantilever sample.
  - Check that the sample is not electrically connected to ground.
  - Ensure all power supply units are sufficiently grounded for safety.

- Basic Operation – Flash Procedure

  - Before flashing ensure that the base pressure in the chamber is sufficient (base pressures $<5\times10^{-11}$ Torr are typically achievable) and that the shield unit is in place.
  - Connect a high-current power supply to the filament coaxial inputs. Gradually increase the current to around 1.3 A.
  - Connect a high-voltage power supply to the sample coaxial input. Apply +1000 V to the sample while carefully monitoring the bombardment current. Assuming fully activated filaments [4, 5], a current of approximately 1.3 A and an accelerating voltage of +1000 V should yield a bombardment current of approximately 1.0 mA; this set of values represents the base bombardment condition. Modulate the filament current as necessary in order to achieve this

condition. (Note: for a fully activated filament the bombardment current is extremely sensitive to small changes in filament current).

- Quickly increase the value of the filament current until a stable bombardment current of approx. 10 mA is observed. This is the condition at which the filament emission is stabilised prior to flashing the sample, while also heating the sample to a relatively high temperature. Maintain this condition for 5 seconds.
- Quickly increase the value of the filament current until a stable bombardment current of approx. 25-28 mA is observed. This is the condition at which the native oxide will be expelled from the sample surface, indicated by the presence of a bright, uniformly distributed, yellow/white sample colour (~1400 K) coupled with a sharp increase in chamber pressure (~3×10^{-10} Torr). Maintain this condition for ~5 seconds; see Fig. H.2.
- Gradually decrease the filament current until the base bombardment condition is observed. Allow the sample to cool for 2 minutes.
- Repeat the above procedure 3 times.

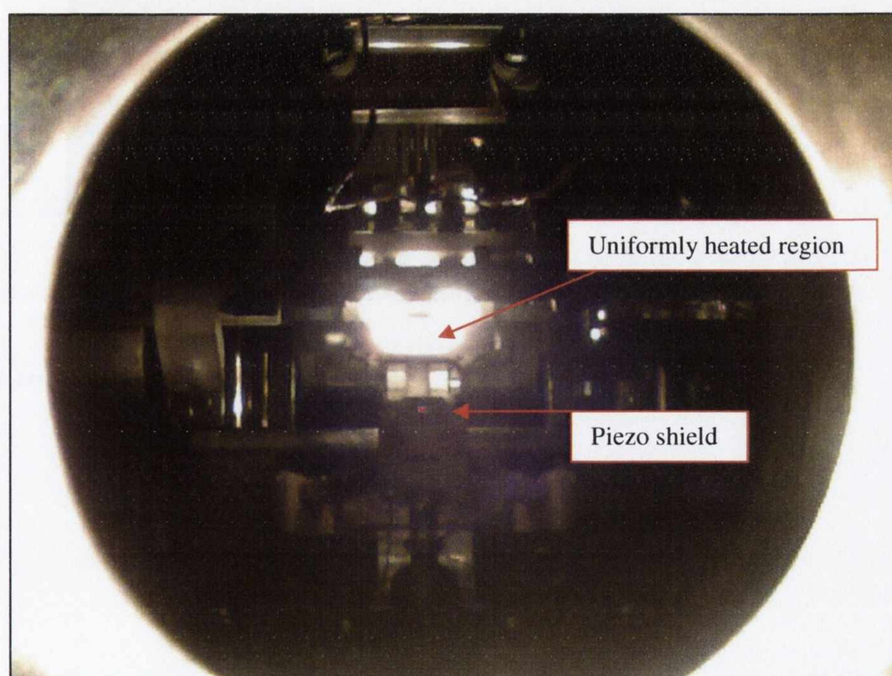

Fig. H.2: On flashing, uniform regionalised heating of the cantilever surface is clearly observed.

H.2. Clean Si(111)-7x7 Surfaces

- As a result of the performing the above procedure, clean Si(111)-7x7 surfaces are easily achievable. A characteristic surface prepared by this heating method is displayed in Fig. H.3. The prepared surface exhibits large carbon free terraces, and virtually defect free 7x7 unit cells.
- This observed surface condition (i.e. large terrace widths and defect free adatom sites) is extremely conducive to stress propagation on reaction.

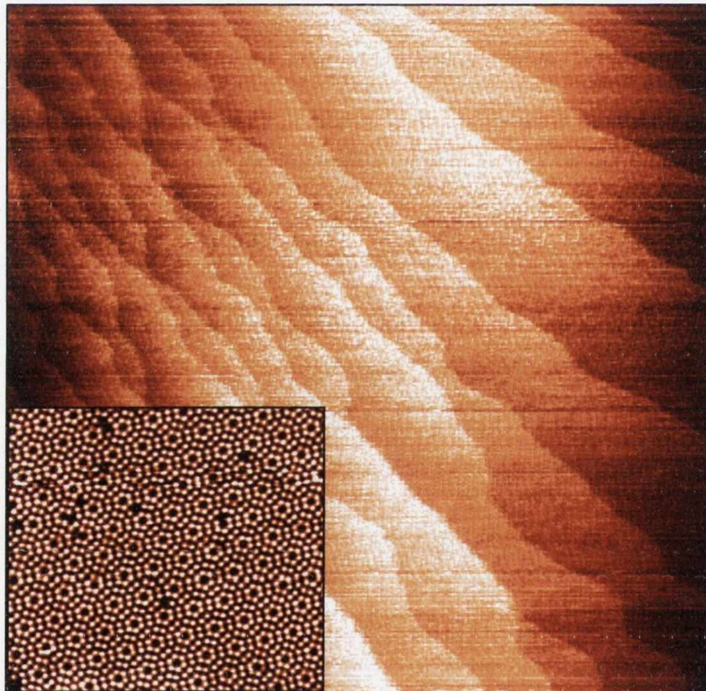

Fig. H.3: Image of a Si(111)-7x7 surface which was successfully prepared via electron bombardment regionalised heating of the cantilever sample.

References:

[1] S. Dushman, Reviews of Modern Physics **3**, 190 (1931).

[2] I. Langmuir, Journal of the Franklin Institute **217**, 543 (1934).

[3] J. T. Yates, *Experimental Innovations in Surface Science: A Guide to Practical Laboratory Methods and Instruments* (Springer, Newark, 1997).

[4] R. O. Jenkins, and W. G. Trodden, British Journal of Applied Physics **10**, 10 (1959).

[5] K. H. Kingdon, and I. Langmuir, Physical Review **22**, 148 (1923).

Appendix I: Capacitance Bridge Operation

The stress-induced deflection of a silicon cantilever sample is monitored by measuring the change in capacitance between the sample and one of two adjacent 1 cm^2 molybdenum electrodes located either side of the sample. Changes in capacitance are measured using a high-precision Andeen Hagerling AH2550A transformer-ratio arm capacitance bridge [1]. These changes in capacitance may be further represented as changes in surface stress by assuming a parallel-plate measurement model and applying the Stoney equation [2]. This appendix provides a brief description of the basic operation principle of the abovementioned capacitance bridge, in addition to presenting measures to ensure and improve accurate high precision cantilever deflection measurements when using capacitive sensing.

I.1. Capacitance Bridge Operation Principle [1]

- Fig. I.1 below presents a schematic of the basic circuit design of our bridge.

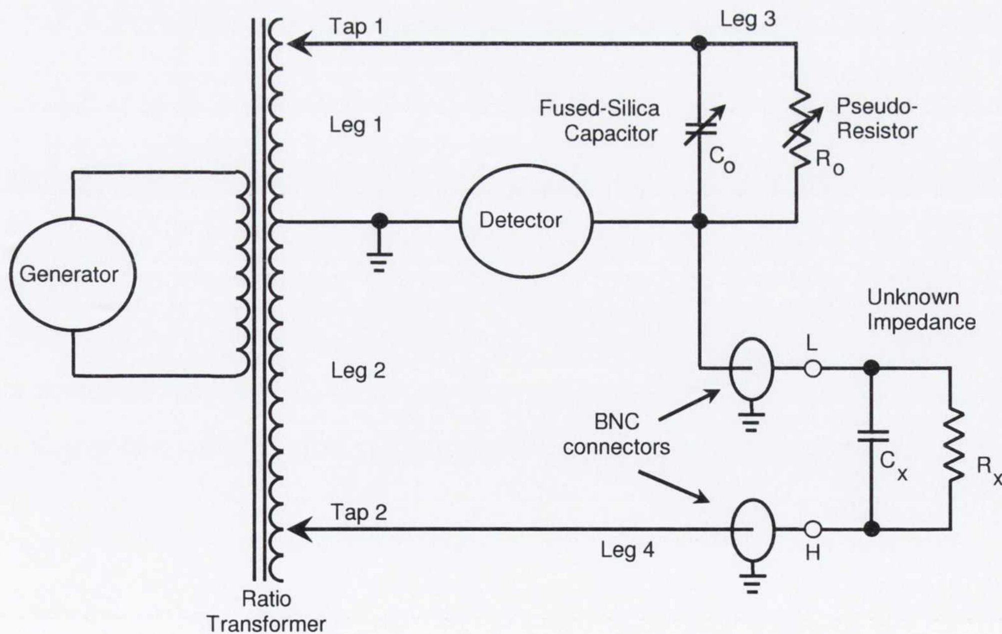

Fig. I.1: Basic capacitance bridge circuit [1].

- The voltage generator produces a sine wave signal at a frequency of 1 kHz. This sine wave signal excites a ratio transformer divided into legs 1 and 2 of the bridge circuit.
- Each of these legs consists of a single tap incorporating a large number of precision-wound coils. The adjustment of these taps permits the application of precisely defined voltages to legs 3 and 4 of the bridge circuit.
- Leg 3 of the bridge circuit consists of a combination of one of several fused-silica reference capacitors and additional circuitry necessary for simulating a stable resistor, while leg 4 consists of the unknown impedance whose capacitive component is to be measured.
- The bridge selects appropriate values for the resistance, R_0, and capacitance, C_0, of leg 3 while precisely balancing the voltage applied to the tap of leg 1, V_1, and the tap of leg 2, V_2, until the voltage measured at the detector reaches a minimum.
- Once this condition has been met, the values of the unknown impedance, R_x, and the unknown capacitance, C_x, can be calculated according to the equations below:

$$C_x = C_0\left(\frac{V_1}{V_2}\right), \; R_x = R_0\left(\frac{V_2}{V_1}\right).$$

I.2. Measures to Ensure Accurate Sensing

- Capacitance values measured using the two-terminal electrode configuration described above may contain a variable parasitic component due to the presence of fringing fields at the electrode edges [3]. This results in reduced measurement linearity.
- This parasitic component is negligible if the distance between the electrodes is significantly less than the respective electrode dimensions, otherwise requiring the use of a geometry-dependent corrective factor in configurations where this is not the case [3].
- The effects of fringing fields at the electrode edges may be significantly reduced by implementing a three-terminal electrode configuration involving the introduction of a

grounded guard electrode [3]. This results in improved measurement linearity, while also shielding the measurement from the presence of noise-inducing electric fields.

- The quality of the parallel-plate measurement model assumed during calculation of changes in surface stress may be improved by electro-polishing the surfaces of the molybdenum electrodes. This results in microscopically flat electrode surfaces better agreeing with the ideal parallel-plate measurement model.
- The linearity and stability of the measurement may be further improved by implementing a differential capacitance configuration [4].

References:

[1] Model AH 2550A, Andeen-Hagerling, Inc., 31200 Bainbridge Road, Cleveland, Ohio 44139-2231 (www.andeen-hagerling.com/ah2550a.htm).

[2] G. G. Stoney, Proceedings of the Royal Society of London, Series A **82**, 172 (1909).

[3] R. Pallàs-Areny, and J. G. Webster, *Sensors and Signal Conditioning* (Wiley Interscience, New York, 2001).

[4] A. L. Hugill, Journal of Physics E: Scientific Instruments **15**, 597 (1982).